



Universiteit  
Leiden  
The Netherlands

## Scaling, clusters and geometry

Qian, Xiaofeng

### Citation

Qian, X. (2006, September 14). *Scaling, clusters and geometry*. Retrieved from <https://hdl.handle.net/1887/4558>

Version: Corrected Publisher's Version

License: [Licence agreement concerning inclusion of doctoral thesis in the Institutional Repository of the University of Leiden](#)

Downloaded from: <https://hdl.handle.net/1887/4558>

**Note:** To cite this publication please use the final published version (if applicable).

# Scaling, Clusters and Geometry

Xiaofeng Qian



# Scaling, Clusters and Geometry

PROEFSCHRIFT

TER VERKRIJGING VAN  
DE GRAAD VAN DOCTOR AAN DE UNIVERSITEIT LEIDEN,  
OP GEZAG VAN DE RECTOR MAGNIFICUS DR. D. D. BREIMER,  
HOGLERAAR IN DE FACULTEIT DER WISKUNDE EN  
NATUURWETENSCHAPPEN EN DIE DER GENEESKUNDE,  
VOLGENS BESLUIT VAN HET COLLEGE VOOR PROMOTIES  
TE VERDEDIGEN OP DONDERDAG 14 SEPTEMBER 2006  
TE KLOKKE 15.15 UUR

DOOR

Xiaofeng Qian

GEBOREN IN 1976 TE JIANGXI, CHINA

Promotor: Prof. dr. H. W. J. Blöte  
Referent: Dr. P. J. H. Denteneer  
Overige leden: Prof. dr. J. M. J. van Leeuwen  
Prof. dr. P. H. Kes  
Prof. dr. W. van. Saarloos  
Prof. dr. B. Nienhuis (Universiteit van Amsterdam)  
Dr. J. R. Heringa (Technische Universiteit Delft)

*'The Master said: I once spent a whole day without food and a whole night without sleep, in order to meditate. It was no use. It is better to learn.'*

Confucius, The Analects.

To the memory of my mother and my grandparents



# Contents

<b>1</b>	<b>Introduction</b>	<b>1</b>
1.1	General introduction to phase transitions . . . . .	1
1.1.1	Phase transitions and their classification . . . . .	1
1.1.2	Nature of phase transitions . . . . .	2
1.2	Investigation tools . . . . .	2
1.2.1	Mathematical tools . . . . .	3
1.2.2	Computational tools . . . . .	6
1.3	Motivation and outline . . . . .	8
	Bibliography . . . . .	11
<b>2</b>	<b>Critical frontier of the triangular Ising antiferromagnet in a field</b>	<b>13</b>
2.1	Introduction . . . . .	13
2.2	Renormalization analysis . . . . .	16
2.2.1	Mapping on the Gaussian model . . . . .	16
2.2.2	Renormalization flow . . . . .	18
2.3	Numerical methods . . . . .	21
2.3.1	Transfer-matrix calculations . . . . .	21
2.3.2	Monte Carlo results . . . . .	25
2.4	Fit and discussion . . . . .	31
2.4.1	Roots of the O(2) invariant polynomials . . . . .	31
2.4.2	Renormalization solution for small field . . . . .	32
2.5	Conclusion . . . . .	33
	Bibliography . . . . .	35
<b>3</b>	<b>Triangular Ising model with nearest- and next-nearest-neighbor couplings in a field</b>	<b>37</b>
3.1	Introduction . . . . .	37
3.2	Numerical methods . . . . .	40
3.2.1	Transfer-matrix calculations . . . . .	40
3.2.2	Monte Carlo simulations . . . . .	42
3.3	Numerical results for zero field . . . . .	42
3.3.1	Results for the ferromagnetic transition ( $K_{nn} > 0$ ) . . . . .	42
3.3.2	Results for the antiferromagnetic region ( $K_{nn} < 0$ ) . . . . .	43

3.3.3	Shape of the critical lines for small $ K_{mn} $ . . . . .	44
3.3.4	The algebraic phase . . . . .	45
3.4	Results for nonzero field . . . . .	48
3.5	Discussion . . . . .	52
	Bibliography . . . . .	55
<b>4</b>	<b>Simulation algorithms for the random-cluster model</b>	<b>57</b>
4.1	Introduction . . . . .	57
4.2	The existing algorithms . . . . .	59
4.3	Tests and application of the exiting algorithms . . . . .	62
4.3.1	Application to specific-heat calculation . . . . .	62
4.3.2	Efficiency of the algorithms . . . . .	64
4.3.3	Dynamic exponent of the cluster algorithm . . . . .	66
4.4	Single-cluster algorithm . . . . .	67
4.4.1	Proof of detailed balance . . . . .	68
4.4.2	Other versions . . . . .	69
4.4.3	Test and dynamic exponent . . . . .	69
4.5	Discussion . . . . .	71
	Bibliography . . . . .	73
<b>5</b>	<b>Percolation in one of <math>q</math> colors near criticality</b>	<b>75</b>
5.1	Introduction . . . . .	75
5.2	Algorithms and critical points . . . . .	77
5.2.1	Critical points . . . . .	77
5.2.2	Percolation algorithms . . . . .	79
5.3	The Ising case $q = 2$ . . . . .	79
5.4	Potts models with $q \neq 2$ . . . . .	82
5.5	Discussion and miscellaneous results . . . . .	83
	Bibliography . . . . .	87
<b>6</b>	<b>Dilute Potts model in two dimensions</b>	<b>89</b>
6.1	Introduction . . . . .	89
6.2	Algorithms . . . . .	92
6.2.1	Transfer matrix technique . . . . .	92
6.2.2	Monte Carlo technique . . . . .	95
6.3	The line of fixed points for $V = 0$ . . . . .	96
6.3.1	Solving the equations for the fixed points . . . . .	96
6.3.2	Polynomial approximations at the line of fixed points . . . . .	100
6.3.3	Consistency with theory and universality . . . . .	102
6.4	Phase diagram for $q = 2 - \sqrt{2}$ . . . . .	104
6.4.1	Equivalences and exact limits . . . . .	104
6.4.2	Numerical results . . . . .	105
6.5	Miscellaneous results . . . . .	107

6.5.1	The Blume-Capel model and the dilute $q = 2$ Potts model . . . . .	107
6.5.2	Geometric tricritical fixed points for noninteger $q$ . . . . .	109
6.6	Conclusion . . . . .	113
	Bibliography . . . . .	115
	Appendix . . . . .	118
<b>7</b>	<b>Equivalent-neighbor Potts models in two dimensions</b>	<b>121</b>
7.1	Introduction . . . . .	121
7.2	Methods and sampled quantities . . . . .	123
7.3	Results for three-state Potts models . . . . .	125
7.3.1	Location and nature of the phase transitions . . . . .	125
7.3.2	Hysteresis loop . . . . .	128
7.3.3	Time evolution, histogram and dynamics . . . . .	129
7.3.4	Mean-field analysis for $q = 3$ . . . . .	131
7.4	Results for four-state Potts models . . . . .	133
7.4.1	Critical points . . . . .	133
7.4.2	Hysteresis loop . . . . .	135
7.5	Discussion and conclusion . . . . .	135
	Bibliography . . . . .	137
<b>8</b>	<b>Critical line of an <math>n</math>-component cubic model</b>	<b>139</b>
8.1	Introduction . . . . .	139
8.2	Self-dual plane of the $(N_\alpha, N_\beta)$ model . . . . .	141
8.3	The transfer matrix . . . . .	142
8.4	Determination of the critical line of the cubic model . . . . .	145
8.5	Universal properties of the cubic model . . . . .	147
8.6	Discussion . . . . .	152
	Bibliography . . . . .	155
<b>9</b>	<b>Universal parameters of three-dimensional Ising systems</b>	<b>157</b>
9.1	Introduction . . . . .	157
9.2	Models, simulations and random-number generator . . . . .	159
9.3	Separate finite-size-scaling analyses . . . . .	161
9.3.1	Dimensionless ratio $Q$ . . . . .	161
9.3.2	The susceptibility $\chi$ . . . . .	164
9.3.3	The derivative $Q_p$ . . . . .	164
9.4	Simultaneous finite-size-scaling analyses . . . . .	166
9.4.1	Simultaneous analysis of $Q$ . . . . .	166
9.4.2	Simultaneous analysis of $\chi$ . . . . .	166
9.4.3	Simultaneous analysis of $Q_p$ . . . . .	168
9.5	Discussion . . . . .	168
	Bibliography . . . . .	171

<b>Summary</b>	<b>173</b>
<b>Samenvatting</b>	<b>175</b>
<b>Acknowledgment</b>	<b>177</b>
<b>Curriculum Vitae</b>	<b>179</b>
<b>List of Publications</b>	<b>181</b>

# Chapter 1

## Introduction

### 1.1 General introduction to phase transitions

#### 1.1.1 Phase transitions and their classification

Our experience in daily life involves, among other things, ice, water, and steam. These are just one chemical compound ( $\text{H}_2\text{O}$ ) in three different states of aggregation. Indeed, theoretical physics satisfactorily explains (see, for instance, [1,2]) transitions between different phases of the same substance when the thermodynamic parameters, such as temperature or pressure, are changed. Such phase transitions are characterized by a singularity in certain thermodynamic properties, for instance, in the specific heat, as a function of the thermodynamic variables.

There are many well known examples of phase transitions, such as 1) transitions between solid, liquid, and gas phases; 2) ferromagnetic phase transitions associated with spin ordering; 3) superconducting transitions in certain metals at low temperatures; 4) Bose-Einstein condensation and the superfluid transition in liquid helium  $^4\text{He}$ ; 5) percolation transitions, which for instance occur when small metal particles are randomly distributed on an insulating substrate. At a rather sharply defined particle density, namely the percolation threshold, the system becomes a conductor.

According to the Ehrenfest classification [3,4], phase transitions can be labeled by the order of the derivatives of the free energy in which a discontinuity appears. Thus, first-order phase transitions are associated with discontinuities in first derivatives of the free energy. For instance, melting, which transforms a solid phase into a liquid phase, is associated with a jump in the energy, and thus is a first-order transition. Similarly, second-order phase transitions are associated with a discontinuity or a divergence in a second derivative of the free energy, for instance the discontinuity in the specific heat in the mean-field model [2]. Indeed, this classification was formulated before the discovery that many phase transitions in nature are not mean-field-like. Nowadays we know infinitely many different types of phase transitions. Maintaining the Ehrenfest classification would mean that we would have to distinguish not only first- and second-order transitions, but also third-, fourth-, fifth-, ..., up to infinite-order transitions. Two examples of such ‘third-order transitions’ are

presented in Chap. 4. We avoid this sort of complication by just talking about continuous transitions when the first derivatives of the free energy are continuous.

### 1.1.2 Nature of phase transitions

A continuous phase transition occurs at a point in the space of thermal parameters where the free energy displays a singularity as a function of these parameters. Such points are called *critical points*. At and near the critical points, there occur lots of interesting phenomena. These phenomena are called *critical phenomena*.

Phase transitions are usually accompanied by a change of symmetry of the system. The transition to a phase with a lower symmetry is called *symmetry-breaking*. For instance, the Ising ferromagnetic ordering transition to a magnetized phase dominated by up- or down-spins breaks the up-down symmetry of the high-temperature phase. Similarly, in the liquid-solid transition, the rotational symmetry of the liquid phase is broken. But in the gas-liquid transition it is not obvious what symmetry is broken.

The theory of phase transitions has shown that continuous phase transitions can be divided in different classes characterized by parameters known as *critical exponents*. For instance, when the temperature  $T$  approaches the critical point  $T_c$  the specific heat  $C$  usually displays a power law behavior as

$$C - C_0 \sim |T_c - T|^{-\alpha}, \quad (1.1)$$

where  $C_0$  is a constant. The exponent  $\alpha$  is called the critical exponent of the specific heat. There are several other critical exponents denoted by Greek symbols as  $\beta$ ,  $\gamma$ ,  $\delta$ ,  $\nu$ , and  $\eta$ , which describe the power-law behavior of various physical observables at and near the phase transition. It appears that phase transitions occurring in totally different systems sometimes are described by the same set of critical exponents. This phenomenon is called *universality*. There exists a lot of evidence to support the validity of universality, especially in two dimensions. We mention exact solutions of various two-dimensional Ising models, which consistently yield identical sets of critical exponents. In three dimensions, the empirical evidence is more limited so that it is necessary to perform numerical investigations.

Universality is satisfactorily explained by the renormalization theory [5–7] of phase transitions. The theory, while not rigorous, satisfactorily predicts that there are large sets of different physical systems in the same universality class. Moreover, the theory also suggests that the universal classification of a model depends only on very few factors, such as the dimensionality, the symmetry of the order parameter, and the range of the interactions. These factors include the microscopic structure of the system only when the type of symmetry breaking depends on it.

## 1.2 Investigation tools

Some statistical-physical models, for instance two-dimensional Ising models, can be (or have been) solved exactly. But for models in more dimensions, such as the three-dimensional

Ising model, or models with interactions of a longer range, such as the 2D Ising model with crossing bonds, exact solutions are available only in special cases. For this reason we need suitable numerical methods in order to obtain results of an approximate nature, but still of a sufficient accuracy to explore the physics of these models.

While Landau theory and mean-field theory provide a good picture of the universal properties of sufficiently high-dimensional systems, for lower dimensional systems, due to the fact that critical fluctuations may become important, we still need approximations involving mathematical and computational tools as alternative approaches.

## 1.2.1 Mathematical tools

### Renormalization group

One of the main mathematical tools to study critical points is the renormalization group (RG), which is based on the apparent fractal or scale-invariant aspects of critical configurations. A rescaling of the system thus leads to essentially the same system but with a reduced size. This concept of self-similarity appears to be very fruitful since it explains universality, and can be used to predict the critical exponents numerically. A renormalization group transformation is one that maps the partition function of a system on that of a smaller system. The new system is described by a set of parameters, such as temperature and magnetic field, that are functions of those of the original system. Renormalization transformations are assumed to be analytic. This means that the renormalized parameters are analytic functions of those of the original system. In general, the transformation appears to have *fixed points*: points that map onto themselves under the transformation. The analyticity of the transformation allows us to ‘linearize’ around the fixed point: in a small neighborhood, the new parameters depend linearly on the old ones. The coefficients describing this linear dependence form a matrix called ‘stability matrix’. Its eigenvectors correspond with directions with respect to the fixed point that are invariant under renormalization, and that may serve to define a coordinate system to describe the position of a model in parameter space. The coordinates in this system are called *scaling fields*. The advantage of using these scaling fields, instead of the original parametrization, is that each scaling field of a system close to the fixed point changes, under the transformation, by a constant factor: the eigenvalue of the corresponding direction of the eigenvector.

One can distinguish three types of scaling fields. Under a RG transformation, the scaling field may be (a) increasing, (b) decreasing or (c) remain unchanged. In the first case, the scaling field is said to be relevant; in the second, irrelevant and in the third, marginal. A remarkable fact is that, among infinitely many scaling fields, only very few are relevant. While we have thus far only spoken about the transformation close to the fixed point, the coordinate system can be extended to describe large parts of the parameter space. However, the relation between the scaling fields and the original parameters is then no longer linear, although still supposed to be analytic.

Phase transitions appear to occur when all relevant fields become zero. The critical singularities are determined by the eigenvalues of the stability matrix at the fixed point, even

if the system does not come close to the fixed point itself, which is the case if there are sufficiently large irrelevant fields. The exponents of the leading singularities in thermodynamic quantities are determined by the relevant eigenvalues.

### Conformal invariance

In general, renormalization transformations are *local* in nature: a local change of the original Hamiltonian leads only to a local change of the renormalized Hamiltonian. This opens the possibility to consider renormalization transformations of which the scale reduction factor is smoothly position dependent. We thus consider mappings between coordinate systems that may change the scale and the orientation while preserving the shape on a sufficiently small scale. In the language of differential geometry, the metric tensor should be a multiple of the unit tensor. But the proportionality ‘constant’ need not be constant in space. Such transformations are called ‘conformal transformations’.

The assumption of conformal invariance implies that the local Hamiltonian is unchanged under a conformal mapping. In general, one may not expect that conformal invariance is exactly satisfied in a critical lattice model; for instance, a regular lattice will in general not map on a regular lattice. Furthermore, the model will in general not be at the fixed points, so that the irrelevant fields will become position dependent. But in many critical systems, we may expect conformal invariance in an asymptotic sense: in sufficiently large systems, and for correlations on a large enough scale.

Assuming conformal invariance, a transformation between different geometries provides a relation between the correlation functions in both geometries. On large scales the mapping will be asymptotically exact. One extremely useful example is Cardy’s mapping [8] between the infinite plane and the surface of a cylinder. According to the mapping, a power-law decay of correlations in the infinite plane corresponds with exponential decay along the cylinder. Moreover, the exponent of the power-law decay is simply related to the correlation length on the cylinder. Since the circumference of the cylinder is finite, it is often feasible to calculate correlation functions along the length direction of the cylinder. Then, the conformal mapping reveals the correlation function in the infinite plane. Indeed, finite-size analyzes of models wrapped on a cylinder, using this conformal mapping, have been and are still being applied extensively, in order to analyze critical properties.

This mapping [8] predicts that the correlation length  $\xi$  on the surface of a cylinder with circumference  $L$  is related with the scaling dimension  $X$  associated with the pertinent critical correlation function, as

$$X \simeq \frac{L}{2\pi\xi}, \quad (1.2)$$

which becomes exact in the large  $L$  limit. For finite  $L$ , corrections to scaling occur which are due to the irrelevant fields. The correlation length  $\xi$  can be calculated from the eigenvalues of the transfer matrix whose transfer direction is along the length of the cylinder.

According to the theory of conformal invariance, the set of critical exponents of a universality class are in general restricted to a spectrum determined by a parameter  $c$ , the conformal anomaly. For ‘unitary’ models, without negative scaling exponents, this

parameter has a discrete spectrum for  $0 \leq c \leq 1$ , according to

$$c = 1 - \frac{6}{m(m+1)}, \quad (1.3)$$

where  $m$  is an integer  $m \geq 2$ . Then, the set of critical exponents is given by a formula known under the name of Kac formula. However, to predict the exponents, we should first know  $c$ , which is unknown in general. Fortunately, it can be calculated [9, 10] from the reduced free energy density  $f(L)$ , using the formula

$$f(L) \simeq f_\infty - \frac{\pi c}{6L^2}, \quad (1.4)$$

where  $f_\infty$  is the reduced bulk free energy density. This formula applies to the large- $L$  limit. The reduced free energy  $f(L)$  follows from the largest eigenvalue  $\lambda_0$  of the transfer matrix as

$$f(L) = -(\ln \lambda_0)/L. \quad (1.5)$$

### Mappings between lattice models

As we mentioned above, under a conformal mapping, a regular lattice can not, in general, be mapped on a regular lattice. However, there are also mappings between different lattice models. One category of such relations can be constructed between two models on lattices that are dual to one another. The essence is that under such a mapping, the partition sum of one model at high (low) temperatures can be expressed in the partition sum of another model at low (high) temperatures. This dual mapping relates the partition sums of two lattice models. These models may be different, in which case the mapping shows that they belong to the same universality class. But it is also possible that the lattice model is its own dual, in which case the dual transformation yields a relation between the partition sums of a lattice model at two temperatures. A mapping of this kind may reveal the location of the phase transition. In general, duality transformations, like renormalization and conformal transformations, are useful tools for the study of phase transitions and phase diagrams.

Besides dual transformations there are mappings that do not invert the temperature scale. They may lead to relations between models that are seemingly very different. For instance, let us consider the antiferromagnetic Ising model on a triangular lattice at zero temperature. This model has a highly degenerate ground state of a critical nature: the correlation functions decay as a power law with distance. When all bonds between pairs of parallel neighbor spins are erased, one obtains a lattice tiling with rhombi. This tiling can also be interpreted as a stack of cubes viewed from the (1,1,1) direction. Thus the zero-temperature antiferromagnetic triangular Ising model is equivalent with a solid-on-solid (SOS) model [11] which involves height variables. Furthermore, a renormalization mapping exists that relates the SOS model with the Gaussian model which is exactly solvable. The Coulomb gas theory yields exact results for many critical exponents. However, the renormalization mapping is not exact in the sense that it does not yield an exact value of the Gaussian temperature. Fortunately, one can exactly calculate the height-height

correlation function of the SOS model, which allows one to find the *exact* link between the SOS model and the Gaussian model.

Another mapping which has been extensively used in the literature and in this thesis, is the Kasteleyn-Fortuin mapping [12]. It provides a relation between the partition sums of the Potts model and the so-called random-cluster model. It generalizes the discrete values of Potts parameter  $q$  to continuous values in the random-cluster model. Another mapping, formulated by Baxter, Kelland and Wu [13], leads from the random-cluster model to the 6-vertex model, which is a limiting case of the Baxter model [14]. This second mapping enables another mapping on an SOS model, and thereby on the Gaussian model, so that the results of the Coulomb gas theory become available for the Potts and random-cluster models.

## 1.2.2 Computational tools

The assistance of computers in performing numerical tasks is very useful. Such computational tools enable the solution of many problems for which other approaches are not feasible. Among various computational methods, here we shall mainly use the Monte Carlo method and the transfer-matrix technique. These two methods are widely used in the study of critical phenomena and phase transitions in statistical physics. Each of them has its own advantages, and which of the two methods is most suitable therefore depends on the nature of the problem that has to be solved.

### Transfer matrix technique

Many physical properties of systems in thermal equilibrium systems can be calculated from the partition function. Once the partition sum  $Z$  is known, the expectation values of the system can be obtained, for instance by differentiation of the free energy which follows from the partition function as  $F = -k_B T \ln Z$ . The transfer matrix can serve as a computational tool to calculate the partition sum and related quantities. These follow from the few largest eigenvalues of the matrix. If a sufficiently large range of finite sizes can be handled in such a calculation, the results may be extrapolated, so that one can predict the physical behavior in the thermodynamic limit.

Direct calculation of a partition sum of a system with many degrees of freedom is not possible because the number of terms in the sum is prohibitively large. The basic idea of transfer-matrix calculations is to effectively reduce the number of degrees of freedom, by means of partial summations, and postponing the introduction of new degrees of freedom until they are needed to enable the summing out of old degrees of freedom. Let us describe the practical context. Consider a spin system with discrete variables that can be divided into  $n$  blocks. The system can be built up sequentially by appending a new block of spins, while keeping track of all necessary information to calculate the partition sum.

Part of this information is the configuration of the site variables close to the open end of system. Thus, the construction of a transfer matrix requires a ‘coding’ of the relevant degrees of freedom at the open end. For discrete spin systems, these degrees of

freedom include the site variables at the open end. For systems with bond variables, they specify the ways in which the sites are connected by the bonds. This information is called ‘connectivity’. A transfer matrix is defined which can be used to build an algorithm that can multiply a vector  $\vec{v}$  by the transfer matrix  $\mathbf{T}$ :

$$\vec{v}' = \mathbf{T} \cdot \vec{v}. \quad (1.6)$$

The availability of a numerical procedure that executes this multiplication is sufficient for the calculation of the few largest eigenvalues. The eigenvalues are very useful for the calculations of physical quantities, such as the partition sum, and thus the free energy and the conformal anomaly, etc. The largest eigenvalues of the transfer matrix and of a slightly modified matrix can also be used to calculate the correlation length. Scaling methods then allow the determination of the critical point if the system undergoes a phase transition. Furthermore, the correlation length is linked with a corresponding scaling dimension which can be calculated by using a conformal mapping as in Eq. (1.2).

### Monte Carlo method

Monte Carlo simulations purportedly describe macroscopically observable quantities on the basis of modeling of the system on a microscopic level, using the laws of probability as specified by statistical mechanics. In the present applications we do not attempt to calculate the partition function or the free energy, but to sample directly the derivatives of the latter quantity.

The Monte Carlo algorithm specifies a set of microscopic transition probabilities which are used to generate a Markov sequence. It is clear that, in order to generate an ensemble of configurations in accordance with Boltzmann statistics, the transition probabilities must satisfy certain conditions. One can prove that it is sufficient that the transition probabilities satisfy two conditions: ergodicity and detailed balance.

For an actual realization of the Markov process, decisions have to be taken with a certain probability, for which random numbers are used. If the probability of a Monte Carlo step is  $p$ , and an uniformly distributed random number  $0 \leq x \leq 1$  is available, then the step is executed if and only if  $x < p$ . Unfortunately, random numbers are not available, they are a mathematical abstraction. In spite of claims of ‘true randomness’ that appear from time to time with regard to quantum noise, actual realizations fail to produce random numbers, although the ‘deviations from randomness’ may be small. Fortunately, the Monte Carlo method does not require random numbers. It is sufficient to use a carefully chosen deterministic, pseudo-random sequences. Of course, for accurate Monte Carlo investigations, it is necessary to perform a quantitative analysis of the possible biases produced by the specific type of pseudo-random number generating algorithm. Extensive investigations have revealed what conditions are important for this purpose, and have thus yielded groups of algorithms that produce biases that are unobservable on today’s computers. Their projected biases, obtained by scaling relations, are a several orders of magnitude smaller than the observation threshold.

Just as transfer matrix algorithms, Monte Carlo algorithms have a region of applicability to problems of a type that cannot easily be solved by other numerical methods. Its efficiency relative to the transfer-matrix method increases when the dimensionality of the problem increases. Of course the efficiency of a Monte Carlo algorithm still depends on the nature of the dynamic variables and the microscopic structure of their interactions and on the update mechanism of the algorithm itself. In the study of phase transitions, there are various types of Monte Carlo algorithms available, including nonlocal cluster-update algorithms and local Metropolis-like algorithms. The cluster algorithms are, in many cases, much more efficient than the local-update algorithms, and in general the fewer components the spins have, the more efficient the simulations are. While in this thesis the emphasis lies on the physics investigated by this type of numerical tools, attempts to increase the efficiency of the computer simulations by developing novel efficient algorithms, is itself also an interesting and challenging subject.

### 1.3 Motivation and outline

By means of the methods introduced above, including analytical approaches and numerical techniques, we are able to investigate various interesting subjects in phase transitions and Monte Carlo algorithms. These techniques and algorithms involve cluster decompositions, geometric clusters, geometric cluster algorithms and finite-size scaling, which aspects are reflected in the title of this thesis. The subjects we studied and our motivations are outlined in the this section.

In the next chapter (Chap. 2), we consider the triangular Ising antiferromagnet in an uniform external magnetic field. The model at zero temperature without magnetic field shows very interesting properties. Our curiosity for the model with nonzero temperature and field is motivated by theoretical predictions [15] concerning the phase diagram including these parameters, and the possibility to verify these predictions numerically.

We use similar numerical techniques in Chap. 3 to study a generalized version of the model of Chap. 2. The Hamiltonian also includes ferromagnetic next-nearest-neighbor couplings. We determine the phase diagram and confirm the character of the critical manifolds. The emphasis of this work is on the case of antiferromagnetic nearest-neighbor couplings, but we also explore the ferromagnetic regime. For ferromagnetic next-nearest-neighbor couplings we check for the predicted [15] existence of a critical phase at zero field, supposedly covering the whole range of the nearest-neighbor coupling between  $-\infty$  and 0. For nonzero fields, we locate expected phase transitions and test for the existence of a line of tricritical points with three-state Potts nature.

Chapter 4 presents a comparison of existing simulation algorithms for the cluster simulation of the random-cluster model, and a description of a new single-cluster algorithm in this category. Cluster simulations for the Potts model with an integer number  $q$  of states are already known for a long time, but they are relatively new in the context of the random-cluster model which serves as a generalization of the Potts model to continuous values of  $q$ . This makes it desirable to compare the efficiencies of the available algorithms.

These include not only a cluster algorithm but also a local bond update method and a statistical reweighting method of percolation configurations. All of these generate Boltzmann statistics but, as expected, their efficiencies appear to be widely different. Remarkably, a single-cluster algorithm for noninteger  $q$  was thus far not available. Here we formulate such an algorithm and explore its dynamic universality class.

The percolation problem in two dimensions and its type of phase transition have already been thoroughly studied in the case that the substrate on which the percolation problem is defined is sufficiently homogeneous. However, such studies are not available for the case that the substrate itself becomes critical. Such critical backgrounds can be defined on the basis of the Potts model or, more generally, on that of the random-cluster model. Therefore we conduct a study of the bond percolation problem between interacting site variables having one out of  $q$  colors. This study is presented in Chap. 5. We use transfer-matrix and Monte Carlo techniques to determine the percolation threshold as a function of the Potts temperature  $T$  in the disordered Potts range  $T_c \leq T < \infty$  for several  $q$ -state Potts Hamiltonians. For high  $T$ , we expect that these transitions fit, irrespective of  $q$ , in the universality class of the ordinary percolation transitions. However, for  $T \downarrow T_c$ , we may expect  $q$ -dependent crossover phenomena. We investigate the possibility of such phenomena as well as the topology of the phase diagram as a function of the number of states  $q$  of the near-critical substrate.

It is known that the introduction of ‘vacancies’, i.e., an additional neutral state to the  $q$  interacting states of the Potts model, can lead to a range of first-order transitions, separated from the critical range by a tricritical point. This scenario is well-tested for some integer values of  $q$  but not so for the less trivial case of noninteger  $q$ . Therefore, in Chap. 6 we study the two-dimensional dilute  $q$ -state Potts model by means of transfer-matrix and Monte Carlo methods. Using the random-cluster representation, we include noninteger values of  $q$ . We explore the phase diagram in the three-dimensional parameter space of  $q$ , the Potts coupling  $K \geq 0$  and the chemical potential of the vacancies. We search for the critical plane and branches of fixed points, parametrized by  $q$  as predicted by the renormalization scenario for the dilute Potts model. We check whether the universal properties of the fixed-point models agree with the theoretical predictions. We also analyze some physical observables, including the density of the vacancies at the fixed points. For  $q = 2 - \sqrt{2}$  we explore the phase diagram in a three-dimensional parameter space that also includes a coupling  $V \geq 0$  between the vacancies. For  $q = 2$ , the latter space contains the Blume-Capel model as a special case. We include a determination of the tricritical point of this model, as well as an analysis of percolation clusters constructed on tricritical Potts configurations for noninteger  $q$ . This percolation study is based on Monte Carlo algorithms that include local updates flipping between Potts sites and vacancies. The bond updates are performed locally for  $q < 1$  and by means of a cluster algorithm for  $q > 1$ . The updates for  $q > 1$  use a number of operations per site independent of the system size. The algorithm is of a type as outlined in Chap. 4 but includes equilibration between vacant and occupied sites.

It is known that an increase of the range of interactions brings a model closer to the mean-field model. For Ising models with variable range, this crossover is uniform and such

that the model belongs to the short-range Ising universality class for all finite values of the range. The crossover range is parametrized by the Ising irrelevant field. This situation may seem similar to the one arising when vacancies are introduced, which can also be interpreted in terms of the irrelevant field. However, a sufficient concentration of vacancies does not lead to mean-field behavior, but instead to a tricritical point. Thus, the question arises whether, for the  $q \neq 2$  Potts model, the increase of the range of interactions leads to a uniform crossover, such as for  $q = 2$ , or to the appearance of a tricritical point, such as for the Potts model with vacancies. Therefore we investigate, in Chap. 7, the ordering transitions in two-dimensional  $q = 3$  and 4 Potts models with medium-range interactions. We use cluster Monte Carlo simulations to locate the phase transitions for several interaction ranges as expressed by the number  $z$  of equivalent neighbors. The algorithm uses an amount of computer time per spin visit that is essentially independent of the number of interacting neighbors. The efficiency of this algorithm enables us to answer the question about the possible existence of a range-dependent tricritical point.

According to the renormalization group theory, the cubic anisotropy acts as an irrelevant perturbation of the critical  $O(n)$  model in two dimensions for  $n < 2$ . While the resulting  $n$ -component cubic model has already been investigated in some detail, there are a few remaining issues. First, the cubic model intersects with the  $(N_\alpha, N_\beta)$  model of Doman and Riedel [16]. Remarkably, the exactly known critical points for  $n = 1$  and 2 of the cubic model under investigation lie exactly in the self-dual plane of the  $(N_\alpha, N_\beta)$  model. In the absence of further exact results, it is thus worthwhile to test numerically if this also holds for other values of  $n$ . Second, accurate tests of the  $O(n)$ -like critical behavior are still lacking for most of the scaling dimensions. For this reason we present a study of the  $n$ -component cubic model on the square lattice in Chap. 8. This model is chosen such that an expansion exists in Ising-like graphs. We construct a transfer matrix and perform a finite-size-scaling analysis to determine the critical points for several values of  $n$  in the range of  $-2 \leq n \leq 2$ . We determine several universal quantities, including three critical exponents.

The absence of exact results for the three-dimensional Ising universality class makes it desirable to continue the efforts to obtain more accurate tests of universality, as well as more accurate results for the universal constants. In the last chapter of this thesis, we study four different models which are generally believed to be in the three-dimensional Ising universality class. These models include: 1) the spin- $\frac{1}{2}$  Ising model with nearest-neighbor interaction on the diamond lattice; 2) the spin- $\frac{1}{2}$  Ising model with nearest-neighbor interactions on the simple cubic lattice; 3) the spin- $\frac{1}{2}$  Ising model on the simple cubic lattice with 32-neighbor interactions which include four shells of equivalent neighbors; 4) the spin-1 Ising model with nearest-neighbor interaction on the simple cubic lattice. The simulations were performed up to system size  $L = 256$  and enable a further narrowing down of the error margins of the universal Ising critical exponents.

# Bibliography

- [1] H. E. Stanley, *Introduction to Phase Transitions and Critical Phenomena*, (Oxford University Press, Oxford, 1971).
- [2] S. K. Ma, *Modern Theory of Critical Phenomena*, (Benjamin, Reading, MA, 1976).
- [3] P. Ehrenfest, Supplement No. 75b zu den Mitteilungen aus dem Kamerlingh Onnes-Institut, Leiden (1933).
- [4] R. Hilfer, Phys. Rev. Lett. **68**, 190 (1992)
- [5] K. G. Wilson, Phys. Rev. B **4**, 3174 (1971).
- [6] K. G. Wilson, Rev. Mod. Phys. **47**, 773 (1975).
- [7] K. G. Wilson in *Phase Transitions and Critical Phenomena*, edited by C. Domb and M. S. Green, (Academic Press, London, 1976), Vol. **6**; see also other chapters in this volume.
- [8] J. L. Cardy, J. Phys. A **17**, L358 (1984).
- [9] H. W. J. Blöte, J. L. Cardy and M. P. Nightingale, Phys. Rev. Lett. **56**, 742 (1986).
- [10] I. Affleck, Phys. Rev. Lett. **56** 746 (1986).
- [11] H. W. J. Blöte and H. J. Hilhorst, J. Phys. A **15**, L631 (1982).
- [12] P. W. Kasteleyn and C. M. Fortuin, J. Phys. Soc. Japan. (Suppl.) **26**, 11 (1969).
- [13] R. J. Baxter, S. B. Kelland and F. Y. Wu, J. Phys. A **9**, 397 (1976).
- [14] R. J. Baxter, Phys. Rev. Lett. **26**, 178 (1971).
- [15] B. Nienhuis, H. J. Hilhorst and H. W. J. Blöte, J. Phys. A **17**, 3559 (1984).
- [16] E. Domany and E. K. Riedel, Phys. Rev. B **19**, 5817 (1979); Phys. Rev. Lett. **40**, 561 (1978).



# Chapter 2

## Critical frontier of the triangular Ising antiferromagnet in a field

We study the critical line of the triangular Ising antiferromagnet in an external magnetic field by means of a finite-size analysis of results obtained by transfer-matrix and Monte Carlo techniques. We compare the shape of the critical line with predictions of two different theoretical scenarios. Both scenarios, while plausible, involve assumptions. The first scenario is based on the generalization of the model to a vertex model, and the assumption that the exact analytic form of the critical manifold of this vertex model is determined by the zeroes of an  $O(2)$  gauge-invariant polynomial in the vertex weights. However, it is not possible to fit the coefficients of such polynomials of orders up to 10, such as to reproduce the numerical data for the critical points. The second theoretical prediction is based on the assumption that a renormalization mapping exists of the Ising model on the Coulomb gas, and analysis of the resulting renormalization equations. It leads to a shape of the critical line that is inconsistent with the first prediction, but consistent with the numerical data.

### 2.1 Introduction

The triangular Ising model with equal nearest-neighbor coupling  $K$  in a magnetic field has the reduced Hamiltonian

$$\mathcal{H}/k_{\text{B}}T = -K \sum_{\langle i,j \rangle} s_i s_j - H \sum_k s_k, \quad (2.1)$$

where  $s_i = \pm 1$ , and  $\langle i, j \rangle$  indicates summation over all pairs of nearest-neighbor sites. According to the exact solution by Houtappel [1] of the triangular Ising model in the absence of a magnetic field, the antiferromagnetic model has no phase transition at nonzero temperatures. The ground state is characterized by the condition that every elementary triangle contains spins of different signs. This constraint still leaves a considerable degeneracy, to such an extent that the zero temperature antiferromagnet has a nonzero entropy. The ground state appears to have interesting properties. It is a *critical* state as shown

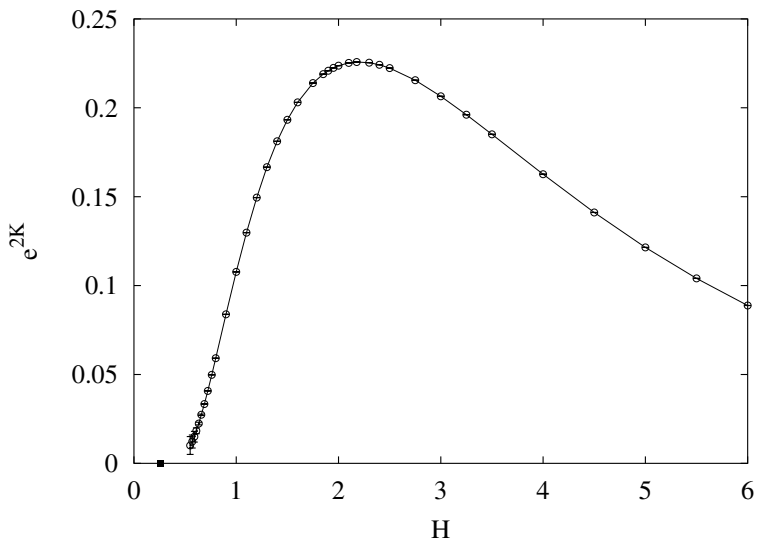


Figure 2.1: Numerical results for the  $(H, e^{2K})$  phase diagram. The circles ( $\circ$ ) denote the data points for Ising temperatures  $T > 0$  and the box ( $\blacksquare$ ) the so-called KT point at  $T = 0$ .

by exact calculations [2] of the spin-spin correlation function which appears to decay as a power-law of the distance. A nonzero temperature  $T > 0$  destroys the critical state: the correlations then decay exponentially. However, for sufficiently low  $T$ , a sufficiently strong field  $H > 0$  induces a phase transition to a long-range ordered state, where the minus spins condense on one of the three sublattices. As noted by Alexander [3], the threefold symmetry of the ordered phase indicates that the transition belongs to the three-state Potts universality class. The nature of the transition was confirmed by Kinzel and Schick [4], using phenomenological scaling [5] and numerical transfer-matrix calculations; see also Noh and Kim [6] and Tamashiro and Salinas [7].

The critical line covers an infinite range of  $K < 0$  and  $H$ . A preview of our numerical data is given in Fig. 2.1. Since the phase diagram is symmetric in  $H$ , we restrict it to  $H \geq 0$ . For  $K \rightarrow -\infty$ ,  $H \rightarrow \infty$  while  $6K + H$  remains finite, the model maps [8] onto Baxter's hard-hexagon lattice gas of which the critical exponents are exactly known, and they do indeed fit the three-state Potts universality class. The asymptotic form of the critical line in this lattice-gas (LG) limit is

$$K_c(H) \simeq -\frac{1}{6}H - \frac{1}{12} \ln \zeta_c, \quad \zeta_c = \frac{11 + 5\sqrt{5}}{2}, \quad (2.2)$$

where  $\zeta_c$  is the exact critical fugacity calculated by Baxter [9].

The critical line also extends to  $K \rightarrow -\infty$  at small fields  $|H|$ . The behavior of the critical line in this limit has attracted attention because of the above peculiar ground-state properties, and the associated analytical and computational difficulties. It has been conjectured [4] that the critical line comes in vertically in the  $\frac{1}{K}$  versus  $\frac{H}{K}$  diagram. In other words, when the Ising temperature goes to zero, also the *reduced* critical field  $H_c$

(which includes a factor  $1/k_B T$ ) was supposed to go to zero. However, Nienhuis *et al.* [10] provided evidence that  $H_c$  instead approaches a nonzero constant when  $K \rightarrow -\infty$ . This result is based on an exact mapping of the zero-temperature Ising model on a solid-on-solid (SOS) model [11]. Using renormalization arguments, Nienhuis *et al.* obtained several critical exponents associated with physical fields. It was found that the reduced magnetic field is *irrelevant*: it does not immediately destroy the critical state at  $K = -\infty$ .

This renormalization analysis is not rigorous but still convincing. Several of its predictions agree with exact calculations [12] at  $H = 0$ . The renormalization picture has been extended to include a nonzero field  $H$  and Ising temperature  $T$ , as well as next-nearest-neighbor interactions [10]. It predicts that for  $T = 0$  the model undergoes an infinite-order transition to a long-range ordered phase at a finite value of the field  $H$ . In the SOS language this is a roughening transition, in the universality class of the Kosterlitz-Thouless (KT) transition [13]. The character of this transition was confirmed [12, 14] and located at  $H_{KT} = 0.266(10)$  by means of transfer-matrix calculations and phenomenological renormalization [12]. The associated finite-size-scaling analysis is problematic because of slow convergence due to logarithmic corrections at the KT transition point. Such corrections are possibly a reason why an analysis by de Queiroz *et al.* [15], without such corrections, yielded a result that is not fully consistent, namely  $H_{KT} = 0.211(7)$  (for the correct interpretation of this result it is essential that the field  $H$  used in Fig. 1 and Table I of Ref. [15] does *not* contain a factor  $1/T$  [16]).

The estimated critical field  $H_{KT}$  at  $T = 0$  appears to be much smaller than estimates obtained at  $T > 0$ . The question thus arises whether the Potts critical line for  $T > 0$  connects to the KT point at  $T = 0$ . It is noteworthy that the renormalization scenario given in Ref. [10], which includes next-nearest-neighbor interactions  $K_{nnn}$ , implies that the line of phase transitions limiting the ordered phase in the  $(K_{nnn}, T)$  plane does *not* connect to the transition line in the  $(K_{nnn}, H)$  plane. Thus one may ask the same question for the  $(K_{nnn}, H)$  and the  $(H, T)$  plane. An answer to this question is provided by renormalization arguments presented in Section 2.2. This approach also predicts the analytical form of the Potts critical line for  $T \rightarrow 0$  while  $H$  remains finite.

A different approach to find the shape of the critical line of an antiferromagnetic Ising model in a field was formulated by Wu [17] who noted that these models can be mapped on vertex models, and that these vertex models have symmetry properties that impose restrictions on the analytic form of their critical manifolds. He also noted that the critical manifolds of the exactly solved vertex models are determined by the zeroes of homogeneous polynomials in the vertex weights that are invariant under the symmetry group of the model. On the basis of the assumption that the latter form of the critical subspace also applies to vertex models that are equivalent with antiferromagnetic Ising models in a field [18], one may thus attempt to solve for the unknown independent coefficients of the homogeneous polynomial, the number of which is dramatically reduced by symmetry restrictions. In actual applications, the number of equations is still not enough to solve all unknown coefficients, and additional numerical input is required, for instance from a numerical transfer-matrix analysis.

This approach is more ambitious than the renormalization analysis in the sense that its

aim is to describe the *whole* critical manifold. It has been applied to the Ising antiferromagnets on the honeycomb lattice [19] and on the square lattice [20]. The transfer-matrix data, with accuracies in the order of  $10^{-10}$ , could be successfully described by such invariant polynomials of relatively low order. Nevertheless one may remark that these analyses did not provide solid evidence for the *exact* form of the critical line of the Ising antiferromagnet.

Application of this approach to the triangular Ising model leads to some additional complications. First, the topology of the phase diagram is less simple, which relates to the fact that the lattice is not bipartite. Second, the 3-state Potts character of the critical line implies that corrections-to-scaling converge less well in comparison with the Ising case, so that it is not feasible to reach the same degree of numerical accuracy.

In this work we compare the results of both theoretical approaches to our numerical data for the triangular Ising antiferromagnet. A summary of the Coulomb gas scenario and an analysis of the renormalization-flow equations follows in Sec. 2.2. The analytic forms of the critical lines predicted by these two scenarios appear to be mutually *inconsistent* for  $T \rightarrow 0$  at finite  $H$ . In Sec. 2.3 we outline our transfer-matrix construction and present accurate results for the critical points. This section also includes a Monte Carlo analysis of the critical amplitudes. An analysis and a discussion of these results is given in Sec. 2.4. Finally, we draw our conclusions in Sec. 2.5.

## 2.2 Renormalization analysis

### 2.2.1 Mapping on the Gaussian model

At zero temperature, the three spins of each elementary triangle cannot have the same sign. Thus each triangle has two bonds between antiparallel spins and one bond between parallel spins. When all bonds between parallel spins are erased, one obtains a lattice tiling with rhombi. This tiling can also be interpreted as a stack of cubes viewed from the (1,1,1) direction. Thus the zero-temperature antiferromagnetic triangular Ising model is equivalent with a solid-on-solid (SOS) model [11]. The SOS model consists of height variables  $h_i$  where  $i$  denotes the lattice site. The height variables assume integer values satisfying  $h_i \bmod 3 = c_i$ , where  $c_i = 0, 1$  or  $2$  denotes the sublattice of site  $i$ . Apart from an infinite constant, the Hamiltonian becomes

$$\mathcal{H}/k_{\text{B}}T = -K_{\infty} \sum_{\langle i,j \rangle} (1 - \delta_{|h_i - h_j|,1})(1 - \delta_{|h_i - h_j|,2}) - H \sum_k (2\delta_{(h_k \bmod 2,0)} - 1), \quad (2.3)$$

where we set  $K_{\infty} \rightarrow -\infty$  so that the product  $(1 - \delta_{|h_i - h_j|,1})(1 - \delta_{|h_i - h_j|,2})$  restricts the height differences between nearest-neighbor sites to 1 or 2. The Kronecker delta in the second term counts the numbers of + spins.

The equivalence with the Ising model (2.1) makes it possible to express the height-height correlation function [10]

$$g(r) = \langle [(h_r - h_0) - \langle h_r - h_0 \rangle]^2 \rangle \quad (2.4)$$

in terms of Ising correlations. From the exact results for  $K = -\infty$ ,  $H = 0$ , it follows [10] that

$$g(r) \simeq \frac{9}{\pi^2} \ln(r) + \text{const}, \quad (2.5)$$

where  $r$  is the distance between the correlated sites. This result is very useful in the context of a renormalization mapping by Nienhuis *et al.* [10] on the Gaussian model with Hamiltonian

$$\mathcal{H}/k_{\text{B}}T = \frac{2\pi}{T_{\text{R}}} \sum_{\langle i,j \rangle} (h_i - h_j)^2 - \sum_p S_p \sum_i \cos \frac{2\pi h_i}{p}, \quad (2.6)$$

where the second summation contains so called spin-wave perturbations of the Gaussian model, *i.e.*, a periodic potential acting on the Gaussian height variables. A term with  $p = 1$  originates from the discreteness of the height variables in Eq. (2.3). A nonzero magnetic field  $H$  favors triangles with only one minus spin; in the SOS model this leads to an energy alternation between even and odd heights. This maps on a spin-wave perturbation with  $p = 2$  in the Gaussian model.

The mapping of Eq. (2.3) to Eq. (2.6) is not exact, so that the renormalized temperature  $T_{\text{R}}$  is in principle unknown. However, the height-height correlation function of the Gaussian model is known to depend on  $T_{\text{R}}$  as

$$g(r) \simeq \frac{T_{\text{R}}}{2\pi^2} \ln(r). \quad (2.7)$$

Comparison with Eq. (2.5) shows that

$$T_{\text{R}} = 18 \quad (2.8)$$

for  $H = 0$ . Once  $T_{\text{R}}$  is known, several quantities of interest can be calculated for the Gaussian model. These quantities include the scaling dimensions associated with the so-called spin-wave and vortex perturbations in the Gaussian model. Since an elementary excitation of the Ising model, *i.e.*, a triangle with three equal Ising spins, leads to an SOS height mismatch of 6 units, the Ising temperature field  $t_{\text{I}}$  is represented by the fugacity  $V_q$  of the  $q = \pm 6$  vortices. On the basis of the known results for the scaling dimensions of  $S_p$  and  $V_q$  in the Gaussian model [22], a number of properties of the triangular Ising model, including a part of the phase diagram extended in the direction of  $T_{\text{R}}$ , have been derived [10]. In this work we make use of the language of the Coulomb gas formulation [23] to express the relevant scaling dimensions. The appropriate parameters are the renormalized coupling constant  $g_{\text{R}}$ , and electric charges  $e$  and magnetic charges  $m$ . Their relation with the parameters of the Gaussian model can be expressed as

$$\begin{aligned} g_{\text{R}} &= 36/T_{\text{R}}, \\ e &= 6/p, \\ m &= q/6. \end{aligned} \quad (2.9)$$

In this language, the scaling dimensions  $X_{e,m}$  associated with the activity of charges  $(e, m)$  are

$$X_{e,m} = \frac{e^2}{2g_R} + \frac{g_R m^2}{2}. \quad (2.10)$$

From Eq. (2.8) we see that  $g_R = 2$  for  $H = 0$ . Since the Ising temperature field is associated with magnetic charges  $\pm 1$ , the Ising temperature renormalization exponent  $y_{t_I} = 2 - X_{0,1} = 1$  is relevant. The system is thus disordered for all  $T > 0$ . However, the exponent  $y_h = 2 - X_{3,0} = -1/4$  associated with the uniform magnetic field  $H$  is irrelevant. Thus, at  $T = 0$  the system remains critical for a certain range of the Ising field  $H$ . In the renormalization scenario outlined in Ref. [10] a phase transition to the long-range ordered phase occurs when  $H$  grows large enough. In the SOS language this ordered phase is flat, and transition is of the ‘roughening’ type, by duality related to the Kosterlitz-Thouless phase transition [13].

### 2.2.2 Renormalization flow

For an analysis of the renormalization flow at nonzero magnetic field  $H$  it is necessary to include the Coulomb gas coupling  $g_R$  because the field, although irrelevant at  $g_R = 2$ , tends to suppress height differences, *i.e.*, to increase  $g_R$ . As deduced in Ref. [10] such an effect can also be realized without breaking the Ising symmetry, by the introduction of ferromagnetic next-nearest-neighbor interactions into the model (2.1). Although we restrict our numerical investigation to the 2-parameter model (2.1), the renormalization analysis still requires a set of 3 nonlinear scaling fields, which are chosen as

$$\begin{aligned} t &= \frac{9}{2g_R} - 2, \\ h &= \alpha_1 H + \alpha_3 H^3 + \dots, \\ t_I &= e^{2K} + \dots. \end{aligned} \quad (2.11)$$

The constant  $\alpha_1$  determines the scale of  $t$  which remains to be determined. Apart from that, the expansion coefficients  $\alpha_j$  are in principle unknown. The Ising temperature field  $t_I$  is in lowest order chosen as the Boltzmann factor of an elementary Ising excitation, *i.e.*, a triangle with three equal spins. It thus describes the activity of the magnetic charges  $m = \pm 1$  in the Coulomb gas. In order to describe the renormalization of these parameters in the immediate vicinity of the fixed line  $h = t_I = 0$ , the following renormalization exponents apply

$$\begin{aligned} y_t &= 0, \\ y_h &= 2 - \frac{9}{2g_R}, \\ y_{t_I} &= 2 - \frac{g_R}{2}, \end{aligned} \quad (2.12)$$

First we address the special case  $T = t_I = 0$ . Because of the marginality of  $t$  we add a nonlinear term in the flow for  $t$ . In differential form, the equations become

$$\frac{dh(l)}{dl} = -ht, \quad \frac{dt(l)}{dl} = -h^2, \quad (2.13)$$

where  $l$  parametrizes the rescaling factor  $b$  as  $b = \exp(l)$ . In principle one has an unknown amplitude in the second equation, but we have disposed of it by a proper choice of  $\alpha_1$ . Thus, the scale of  $t$  is set such as to simplify the renormalization equations to (2.13). The equation for  $h$  follows from the usual form  $h' = b^{y_h}h$  after substitution of  $b$  in terms of  $l$ , of  $y_h$  using Eq. (2.12), and  $g_R$  in terms of  $t$ . The sign in the equation for  $t$  follows because  $h$  suppresses the height differences in the SOS language. The flow equations (2.13) are equivalent to those describing the Kosterlitz-Thouless [13] and roughening transitions. Elimination of  $l$  from Eq. (2.13) and integration yields the trajectory in the  $h, t$  plane as

$$h^2 = t^2 + c^2, \quad (2.14)$$

where the constant  $c$  follows from the initial conditions which are chosen as  $h(0) = 1/4 + \delta h$ ,  $t(0) = 1/4$ . The physical motivation of this choice is that the KT transition line obeys  $h = t$ , so that we select a point at a distance  $\delta h$  to the KT point of the nearest-neighbor model Eq. (2.1). For small  $\delta h$  one finds  $c^2 \approx \delta h/2$ . Elimination of  $h$  in Eq. (2.13) leads to

$$\frac{dt(l)}{dl} = -t^2 - c^2. \quad (2.15)$$

Integration, substitution of the initial conditions and some rearrangement lead to the renormalization flow for  $t_I = 0$  as

$$t = \frac{\sqrt{\delta h/2}}{\tan(\sqrt{8\delta h} + l\sqrt{\delta h/2})}. \quad (2.16)$$

Next we introduce a nonzero Ising temperature  $T$  so that also  $t_I > 0$ . It seems reasonable to assume that the renormalization flow of  $h$  and  $t$  is not seriously affected for small  $t_I$ . For simplicity we make a stronger assumption, namely that the flow of  $h$  and  $t$  is independent of that of  $t_I$ . We first focus on the question whether the 3-state Potts critical line in the  $(H, T)$  plane extends to the KT transition at  $T = 0$ , or, in other words, whether there are points in the immediate vicinity of  $(H = H_{KT}, T = 0)$  that flow towards a region where we can be confident that a Potts-like transition occurs. For small  $\delta h/2$  and  $t_I$  the first part of the path will be governed by the KT fixed point. We assume that the flow will bring the system to a boundary which separates the regions governed by the KT and Potts fixed points. This boundary is obviously not determined in a quantitative sense, but this does not matter for the present scaling argument. Let it be sufficient to define this region by requiring that  $h$  and  $t_I$  reach values of order 1.

We search for this region by choosing the (somewhat arbitrary) renormalized temperature  $g_R = 3$  where we have evidence [24] (see also Chap. 3) that the Potts transition

connects to the neighborhood of  $T = H = 0$ . The shape of the critical line at  $g_R = 3$  is determined by the flow equations for  $t_I$  and  $h$ , namely

$$\begin{aligned} t_I(b) &= b^{y_{t_I}} t_I, \\ h(b) &= b^{y_h} h, \end{aligned} \quad (2.17)$$

where one may take  $y_{t_I} = y_h = 1/2$  as long as  $t_I$  and  $h$  are small so that the change of  $g_R$  can be neglected. Then,  $t_I(b)/h(b)$  is constant along a flow line and can be chosen such that the model is critical, say for

$$t_I(b)/h(b) = \beta, \quad (2.18)$$

where  $\beta$  is a constant of order 1. For larger values of  $t_I$  and  $h$  the relation will no longer be linear but it is reasonable to expect, and in agreement with numerical results [24, 25], that there is a fair range where  $\beta$  is still of order 1.

Thus we consider a point  $h(0) = 1/4 + \delta h$ ,  $t(0) = 1/4$ ,  $t_I(0) = \delta t_I$  in the vicinity of the KT point and apply a transformation such that the system flows to  $g_R = 3$  or  $t = -1/2$ . According to Eq. (2.16) the scale factor of this transformation is  $b = \exp(l) = \exp(\pi\sqrt{2/\delta h})$ . It follows from Eq. (2.16) that (for small  $\delta h$  and  $\delta t_I$ ) the system is located near the KT fixed point  $h = 0$ ,  $t = 0$  for most of the range of  $l$ . Therefore, the flow of the Ising temperature field  $t_I$  is determined by the exponent  $y_{t_I} = 7/8$  at  $g_R = 9/4$  or  $t = 0$ . Thus, at  $g_R = 3$  it reaches the value  $t_I = b^{7/8}\delta t_I = \exp(7\pi/4\sqrt{2\delta h})\delta t_I$ . Since  $h = -t = 1/2$  up to unimportant corrections, Eq. (2.18) leads to

$$\delta t_I = \frac{\beta}{2} \exp\left(-\frac{7\pi}{4\sqrt{2\delta h}}\right), \quad (2.19)$$

which solves  $\delta t_I$  for all  $\delta h > 0$ . This implies that the Potts critical sheet connects to the KT point. The resulting renormalization flow is sketched in Fig. 2.2. Substitution of Eq. (2.11) and  $H = H_{KT} + \delta H$  leads in lowest order to

$$K \simeq \frac{1}{2} \left[ \ln \frac{\beta}{2} - \frac{7\pi}{4\sqrt{2\alpha(H - H_{KT})}} \right], \quad (2.20)$$

where  $\alpha$  is a function of the  $\alpha_j$ . This equation determines the shape of the critical line near the KT point of the model (2.1) and is clearly incompatible with the prediction of the invariant-polynomial scenario as

$$K(H) = \frac{1}{4m} \ln(H_c - H_{KT}) + \text{const}, \quad (2.21)$$

as derived by Wegewijs, *et al.* in Sec. II of Ref. [26], see Eq. (9) of that work, which is the central result of a dual transformation of O(2) invariant-polynomial scenario analysis and it is *logarithmic* divergent when  $H \rightarrow H_{KT}$ .

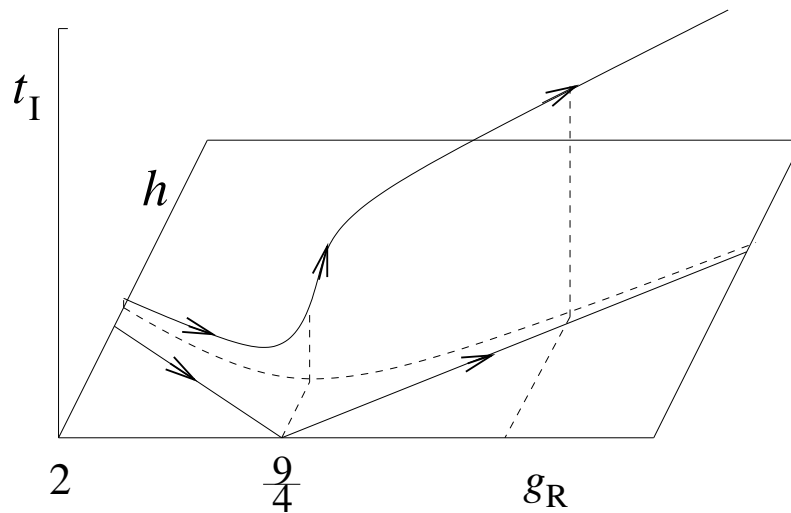


Figure 2.2: Sketch of the renormalization flow in the parameter space of the renormalized coupling  $g_R$ , the scaling field  $h$  and the Ising temperature field  $t_I$ . The flow of  $g_R$  and  $h$  is anomalously slow near the point  $g_R = 9/4$ ,  $h = 0$ : most of the growth of  $t_I$  occurs here.

## 2.3 Numerical methods

### 2.3.1 Transfer-matrix calculations

Most of the transfer-matrix calculations were performed for  $T > 0$  so that we had to use a binary representation for the Ising spins, leading to a transfer matrix of size  $2^L \times 2^L$  for a system with finite size  $L$ . We define the spin lattice on the surface of a cylinder, whose axis determines the transfer direction. We have used two choices for the orientation of the lattice: one set of bonds parallel or perpendicular with respect to the axis of the cylinder. In the first case, the transfer matrix adds an array of spins that is vertical as shown in Fig. 3.1. However, the construction of a symmetric transfer matrix would require a decoration transformation to one half of the parallel bonds in order to construct a symmetric transfer matrix. However, the decoration of antiferromagnetic bonds leads to complex weights which we wish to avoid. We have thus used a non-symmetric transfer matrix, in combination with a suitable tridiagonalization method to find the leading eigenvalues. These were obtained for even linear system sizes up to  $L = 22$ , which corresponds with an actual finite size of  $11\sqrt{3}$  nearest-neighbor bonds. The second construction, with a set of edges perpendicular to the transfer direction, adds a horizontal layer of spins as appears in Fig. 3.1. This leads to a symmetric matrix when two layers of spins are added. This allows the use of the conjugate-gradient method which is, in our applications, more stable than the tridiagonalization method. Finite-size calculations with  $L$  multiples of 3 up to  $L = 24$  were performed using this second construction.

A sparse-matrix decomposition was used for both constructions. Most of the technique is already implicit in the work of Nightingale [5]. Further details are listed in Ref. [27] which concerns the case of the honeycomb lattice, but the essential steps are applicable to

the triangular lattice as well. During the analysis of the results of both types of transfer matrix we found that they were mutually consistent. Furthermore it became clear that the second transfer matrix, with a set of bonds perpendicular to the transfer direction, allowed a somewhat more accurate analysis. In the following we describe the situation of the second construction.

For  $T = 0$  the transfer matrix decomposes in a number of diagonal submatrices characterized by a conserved number of ‘strings’ so that the numerical diagonalization task simplifies. The transfer-matrix construction for this case has been outlined in Ref. [12] and enabled the study of systems with linear sizes up to  $L = 27$ .

The magnetic correlation function along the coordinate  $r$  in the length direction of the cylinder is defined as  $g_m(r) = \langle s_0 s_r \rangle$ . At large  $r$ , this correlation function decays exponentially with a characteristic length scale  $\xi$  that depends on  $K$ ,  $H$  and  $L$

$$g_m(r) \propto e^{-r/\xi(K,H,L)}, \quad (2.22)$$

and can be calculated from the largest two eigenvalues  $\lambda_0$  and  $\lambda_1$  of the transfer matrix:

$$\xi^{-1}(K, H, L) = \frac{1}{\sqrt{3}} \ln(\lambda_0/\lambda_1), \quad (2.23)$$

where the factor  $\sqrt{3}$  is a geometric factor, *i.e.*, the ratio between the thickness of two layers added by the transfer matrix and the length of a nearest-neighbor bond. The significance of these relations lies in the fact that the assumption of conformal invariance [28] links  $\xi$  on the cylinder with the magnetic scaling dimension  $X_m$  (one half of the magnetic correlation function exponent  $\eta$ ). In terms of the scaled gap

$$X_m(K, H, L) \equiv \frac{L}{2\pi\xi(K, H, L)} \quad (2.24)$$

one has  $X_m(K, H, L) \simeq X_m$  in the limit of large  $L$ . Since the three-state Potts universal value of the magnetic scaling dimension is known to be  $X_m = \frac{2}{15}$ , and the transfer-matrix algorithm evaluates  $X_m$  as a function of its arguments, one can find a numerical approximation to the critical value of  $K$  for a given value of  $H$  or vice versa. The shape of the critical line prescribes the use of different ways in different regions. For small  $H$  and large  $|K|$ , the critical line is almost parallel to the zero-field line, so that it becomes more efficient to solve for  $H$  than for  $K$ .

As a consequence of corrections to scaling, the solution will not precisely coincide with the critical point. The effects of an irrelevant scaling field  $u$  and a small deviation  $t$  with respect to the critical value of  $H$  or  $K$  are expressed by

$$X_m(K, H, L) = X_m + auL^{y_i} + btL^{y_t} + \dots, \quad (2.25)$$

where  $a$  and  $b$  are unknown constants,  $X_m = \frac{2}{15}$ ,  $y_i = -\frac{4}{5}$  and  $y_t = \frac{6}{5}$  for the 3-state Potts universality class. Thus the solution for  $K$  of

$$X_m(K, H, L) = \frac{2}{15}, \quad (2.26)$$

Table 2.1: Extrapolated results for selected points on the critical line.

#	$H$	$K$	#	$H$	$K$
1	0.55(5)	-2.3	20	1.85	-0.759438 (2)
2	0.57(3)	-2.2	21	1.90	-0.755049 (1)
3	0.59(2)	-2.1	22	1.95	-0.751498 (2)
4	0.610(10)	-2.0	23	2.0	-0.748715 (2)
5	0.634(4)	-1.9	24	2.1	-0.745199 (1)
6	0.658(2)	-1.8	25	2.178	-0.744130 (1)
7	0.6885(10)	-1.7	26	2.3	-0.744958 (1)
8	0.7219(3)	-1.6	27	2.4	-0.747586 (1)
9	0.7607(1)	-1.5	28	2.5	-0.751708 (1)
10	0.8	-1.414 (1)	29	2.75	-0.7673233(4)
11	0.9	-1.2395 (2)	30	3.0	-0.7887774(4)
12	1.0	-1.11422 (1)	31	3.25	-0.8145143(3)
13	1.1	-1.02100 (1)	32	3.5	-0.8434661(2)
14	1.2	-0.95030 (1)	33	4.0	-0.9082113(2)
15	1.3	-0.896040 (5)	34	4.5	-0.9791030(2)
16	1.4	-0.854175 (2)	35	5.0	-1.0539340(2)
17	1.5	-0.821890 (1)	36	5.5	-1.1313743(2)
18	1.6	-0.797164 (2)	37	6.0	-1.2105830(3)
19	1.75	-0.771064 (3)			

which is denoted  $K_c^{(1)}(H, L)$ , depends on the finite size  $L$  and the irrelevant field as

$$K_c^{(1)}(H, L) = K_c + c_1 L^{y_i - y_t} + \dots, \quad (2.27)$$

because the two correction terms in Eq. (2.25) must cancel and  $t \propto K_c^{(1)}(H, L) - K_c$ . We thus generated sequences of iterated estimates of  $K_c$  by solving  $K_c^{(2)}(H, L)$  and  $c_1(L)$  in the equations

$$K_c^{(2)}(H, L) = K_c^{(1)}(H, l) + c_1(L) l^{y_i - y_t} \quad (2.28)$$

for  $l = L$  and  $L + 1$ . These sequences appear to converge faster with increasing  $L$  than the  $K_c^{(1)}(H, L)$ . Remaining corrections may be due to additional contributions to Eq. (2.25), for instance scaling as  $L^{2y_i}$ . Thus we defined  $K_c^{(3)}(H, L)$  by solving the equation

$$K_c^{(3)}(H, L) = K_c^{(2)}(H, l) + c_2(L) l^{2y_i - y_t} \quad (2.29)$$

for  $l = L$  and  $L + 1$ . Further estimates can be obtained with correction exponents  $2y_i - 2y_t$ , or by treating the correction exponents as a free variable in which case three values of  $l$  have to be used. Several variations of this procedure were tried which leads to some insight in the numerical inaccuracies of the fitting procedure.

Our final estimates of the critical points for  $T > 0$  are listed in Tab. 2.1. The apparent accuracy of the critical points is satisfactory for most of the field range, but it deteriorates

rapidly at small fields. Nevertheless this region has our special interest: we wish to determine how the Potts line connects to the KT point on the  $T = 0$  line, because this is where the theoretical predictions (see Section II in Ref. [26] and Section 2.2) are markedly different.

We have also reconsidered the determination of the KT point at  $T = 0$  given in Ref. [12]. In that work, the finite-size data for the critical field  $H_{\text{KT}}$  were obtained by requiring that the scaled gap associated with the spin waves of period 6, *i.e.*, electric charges  $e = \pm 1$  were equal to the expected value  $X_{1,0} = 2/9$  at the KT transition. These estimates  $H_{\text{KT}}(L)$  of the KT point, which were obtained for system sizes up to  $L = 27$ , were found to be considerably size-dependent. They were fitted according to  $H_{\text{KT}}(L) = H_{\text{KT}} + a/(b + \ln L) + cL^{-2}$  which led to extrapolated estimates  $H_{\text{KT}}$  that displayed only a remarkably small size-dependence. On this basis, the final estimate was given as  $H_{\text{KT}} = 0.266 \pm 0.010$  in Ref. [12]. In our present work we have reproduced these data for  $H_{\text{KT}}(L)$ . We have not used the procedure that requires that the scaled gap is equal for two subsequent system sizes. Since all points in the range  $H \leq H_{\text{KT}}$  satisfy this scaling equation asymptotically, the solutions may converge to any point in this range, depending on the corrections to scaling. This is another reason behind the discrepancy mentioned in Sec. 2.1 concerning an earlier result for the location of the KT point [15]. We have used the  $H_{\text{KT}}(L)$  data as input for several other iterated fit procedures consisting of subsequent extrapolation steps according to  $L^{-2}$  behavior, and powers of  $1/\ln L$ . These fits led to results for  $H_{\text{KT}}$  that were rather consistently close to 0.26, with differences up to 0.02.

As an independent approach we have estimated  $H_{\text{KT}}$  from the requirement that the scaled gap based on the magnetic dimension  $X_{0,1/3}$  is equal to the expected value  $1/8$  at  $g_{\text{R}} = 9/4$ . Since such fractional magnetic charges (corresponding with vortices of strength 2) do not exist in this model, this scaled gap cannot directly be calculated for a fixed system size  $L$ . However, it can be obtained by combining free-energy data for system sizes  $L = 3(n \pm 1)$ , where  $n$  is an integer, as explained in Ref. [12]. The same extrapolation procedures as above were tried, and led to results again consistent with  $H_{\text{KT}} = 0.26$ , but with differences up to about 0.04. Our final conclusion is  $H_{\text{KT}} = 0.26 \pm 0.02$ , similar to the value presented in Ref. [12] but with a slightly more conservative error estimate.

The numerical results for the critical points are combined in Fig. 2.1, the phase diagram in the  $(H, e^{2K})$  plane. We remark that for large  $|K|$  and relatively small  $H$ , the solutions for  $H$  become strongly finite-size dependent and slowly convergent. This problem is apparently due to the proximity of the KT transition at  $K = -\infty$ . This is illustrated in Fig. 2.3, in which a set of lines represent the finite-size solutions for  $L = 3, 6, \dots, 24$  together with the extrapolated critical line. On the basis of our limited range of finite system sizes, the estimation of the critical points thus becomes increasingly difficult for large  $|K|$ .

In order to provide further justification for our assumption that the critical line belongs to the 3-state Potts universality class (used for the determination of the critical points) we perform a consistency test by calculating the conformal anomaly  $c$  at the estimated critical points at  $H = 1.5, 2.5, 3.5$  and  $4.5$ . Iterated fits similar to those used for the calculation of the critical points were applied. All these results are consistent with the exact value  $c = \frac{4}{5}$ .

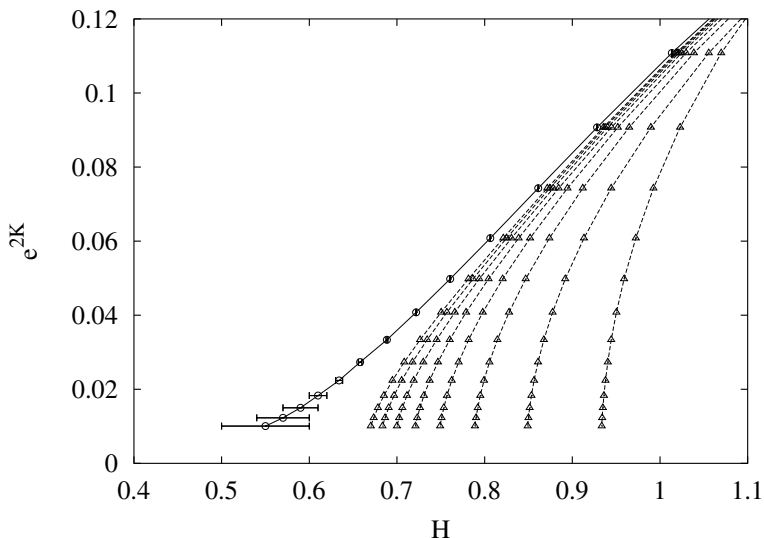


Figure 2.3: Finite-size solutions for the critical points, and our final estimates in the region of small field and temperature. The dashed lines connect the solutions shown as triangles ( $\triangle$ ). From right to left the lines show data for finite sizes  $L = 3, 6, \dots, 24$ . The solid line with circles ( $\circ$ ) indicates our final estimated result for the critical line.

The error margin varies between a few times  $10^{-3}$  for  $H = 1.5$  and a few times  $10^{-5}$  for  $H = 3.5$ . In comparison with previous work [6], these results further restrict the scale of possible deviations from 3-state Potts universality.

### 2.3.2 Monte Carlo results

The apparent difficulty to obtain accurate critical points for small  $H$  by the transfer-matrix method invites further investigation by means of Monte Carlo simulations, which allow the use of much larger finite sizes. In particular we determine how the critical amplitudes behave for small  $T$ , and make a comparison with the renormalization prediction. To this purpose we define a specific-heat-like quantity  $C$ , *i.e.*, the second order derivative of the free energy to a parameter conjugate to an energy-like density in the Hamiltonian, for which we may take the magnetization. Indeed the Ising field  $H$  drives the Potts-like transition to the ordered state (except at the maximum of the  $T$  vs.  $H$  curve) and thus plays the role of the temperature in the Potts model. We thus define  $C$  by

$$C = \frac{\partial^2 f}{\partial H^2} = N(\langle m^2 \rangle - \langle m \rangle^2), \quad (2.30)$$

where  $m$  is the Ising magnetization. Similarly, we define a quantity similar to the magnetic susceptibility of the Potts model. In the  $q = 3$  Potts model, the zero-field magnetic susceptibility can be expressed in magnetization fluctuations by

$$\chi = N\langle m_P^2 \rangle, \quad (2.31)$$

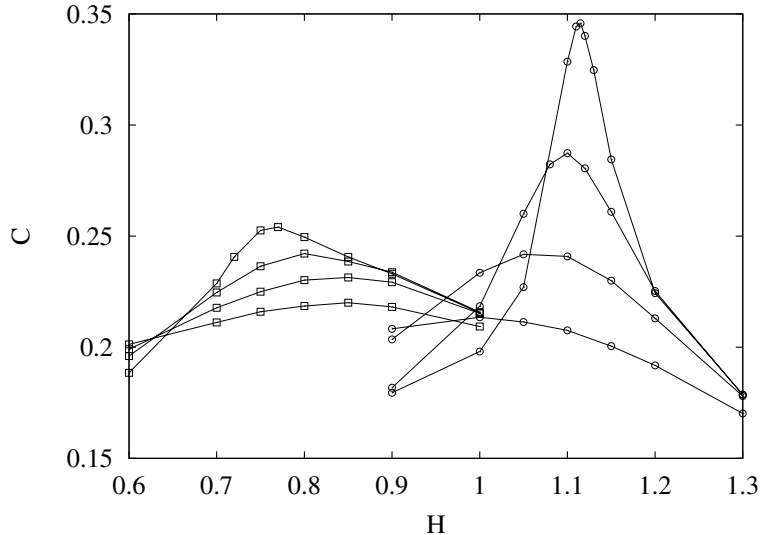


Figure 2.4: Specific heat-like quantity  $C$  versus field  $H$  for two values of the Ising coupling,  $K = -1.0$  ( $\circ$ ) and  $-1.5$  ( $\square$ ). Both sets of lines display data for system sizes  $L = 12, 24, 48,$  and  $96$ . These two cases indicate that the amplitude of the divergence of  $C$  decreases with decreasing field  $H$ .

where  $m_{\text{P}}^2 = n_1^2 + n_2^2 + n_3^2 - n_1n_2 - n_2n_3 - n_3n_1$  expresses the Potts magnetization in terms of the densities  $n_i$  of Potts variables in state  $i$ . In the scaling context of the present scaling analysis, the densities  $n_i$  may be defined as the number of minus-spins on sublattice  $i$ . Thus  $\chi$  describes the response of the model to staggered fields acting on the Ising spins.

The simulations used triangular  $L \times L$  lattices with periodic boundary conditions. We used a combination of the standard Metropolis algorithm and the geometric cluster method [29]. The latter method executes nonlocal updates and leads to a faster relaxation. But it does not change the Ising magnetization. For this reason also Metropolis steps were included. First we sampled  $C$  in a suitable range of  $H$ , to study its divergence, at fixed values of coupling  $K$  which are taken from Table 2.1. The results are shown in Figs. 2.4 and 2.5 and show that the finite-size divergence of  $C$  at the critical line becomes weaker when  $H$  decreases. In order to study this phenomenon in a more quantitative sense, we have determined  $C$  and  $\chi$  at several critical points taken from Table 2.1 for several system sizes. Results for  $H = 0.61, 0.658, 0.8, 1.0, 1.5, 2.0$  and  $5.0$  are shown in Fig. 2.6 and Fig. 2.7.

Finite-size scaling of the free energy density of a system with finite size  $L$  can be expressed by

$$f(t, h, u, L) = L^{-d} f(L^{y_t} t, L^{y_h} h, L^{y_u} u, 1) + g(t, h, u), \quad (2.32)$$

where  $t$ ,  $h$ , and  $u$  denote the temperature, magnetic field and irrelevant field respectively, and  $g$  the regular part of the transformation. Differentiation of  $f$  yields the scaling behavior

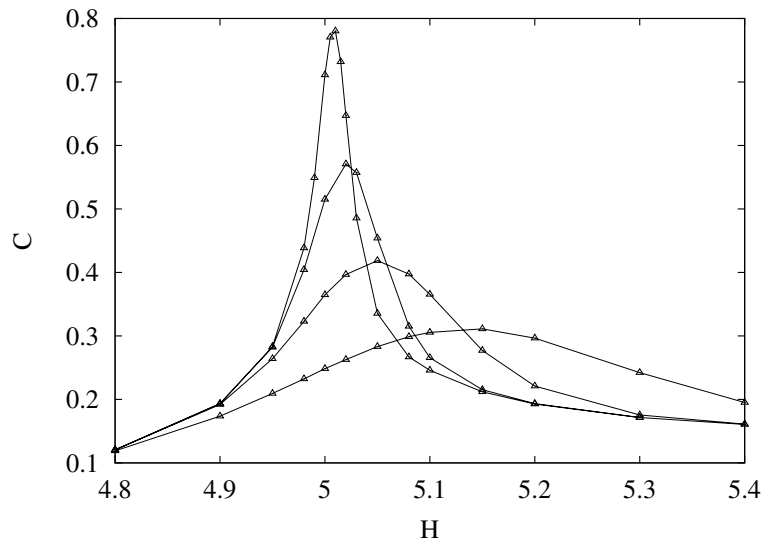


Figure 2.5: Specific heat-like quantity  $C$  versus  $H$  at Ising coupling  $K = -1.053934$ , near the critical point at  $H = 5.0$ . In comparison with Fig. 2.4, the finite-size divergence is much stronger.

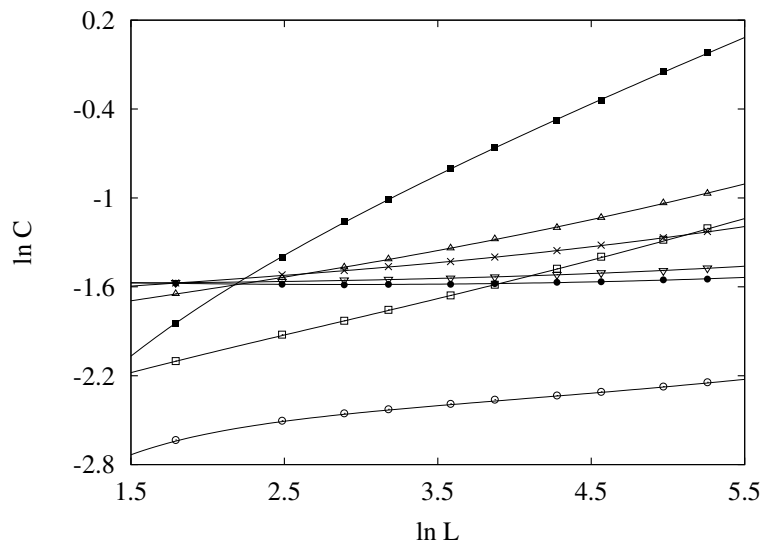


Figure 2.6: Specific heat-like quantity  $C$  versus system size on a double logarithmic scale. Data are shown for system sizes  $6 \leq L \leq 192$  at seven points  $(H, K)$  on the critical line. The symbol  $\bullet$  represents  $H = 0.61$ ;  $\nabla$ :  $H = 0.658$ ;  $\times$ :  $H = 0.8$ ;  $\triangle$ :  $H = 1.0$ ;  $\square$ :  $H = 1.5$ ;  $\circ$ :  $H = 2.0$ ;  $\blacksquare$ :  $H = 5.0$ . The seven lines represent the fitted results. The statistical errors are not shown in this figure. They do not exceed the thickness of the lines.

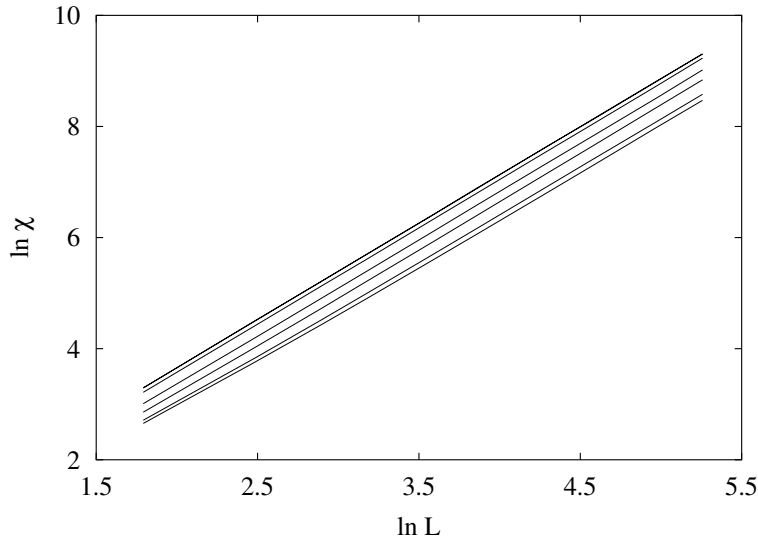


Figure 2.7: Susceptibility-like quantity  $\chi$  versus system size  $L(= 6, \dots, 192)$  on a double logarithmic scale. Data are shown for seven points  $(H, K)$  on the critical line. From bottom to top:  $H = 0.61, 0.658, 0.8, 1.0, 1.5, 2.0,$  and  $5.0$  respectively. The two lines for  $H = 2.0$  and  $5.0$  coincide on this scale. The statistical errors are not shown in this figure. They do not exceed the thickness of the lines.

Table 2.2: Parameters describing the finite-size behavior of the specific heat-like quantity  $C$ . The third column is the amplitude  $b_0$  of the leading divergent term. The amplitudes for  $H = 1.5, 2.0$  are relatively small because the critical line runs almost parallel to the field direction. The columns corresponding with  $b_i$  ( $i = 1, 2$ ) show the irrelevant correction amplitudes.

$H$	$C_0$	$b_0$	$b_1$	$b_2$
0.61	0.188(2)	0.0026(2)	0.027(3)	—
0.658	0.196(2)	0.0039(3)	0.007(3)	—
0.8	0.192(3)	0.0126(4)	-0.022(4)	—
1.0	0.151(3)	0.0285(6)	-0.035(5)	—
1.5	0.097(2)	0.0254(4)	-0.055(3)	—
2.0	0.084(3)	0.0029(3)	-0.015(6)	-0.097(2)
5.0	-0.096(6)	0.131(2)	-0.031(9)	—

Table 2.3: Parameters describing the finite-size behavior of the susceptibility-like quantity  $\chi$ . The third column is the amplitude  $b_0$  of the leading divergent term. It decreases regularly with the field. The next columns show the irrelevant correction amplitudes  $b_i$  ( $i = 1, 2$ ).

$H$	$\chi_0$	$b_0$	$b_1$	$b_2$
0.61	-17.5(18)	0.5281(12)	-0.143(50)	16.3(16)
0.658	-10.5(20)	0.5896(14)	-0.142(55)	2.88(36)
0.8	-18.7(37)	0.7675(24)	-0.75(10)	18.1(33)
1.0	0.95(11)	0.9046(17)	-0.164(25)	—
1.5	0.41(10)	1.1209(12)	-0.103(24)	—
2.0	0.10(14)	1.2130(24)	-0.003(34)	—
5.0	-0.51(14)	1.2133(22)	0.070(37)	—

of the quantities  $C$  and  $\chi$  as

$$C(u, L) = C_0 + L^{2y_t-d} C(L^{y_i} u, 1) = C_0 + L^{2y_t-d} (b_0 + b_1 L^{y_i} u + b_2 L^{2y_i} u^2 + \dots), \quad (2.33)$$

and

$$\chi(u, L) = \chi_0 + L^{2y_h-d} \chi(L^{y_i} u, 1) = \chi_0 + L^{2y_h-d} (b_0 + b_1 L^{y_i} u + b_2 L^{2y_i} u^2 + \dots). \quad (2.34)$$

We have fitted the numerical data by these two equations and thus derived the amplitudes listed in Tab. 2.2 and Tab. 2.3. The amplitude  $b_0$  of the leading divergence of  $C$  decreases with field except close to the maximum of the critical line in the  $(H, T)$  plane. At the maximum the field  $H$  fails to bring the system into the ordered phase and the amplitude  $b_0$  thus vanishes. Also for the susceptibility-like quantity  $\chi$  the amplitude  $b_0$  of the finite-size divergence, shown in Tab. 2.3, decreases regularly when the KT point is approached.

The behavior of the amplitude  $b_0$  at small field and low temperature follows from the renormalization-flow analysis. Starting from a point in the vicinity of the KT point, we renormalize until we arrive at the boundary with the region dominated by the 3-state Potts fixed point. Let  $b_{\text{KT}}$  be the corresponding scale factor. Since the specific heat-like quantity  $C$  is defined by means of differentiation of the free energy to the uniform field  $H$ , we keep track of how  $H$  changes under this transformation. The marginality of  $\delta h$  at  $g_R = 9/4$  is expressed by Eq. (2.14): when we write  $h = t + \delta h$ , it is clear that  $\delta h$  varies only by a factor of order 1 as long as  $t$  is of order 1. In the context of scaling, we thus have  $\delta h' \approx \delta h$  where the prime indicates the value at the boundary. Within the Potts region we rescale the system to size 1 with the remaining scale factor  $L/b_{\text{KT}}$

$$\delta h'' = \left( \frac{L}{b_{\text{KT}}} \right)^{\frac{6}{5}} \delta h' \approx L^{\frac{6}{5}} b_{\text{KT}}^{-\frac{6}{5}} \delta h, \quad (2.35)$$

where the Potts temperature exponent  $\frac{6}{5}$  applies because it corresponds with the Ising magnetic field. The behavior of  $C$  follows as

$$C = \frac{\partial^2 f}{\partial h^2} = L^{-d} \frac{\partial^2}{\partial h^2} f(L^{\frac{6}{5}} b_{\text{KT}}^{-\frac{6}{5}} h, 1) = L^{\frac{2}{5}} b_{\text{KT}}^{-\frac{12}{5}} f'' + \text{const}. \quad (2.36)$$

The susceptibility-like quantity  $\chi$  is obtained by differentiation of  $f$  to the staggered Ising field, which, as explained in Ref. [10], is associated with a Gaussian spin wave perturbation of period  $p = 6$ , *i.e.*, with electric charges  $e = \pm 1$ . The exponent of the staggered field thus takes the value  $2 - X_{1,0} = 16/9$  at the KT fixed point. Therefore, at the boundary with the Potts region we have

$$h'_{\text{st}} = b_{\text{KT}}^{\frac{16}{9}} h_{\text{st}}. \quad (2.37)$$

Within the region dominated by the Potts fixed point, the magnetic exponent  $y_m = 28/15$  applies. Renormalization with the remaining scale factor  $L/b_{\text{KT}}$  leads to

$$h''_{\text{st}} = \left( \frac{L}{b_{\text{KT}}} \right)^{\frac{28}{15}} h'_{\text{st}} = L^{\frac{28}{15}} b_{\text{KT}}^{-\frac{4}{45}} h_{\text{st}}, \quad (2.38)$$

so that  $\chi$  scales as

$$\chi = \frac{\partial^2 f}{\partial h_{\text{st}}^2} = L^{-d} \frac{\partial^2}{\partial h_{\text{st}}^2} f(L^{\frac{28}{15}} b_{\text{KT}}^{-\frac{4}{45}} h_{\text{st}}, 1) = L^{\frac{26}{15}} b_{\text{KT}}^{-\frac{8}{45}} f'' + \text{const}. \quad (2.39)$$

According to Sec. 2.2.2, rescaling by a factor  $b_{\text{KT}}$  results in an Ising temperature field  $b_{\text{KT}}^{\frac{7}{8}} e^{2K} = \beta/2$  so that  $b_{\text{KT}} \propto e^{-\frac{16}{7}K}$ . For strong coupling the renormalization scale  $b_{\text{KT}}$  is large, which is indicative of the crossover phenomenon close to the KT transition. There we need large system sizes  $L > b_{\text{KT}}$  in order to reach the vicinity of the Potts fixed point. The substitution of  $b_{\text{KT}}$  into Eq. (2.36) and Eq. (2.39), leads to

$$C = L^{\frac{2}{5}} e^{\frac{192}{35}K} f'' + \text{const}, \quad (2.40)$$

and

$$\chi = L^{\frac{26}{15}} e^{\frac{128}{315}K} f'' + \text{const}. \quad (2.41)$$

From a comparison of Eqs. (2.33) and (2.40), and of Eqs. (2.34) and (2.41), we expect that  $b_0 \propto e^{\frac{192}{35}K}$  for  $C$ , and  $b_0 \propto e^{\frac{128}{315}K}$  for  $\chi$ , when  $|K|$  is large enough. We thus expect a linear relation between  $\ln b_0$  and  $K$  for sufficiently strong coupling  $K$ . A fit to the numerical data yields the slopes as about 2.8(1) for  $C$  and 0.64(4) for  $\chi$ . These slopes do not agree accurately with the analytic values. This suggests that the Ising temperature used for the calculation of the amplitudes is not small enough. However, the qualitative amplitude dependence is reproduced, and the rough agreement suggests that we are not far away from the asymptotic regime.

## 2.4 Fit and discussion

### 2.4.1 Roots of the O(2) invariant polynomials

The idea to describe the critical line of the present model by means of an O(2) invariant polynomial is based on an idea of F.Y. Wu [17] and works as follows. A graph expansion of the Ising model in a field, using 2-state bond variables, leads to a vertex model. The bond variables are independent: odd graphs are allowed if the field is nonzero. The present Ising model thus maps on a 64-vertex model. Neighboring vertices are not independent, because they have one bond in common. Let the state of one bond be specified by an integer  $i = 1$  or  $2$ . Then, the weight of a vertex connected to that bond has the form  $w_1(\dots, i, \dots)$  where the position of  $i$  in the list of subscripts specifies the orientation of the bond with respect to the vertex. The weight of the other vertex connected to the bond has the value  $w_2(\dots, i, \dots)$ , with  $i$  on the conjugate position as in  $w_1$ . The partition sum thus contains  $\sum_i w_1(\dots, i, \dots)w_2(\dots, i, \dots)$  which has the form of a scalar product. The aforementioned O(2) invariance pertains to this product. Rotations may be applied to all bonds in the system at the same time. While this changes the vertex weights, the partition sum remains invariant.

The number of 37 critical points in Table 2.1 together with the additional KT point  $(h, z) = (h_{\text{KT}}, -1)$  (where  $h = \tanh H$  and  $z = \tanh K$ ) is sufficient to attempt fits of O(2) invariant polynomials up to order 10

$$f_{2e} = \sum_{j=0}^e \left[ \sum_{l=0}^j \kappa_l^j \Omega_2^l \Omega_3^{j-l} u^{2l} + \sum_{l=1}^j \kappa_{j+l}^j \Omega_1^l \Omega_2^{j-l} u^{2l+2j} \right] u^{6(e-j)} s^j \quad (2.42)$$

as derived by Wegewijs *et al.* in Sec. II of Ref. [26], see Eq. (19) of that work, which also contains the definitions of the  $\Omega_l$ ,  $u$  and  $s$  as a function of  $H$  and  $K$ .

We have not used data points 1 and 2 in Table 2.1 because of their limited accuracy, and performed a least-squares fit to the remaining 35 data points for  $z > -1$ . We have also tried direct fits to several subsets of these. In each case we have investigated the effect of enforcing the curve to pass through the KT point, or to extract the value of  $h_{\text{KT}}$  from the fit. It is found that the coefficients in the equation  $f_4 = 0$  are not flexible enough to even qualitatively fit the numerical data. The least-squares fit to  $f_6 = 0$  excluding the KT point consists of two avoiding solutions, which lead to 2 disconnected ‘critical’ lines which have unphysical ranges. For  $z = -1$  one line terminates at  $h^* \approx 0.501 > h_{\text{KT}}$ . When enforcing the KT point at  $h_{\text{KT}} = 0.25$ , the two avoiding branches repel one another even stronger. Direct fits to different subsets of critical points lead to similar results. Fits to higher order equations  $f_8 = 0$  and  $f_{10} = 0$  display the same problems. Even more avoiding solutions enter. The numerical problems are clearly displayed by the values of the fitted coefficients, which span a range of many orders of magnitude. In summary, the roots of invariant polynomial equations cannot fit the critical curve. The main problem is the approach of the curve to the KT limit imposed by Eq. (2.21): all such roots approach the KT point vertically in the  $(h, z)$  plane, whereas the numerical data in Fig. 2.8 indicate a horizontal approach.

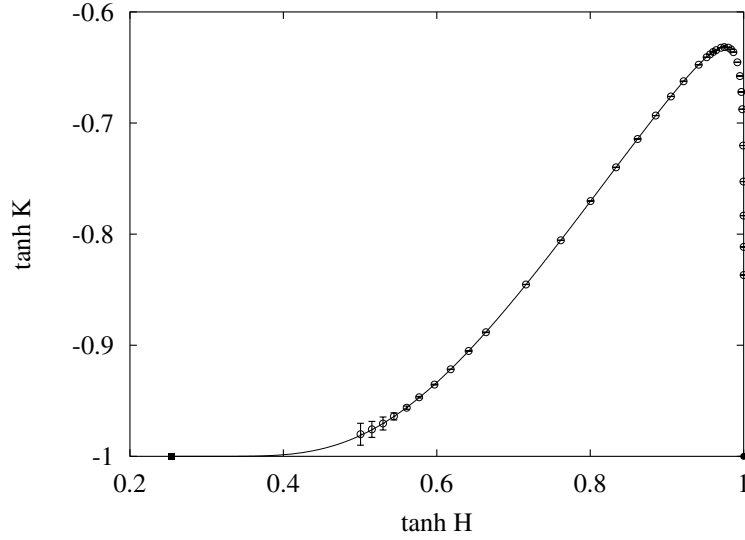


Figure 2.8: Phase diagram in the  $(h, z)$  plane (where  $h = \tanh H$  and  $z = \tanh K$ ). The KT point is denoted as  $\blacksquare$ , and the LG point, which is Baxter's hard-hexagon model, as  $\bullet$ .

Table 2.4: Coefficients  $\kappa_i^j$  ( $i = 0, \dots, 6; j = 1, 2, 3$ ) of the invariant polynomial  $f_6$ , Eq. (2.42). The condition for criticality reads  $f_6 = 0$ .

$\kappa_0^1$	$\kappa_1^1$	$\kappa_2^1$
-0.002942307242	-0.097656582607	2.725303204552
$\kappa_0^2$	$\kappa_1^2$	$\kappa_2^2$
-0.000000000017	0.000351055639	-0.020534345140
$\kappa_3^2$	$\kappa_4^2$	$\kappa_3^3$
0.044511873969	0.660086779714	0.000001077354
$\kappa_4^3$	$\kappa_5^3$	$\kappa_6^3$
-0.002865984972	-0.084578467922	1.000000000000

Sufficiently far away from the KT point, the problem dissolves, and our numerical data for the critical points can well be approximated by means of invariant polynomials. For example, the polynomial of order 6 can reproduce the critical points for  $H \geq 1.5$  within the error margins quoted in Table 2.1. The coefficients, determined by means of a least-squares fit, are listed in Tab. 2.4.

## 2.4.2 Renormalization solution for small field

For small field we expand Eq. (2.20) and take into account higher order terms in the physical fields. This leads to

$$-\frac{1}{K} = \sum_{j=1,2,\dots} a_j (H - H_{\text{KT}})^{j/2}. \quad (2.43)$$

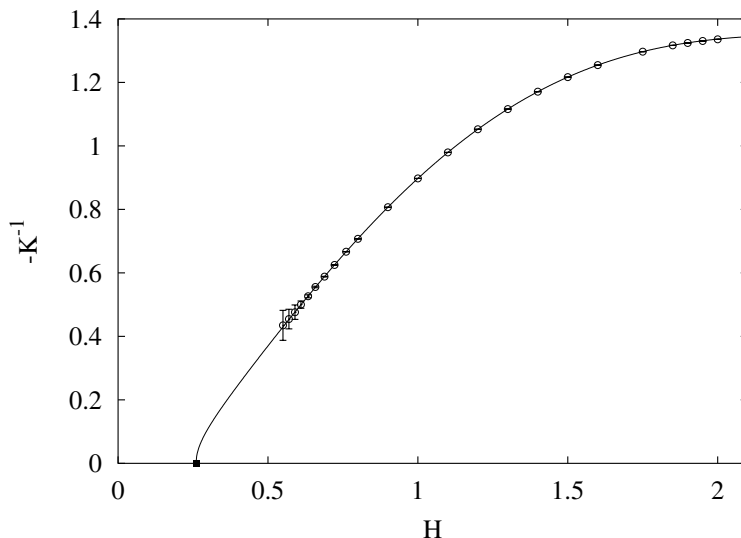


Figure 2.9: Phase diagram in the  $(H, K^{-1})$  plane. The symbol  $\circ$  denotes the Potts transition points;  $\blacksquare$  the KT point; and the solid line describes the fit of the expression based on the renormalization prediction for the critical line in the small field region.

Table 2.5: Coefficients  $a_j$  of the expansion (2.43) of  $-K^{-1}$  in powers of  $(H - H_{\text{KT}})^{\frac{1}{2}}$ .

$a_1$	$a_2$	$a_3$	$a_4$	$a_5$	$a_6$
0.487432	0.119116	0.765066	1.017104	-1.949253	0.652161

The numerical data for the critical points for  $H \leq 1.75$  are fitted satisfactorily (*i.e.*, within the error margins quoted in Table 2.1) by this formula using 6 coefficients. The numerical results and the fitted function are shown in Fig. 2.9. The values of the coefficients are listed in Tab. 2.5.

## 2.5 Conclusion

The invariant-polynomial scenario formulated in Sec. II in Ref. [26] and the renormalization scenario formulated in Sec. 2.2 lead to analytic expressions for the critical line in the  $(H, T)$  diagram that are mutually inconsistent for  $T \downarrow 0$  at finite  $H$ . This shows that at least one of the underlying assumptions must be incorrect. The renormalization prediction appears to successfully describe the numerical data for small  $|H|$ . Although the asymptotic regime is not quite reached (as can, for instance, be seen in Fig. 2.9 where the leftmost points behave almost linearly instead of as a square root), an asymptotic expansion leads to an accurate description of the data, and allows a smooth extrapolation to zero Ising temperature in agreement with Eq. (2.20). The analysis in Sec. 2.3.2 of the critical amplitudes fits precisely in this picture. Thus our analysis does not give reasons to doubt that the renormalization

scenario correctly describes the essential physics of the model near the KT transition.

In contrast, the invariant-polynomial scenario does not agree with the numerical data. It predicts a ‘vertical’ approach to the KT point in the  $(h, z)$  diagram (see Fig. 2.8) where it should be horizontal. Our interpretation is that the assumption of analyticity of the critical line in the  $(h, z)$  parametrization is false at the KT point, so that the line cannot be described by the zeroes of a polynomial of a finite order.

Since it now appears that the invariant-polynomial scenario fails in the case of the triangular-lattice Ising model, the question arises whether similar, apparently successful, analyses of the critical lines of the honeycomb- and the square-lattice Ising model in terms of invariant polynomials [19,20] have to be reconsidered. Here we may point at the simpler topology of the  $(H, T)$  diagram for the honeycomb and the square lattices: the critical line connects to  $T = 0$  only in the lattice-gas points  $H = \pm\infty$ . In the case of the triangular lattice model, crossover phenomena near the KT point are responsible for the nonanalytic ‘shape’ of the critical line. In the absence of such crossover phenomena, there is no inconsistency with the invariant-polynomial scenario, and our present analysis has therefore no direct consequences for the work presented in Refs. [19,20].

# Bibliography

- [1] R. M. F. Houtappel, *Physica* **16**, 425 (1950).
- [2] J. Stephenson, *J. Math. Phys.* **11**, 413 (1970).
- [3] S. Alexander, *Phys. Lett. A* **54**, 353 (1975).
- [4] W. Kinzel and M. Schick, *Phys. Rev. B* **23**, 3435 (1981).
- [5] M. P. Nightingale, *Proc. K. Ned. Akad. Wet., Ser. B: Phys. soc.*, **82**, 235 (1979).
- [6] J. D. Noh and D. Kim, *Int. J. Mod. Phys. B* **6**, 2913 (1992).
- [7] M. N. Tamashiro and S. R. Salinas, *Phys. Rev. B.* **56**, 8241 (1997).
- [8] Z. Ràcz, *Phys. Rev. B.* **21**, 4012 (1980).
- [9] R. J. Baxter, *Exactly Solved Models in Statistical Mechanics* (Academic Press, New York, 1982).
- [10] B. Nienhuis, H.J. Hilhorst and H. W. J. Blöte, *J. Phys. A* **17**, 3559 (1984).
- [11] H. W. J. Blöte and H. J. Hilhorst, *J. Phys. A* **15**, L631 (1982).
- [12] H. W. J. Blöte and M. P. Nightingale, *Phys. Rev. B* **47**, 15046 (1993).
- [13] J. M. Kosterlitz and D. J. Thouless, *J. Phys. C* **5** L124 (1973); *J. Phys. C* **6** 1181 (1973).
- [14] H. W. J. Blöte, M. P. Nightingale, X. N. Wu and A. Hoogland, *Phys. Rev. B* **43**, 8751 (1991).
- [15] S. L. A. de Queiroz, T. Paiva, J. S. de Sá Martins and R. R. dos Santos, *Phys. Rev. E.* **59**, 2772 (1999).
- [16] S. L. A. de Queiroz, private communication (2003). The extrapolated slope  $S_L$  in Table I of the preceding reference is thus the inverse of our  $H_{KT}$ .
- [17] F. Y. Wu, *J. Math. Phys. (NY)* **15**, 687 (1974).

- [18] F. Y. Wu and X. N. Wu, J. Stat. Phys. **90**, 41 (1988).
- [19] F. Y. Wu, X. N. Wu and H. W. J. Blöte, Phys. Rev. Lett. **62**, 2773 (1989).
- [20] H. W. J. Blöte and X. N. Wu, J. Phys. A **23**, L627 (1990).
- [21] J. H. H. Perk, F. Y. Wu and X. N. Wu, J. Phys. A **23**, L131 (1990).
- [22] J. V. José, L.P. Kadanoff, S. Kirkpatrick and D. R. Nelson, Phys. Rev. B **16**, 1217 (1977).
- [23] B. Nienhuis, in *Phase Transitions and Critical Phenomena*, edited by C. Domb and J. L. Lebowitz (Academic Press, London, 1987), Vol. **11**.
- [24] We have introduced next-nearest neighbor interactions  $K_{\text{nnn}}$  and used a transfer-matrix method to locate the  $g_{\text{R}} = 3$  point and the approximate location of the Potts critical line for that value of  $K_{\text{nnn}}$  (see chapter 3 of this thesis and X. Qian and H.W.J. Blöte, Phys. Rev. E **70**, 036112 (2004)).
- [25] D. P. Landau, Phys. Rev. B **27**, 5604 (1983).
- [26] X. Qian, M. Wegewijs and H. W. J. Blöte, Phys. Rev. E **69**, 036127 (2004).
- [27] H. W. J. Blöte, F. Y. Wu and X. N. Wu, Int. J. Mod. Phys. B **4**, 619 (1990).
- [28] J. L. Cardy, J. Phys. A **17**, L358 (1984).
- [29] J. R. Heringa and H. W. J. Blöte, Phys. Rev. E **57**, 4976 (1998).

# Chapter 3

## Triangular Ising model with nearest- and next-nearest-neighbor couplings in a field

We study the Ising model on the triangular lattice with nearest-neighbor couplings  $K_{\text{nn}}$ , next-nearest-neighbor couplings  $K_{\text{nnn}} > 0$ , and a magnetic field  $H$ . This work is done by means of finite-size scaling of numerical results of transfer matrix calculations, and Monte Carlo simulations. We determine the phase diagram and confirm the character of the critical manifolds. The emphasis of this work is on the antiferromagnetic case  $K_{\text{nn}} < 0$ , but we also explore the ferromagnetic regime  $K_{\text{nn}} \geq 0$  for  $H = 0$ . For  $K_{\text{nn}} < 0$  and  $H = 0$  we locate a critical phase presumably covering the whole range  $-\infty < K_{\text{nn}} < 0$ . For  $K_{\text{nn}} < 0$ ,  $H \neq 0$  we locate a plane of phase transitions containing a line of tricritical three-state Potts transitions. In the limit  $H \rightarrow \infty$  this line leads to a tricritical model of hard hexagons with an attractive next-nearest-neighbor potential.

### 3.1 Introduction

The Ising model on the triangular lattice with nearest-neighbor couplings  $K_{\text{nn}}$ , next-nearest-neighbor couplings  $K_{\text{nnn}}$ , and a magnetic field  $H$ , is defined by the reduced Hamiltonian

$$\mathcal{H}/k_{\text{B}}T = -K_{\text{nn}} \sum_{\langle \text{nn} \rangle} s_i s_j - K_{\text{nnn}} \sum_{[\text{nnn}]} s_k s_l - H \sum_m s_m, \quad (3.1)$$

where  $s_i = \pm 1$ , and  $\langle \text{nn} \rangle$  and  $[\text{nnn}]$  indicate summations over all pairs of nearest neighbors and of next-nearest neighbors, respectively, as illustrated in Fig. 3.1.

This model, in particular the antiferromagnetic model ( $K_{\text{nn}} < 0$ ), displays interesting behavior. For  $K_{\text{nnn}} = 0$ ,  $H = 0$  the model has been solved exactly [1]. A ferromagnetic transition occurs at  $K_{\text{nn}} = \ln(3)/4$ . An antiferromagnetic ( $K_{\text{nn}} < 0$ ) mirror image of this transition is absent. This is related to the fact that the triangular lattice is not bipartite. However, at zero temperature, i.e., for  $K_{\text{nn}} \rightarrow -\infty$ , the model displays a critical phase

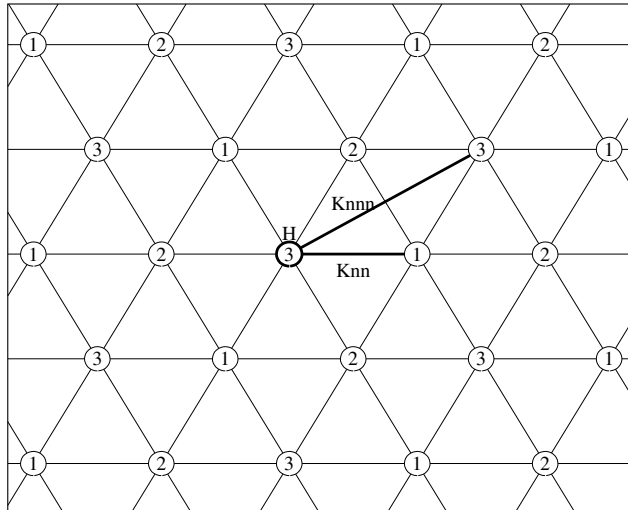


Figure 3.1: The triangular lattice with nearest-neighbor couplings  $K_{nn}$ , next-nearest-neighbor couplings  $K_{nnn}$  (examples of which are shown as bold bonds), and a field  $H$  (bold circle). The lattice is divided into three sublattices labeled 1, 2 and 3.

with algebraically decaying correlations [2]. This zero-temperature model can be exactly mapped on a solid-on-solid (SOS) model [3]. Under renormalization, it is assumed to map on the Gaussian model [4] and on the related Coulomb gas [5]. The coupling constant  $g_R$  of the Coulomb gas can thus be obtained exactly as  $g_R = 2$  so that a number of critical exponents can be calculated. The Ising temperature  $T \propto -K_{nn}^{-1}$  appears to be *relevant*: the critical state is destroyed for all  $T > 0$ . Commensurate-incommensurate transitions occur when finite differences between the infinite nearest-neighbor couplings in the three lattice directions are introduced [3, 4].

Next we consider the case of  $H = 0$  and  $K_{nnn} \neq 0$ . The mapping on the SOS model (and we may also assume this for the Coulomb gas) is still valid for  $K_{nn} \rightarrow -\infty$  but, in the absence of an exact solution,  $g_R$  is no longer exactly known. It has, however, been deduced [4] that  $g_R$  is an increasing function of  $K_{nnn}$ . The Coulomb gas analysis predicts that, for sufficiently large  $g_R$ , the Ising temperature becomes irrelevant, so that the algebraic phase extends to nonzero temperatures. This analysis also predicts that for even larger  $g_R$  a phase transition to a flat SOS phase occurs, both at zero and at nonzero temperatures.

Somewhat earlier, part of this scenario had already been described by Landau [6]. Via the lattice-gas representation of Eq. (3.1), he used the connection with the XY model in the presence of a six-state clock-like perturbation, made earlier by Domany *et al.* [7]. He could thus make use of their results [7] for this model which allow for the existence of a critical, XY-like phase in a nonzero range  $K_{nn} > 0$ . Furthermore, Landau [6] used the Monte Carlo method to verify the existence and nonuniversal character of this critical phase for the case of a fixed ratio  $K_{nnn}/K_{nn} = -1$ .

Another tool to study the model with nonzero next-nearest-neighbor couplings  $K_{\text{nnn}}$  is provided by the transfer-matrix technique. A simplification has been used in the latter approach:  $K_{\text{nnn}}$  was taken to be nonzero only for four out of the six next-nearest neighbors [8–10]. This leads to a substantial simplification of the transfer matrix calculations, but the resulting system lacks isotropy, so that applications of conformal mappings become difficult. On this basis, limited evidence [10] for the existence of the critical phase was reported; the limitation of this evidence is obviously related to the lack of sixfold symmetry.

Next we consider the consequences of a nonzero field  $H > 0$ . On the basis of the relation with the Coulomb gas it has been derived [4] that, for  $K_{\text{nn}} \rightarrow -\infty$  and  $K_{\text{nnn}} = 0$ , the magnetic field  $H$  is *irrelevant*: the critical state is not destroyed by a sufficiently small field  $H \neq 0$ . However, the magnetic field tends to increase the Coulomb gas coupling constant  $g_R$ . The field will become marginally relevant at  $g_R = 9/4$  and a transition of the Kosterlitz-Thouless (KT) type or, in this context more appropriate, of the roughening type is thus expected. This transition separates the critical phase from a long-range ordered phase, where the majority of the minus-spins have condensed on one of the three sublattices of the triangular lattice. This prediction has been confirmed [11, 12] by means of numerical methods. The long-range ordered phase extends to nonzero temperature  $T > 0$  and is separated from the disordered phase by a line of phase transitions in the  $(H, T)$  plane that belongs to the three-state Potts universality class [12–16].

Since the Ising model in a field can be mapped on a vertex model, and the critical manifolds of solvable vertex models are described by the zeroes of simple polynomials in the vertex weights [17], it may be assumed that also for the triangular lattice the critical line in the  $(H, T)$  is described by such a polynomial. This assumption was recently refuted by Qian *et al.* [12]. The shape of the critical line, as deduced from this assumption, was found to be inconsistent with the numerical evidence. They also found that the renormalization ideas originally outlined by Nienhuis *et al.* [4] could be applied to predict the shape of the critical line in the  $(H, T)$  plane for small  $T$ . This shape was found to be consistent with their numerical data for the critical line.

The aforementioned three-state Potts-like critical line is naturally part of a critical surface extending to nonzero  $K_{\text{nnn}}$ . The more involved problem to find the phase diagram in the three-parameter  $(H, K_{\text{nnn}}, K_{\text{nn}})$  space has already been partly explored. On the basis of renormalization arguments, Nienhuis *et al.* [4] obtained information about the shape of the critical surface in the limit  $H \rightarrow 0$ . Landau [6] performed Monte Carlo simulations for a fixed ratio  $K_{\text{nnn}}/K_{\text{nn}} = -1$ . He determined the line of phase transitions as a function of  $H$  and noted that the three-state Potts character along this line changes at a tricritical point beyond which the transition turns first-order.

In this work we verify the predictions in Ref. [4] and determine the critical values of  $K_{\text{nnn}}$  corresponding to several relevant values of the Coulomb gas coupling constant  $g_R$ , both for finite and infinite  $K_{\text{nn}}$ . We verify the character of the predicted critical phase at  $H = 0$ . We also study the critical phenomena associated with the introduction of a nonzero magnetic field and explore the full three-parameter phase diagram for  $K_{\text{nnn}} \geq 0$ .

This chapter is organized as follows. In Sec. 3.2, we summarize our numerical methods which include Monte Carlo algorithms and the construction of a transfer matrix. We define

the observables that will be the subject of our numerical analysis. The study of the phase transitions of the triangular Ising model with nearest- and next-nearest-neighbor couplings in a zero field is presented in Sec. 3.3, and in Sec. 3.4 we describe our results for a nonzero magnetic field; we conclude with a discussion in Sec. 3.5.

## 3.2 Numerical methods

### 3.2.1 Transfer-matrix calculations

Most of the transfer-matrix calculations were performed for  $T > 0$  so that we had to use a binary representation for the Ising spins, leading to a transfer matrix of size  $2^L \times 2^L$  for a system with finite size  $L$ . For  $T = 0$  one can use a simplified transfer matrix of a smaller size [11]. We define the spin lattice on the surface of a cylinder, and take the transfer direction perpendicular to a set of nearest-neighbor edges. The lattice is divided into three sublattices denoted as 1, 2 and 3, respectively, as shown in Fig. 3.1. Nearest-neighbor interactions occur only between different sublattices and next-nearest-neighbor interactions occur within the same sublattice.

To enable calculations for system as large as possible, a sparse matrix decomposition has been used. This leads to a very significant reduction of the required computer time and memory. The transfer matrices are defined in [11, 12] for the nearest-neighbor model. Here we modify the transfer matrix to include all next-nearest-neighbor interactions. This makes it necessary to code two (instead of one) layers of spins as the transfer matrix index. Finite-size calculations with  $L$  multiples of 6 up to  $L = 24$  were performed. The maximum finite size  $L = 24$  corresponds to a cylinder with a circumference of only 12 nearest-neighbor bonds.

The magnetic correlation function along the coordinate  $r$  in the length direction of the cylinder is defined as:

$$g_m(r) = \langle s_0 s_r \rangle. \quad (3.2)$$

At large  $r$ , this correlation function decays exponentially with a characteristic length scale  $\xi_m$  that depends on  $K_{nn}$ ,  $K_{nnn}$ ,  $H$ , and  $L$ :

$$g_m(r) \propto e^{-r/\xi_m(K_{nn}, K_{nnn}, H, L)}, \quad (3.3)$$

which can be calculated from the largest two eigenvalues  $\lambda_0$  and  $\lambda_1$  of the transfer matrix:

$$\xi_m^{-1}(K_{nn}, K_{nnn}, H, L) = \frac{1}{2\sqrt{3}} \ln(\lambda_0/\lambda_1), \quad (3.4)$$

where the factor  $2\sqrt{3}$  is a geometric factor for two layers of spins. For the calculation of  $\xi_m$ , we make use of the symmetry of the eigenvectors associated with  $\lambda_0$  and  $\lambda_1$ . The leading eigenvector (for  $\lambda_0$ ) is invariant under a spatial inversion. In contrast, the second eigenvector is antisymmetric under inversion.

The theory of conformal invariance [18] relates  $\xi_m$  on the cylinder with the magnetic scaling dimension  $X_m$  (one half of the magnetic correlation function exponent  $\eta$ ). This exponent may be estimated as

$$X_m(K_{\text{nn}}, K_{\text{nnn}}, H, L) = \frac{L}{2\pi\xi_m(K_{\text{nn}}, K_{\text{nnn}}, H, L)}. \quad (3.5)$$

Asymptotically for a critical model with large  $L$  we have

$$X_m(K_{\text{nn}}, K_{\text{nnn}}, H, L) \simeq X_m, \quad (3.6)$$

where  $X_m = 1/(2g_R)$  in the language of Coulomb gas. This equation allows us to estimate  $X_m$  numerically and thus to obtain evidence about the universality class of the model. Or, if the universality class, and thus  $X_m$ , are considered known, Eq. (3.6) and be used to determine the critical surface, e.g. to solve for  $K_{\text{nnn}}$  for given values of  $K_{\text{nn}}$ ,  $H$  and  $L$ . As a consequence of corrections to scaling, the solution will not precisely coincide with the critical point. The effects of an irrelevant scaling field  $u$  and a small deviation  $t$  with respect to the critical value of  $K_{\text{nn}}$ , or  $K_{\text{nnn}}$ , or  $H$  are expressed by

$$X_m(K_{\text{nn}}, K_{\text{nnn}}, H, L) = X_m + auL^{y_i} + btL^{y_t} + \dots, \quad (3.7)$$

where  $a$  and  $b$  are unknown constants,  $y_i$  is the leading irrelevant exponent and  $y_t$  is the temperature exponent. For the solution of the equation  $X_m(K_{\text{nn}}, K_{\text{nnn}}, H, L) = X_m$  we thus have  $auL^{y_i} + btL^{y_t} \approx 0$ , so that we expect corrections proportional to  $L^{y_i - y_t}$  in the critical point estimates. For instance, for three-state Potts universality one has  $y_t = 6/5$  and  $y_i = -4/5$  so that the leading finite-size dependence of the estimated critical points is as  $L^{-2}$ . This knowledge is helpful for the extrapolation to the actual  $L = \infty$  critical point.

In addition to  $\xi_m$ , it is possible to determine a second correlation length  $\xi_t$  describing the exponential decay of the energy-energy correlation function. It is associated with a third eigenvalue  $\lambda_2$  of the transfer matrix with an eigenvector that is symmetric under a spatial inversion, just as the one with eigenvalue  $\lambda_0$ . The pertinent eigenvalue is thus solved by means of orthogonalization with respect to the first eigenvector. In analogy with the case of the magnetic correlation length we can use the third eigenvalue  $\lambda_2$  to estimate the temperature-like scaling dimension  $X_t$  as

$$X_t(K_{\text{nn}}, K_{\text{nnn}}, H, L) = \frac{L}{2\pi\xi_t(K_{\text{nn}}, K_{\text{nnn}}, H, L)}, \quad (3.8)$$

where  $\xi_t^{-1} = \frac{1}{2\sqrt{3}} \ln(\lambda_0/\lambda_2)$ . At criticality, it behaves for large  $L$  as:

$$X_t(K_{\text{nn}}, K_{\text{nnn}}, H, L) \simeq X_t. \quad (3.9)$$

Combining Eqs. (3.6) and (3.9), we can solve for two unknowns simultaneously, using the known [5] values of the tricritical three-state Potts model, namely  $X_m = 2/21$  and  $X_t = 2/7$ . In this way, we can estimate the tricritical point  $(K_{\text{nnn}}, K_{\text{nn}})$  for a given  $H$ . The corrections can be argued to be proportional to  $L^{y_i - y_{t2}}$  where  $y_{t2} = 4/7$  and  $y_i = -10/7$ , i.e., the corrections decay as  $L^{-2}$ .

### 3.2.2 Monte Carlo simulations

Since transfer-matrix calculations are, although highly accurate, restricted to small systems, we have also written Monte Carlo algorithms for the present model. To obtain good statistical accuracies we included not only a Metropolis algorithm, but also a Wolff and a geometric cluster algorithm. Which algorithm is used depends on the location in the phase diagram. The Wolff algorithm is applicable only in the case of zero magnetic field. The geometric algorithm [19] conserves the magnetization and was therefore used in combination with the Metropolis algorithm. This combination was found to work faster than the Metropolis method, but the gain in efficiency depends on the position in the three-parameter space.

Several quantities were sampled using these algorithms in order to explore the phase diagram. First we define the uniform magnetization as  $m \equiv L^{-2} \sum_k s_k$  which tends to  $\pm 1/3$  in the long-range ordered antiferromagnetic or ‘flat’ phases, and to zero in the disordered (paramagnetic) phase. From its moments we define the magnetic Binder ratio as

$$Q_m = \frac{\langle m^2 \rangle^2}{\langle m^4 \rangle}. \quad (3.10)$$

Next, we consider the three-state Potts-like order parameter or, in the language of the present Ising model, the three sublattice magnetizations. We denote the magnetization density of sublattice  $i$  ( $i = 1, 2, \text{ or } 3$ ) as  $m_i$ . On the basis of the staggered magnetizations we write the variance of the Potts order parameter as

$$m_s^2 = m_1^2 + m_2^2 + m_3^2 - m_1 m_2 - m_2 m_3 - m_3 m_1 \quad (3.11)$$

and the corresponding dimensionless ratio as

$$Q_s = \frac{\langle m_s^2 \rangle^2}{\langle m_s^4 \rangle}. \quad (3.12)$$

At criticality, the quantities  $Q_m$  and  $Q_s$  scale as a constant plus irrelevant corrections, i.e., they converge to a constant as  $L$  increases. This property can be used for the determination of critical points.

## 3.3 Numerical results for zero field

We restrict this work to ferromagnetic next-nearest-neighbor interactions ( $K_{\text{nnn}} > 0$ ). First, we consider the Ising model in a zero field ( $H = 0$ ), and study the phase diagram in  $(K_{\text{nnn}}, K_{\text{nn}})$  plane. We distinguish the cases  $K_{\text{nn}} > 0$  and  $K_{\text{nn}} < 0$ .

### 3.3.1 Results for the ferromagnetic transition ( $K_{\text{nn}} > 0$ )

For the Ising model we have  $X_m = 1/8$  so that at criticality we expect that asymptotically for large  $L$

$$X_m(K_{\text{nn}}, K_{\text{nnn}}, 0, L) \simeq \frac{1}{8} \quad (3.13)$$

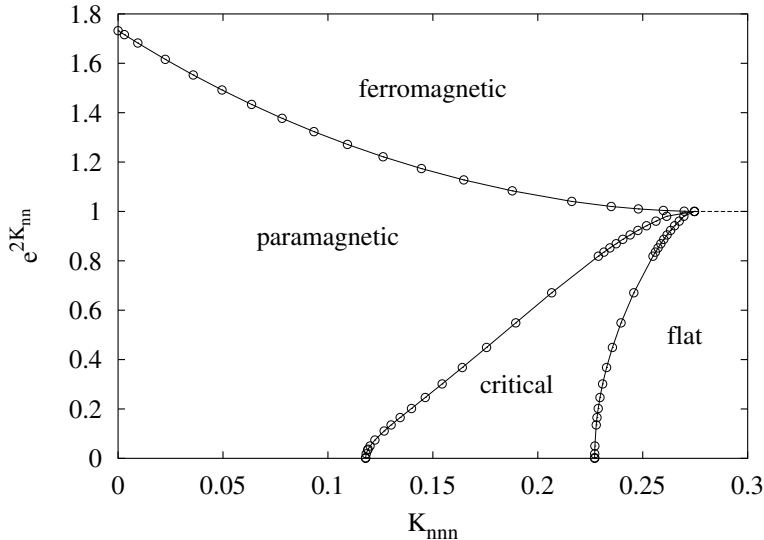


Figure 3.2: Three lines of phase transitions in the  $(K_{\text{nnn}}, K_{\text{nn}})$  plane. The numerically determined data points are shown as circles. The upper line displays the ferromagnetic critical line for  $K_{\text{nn}} > 0$ . For  $K_{\text{nn}} < 0$  there are two more lines which represent the boundaries of a critical phase which resembles the low-temperature phase of the XY model. The two lines appear to meet at a single point, the decoupling point, at  $K_{\text{nn}} = 0$ . The right hand critical line marks a roughening transition to a flat SOS phase, the left hand line a KT-like transition between the disordered and the critical phases. The numerical errors in the ferromagnetic region are much smaller than the size of the symbols; for the remaining data they are difficult to estimate but believed to be at most of the same order as the symbol size.

from which one can estimate critical points e.g. by solving for  $K_{\text{nnn}}$  at a given value of  $K_{\text{nn}}$  or vice versa. In certain cases, critical points can be determined accurately by extrapolating to  $L = \infty$ . For instance, for  $K_{\text{nnn}} = 0$  we obtain the critical value of the nearest-neighbor coupling  $K_{\text{nn}} = 0.2746528(10)$ , which is consistent with the exact result  $K_{\text{nn}} = \ln(3)/4$ . The results are shown in Fig. 3.2.

We also checked that, at the decoupling point ( $K_{\text{nn}} = 0$ ) the critical value of the next-nearest-neighbor coupling  $K_{\text{nnn}}$  equals the exact value  $\ln(3)/4$ . The three sublattices, which are also triangular lattices, become independent at the decoupling point.

### 3.3.2 Results for the antiferromagnetic region ( $K_{\text{nn}} < 0$ )

At finite  $K_{\text{nn}} < 0$  and small  $K_{\text{nnn}} > 0$ , the model is obviously disordered. As described in the Introduction, with increasing  $K_{\text{nnn}}$  the model is expected to undergo: 1) a Kosterlitz-Thouless transition to a critical phase at the point where the Coulomb gas coupling reads  $g_R = 4$ , and the corresponding value of the magnetic dimension is  $X_m = 1/(2g_R) = 1/8$ ; 2) a roughening transition to a flat phase, and the corresponding value of the magnetic

dimension is thus  $X_m = 1/18$  at  $g_R = 9$ . We have solved  $K_{nnn}$  from Eq. (3.6) for these two values of  $X_m$ , at several fixed values of  $K_{nn}$ . The results were extrapolated to  $L = \infty$  by means of three-point fits involving a constant (the estimated value of  $K_{nnn}$ ) plus a finite-size correction involving a free exponent. The final estimates are included in the phase diagram Fig. 3.2. They suggest that the two boundaries of the

critical phase merge at the decoupling point  $K_{nn} = 0$ . Our numerical results include a few special points at zero temperature ( $K_{nn} \rightarrow -\infty$ ). In the renormalization scenario, their meaning is as follows:

1. For  $g_R = 9/4$  we obtain  $K_{nnn} = 0.0185$  (4). This is where the line of roughening transitions in the  $(K_{nnn}, H)$  plane meets the  $K_{nnn}$  axis.
2. For  $g_R = 3$  we obtain  $K_{nnn} = 0.0667$  (2). This is where the line of three-state Potts transitions in the plane perpendicular to the  $K_{nnn}$  axis comes in as a straight line with a nonzero, finite slope as argued in Ref. [12].
3. For  $g_R = 4$  we obtain  $K_{nnn} = 0.1179$  (2). This is where the KT-like line in the  $(K_{nnn}, K_{nn})$  plane meets the  $K_{nnn}$  axis.
4. For  $g_R = 9$  we obtain  $K_{nnn} = 0.226$  (2). This is where the line of roughening transitions in the  $(K_{nnn}, K_{nn})$  plane meets the  $K_{nnn}$  axis. This point corresponds with an actual phase transition on the  $K_{nnn}$  axis. We note that, in cases 1 and 3, the  $K_{nnn}$  axis meets with other lines of phase transitions. However, phase transitions do not occur at points 1 and 3 because the critical amplitudes vanish on the  $K_{nnn}$  axis.

### 3.3.3 Shape of the critical lines for small $|K_{nn}|$

On the basis of an argument due to van Leeuwen [20], the scaling behavior of  $K_{nn}$  near the decoupling point ( $K_{nnn} = \ln(3)/4$ ,  $K_{nn} = 0$ ), is governed by a new critical exponent  $y_a = 7/4$ . This exponent thus determines the shape of the critical lines for small  $|K_{nn}|$  according to

$$K_{nn} \propto \left( \frac{\ln 3}{4} - K_{nnn} \right)^{7/4}. \quad (3.14)$$

One can find the critical exponent  $y_a$  exactly from the known properties of the magnetic correlation function of the critical Ising model. The spin-spin correlation behaves as

$$g_m(r) \propto r^{-2X_m},$$

where  $X_m = 1/8$  for the 2D Ising model. This also applies to the decoupling point where the model decomposes in three independent sublattices. This determines the scaling behavior of a four-spin correlation function involving spins in different sublattices in the limit of  $K_{nn} \rightarrow 0$

$$g_a(r) = \langle s_{00}s_{01}s_{r0}s_{r1} \rangle = [g_m(r)]^2 \propto r^{-4X_m}, \quad (3.15)$$

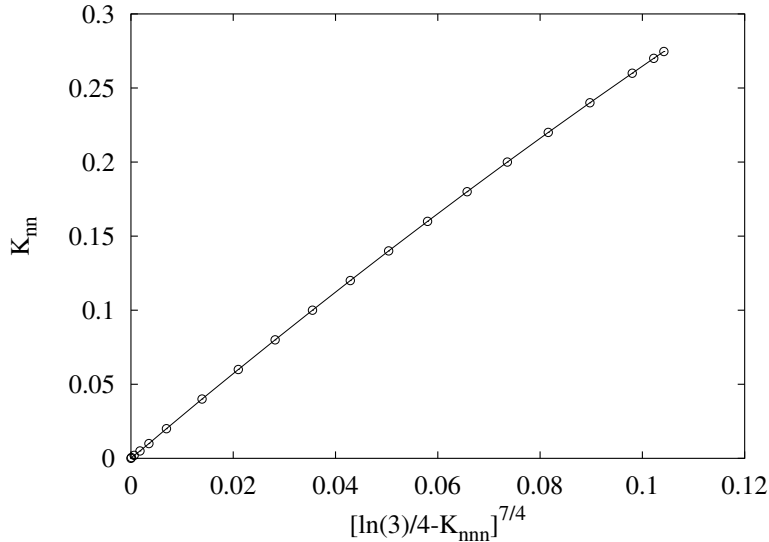


Figure 3.3: The ferromagnetic critical line, plotted as  $K_{\text{nn}}$  versus  $[\ln(3)/4 - K_{\text{nnn}}]^{7/4}$ . The approximate linear behavior confirms that the exponent  $y_a$  associated with  $K_{\text{nn}}$  obeys the theoretical prediction  $y_a = 7/4$ . The estimated errors are smaller than the symbol size.

where  $s_{00}$  and  $s_{01}$  are nearest-neighbor spins belonging to different sublattices, say sublattices 1 and 2. The same applies to the pair  $(s_{r0}, s_{r1})$  at a distance  $r$ . Eq. (3.15) describes the energy-energy correlation associated with  $K_{\text{nn}}$ . Its power-law decay is thus expressed by

$$g_a(r) \propto r^{-2X_a}, \quad (3.16)$$

where  $X_a$  is the scaling dimension of the nearest-neighbor energy density. Comparing the two Eq. (3.15) and Eq. (3.16), we conclude that  $X_a = 2X_m = 1/4$  and  $y_a = 7/4$ .

We verify Eq. (3.14) by plotting  $K_{\text{nn}}$  versus  $[\ln(3)/4 - K_{\text{nnn}}]^{7/4}$  for the ferromagnetic critical line in Fig. 3.3, and for the two lines containing the algebraic phase in the antiferromagnetic region in Fig. 3.4. In all these cases we find approximate linear behavior near the decoupling point which confirms the predicted value of  $y_a$ .

### 3.3.4 The algebraic phase

The renormalization scenario predicts that, in the algebraic phase the estimates of  $X_m$ , as obtained from Eq. (3.5), will converge to a  $K_{\text{nnn}}$ -dependent limit when the finite size  $L$  increases. However, in the disordered and flat phases, the system will renormalize away from the nonuniversal fixed line, and the data for  $X_m$  are therefore predicted to fan out for different values of  $L$ . We calculated  $X_m$  by solving Eq. (3.6) in a suitable range of  $K_{\text{nnn}}$  at fixed values of  $K_{\text{nn}}$ , namely  $K_{\text{nn}} = -\infty, -0.6, -0.4, -0.2$  and  $-0.1$ . These results confirm the renormalization predictions, as illustrated in Figs. 3.5 and 3.6.

Fig. 3.5 shows that, for  $K_{\text{nn}} = -\infty$  and  $H = 0$ , the data of  $X_m$  converge to a  $K_{\text{nnn}}$ -dependent constant in a range of  $K_{\text{nnn}}$  from zero to  $K_{\text{nnn}} = 0.226$  (2) as determined

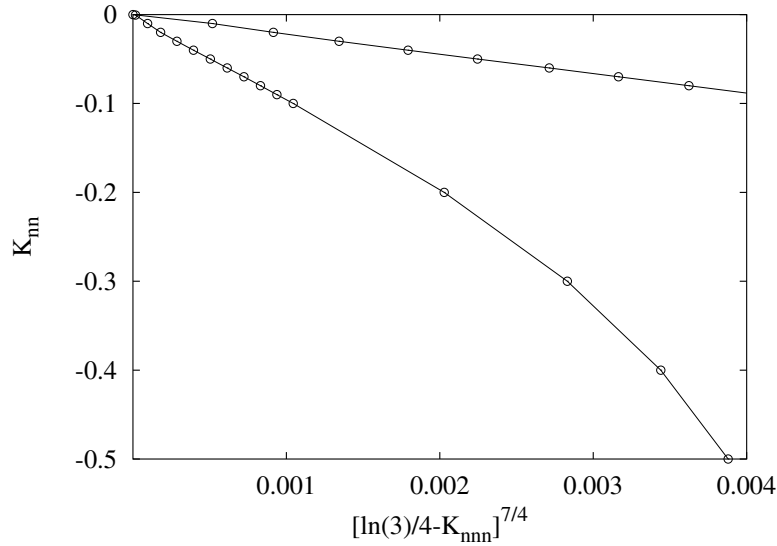


Figure 3.4: Antiferromagnetic ( $K_{nn} < 0$ ) critical lines near the decoupling point. The numerical results (circles) are plotted as  $K_{nn}$  versus  $[\ln(3)/4 - K_{nnn}]^{7/4}$ . The approximate linear behavior at small  $|K_{nn}|$  confirms that the exponent associated with the scaling of  $K_{nn}$  obeys the theoretical prediction  $y_a = 7/4$ . The estimated errors in the data points are at most of the same order as the symbol size.

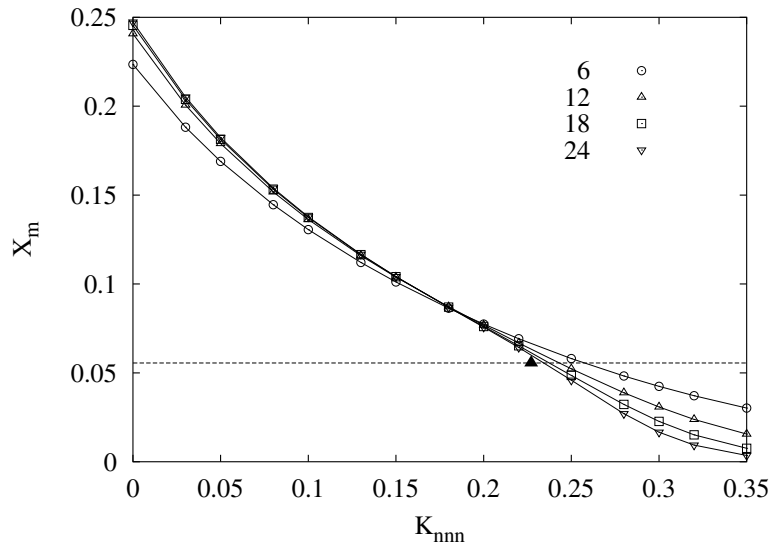


Figure 3.5: Finite-size estimates of the magnetic scaling dimension  $X_m$  versus next-nearest-neighbor coupling  $K_{nnn}$  at  $K_{nn} = -\infty$ . For clarity we include four lines connecting data points for system sizes  $L = 6, 12, 18, 24$  respectively. The dashed line indicates the special value  $X_m = 1/18$ , and the black triangle shows the estimated critical value of  $K_{nnn}$  for  $K_{nn} \rightarrow -\infty$ .

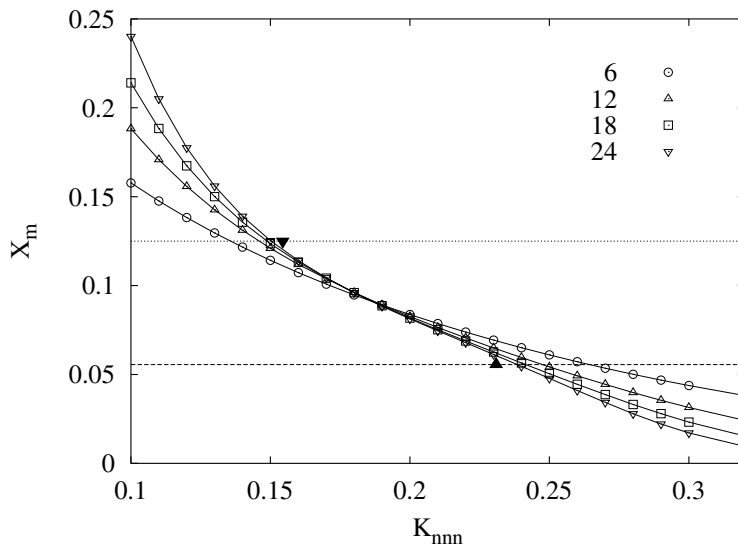


Figure 3.6: Finite-size estimates of  $X_m$  versus  $K_{\text{nnn}}$  at  $K_{\text{nn}} = -0.6$ . For clarity we include four lines connecting data points for system sizes  $L = 6, 12, 18, 24$  respectively. The dotted and dashed lines indicate the special values  $X_m = 1/8$  and  $X_m = 1/18$  respectively. The two black triangles show the estimated critical values of  $K_{\text{nnn}}$  at  $K_{\text{nn}} = -0.6$ .

above. This confirms that for  $H = 0$ ,  $K_{\text{nn}} = -\infty$  the system indeed remains critical until  $K_{\text{nnn}}$  induces a transition to a flat phase. In contrast, Fig. 3.6 indicates that for nonzero temperature the critical phase starts at a positive value of  $K_{\text{nnn}}$ . Fig. 3.7 shows the inverse of  $X_m$  and provides a clearer picture of the transition at the large  $K_{\text{nnn}}$  side. We have numerically calculated the average slopes  $S_L$  of the finite-size curves in intervals specified in Table I, and fit them as follows:

$$S_L = S_\infty + aL^{y_c} + \dots, \quad (3.17)$$

where  $S_\infty$  is constant, and  $y_c$  denotes the exponent of the leading finite-size correction. Results listed in Table 3.1 indicate that the finite-size dependence of the slopes is governed by a *negative* exponent  $y_c$  of  $L$ , which indicates that the slope  $S_L$  converges to a constant for  $L \rightarrow \infty$ , as expected in the critical range.

In order to provide independent confirmation of the algebraic phase, we also used the Monte Carlo method. Simulations were done for  $L \times L$  systems of size  $L = 24, 36, 48$ , and  $60$ . Examples of the results for  $Q_s$  and  $Q_m$  are given in Fig. 3.8 and Fig. 3.9 respectively, as a function of  $K_{\text{nnn}}$ , for  $K_{\text{nn}} = -0.2$ . These data behave similarly as those for  $X_m$ , and show good apparent convergence to a nonuniversal,  $K_{\text{nnn}}$ -dependent constant in the pertinent range. Note that the curves for  $Q_s$  display intersections near  $K_{\text{nnn}} \approx 0.207$ , and those for  $Q_m$  near  $K_{\text{nnn}} \approx 0.245$ , apparently at different sides of the algebraic phase as shown in Fig. 3.2. We interpret these intersections, i.e., solutions of Eq. (3.6) coinciding for different  $L$ , as the cancellation of the leading two  $L$ -dependent terms. Such terms are likely associated with 1) the corrections as naturally associated with irrelevant fields in the

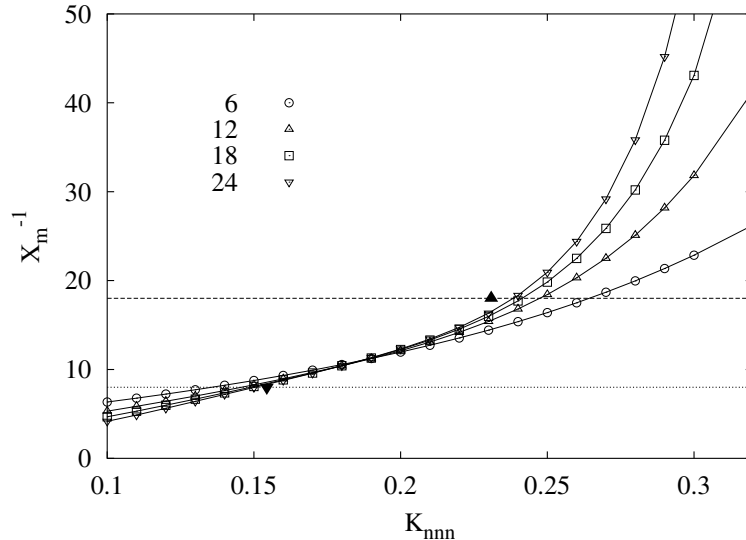


Figure 3.7: Finite-size estimates of the inverse magnetic scaling dimension  $X_m^{-1}$  versus next-nearest-neighbor coupling  $K_{nnn}$  at  $K_{nn} = -0.6$ . The meaning of the lines and symbols are the same as in Fig. 3.6. The phase transition to flat phase is clearly visible in this figure.

Table 3.1: Fitted results for the extrapolated average slope  $S_\infty \approx dX_m/dK_{nnn}$  in the algebraic phase. The last column shows the exponent  $y_c$  of finite-size correction. The increase of  $|S_\infty|$  with  $K_{nnn}$  corresponds with the narrowing of the algebraic phase when the decoupling point  $K_{nn} = 0$  is approached. The intervals of  $K_{nnn}$  in which the average slopes are calculated are listed in the second column.

$K_{nn}$	$K_{nnn}$	$S_\infty$	$y_c$
$-\infty$	0.18 - 0.20	-0.59 (3)	-1.1 (2)
-0.6	0.18 - 0.20	-0.78 (2)	-1.2 (2)
-0.4	0.18 - 0.22	-1.20 (8)	-0.7 (2)
-0.2	0.21 - 0.22	-3.3 (5)	-0.3 (1)
-0.1	0.23 - 0.25	-5.0 (10)	-0.2 (1)

algebraic phase; and 2) the ‘fanning-out’ phenomenon mentioned above. It appears that the first types of corrections in  $Q_s$  and  $Q_m$  are of a different sign.

### 3.4 Results for nonzero field

In view of the Ising character of (3.1), we restrict ourselves to  $H \geq 0$  without loss of generality. The phase diagram without next-nearest-neighbor interactions, i.e., in the  $(H, K_{nn})$  plane has already been determined by Qian *et al.* [12], with special emphasis on the limit  $K_{nn} \rightarrow -\infty$ . In that limit, a roughening-type transition is located [11, 12]

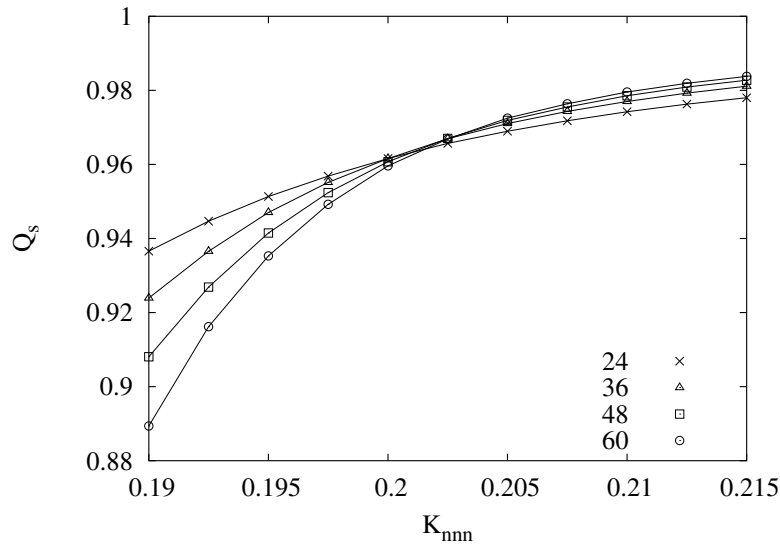


Figure 3.8: Dimensionless amplitude ratio  $Q_s$  versus  $K_{nnn}$  at  $K_{nn} = -0.2$ . Intersections are found to occur near the transition point between the disordered and the algebraic phases. The four lines connecting the data points represent, with increasing slope, system sizes  $L = 24, 36, 48,$  and  $60$ , respectively. The numerical uncertainty margins are much smaller than the size of the data points.

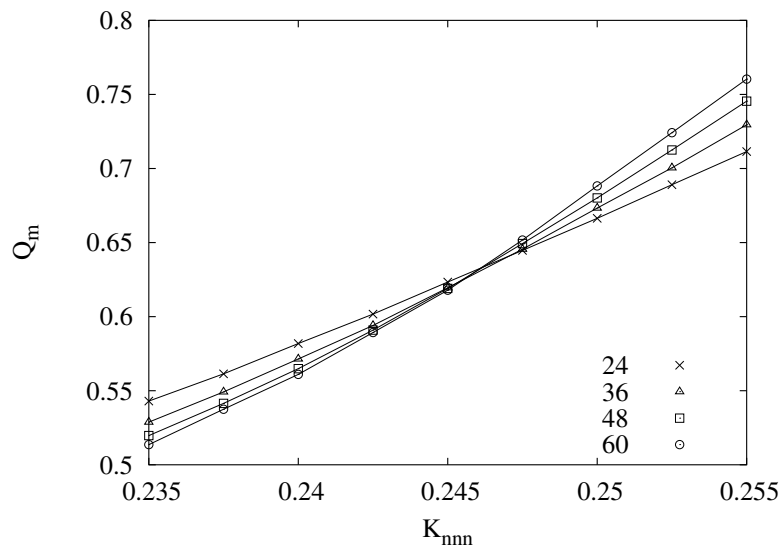


Figure 3.9: Dimensionless amplitude ratio  $Q_m$  versus  $K_{nnn}$  at  $K_{nn} = -0.2$ . Intersections are found to occur near the transition point between the algebraic and the flat SOS phases. The four lines connecting the data points represent, with increasing slope, system sizes  $L = 24, 36, 48,$  and  $60$ , respectively. The numerical uncertainty margins are much smaller than the size of the data points.

near  $H = 0.266$ . As mentioned above, the algebraic phase becomes less stable against perturbation by  $H$  when  $K_{\text{nnn}}$  increases, and the algebraic phase in the  $(K_{\text{nnn}}, H)$  plane shrinks to zero at  $g_R = 9/4$  which corresponds, as mentioned above, to  $K_{\text{nnn}} = 0.0185$ .

The line connecting the two points  $(K_{\text{nnn}}, H) = (0, 0.266)$  and  $(0.0185, 0)$  is a line of roughening transitions separating the algebraic and the ordered phases. The renormalization description implies that this line is a straight line when expressed in the scaling fields. In view of the proximity of both numerically determined points, we expect an almost straight line in the  $(K_{\text{nnn}}, H)$  plane. The connection of the three-state Potts transition line and the roughening transition point in  $(H, K_{\text{nn}})$  plane has been analytically investigated by Qian *et al.* using renormalization arguments. Their analysis indicates that the roughening transition at  $H = 0.266$  is the end point of the Potts transition line in  $(H, K_{\text{nn}})$  plane for  $T \downarrow 0$ . Their result applies similarly to other points on the line of roughening transitions. We thus believe that this whole line serves as a frontier of the Potts critical surface, as well as the part of the  $K_{\text{nnn}}$  axis with  $g_R$  between  $9/4$  and  $4$  as determined in Sec. 3.3.1.

Since three-state Potts universality implies  $X_m = 2/15$  at criticality, we expect that asymptotically for large  $L$

$$X_m(K_{\text{nn}}, K_{\text{nnn}}, H, L) \simeq \frac{2}{15} \quad (3.18)$$

from which one can estimate critical points by solving for one of the three variables  $(K_{\text{nn}}, K_{\text{nnn}}, H)$  for specified values of the other two, and subsequent extrapolation to  $L = \infty$ . We thus calculated critical points on several lines at fixed values of  $H$ . The results are shown as lines connecting these points in Fig. 3.10. In order to zoom in on the connection of the three-state Potts transition surface and the transition lines in the  $(K_{\text{nnn}}, K_{\text{nn}})$  plane, we have also estimated critical values of  $H$  at fixed values of  $K_{\text{nn}}$ , for a suitably chosen range of  $K_{\text{nnn}}$ . Results for  $K_{\text{nn}} = -0.8, -0.1, -0.15$  are included in Fig. 3.10. They fit well with the qualitative predictions for the shape of the critical surface [4] for small  $H$ . Furthermore, our data for the critical points at  $K_{\text{nnn}} = 0.0667$ , corresponding with  $g_r = 3$ , agree with the linear behavior as mentioned in Sec. 3.3.1.

Our results confirm that, when the next-nearest-neighbor coupling  $K_{\text{nnn}}$  becomes sufficiently strong, the transition from the disordered phase to the ordered phase changes character at a tricritical line, beyond which the transition turns first-order. We have located the tricritical line using transfer-matrix calculations. By solving Eqs. (3.6) and (3.9) simultaneously for  $K_{\text{nn}}$  and  $K_{\text{nnn}}$  at specified values of  $H$ , we obtain results shown in Table 3.2, and included in Fig. 3.10. In comparison with transfer-matrix calculations involving only  $X_m$ , the memory requirements are somewhat larger. As a consequence only 3 values of  $L$  up to 18 could be used. But we found that finite-size corrections are relatively small, and we are confident that the tricritical line is well determined.

For sufficiently large fields  $H$ , triangles may contain at most one minus-spin and the tricritical line approaches a tricritical lattice-gas limit. In this limit the nearest-neighbor coupling and the field satisfy a linear relation

$$K_{\text{nn}} = -\frac{H}{6} + C. \quad (3.19)$$

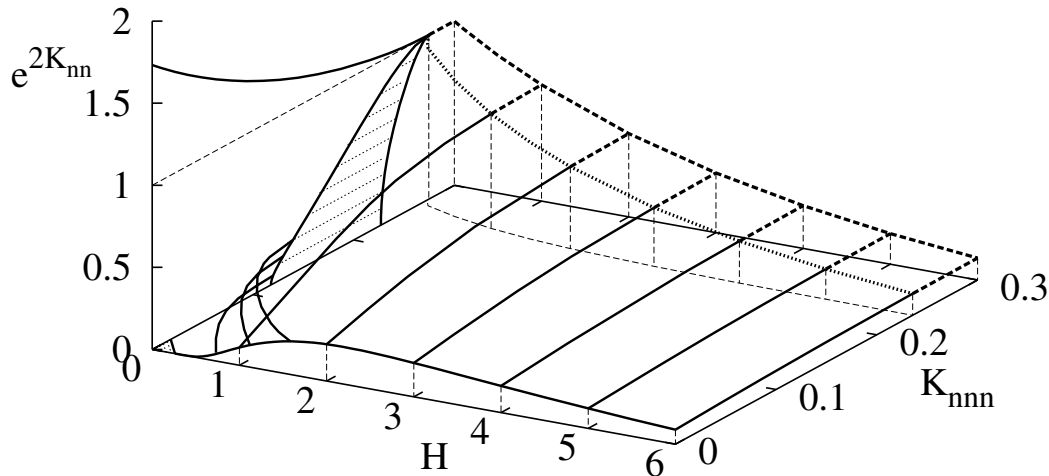


Figure 3.10: The complete phase diagram in the three-parameter space  $(H, K_{\text{mnn}}, e^{2K_{\text{mn}}})$ . The solid lines denote second-order phase transitions, and the heavy dotted line is the tricritical line separating the three-state Potts critical sheet from the first-order sheet which is shown by heavy dashed lines. The three-state Potts critical surface is believed to connect to the  $e^{2K_{\text{mn}}} = 0$  plane at the KT line near the origin, and at the  $K_{\text{mnn}}$  axis until the appearance of the critical phase. The algebraic phases for  $H = 0$  and for  $T = 0$  are lightly shaded, and the thin dashed lines are projection lines added for clarity. The error margins are at most of the same order as the thickness of the lines.

As illustrated in Fig. 3.11, the numerical data fit this expression well, except at small  $H$ . In order to obtain a satisfactory fit to the numerical data for  $H \geq 1$ , we added terms proportional to  $e^{-2H/3}$  and  $e^{-4H/3}$  to Eq. (3.19). This fit yielded  $C = -0.01481$  (5). A similar fit without a term proportional to  $H$  yielded  $K_{\text{mnn}} = 0.23514$  (7) for the tricritical lattice gas limit.

We have used Monte Carlo simulations to determine the location of the sheet of first-order transitions at  $K_{\text{mnn}} = 0.3$ . We found that, depending on  $K_{\text{mn}}$  and  $H$ , a randomly initialized system evolved to a phase either largely magnetized, or resembling one of the three ordered Potts states. The threshold values between these two regimes are shown by the heavy dashed lines in Fig. 3.10. They fit smoothly with the results obtained in the critical range and for the tricritical line.

Table 3.2: Tricritical points as obtained by the transfer matrix method for several values of  $H$ . The decoupling point  $K_{nn} = 0$  is included here as the end point of the tricritical line, although it does itself not belong to the tricritical three-state Potts universality class.

$H$	$K_{nn}$	$K_{nnn}$
0.00	0.0000 (0)	$\ln(3)/4$ (0)
0.05	-0.0107 (12)	0.269 (1)
0.10	-0.0214 (10)	0.2654 (5)
0.5	-0.0937 (5)	0.2572 (5)
1.0	-0.1799 (2)	0.2500 (2)
1.5	-0.2644 (2)	0.2452 (2)
2.0	-0.3481 (2)	0.2421 (2)
3.0	-0.5150 (1)	0.23845 (8)
4.0	-0.6816 (1)	0.23678 (8)
5.0	-0.84823 (5)	0.23599 (8)
6.0	-1.01487 (5)	0.23560 (8)

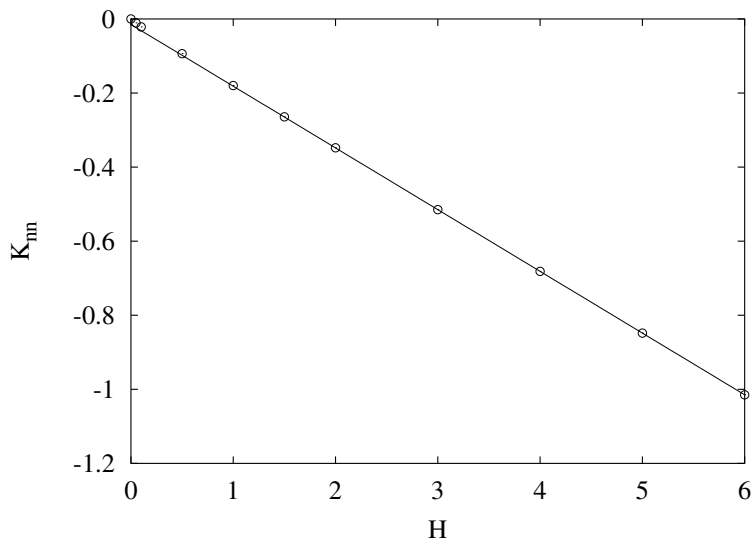


Figure 3.11: The tricritical line shown as  $K_{nn}$  versus  $H$ . The numerically determined tricritical points are shown as circles, and the solid line represents the tricritical lattice-gas limit as  $K_{nn} = -H/6 - 0.01481$ .

### 3.5 Discussion

We have determined the phase diagram of the model Eq. (3.1) for  $K_{nnn} \geq 0$ . We locate a surface of phase transitions. This surface divides into a three-state Potts-like critical sheet and a first-order part. The two parts are separated by a tricritical line. While the determination of tricritical line becomes less accurate for small  $|K_{nn}|$ , our data suggest

that it spans the whole range  $-\infty < K_{\text{nn}} < 0$ . This is in agreement with the minimal renormalization scenario in which the tricritical line is a flow line leading directly from the decoupling point to the tricritical fixed point.

For  $H \rightarrow \infty$ , minus-spins are excluded on nearest-neighbor sites and the substitution  $\sigma_i = (1 - s_i)/2$  reduces the model to a hard-hexagon lattice gas described by the reduced Hamiltonian

$$\mathcal{H}_{hh}/k_{\text{B}}T = V_{\text{nn}} \sum_{\langle \text{nn} \rangle} \sigma_i \sigma_j + V_{\text{nnn}} \sum_{[\text{nnn}]} \sigma_k \sigma_l - \mu \sum_m \sigma_m, \quad (3.20)$$

where the site variables assume values  $\sigma_i = 0, 1$  and  $V_{\text{nn}} \rightarrow \infty$  so that nearest-neighbor exclusion applies. The chemical potential of the lattice-gas particles depends on the Ising parameters as  $\mu = -12K_{\text{nn}} - 12K_{\text{nnn}} - 2H$ , and the next-nearest-neighbor potential as  $V_{\text{nnn}} = -4K_{\text{nnn}}$ . For  $V_{\text{nnn}} = 0$  this model reduces to Baxter's hard-hexagon lattice gas [21]. According to the analysis presented in Sec. 3.4, the tricritical line persists in the lattice-gas limit. The Ising parameters  $C$  and  $K_{\text{nnn}}$  determine the tricritical parameters of the lattice-gas as  $\mu = -2.644$  (1) and  $V_{\text{nnn}} = -0.9406$  (3). Our findings may be compared with those of Verberkmoes and Nienhuis [22] for a model with  $V_{\text{nnn}} = 0$  but including additional smaller hexagons. They also report a tricritical point, attributed to an effective attraction between the hard hexagons, induced by entropic effects associated with the small hexagons.

An Ising-like tricritical point is known to occur also in the analogous case of the hard-square lattice gas [21,23,24]. Our result thus confirms that tricriticality is a generic property of hard-core lattice gases with attractive next-nearest-neighbor interactions.

Since we do not doubt the universality class of the tricritical line, we have not explicitly determined its critical exponents. However, we remark that the fast apparent convergence of the estimated tricritical points confirms that the values of the Potts tricritical exponents  $X_m$  and  $X_t$ , as used to solve Eqs. (3.6) and (3.9), do indeed apply.

Renormalization analysis predicts that the uniform magnetic field  $H$  is relevant, except for a small range  $2 \leq g_R \leq 9/4$ . Thus the plane  $H = 0$  qualifies as a possible locus of new universality classes, in line with the existence of a critical phase such as predicted by the renormalization scenario and confirmed numerically. We finally note that the renormalization equations for the KT transitions imply that the line of KT transitions, as shown in Fig. 3.2 on the left hand boundary of the critical phase, should come in as a straight line on the horizontal axis, in contrast with the numerical results which there display a small part with a sudden curvature. We believe that this is a finite-size effect, explained by the same renormalization equations, which involve the marginally irrelevant temperature field parametrizing the line of KT transitions. This scaling field generates slowly converging finite-size corrections. This field and its associated finite-size effects vanish at  $K_{\text{nn}} = -\infty$ .



# Bibliography

- [1] R. M. F. Houtappel, *Physica* **16**, 425 (1950).
- [2] J. Stephenson, *J. Math. Phys.* **11**, 413 (1970).
- [3] H. W. J. Blöte and H. J. Hilhorst, *J. Phys. A: Math. Gen* **15**, L631 (1982).
- [4] B. Nienhuis, H. J. Hilhorst and H. W. J. Blöte, *J. Phys. A: Math. Gen* **17**, 3559 (1984).
- [5] B. Nienhuis, in *Phase Transitions and Critical Phenomena*, edited by C. Domb and J. L. Lebowitz (Academic Press, London, 1987), Vol. **11**.
- [6] D. P. Landau, *Phys. Rev. B*, **27**, 5604 (1983).
- [7] E. Domany, M. Schick, J. S. Walker and R. B. Griffiths, *Phys. Rev. B*, **18**, 2209 (1978).
- [8] H. Kitatani and T. Oguchi, *J. Phys. Soc. Jpn.* **57**, 1344 (1988).
- [9] S. Miyashita, H. Kitatani and Y. Kanada, *J. Phys. Soc. Jpn.* **60**, 1523 (1991).
- [10] S. L. A. de Queiroz and E. Domany, *Phys. Rev. E* **52**, 4768 (1995).
- [11] H. W. J. Blöte and M. P. Nightingale, *Phys. Rev. B* **47**, 15046 (1993).
- [12] Chapter 2 of this thesis; and see also X. Qian, M. Wegewijs and H. W. J. Blöte, *Phys. Rev. E* **69**, 036127 (2004).
- [13] S. Alexander, *Phys. Lett. A* **54**, 353 (1975).
- [14] W. Kinzel and M. Schick, *Phys. Rev. B* **23**, 3435 (1981).
- [15] J. D. Noh and D. Kim, *Int. J. Mod. Phys. B* **6**, 2913 (1992).
- [16] M. N. Tamashiro and S. R. Salinas, *Phys. Rev. B* **56**, 8241 (1997).
- [17] F. Y. Wu, *J. Math. Phys.* **15**, 687 (1974).
- [18] J. L. Cardy, *J. Phys. A* **17**, L358 (1984).

- [19] J. R. Heringa and H. W. J. Blöte, Phys. Rev. E **57**, 4976 (1998).
- [20] J. M. J. van Leeuwen, Phys. Rev. Lett. **34**, 1056 (1975).
- [21] R. J. Baxter, J. Phys. A **13**, L61 (1980).
- [22] A. Verberkmoes and B. Nienhuis, Phys. Rev. E **60**, 2501 (1999).
- [23] R. J. Baxter, *Exactly Solved Models in Statistical Mechanics* (Academic press, New York, 1982).
- [24] D. A. Huse, J. Phys. A **16**, 4357 (1983).

# Chapter 4

## Simulation algorithms for the random-cluster model

We compare the performance of the existing Monte Carlo algorithms for the simulation of the random-cluster representation of the  $q$ -state Potts model for continuous values of  $q$ . In particular we consider a local bond update method, a statistical reweighting method of percolation configurations, and a cluster algorithm, all of which generate Boltzmann statistics. The dynamic exponent  $z$  of the cluster algorithm appears to be quite small, and to assume the values of the Swendsen-Wang algorithm for  $q = 2$  and  $3$ . The cluster algorithm appears to be much more efficient than our versions of the other two methods for the simulation of the random-cluster model. The higher efficiency of the cluster method with respect to the local method is primarily due to the fact that the computer time usage of the local method increases more rapidly with system size; the difference between the dynamic exponents is less important. Furthermore, we formulate a new Monte Carlo algorithm for the simulation of the random-cluster model for continuous values of  $q$ . It does not use a full cluster decomposition, but flips only one cluster per step, just as the single cluster algorithm for integer  $q$ . This algorithm can indeed reduce to the Wolff method for integer  $q$ . We compare its performance with the algorithm that involves full cluster decomposition of each configuration. In contrast to the case of integer  $q$ , where the single-cluster (Wolff) algorithm is more efficient than the full cluster decomposition (Swendsen-Wang) algorithm, the present single-cluster algorithm for non-integer  $q$  has a larger dynamic exponent than the full cluster decomposition algorithm.

### 4.1 Introduction

The Potts model [1], which can be seen as a generalization of the Ising model, has been the subject of considerable research in recent decades [2]. Many of these investigations make use of the Kasteleyn-Fortuin mapping on the random-cluster model [3]. Remarkably, the symmetry parameter  $q$  of the  $q$ -state Potts model appears as a continuous parameter in the random-cluster model. Thus, the random-cluster model is a generalization of the Potts

model to non-integer values of  $q$  (and on this basis one might even choose to refer to such a model with non-integer  $q$  as a Potts model). For the integer  $q = 1$ , the random-cluster model reduces to the bond-percolation model.

Another mapping, formulated by Baxter, Kelland and Wu [4], leads from the random-cluster model on a planar lattice to the 6-vertex model, which is a limiting case of Baxter's 8-vertex model [5]. This second mapping lends further physical meaning to the random-cluster model.

While many questions concerning the random-cluster model could be answered exactly [6, 7], in many cases, especially in more than two dimensions, numerical approximations are needed. For integer  $q > 1$  one can obviously apply a Metropolis-type algorithm to the Potts representation of the model. However, such simulations suffer from the critical-slowness phenomenon, which inhibits the investigation of relatively large system sizes. This problem was partly solved by Swendsen and Wang [8]. Their algorithm is non-local in the sense that arbitrarily large groups of Potts variables are flipped at the same time. As a result, critical slowing down, as expressed by the dynamic exponent  $z$ , is reduced, though not eliminated. The dynamic exponent is still dependent on the number of states  $q$  and the dimensionality  $d$ , as reviewed in Ref. [9].

Simulation methods have been developed as well for noninteger  $q$ . While the random-cluster model is rich and interesting in its own right, the work on such algorithms for general  $q$  may further be justified by fundamental questions such as whether the renormalization scenario [10] for the two-dimensional Potts model does also apply in more than two dimensions. Although this question can also be studied by means of analytical approximations [11, 12], their accuracy is difficult to estimate and numerical tests are thus desirable. Furthermore, some critical exponents, for instance, the so-called backbone exponent of the Potts model is not exactly known, even in two dimensions. It may be determined numerically as a function of  $q$  by means of Monte Carlo methods, and then it is natural to include non-integer values of  $q$  [13] for a more complete coverage.

A local Monte Carlo algorithm for the non-integer  $q$  random-cluster model in two dimensions was formulated by Sweeny [14]. It updates individual bond variables. Although it has been reported that critical slowing down is absent [15], the Li-Sokal method [16] is also applicable here and it follows that  $z \geq \alpha/\nu$  where  $\alpha$  and  $\nu$  are the specific-heat and correlation-length exponents respectively. Therefore systems with a positive specific-heat exponent  $\alpha$  *must* display critical slowing down, as has been confirmed later [17]. In this algorithm, the transition probabilities depend on non-local information: whether neighbor sites are connected by a percolating path of bond variables. Thus the execution of a bond update may require the exploration of a large percolation cluster. Since the pertinent cluster size is divergent at criticality, the number of operations needed for an update of the system increases faster than the number of sites  $N$  in the system. How much faster it increases still depends on the sophistication of the algorithm; the Sweeny [14] algorithm is relatively efficient because it avoids the formation of a whole cluster by following only its perimeter instead.

In a different approach, Hu [18] applied a statistical reweighting procedure to bond percolation configurations in order to sample the  $q \neq 1$  random-cluster model. While this

model has no critical slowing down in the sense that it generates uncorrelated configurations, the number of samples needed before a significant weight occurs increases rapidly with the system size [19]. In practice, this effect is similar to critical slowing down in the sense that many simulation steps have to be performed before a meaningful new sample is obtained.

Given the recent simulations [13, 15] that have been performed using the local bond update method, it would be interesting to compare with the performance of a cluster algorithm for continuous  $q$  random-cluster models. Indeed the Swendsen-Wang algorithm can be adapted to include non-integer values of  $q$ ; such an algorithm was described by Chayes and Machta [20]. The resulting cluster algorithm is simple, and requires only of order  $N$  operations for an update of the system. But it is applicable only for  $q \geq 1$ .

In this work we report a comparison between our versions of these three algorithms for non-integer values of  $q$ . We illustrate their performance by means of simple applications, and we estimate the dynamic exponent of the cluster algorithm for three values of  $q$ . We feel that our findings may be of some use for those planning numerical investigations of the random-cluster model. In Section 4.2 we summarize the algorithms, and we report our results in Section 4.3. Furthermore, in Section 4.4 we formulate a new single-cluster algorithm for the random-cluster model with real  $q > 1$ . Since for integer  $q$ , the Wolff method is generally more efficient than the Swendsen-Wang algorithm, it is of interest to test if the same holds for our single-cluster algorithm in comparison with the full cluster decomposition algorithm for non-integer  $q$ . However, after comparing the dynamic exponents of both algorithms, we find that that this is not the case. Remarkably, the single-cluster algorithm formulated in this work represents a new dynamic universality class.

## 4.2 The existing algorithms

For the convenience of the reader, we summarize the three algorithms for the simulation of the random-cluster model. To expose the close relation with the discrete- $q$  Potts model, we start from the Potts partition sum

$$Z_\sigma = \left[ \prod_{i=1}^N \sum_{\sigma_i=1}^q \right] \prod_{\langle ij \rangle} \exp(K \delta_{\sigma_i \sigma_j}), \quad (4.1)$$

where the  $\sigma_i$  are site variables, and the second product is over all nearest-neighbor pairs  $\langle ij \rangle$ . The coupling  $K$  includes a factor  $1/k_B T$  and is restricted to  $K \geq 0$ . The mapping on the random-cluster model [3] eliminates the site variables  $\sigma_i = 1, 2, \dots, q$  after introducing bond variables  $b_{ij} = 0$  or  $1$  between neighboring sites  $i$  and  $j$ . Bonds  $b_{ij} = 1$  ( $0$ ) are considered to be present (absent). In terms of the new variables one obtains the random-cluster partition sum

$$Z_\sigma = Z_b \equiv \left[ \prod_{\langle ij \rangle} \sum_{b_{ij}=0}^1 \right] q^{n_c} u^{n_b} = \sum_{\{b\}} \prod_{k=1}^{n_c} q u^{n_b^{(k)}}, \quad (4.2)$$

where  $u \equiv e^K - 1$ ,  $n_b$  is the number of present bonds, and  $n_c$  the number of clusters (or components) formed by these bonds. The sum on  $\{b\}$  is shorthand for the sum on all bond variables, and  $n_b^{(k)}$  is the number of nonzero bonds in the  $k$ -th cluster.

Eq. (4.2) can serve directly to formulate a Metropolis-type importance-sampling algorithm for local updates of the bond variables  $b_{ij}$ . A bond ( $b_{ij} = 1$ ) contributes a reduced (i.e., divided by  $k_B T$ ) energy  $\ln(1/u)$  if sites  $i$  and  $j$  are already connected by some other path of such bonds, or  $\ln(q/u)$  if they are not connected. Thus the local update of a bond variable requires the performance of a task that is essentially nonlocal: to determine whether  $i$  and  $j$  belong to the same cluster. After completion of this task, the energy change due to the bond ‘flip’ is known, and thereby the transition probabilities. Given the time-consuming nature of the task mentioned, one naturally avoids it if not necessary [15]. The latter possibility arises if the value of the random number used for the bond update is such that the result ( $b_{ij} = 0$  or  $1$ ) does not depend on whether  $i$  and  $j$  are connected.

In the statistical reweighting method as formulated by Hu [18] one generates independent configurations of bond variables using the percolation model. This ensemble of configurations can be described by Eq. (4.2) with  $q = 1$ . The bond probability is  $p = u/(u + 1)$ . Thus, the probability distribution of  $\{b\}$  is

$$P_{q=1}(\{b\}) = p^{n_b}(1-p)^{N_b-n_b} = u^{n_b}/Z_{q=1}, \quad (4.3)$$

with

$$Z_{q=1} = \left[ \prod_{\langle ij \rangle} \sum_{b_{ij}=0}^1 \right] u^{n_b} = (1+u)^{N_b}, \quad (4.4)$$

where  $N_b$  is the total number of nearest-neighbor bonds in the system. The expectation value of an observable  $A$  depending on  $\{b\}$  is, in the random-cluster model,

$$\langle A \rangle_{RC} = \left[ \prod_{\langle ij \rangle} \sum_{b_{ij}=0}^1 \right] A q^{n_c} u^{n_b} / Z_b. \quad (4.5)$$

This can be rewritten as

$$\langle A \rangle_{RC} = \frac{\left[ \prod_{\langle ij \rangle} \sum_{b_{ij}=0}^1 \right] A q^{n_c} u^{n_b}}{Z_{q=1}} \times \frac{Z_{q=1}}{Z_b} = \langle A q^{n_c} \rangle_P / \langle q^{n_c} \rangle_P, \quad (4.6)$$

where the subscript  $P$  denotes averaging on percolation configurations generated by Eq. (4.3). The advantage of this method is that the relevant quantities  $A q^{n_c}$  and  $q^{n_c}$  can be sampled on the basis of percolation configurations which are uncorrelated, and simple to generate. The disadvantage is that the reweighting factor  $q^{n_c}$  can vary, in particular for large system sizes, over such a large range that, among the generated configurations  $\{b\}$ , those which contribute significantly to the  $\langle \dots \rangle_P$  averages become very scarce [19].

The cluster algorithm can conveniently be described in terms of a mapping between the random-cluster model, Eq. (4.2), and a model with site as well as bond variables. To this

purpose one defines auxiliary ‘color’ variables  $\tilde{t}_k=0$  or 1 for each cluster  $k = 1, 2, \dots, n_c$ :

$$Z_b = \sum_{\{b\}} \prod_{k=1}^{n_c} \sum_{\tilde{t}_k=0}^1 u^{n_b^{(k)}(1-\tilde{t}_k)} [(q-1)u^{n_b^{(k)}}]^{\tilde{t}_k}. \quad (4.7)$$

Clusters of color 0 and 1 have weight 1 and  $q-1$  respectively. The sum over the colors can be replaced by a sum over  $N$  site-color variables  $t_i = 0$  or 1 if, at the same time, one includes a factor  $\delta_{t_i t_j}^{b_{ij}}$  (with the convention  $0^0=1$ ) for each bond variable, so that all sites in one cluster have the same color:

$$Z_b = Z_{tb} \equiv \sum_{\{t\}} \sum_{\{b\}} \prod_{\langle ij \rangle} (u \delta_{t_i t_j}^{b_{ij}})^{b_{ij}} \prod_{k=1}^{n_c} (q-1)^{t_{s(k)}}, \quad (4.8)$$

where  $s(k)$  is a site in the  $k$ -th cluster. For a given site configuration  $\{t\}$  one distinguishes three types of bonds ( $ij$ ):

$$\begin{aligned} \text{type 0} & : t_i = t_j = 0 ; \\ \text{type 1} & : t_i = t_j = 1 ; \\ \text{type 2} & : t_i + t_j = 1 . \end{aligned}$$

Accordingly, superscripts are appended to the pertinent summation and product signs

$$Z_{tb} = \sum_{\{t\}} \left[ \sum_{\{b\}}^{(0)} \prod_{\langle ij \rangle}^{(0)} u^{b_{ij}} \right] \left[ \sum_{\{b\}}^{(1)} \prod_{\langle ij \rangle}^{(1)} u^{b_{ij}} \prod_{k=1}^{n_c^{(1)}} (q-1) \right] \left[ \sum_{\{b\}}^{(2)} \prod_{\langle ij \rangle}^{(2)} (1-b_{ij}) \right], \quad (4.9)$$

where the clusters of color 1 are labeled  $1, 2, \dots, n_c^{(1)}$ . Execution of the type 0 and 2 sums, and rewriting the type 1 sum yields the partition sum expressed in site variables, and bond variables only of type 1:

$$Z_{tb} = Z_{tb1} \equiv \sum_{\{t\}} \left[ \prod_{\langle ij \rangle}^{(0)} (1+u) \right] \sum_{\{b\}}^{(1)} \left[ \prod_{k=1}^{n_c^{(1)}} (q-1) u^{n_b^{(k)}} \right]. \quad (4.10)$$

Just as Eq. (4.2) describes the probability distribution of bond configurations of the random-cluster model, Eq. (4.10) represents the probability distribution of a system with both site variables  $t_i = 0, 1$  and bond variables  $b_{ij}$  between nearest-neighbor sites of type 1. The random selection of clusters of color 0 with probability  $1/q$  leads to the ensemble of Eq. (4.8) which describes a system of both site and bond variables. A partial summation on bond variables then leads to Eq. (4.10). In a Monte Carlo application of this mapping one makes use of the fact that the terms in the partition sums are proportional to the probability corresponding configuration. Subsequent assignments of values to random variables in the Monte Carlo procedure are decided such that the resulting probability of each configuration is in agreement with the partition function as expressed in the pertinent variables. This guarantees that the equilibrium distribution is always maintained. Thus, starting from a bond configuration drawn from the equilibrium ensemble of Eq. (4.2):

1. Assign color 0 to each cluster with probability  $1/q$ ;
2. Erase all bonds  $b_{ij} = 1$  between type-0 sites;
3. Choose new bonds  $b_{ij} = 1$  between type-0 sites with probability  $u/(u + 1)$ ;
4. Form clusters on the type-0 sites;
5. Erase the color variables.

Here we have stochastically executed the step from Eq. (4.2) to Eq. (4.7), followed by the steps leading to Eq. (4.10); and then, in reverse order, back to Eq. (4.2). This leads to a new bond configuration that again satisfies the equilibrium statistics of Eq. (4.2). We note that these steps resemble the Swendsen-Wang procedure; a difference is that one here uses 2 instead of  $q$  colors, and that they are not treated equivalently. The use of a probability  $1/q$  restricts the useful range of the algorithm to  $q > 1$ . The above description of the algorithm is given such as to closely follow the mapping; the actual procedure is even simpler because it is not necessary to keep track of the bond variables  $b_{ij}$ . These variables are only needed during the cluster formation process. The information to which cluster a site belongs is stored as an integer that is unique for each cluster.

### 4.3 Tests and application of the exiting algorithms

We have tested the three algorithms under investigation by comparing their numerical results mutually and, for  $q = 2$ , with those of conventional algorithms. The results agree within the statistical errors.

#### 4.3.1 Application to specific-heat calculation

To illustrate the use of the Monte Carlo algorithms under consideration, we have calculated the Potts specific heat for the random-cluster model on the square lattice for two non-integer values  $q$ . These are  $q = 4 \cos^2(7\pi/22) = 1.169\dots$  and  $q = 4 \cos^2(5\pi/14) = 0.753\dots$ . The dimensionless specific heat (specific heat divided by  $Nk_B$ ) is here defined on the basis of differentiation of the free energy density  $\ln Z$  to the Potts coupling  $K$ , with  $Z$  e.g. defined as in Eq. (4.2):

$$C \equiv \frac{K^2}{N} \frac{\partial^2 \ln Z}{\partial K^2} \quad (4.11)$$

with  $\partial/\partial K = e^K \partial/\partial u$ . Since the sum  $n_b$  of the bond variables is conjugate to  $\ln u$ , the specific heat can be obtained from the fluctuations of  $n_b$ . It is sufficient to sample the first two moments of  $n_b$ :

$$C = \frac{K^2}{N} \left[ \frac{(u+1)^2}{u^2} (\langle n_b^2 \rangle - \langle n_b \rangle - \langle n_b \rangle^2) + \frac{u+1}{u} \langle n_b \rangle \right]. \quad (4.12)$$

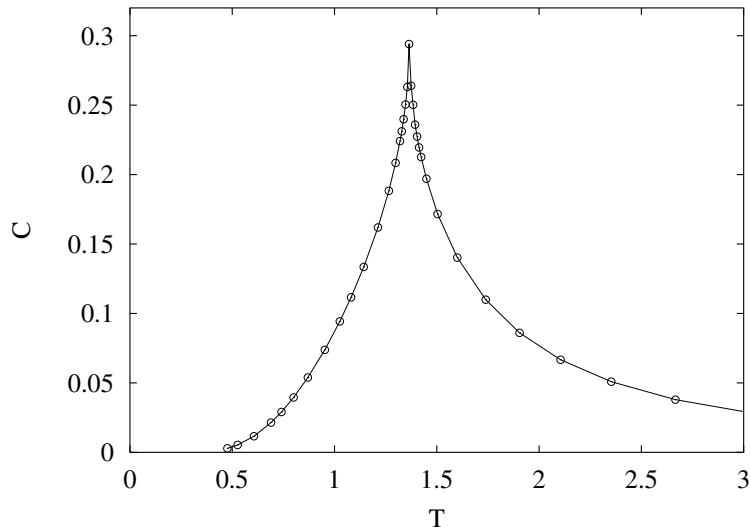


Figure 4.1: Dimensionless Potts specific heat  $C$  of the  $q = 4 \cos^2(7\pi/22) = 1.169\dots$  random-cluster model versus temperature  $T = 1/K$ . The statistical errors do not exceed the size of the data points. The data points are extrapolations of finite-size data in the range  $6 \leq L \leq 384$ , obtained by means of the cluster Monte Carlo algorithm. The finite-size data converge exponentially except at the critical point where power-law behavior occurs. Satisfactory convergence was found for all  $T$  except in very narrow ranges ( $\Delta T \approx 0.02$ ) on both sides of the critical point.

The value of the temperature exponent of the Potts model is known as a function of  $q$ . This expression was first conjectured by den Nijs [21]; see also [7]. For the specific-heat exponent  $\alpha$  this expression leads to  $\alpha = 4/3 - 2/[3 - 6 \arccos(\sqrt{q}/2)/\pi]$ . This formula allows us to select the value of  $q$  corresponding to a given value of  $\alpha$ .

We first simulated the  $q = 4 \cos^2(7\pi/22)$  Potts model, which has a specific-heat exponent  $\alpha = -1/2$ . We have calculated the Potts specific heat  $C$  of the square-lattice model in a suitable temperature range, and obtained the curve shown in Fig. 4.1, which does indeed display a square-root type cusp as implied by  $\alpha = -1/2$ . During these simulations we found that the cluster algorithm was the most efficient one, i.e., produced a more accurate result in a given computer time. The results in Fig. 4.1 are those generated by the cluster algorithm.

Next, we simulated the square-lattice  $q = 4 \cos^2(5\pi/14)$  Potts model, which has a specific-heat exponent  $\alpha = -1$ . We have calculated the Potts specific heat and obtained the curve shown in Fig. 4.2, which does indeed display a pronounced kink as implied by  $\alpha = -1$ . The results in Fig. 4.2 are those generated by the local bond update algorithm, because it became clear that it was more efficient than the reweighting algorithm.

These two figures, together with the well-known logarithmic divergence of the specific heat for  $q = 2$ , illustrate that the critical singularity becomes less strong when  $q$  decreases.

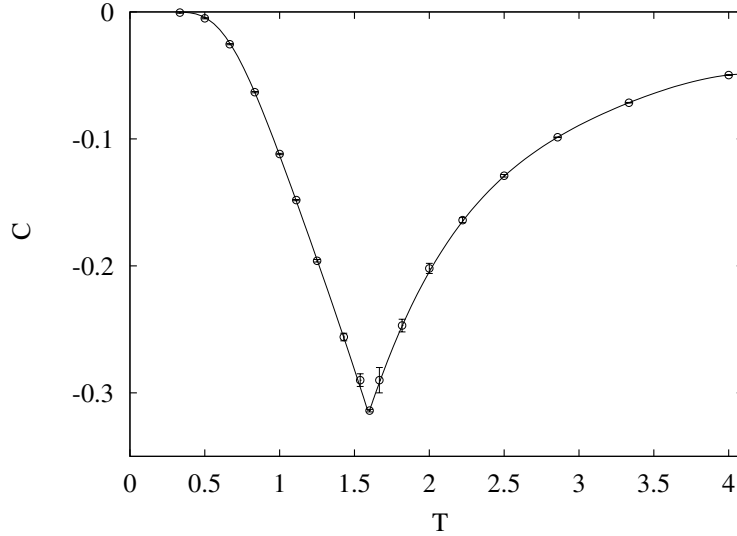


Figure 4.2: Dimensionless Potts specific heat  $C$  of the  $q = 4 \cos^2(5\pi/14) = 0.753\dots$  random-cluster model versus temperature  $T = 1/K$ . The statistical errors are larger than in the preceding figure, in some cases they exceed the symbol size. The data points are extrapolations of finite-size data in the range  $4 \leq L \leq 40$ , obtained by means of the local bond-update Monte Carlo method. The finite-size data converge exponentially except at the critical point where power-law behavior occurs. Satisfactory convergence was found for all  $T$  except in narrow ranges ( $\Delta T \approx 0.2$ ) on both sides of the critical point.

The use of  $K$  as the temperature parameter facilitates a comparison with the results for the integer- $q$  Potts model. The negative specific heat for  $q = 4 \cos^2(5\pi/14) < 1$  reflects the fact that the Potts energy per bond decreases with temperature: the reduced energy is  $K$  in the ordered state and  $K/q$  in the disordered one. This illustrates the unphysical nature of the Potts model for  $q < 1$ . We note however that the random-cluster model *is physical*. For instance, its energy (not reduced)  $E_{RC} = -k_B T \langle n_c \ln q + n_b \ln u \rangle$  is a well-behaved, increasing function of the temperature  $T$  when the non-reduced parameters  $k_B T \ln q$  and  $k_B T \ln u$  are kept constant.

### 4.3.2 Efficiency of the algorithms

While the dynamical exponent is an important factor in the efficiency of an algorithm, it is not the only one. The degree of overlap between generated and target distributions is crucial in reweighting methods, and furthermore, the computer time per spin update may depend strongly on the system size. From a practical point of view one may be interested in the computer time needed to reach a result with a given statistical accuracy. Thus, to compare the performance of the three algorithms in a quantitative way, we have simulated the two-dimensional random-cluster model on the square lattice, and determined

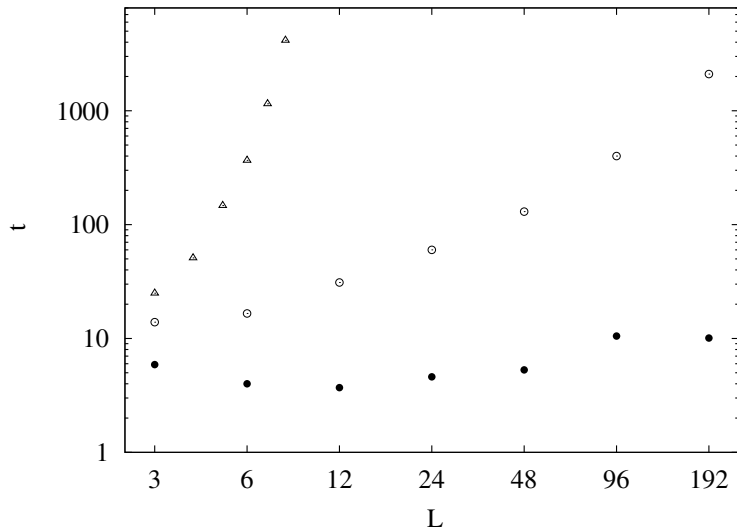


Figure 4.3: Computer time usage  $t$  of the three algorithms for the simulation of the continuous- $q$  random-cluster model, versus linear system size  $L$ . The time  $t$  is determined as the computer time in seconds per lattice site required to reach an accuracy of  $10^{-4}$  in the dimensionless ratio  $Q$  of the random-cluster representation of the critical  $q = 2$  Potts model. The data points apply to the statistical reweighting method ( $\Delta$ ), to the local bond update method ( $\circ$ ) and to cluster updates ( $\bullet$ ).

a dimensionless ratio  $Q$  similar to the Binder cumulant [22]. To this purpose we sampled powers of the cluster sizes

$$S^{(m)} \equiv \sum_{k=1}^{n_c} c_k^m, \quad (4.13)$$

where  $c_k$  is the size of the  $k$ -th cluster, for  $m = 2$  and 4. Then the ratio  $Q$  is defined as

$$Q \equiv \frac{\langle S^{(2)} \rangle^2}{\langle 3(S^{(2)})^2 - 2S^{(4)} \rangle}, \quad (4.14)$$

which, for the case  $q = 2$ , reduces to the ratio of magnetization moments  $\langle m^2 \rangle^2 / \langle m^4 \rangle$ . The computer time  $t$  per lattice site needed to reach a statistical accuracy of  $10^{-4}$  in  $Q$  serves as an inverse measure of the efficiency. The results in terms of  $t = (10^4 \delta Q / L)^2 t_R$ , where  $t_R$  is the CPU time of a run in seconds,  $\delta Q$  the statistical error in  $Q$  and  $L$  the linear system size, are shown in Fig. 4.3. These results indicate that the cluster algorithm is more efficient than the other two, increasingly so for larger system sizes. The reweighting method appears to become rapidly inefficient with increasing system sizes. Here one may remark that a simple statistical analysis of the probability that the Monte Carlo algorithm generates a state in the center of the target distribution yields factors in which  $N$  appears *in the exponent*. This argument thus indicates that the data for  $t$  obtained by the reweighting

method increase exponentially with  $L^2$ . The interpretation of the results in Fig. 4.3 still requires some reservation. First, the reweighting method naturally becomes more efficient when  $q$  approaches 1. Nevertheless, the data shown are clear enough to indicate that the useful range of  $q$  is quite narrow for the reweighting method. Second, our version of the local bond-update algorithm is relatively simple and forms clusters, instead of tracing their perimeter as in Sweeny's version. Since the fractal dimension of the perimeter is smaller than that of the cluster itself, Sweeny's version is expected to be more efficient than ours for sufficiently large system sizes, but at the expense of a more complicated code. Given the simplicity and efficiency of the cluster algorithm, we consider it the best choice for the investigation of  $q > 1$  models.

### 4.3.3 Dynamic exponent of the cluster algorithm

As mentioned in the Introduction, the reweighting method does not suffer, at least formally, from any critical slowing down, and thus its dynamic exponent is  $z = 0$ . The dynamic exponent of the local bond-update method has recently been investigated by Wang et al. [17] for  $q = 2$  and 3. Their analysis, apparently more accurate than earlier investigations [14, 15], reported nonzero but still rather small values of  $z$  that are, depending on the value of  $q$ , comparable with, or even somewhat smaller than those of the Swendsen-Wang algorithm. For  $q \rightarrow 1$  one expects  $z \rightarrow 0$  because the bond variables become independent. To evaluate the dynamic universality class of the cluster algorithm for continuous  $q$ , we have determined the dynamic exponent  $z$  for three different values of  $q$ , on the basis of simulations of  $L \times L$  square lattices with sizes  $L = 6, 12, \dots, 160$ . We sampled the energy and determined its autocorrelation times  $\tau_L$ , in units of cluster steps as described in Sec. 4.2, from least-squares fits to the exponentially decaying autocorrelation function. The results are shown in Fig. 4.4. We have analyzed their  $L$ -dependence as  $\tau_L \simeq L^z$  by means of least-squares fits. We obtain  $z = 0.08(1)$  for  $q = 4 \cos^2(7\pi/22)$ , and  $z = 0.551(8)$  for  $q = 3$ . The result for  $q = 3$  is consistent with an existing result for the Swendsen-Wang algorithm, namely  $z = 0.56(1)$  [17], but it is larger than the result of a more detailed study [23], using system sizes up to  $L = 1024$ , which is  $z = 0.515(6)$ . The question thus arises whether the difference with the continuous- $q$  cluster algorithm, which amounts to a few standard deviations, indicates that the dynamic universality classes of the two algorithms are different. We do not consider the numerical evidence to be sufficient to reach such a conclusion: it was noted in Ref. [23] that the largest system sizes ( $L \geq 128$ ) led to a significantly smaller result in comparison with the smaller system sizes. This suggests the presence of slowly converging correction terms in the autocorrelation times; such corrections could also be present in our results for the continuous- $q$  cluster algorithm, and thus also explain the difference with our value of  $z$ . Especially for  $q = 2$  the autocorrelation times are not well described by a single power law; the fits suggest the presence of a second term proportional to  $L^{z'}$  with  $z' \approx -0.4$ . Allowing for such a contribution we obtain  $z = 0.254(10)$  for  $q = 2$ , which is consistent with a result  $z = 0.25(1)$  [24] for the Swendsen-Wang algorithm, but larger than a more recent determination [9, 25] which led to  $z = 0.222(7)$  on the basis of system sizes up to  $L = 512$ . We found that our  $q = 2$  result

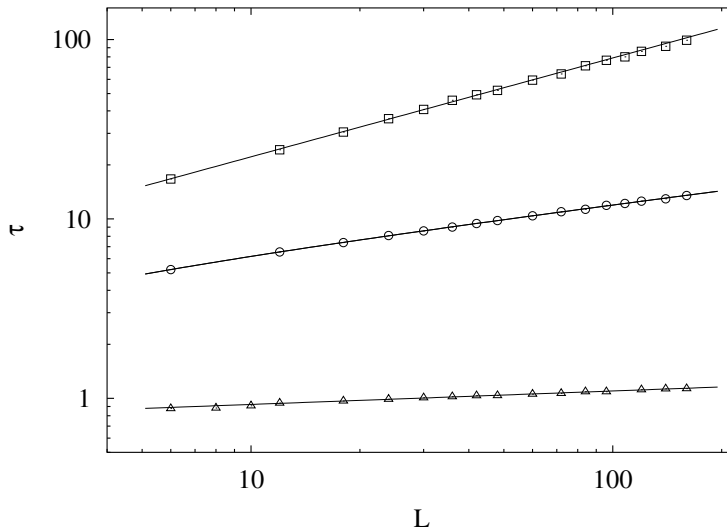


Figure 4.4: Autocorrelation times  $\tau$  versus system size  $L$  for three critical Potts models:  $q = 1.169\dots$  ( $\triangle$ ),  $q = 2$  ( $\circ$ ), and  $q = 3$  ( $\square$ ) on logarithmic scales. These results were obtained using the continuous- $q$  cluster algorithm. The statistical errors do not exceed the size of the data points.

for  $z$  depends considerably on the choice of the fit formula and the range of  $L$ . Instead of adding a second term, one can choose to skip the smallest system sizes in order to obtain an acceptable value of the residual  $\chi^2$ . For system sizes in the range  $60 \leq L \leq 160$  we thus find  $z = 0.265(5)$ . This number, as well as  $\chi^2$ , increases when the lower limit of the  $L$ -range is decreased (these numbers agree better with earlier determinations [8, 26] which are close to  $z = 0.3$ ). Under these circumstances, we do not assign much significance to the differences between the reported values of  $z$  for the Swendsen-Wang algorithm and the continuous- $q$  cluster algorithm. These differences are of the same order as those between different results reported for the Swendsen-Wang algorithm and may be attributed to unresolved corrections to scaling.

## 4.4 Single-cluster algorithm

Each term in the second sum in Eq. (4.10) specifies a cluster decomposition  $\mathcal{D}(\{b\})$  of the sublattice formed by sites  $k$  with  $t_k = 1$ . Different sets of bond variables  $\{b\}$  may still correspond with the same cluster decomposition. Thus, if we replace the sum on  $\{b\}$  by a sum on all cluster decompositions of the color-1 regions, we have to insert a summation

on all  $\{b\}$  that are consistent with  $\mathcal{D}$ :

$$Z_{tb} = Z_{t\mathcal{D}} \equiv \sum_{\{t\}} \prod_{\langle ij \rangle}^{(0)} (1+u) \sum_{\{\mathcal{D}\}}^{(1)} \sum_{\{b\}|\mathcal{D}} \left[ \prod_{k=1}^{n_c^{(1)}} (q-1) u^{n_b^{(k)}} \right]. \quad (4.15)$$

Eq. (4.15) can serve as the basis on which a single-cluster Monte Carlo algorithm can be constructed. This algorithm is applied as follows to a mixed configuration specified by the site variables  $t_i$  and a cluster decomposition  $\mathcal{D}$  of the color-1 sites.

Choose a random site  $i$ . The action taken by the algorithm depends on the color variable  $t_i$ . If

1.  $t_i = 0$ , do with probability  $p_1 = (q-1)/q$  the following: form a random cluster around site  $i$  with bond probability  $p = u/(u+1)$  between sites of color 0. The sites  $j$  in the newly formed cluster are assigned color 1 (i.e.  $t_j = 1$ ) and the number  $n_c^{(1)}$  of clusters of color 1 is thus increased by 1.
2.  $t_i = 1$ , do with probability  $p_2 = 1/q$  the following: assign color 0 to all sites of the cluster containing site  $i$ , and thus decrease the number of clusters of color 1 by 1.

#### 4.4.1 Proof of detailed balance

The proof of detailed balance can be formulated as follows. Consider two mixed configurations  $S_1$  and  $S_2$ , which differ only in a region  $\mathcal{C}$  whose sites  $j$  have color  $t_j = 0$  in  $S_1$ , and whose sites belong to a single cluster in  $S_2$ , and thus have color  $t_j = 1$ . The probability to move from  $S_1$  to  $S_2$  is

$$T(2,1) = \frac{(q-1)N_c}{qN} \sum_{\{b\}|\mathcal{C}} \left( \frac{u}{u+1} \right)^{n_b} \left( \frac{1}{u+1} \right)^{n_p + n_{nn} - n_b}, \quad (4.16)$$

where  $N_c$  is the number of sites in region  $\mathcal{C}$ ;  $N$  is the total number of sites in the system;  $\{b\}$  stands for the  $n_{nn}$  bond variables on the edges between nearest-neighbor sites in  $\mathcal{C}$ ; the combination on  $\{b\}|\mathcal{C}$  indicates the sum on all configurations  $\{b\}$  that connect all sites in  $\mathcal{C}$  into a single cluster;  $n_b$  denotes the number of nonzero bond variables in  $\{b\}$ ;  $n_p$  is the number of bond variables connecting sites inside  $\mathcal{C}$  with those outside  $\mathcal{C}$  of color 0 (i.e., the number of bonds along the boundary of  $\mathcal{C}$  that is broken when the color of  $\mathcal{C}$  is changed). The prefactor  $(q-1)N_c/qN$  describes the probability that the cluster formation starts within  $\mathcal{C}$ . Each of the  $n_b$  ‘present’ bonds contributes a factor  $u/(u+1)$ , and each of the  $n_{nn} - n_b$  ‘absent’ bonds a factor  $1/(u+1)$ . Also each ‘broken’ bond along the perimeter of  $\mathcal{C}$  contributes a factor  $1/(u+1)$ .

According to the rule given above, the probability of the inverse move from  $S_2$  to  $S_1$  is simply

$$T(1,2) = \frac{N_c}{qN}. \quad (4.17)$$

The condition of detailed balance requires that the transition probabilities  $T(2, 1)$  and  $T(1, 2)$  are related to the equilibrium probabilities  $P(1)$  and  $P(2)$  of configurations 1 and 2 respectively:

$$T(2, 1)/T(1, 2) = P(2)/P(1). \quad (4.18)$$

Since the probabilities  $P(1)$  and  $P(2)$  are proportional to the weights specified by Eq. (4.10), we may write

$$P(2)/P(1) = W(2)/W(1), \quad (4.19)$$

where the weights associated with region  $\mathcal{C}$  in Eq. (4.10) are

$$W(1) = (1 + u)^{n_p + n_{nn}}, \quad (4.20)$$

and

$$W(2) = (q - 1) \sum_{\{b\}|\mathcal{C}} u^{n_b}. \quad (4.21)$$

From Eqs. (4.16) and (4.17), and from Eqs. (4.20) and (4.21), we conclude that

$$T(2, 1)/T(1, 2) = (q - 1)(1 + u)^{-n_p - n_{nn}} \sum_{\{b\}|\mathcal{C}} u^{n_b} = W(2)/W(1), \quad (4.22)$$

which shows that the condition of detailed balance indeed is satisfied.

#### 4.4.2 Other versions

The probabilities  $p_1$  and  $p_2$  can be chosen differently, depending on the value of  $q$ . For  $1 < q < 2$  we may take  $p_1 = q - 1$  and  $p_2 = 1$ . For  $q > 2$ , this is not possible but other possibilities arise. One can generalize the algorithm by allowing more than two values of the color variables  $t_i$ . The most obvious way is to allow  $n \equiv [q]$  (the integer part of  $q$ ) values with weight one, and one special value with weight  $q - n$ . Sites of the latter color are divided in clusters (just as before); sites of the  $n$  remaining colors are not. A cluster step starting from a randomly chosen site can then be specified as follows: if that site belongs to a cluster (thus, of the special color), then the cluster is erased and its sites are given a random color  $1, 2, \dots, n$  with probability  $1/n$  each. If the cluster step starts from a randomly chosen site of color  $1, 2, \dots, n$ , then a single cluster is formed. Its sites receive one of the  $n - 1$  other weight-1 colors with probability  $(2n - q)/(n(n - 1))$  each, and the cluster receives the special color with probability  $(q - n)/n$ . This choice of probabilities satisfies detailed balance and maximizes the probability of a cluster flip. For integer  $q$  it reduces to the Wolff algorithm.

#### 4.4.3 Test and dynamic exponent

##### Test of the algorithm

We tested the single-cluster algorithm for the  $q = 2, 3$ , and 4 Potts model, by comparing their numerical results with those of the Wolff algorithm. We let  $n = q - 1$  and the special

value be  $q - n = 1$ . Simulations were performed on the  $L \times L$  square lattice with periodic boundary conditions. We sampled various quantities, including the second moment of the magnetization  $m_2 = \langle m^2 \rangle$  and the average size  $s$  of the clusters formed by the algorithm. The quantity  $m_2$  is defined as

$$m_2 = \frac{1}{q-1} \left\langle \sum_{i=1}^{q-1} \sum_{j=i+1}^q (\rho_i - \rho_j)^2 \right\rangle, \quad (4.23)$$

where  $\rho_i$  is the density of sites in state  $i$ . The cluster size  $s$  is counted as the total number of lattice sites in the cluster. It can be easily shown that, within the statistical error margins, the two quantities  $m_2$  and  $s$  are equal to each other. As expected, for the same model with the same values of  $q, K, L$ , the Wolff and the present algorithm indeed yielded identical results for  $m_2$  and  $s$ ; the values of  $m_2$  and  $s$  also agree with one another. For an illustration, the  $m_2$  and  $s$  data for the critical Ising model are shown in Table 4.1. Since

Table 4.1: Data for  $m_2$  and  $s$  in the critical Ising model, as obtained by the Wolff (W) and the present single-cluster algorithm (S). The parameter  $L$  specifies the linear system size. The number of samples per system size is  $4 \times 10^6$  for each simulation, and the number of clusters formed between subsequent samples is 2 for  $L \leq 24$  and 3 for  $L = 32$ . The numbers in the brackets represent the statistical error margins in the last two decimal places.

$L$	$m_2$ (W)	$m_2$ (S)	$s$ (W)	$s$ (S)
8	0.64693(18)	0.6478(6)	0.64666(18)	0.6470(6)
12	0.58581(18)	0.5861(8)	0.58581(18)	0.5860(8)
16	0.54537(17)	0.5442(9)	0.54544(17)	0.5441(9)
20	0.51584(16)	0.5164(10)	0.51594(16)	0.5165(10)
24	0.49305(17)	0.4932(13)	0.49311(17)	0.4932(13)
32	0.45874(14)	0.4610(12)	0.45878(14)	0.4610(12)

both simulations involve the same number of samples, the statistical error uncertainties, shown in the brackets in Table 4.1, reflect the relative efficiency of the Wolff and the single-cluster algorithm. For size  $L = 8$ , the Wolff method is about 10 times as efficient as the present algorithm, while for  $L = 32$  it is about 100 times. Therefore, the two algorithms have different dynamic exponents.

### Dynamic exponent of the algorithm

To study the dynamic universality class of the present single-cluster algorithm, we simulated the  $q = 4, 3, 2$ , and  $4 \cos^2(7\pi/22)$  Potts models on a square lattice with periodic boundary conditions. Similar to what we did in Sec. 4.3.2, we sampled the energy and determined its autocorrelation times  $\tau_L$  for 10 different system sizes  $L$  with  $8 \leq L \leq 48$ . The data of  $\tau_L$  are shown in Fig. 4.5. We fitted the finite-size data by

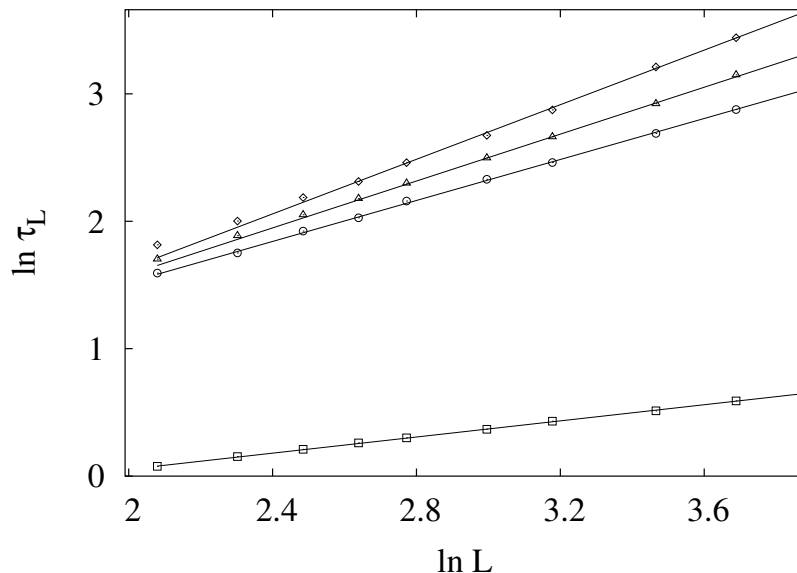


Figure 4.5: Autocorrelation time  $\tau_L$  for several critical Potts models, shown as  $\ln \tau_L$  versus  $\ln L$ . The data for  $q = 4 \cos^2(7\pi/22)$ , 2, 3, and 4 are represented by symbols  $\square$ ,  $\circ$ ,  $\triangle$ , and  $\diamond$ , respectively.

$$\tau_L = L^z(a + bL^{y_i}), \quad (4.24)$$

where a correction term is introduced and the correction exponent was taken [27] as  $y_i = -28/15$  for  $q = 4 \cos^2(7\pi/22)$ ,  $y_i = -2$  for  $q = 2$ , and  $y_i = -4/5$  for  $q = 3$ . For  $q = 4$ , in addition to the term with exponent  $y_i = -2$ , we included  $c/\ln L$  in the brackets of Eq. (4.24). We obtain  $z = 0.27(2)$  for  $q = 4 \cos^2(7\pi/22)$ ,  $z = 0.80(2)$  for  $q = 2$ ,  $z = 0.94(2)$  for  $q = 3$ , and  $z = 1.17(2)$  for  $q = 4$ . A comparison of these dynamic exponents and those of the full-cluster decomposition algorithm described in Sec. 4.3.2 (see also Ref. [20]) indicates they are in different dynamic universality classes.

## 4.5 Discussion

The single-cluster algorithm described above is obviously related to the Wolff [28] algorithm as defined for discrete- $q$  Potts models; it can reduce to the Wolff method if  $q$  is an integer. On the other hand, it is different in the sense that the single-cluster algorithm acts on a mixed configuration of site variables and random-cluster variables. In contrast to the fact that the Wolff method is generally more efficient than the full-cluster decomposition algorithm for integer  $q$ , the present method is much less efficient in comparison with the full-cluster decomposition algorithm. This can be understood as follows. In the single-cluster algorithm, the cluster decompositions of the special state  $q - [q]$  is stored in computer memory, while direct spin values are assigned to lattice sites for the other  $[q]$  Potts states.

As described in Sec. 4.4.2, the formed clusters for the special state will be flipped back into the integer spin states. Thus, it seems that one gains little by forming a cluster for the special state from one of the  $[q]$  Potts states. More importantly, the autocorrelation function for the cluster decompositions has a long time "tail" during simulations, because the smaller a cluster is, the less probable it is to be visited. This long "tail" is mainly responsible for the relatively large dynamic exponent of the single-cluster method.

# Bibliography

- [1] R. B. Potts, Proc. Cambridge Philos. Soc. **48**, 106 (1952).
- [2] F. Y. Wu, Rev. Mod. Phys. **54**, 235 (1982).
- [3] P. W. Kasteleyn and C. M. Fortuin, J. Phys. Soc. Japan. (Suppl.) **26**, 11 (1969).
- [4] R. J. Baxter, S. B. Kelland and F. Y. Wu, J. Phys. A **9**, 397 (1976).
- [5] R. J. Baxter, Phys. Rev. Lett. **26**, 178 (1971).
- [6] R. J. Baxter, J. Phys. C **6**, L445 (1973).
- [7] B. Nienhuis, in *Phase Transitions and Critical Phenomena*, edited by C. Domb and J. L. Lebowitz (Academic Press, London, 1987), Vol. **11**, p.1.
- [8] R. H. Swendsen and J. S. Wang, Phys. Rev. Lett. **58**, 86 (1987).
- [9] G. Ossola and A. D. Sokal, Nucl. Phys. B **691**, 259 (2004).
- [10] B. Nienhuis, A. N. Berker, E. K. Riedel and M. Schick, Phys. Rev. Lett. **43**, 737 (1979).
- [11] B. Nienhuis, E. K. Riedel and M. Schick, Phys. Rev. B **23**, 6055 (1981).
- [12] S. Grollau, M. L. Rosinberg and G. Tarjus, Physica A **296**, 460 (2001).
- [13] Y. Deng, H. W. J. Blöte and B. Nienhuis, Phys. Rev. E **69**, 026114 (2004).
- [14] M. Sweeny, Phys. Rev. B **27**, 4445 (1983).
- [15] F. Gliozzi, Phys. Rev. E **66**, 016115 (2002).
- [16] X. J. Li and A. D. Sokal, Phys. Rev. Lett. **63**, 827 (1989).
- [17] J. -S. Wang, O. Kozan and R. H. Swendsen, Phys. Rev. E **66**, 057101 (2002).
- [18] C. -K. Hu, Phys. Rev. Lett. **69**, 2739 (1992).
- [19] J. R. Heringa and H. W. J. Blöte, Phys. Rev. Lett. **70**, 2044 (1993).

- [20] L. Chayes and J. Machta, *Physica A* **254**, 477 (1998).
- [21] M. P. M. den Nijs, *J. Phys. A* **12**, 1857 (1979).
- [22] K. Binder, *Z. Phys. B***43**, 119 (1981).
- [23] J. Salas and A. D. Sokal, *J. Stat. Phys.* **87**, 1 (1997).
- [24] P. D. Coddington and C. F. Baillie, *Phys. Rev. Lett.* **68**, 962 (1992).
- [25] J. Salas and A. D. Sokal, e-print cond-mat/9904038v1, Sec. 6.
- [26] C. F. Baillie and P. D. Coddington, *Phys. Rev. B* **43**, 10617 (1991).
- [27] J. L. Cardy, in *Phase Transitions and Critical Phenomena*, edited by C. Domb and J. L. Lebowitz (Academic Press, London, 1987), Vol. 11, p.55.
- [28] U. Wolff, *Phys. Rev. Lett.* **62**, 361 (1989).

# Chapter 5

## Percolation in one of $q$ colors near criticality

We study bond percolation in two dimensions between random site variables having one out of  $q$  colors, using transfer-matrix and Monte Carlo techniques. We determine the percolation threshold as a function of the Potts temperature  $T$  in the disordered Potts range  $T_c \leq T < \infty$  for several  $q$ -state Potts Hamiltonians. For high  $T$ , these transitions fit, irrespective of  $q$ , in the universality class of the ordinary percolation transitions. However, for  $T \downarrow T_c$ ,  $q$ -dependent crossover phenomena appear. The topology of the phase diagram changes in a qualitative sense at  $q = 2$ . For  $q < 2$  the Potts critical state appears to enhance percolation, for  $q > 2$  it appears to suppress it. Remarkably, for  $q = 2$  the percolation line coincides with the *only* flow line extending to  $T > T_c$  from the critical fixed point associated with Potts clusters.

### 5.1 Introduction

The universal properties of the pure percolation problem in two dimensions are well understood. While short-range correlations in the substrate do not influence the universality class of the percolation transition, percolation phenomena on critical substrates display new universal behavior. Such correlated percolation models have already been the subject of various investigations. For instance, motivated by the prospect to find new types of critical behavior, the study of percolation phenomena in  $q$ -state Potts configurations has received considerable attention [1–6]; see also references therein. The correlated percolation problem, while interesting in its own right, is also relevant for several other fields of research, see for instance Refs. [7–9] and references therein. These fields include colossal magnetoresistance, correlated resistor networks and the quantum-Hall transition.

The reduced Hamiltonian of the  $q$ -state Potts model is

$$\mathcal{H}/k_B T = -K \sum_{\langle ij \rangle} \delta_{\sigma_i, \sigma_j}, \quad (5.1)$$

with Potts variables  $\sigma_i (= 1, 2, \dots, q)$ , and  $\langle ij \rangle$  runs over all interacting pairs of such variables. The Kasteleyn-Fortuin mapping [10] of Eq. (5.1) on the random-cluster model generalizes it to continuous  $q$ . This mapping involves the formation of percolation clusters: each pair  $(ij)$  with  $\sigma_i = \sigma_j$  is connected by a bond  $b_{ij} = 1$  with probability  $p = 1 - e^{-K}$ . After summing out the Potts variables, only bond variables remain in the partition sum:

$$Z(q; K) = \sum_{\{b\}} u^{n_b} q^{n_c}, \quad (5.2)$$

where the sum is on all  $b_{ij} = 0, 1$ ;  $u \equiv e^K - 1$ ,  $n_b$  is the number of bonds, and  $n_c$  the number of clusters. The percolation threshold of the random-cluster model appears to coincide with the Potts critical point, and the critical exponents describing its percolation and thermodynamic properties appear to depend continuously on  $q$ .

While the bond percolation probability  $p$  in the random-cluster model is determined by the Potts coupling  $K$ , here we consider the more general case that  $p$  is independent of  $K$ . Since all Potts colors are equivalent, it is sufficient to form clusters of one color, say  $\sigma_i = 1$ . These sites are considered ‘occupied’ and percolation bonds are added between occupied sites with probability  $p$ . The resulting partition sum

$$Z = \left[ \prod_k \sum_{\sigma_k=1}^q \right] \left[ \prod_{\langle ij \rangle} \exp(K \delta_{\sigma_i, \sigma_j}) \sum_{b_{ij}=0}^1 \{1 - b_{ij} + p(2b_{ij} - 1) \delta_{\sigma_i, 1} \delta_{\sigma_j, 1}\} \right] \quad (5.3)$$

is equal to the Potts partition sum, but its terms include percolation degrees of freedom. Two special cases are 1)  $p = 1$ , leading to so-called Potts clusters, and 2)  $p = 1 - e^{-K}$  reproducing random clusters [10]. Most work has thus far focused on these two cases at the Potts critical point  $K = K_c$  [1–6]. The results for the Ising case  $q = 2$  in terms of the phase diagram and the renormalization flow are summarized in Fig. 5.1. The qualitative characteristics are, however, believed to apply more generally than just for  $q = 2$ . Along the critical line  $K = K_c$  the bond probability is relevant at the random-cluster fixed point. The flow in the  $p$ -direction is governed by the so-called red-bond exponent [2]. Thus we expect stable fixed points on either side. A trivial fixed point naturally occurs at  $p = 0$ , but the location of the stable fixed point at  $p_s > 1 - e^{-K}$  is not well known. Furthermore, there are fixed points at infinite Potts temperature  $K = 0$ , of which we mention the fully stable trivial one at  $p = 0$ , and the one at the percolation threshold  $p_c$ . The latter fixed point is thus unstable in the  $p$ -direction. It describes a mixed site-bond percolation problem where sites are occupied with probability  $1/q$ .

In particular the percolation phenomena at and near Potts criticality remain largely unexplored. It is therefore the subject of this chapter to determine how the  $K = 0$  percolation transition continues for  $K > 0$ , how it connects to the critical line  $K = K_c$ , and how the resulting phase diagram and its underlying flow-line structure depend on the number of Potts states  $q$ . The outline of this chapter is as follows. In Section 5.2 we summarize the numerical techniques and describe the determination of the critical points needed in the following calculations. Sections 5.3 and 5.4 present our results for the Ising

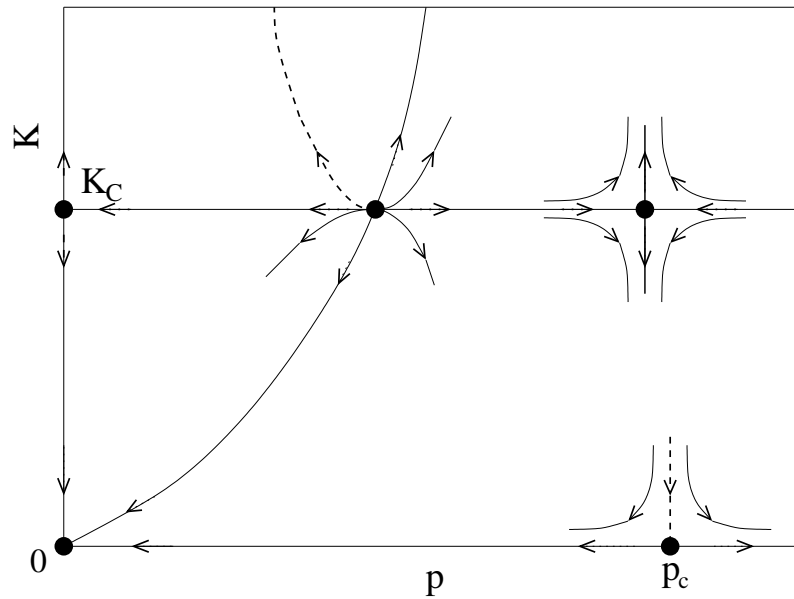


Figure 5.1: The  $(p, K)$  diagram. The curve connecting to  $K = p = 0$  represents the random-cluster model. Arrows indicate the renormalization flow. Dashed lines show the percolation threshold in the ordered phase ( $K > K_c$ ) and for small  $K$ .

case  $q = 2$ , and for  $q \neq 2$  respectively. Section 5.5 concludes this chapter with a brief discussion and an investigation of some remaining questions.

## 5.2 Algorithms and critical points

### 5.2.1 Critical points

The critical couplings  $K_c$  of the models that are investigated in the following sections, are available from various sources including exact analysis, duality transformations, transfer-matrix calculations and Monte Carlo simulations. First, the critical point of the nearest-neighbor Potts model on the square lattice is known from duality [11] as  $K_c = \ln(1 + \sqrt{q})$ . The transformation [10] of the Potts partition sum into a Whitney polynomial, which is self-dual [12], enables the generalization of this result to non-integer  $q$ . The critical point of the exactly solved [13] triangular  $q = 2$  model is  $K_c = \ln(3)/2$ .

The determination of the critical points of the other systems investigated requires the use of numerical means. The square-lattice Ising model with eight equivalent neighbors has been analyzed by means of a transfer-matrix method [14]. In terms of the Potts coupling (which is twice the coupling in the equivalent Ising Hamiltonian) the critical point is thus known as  $K = 0.3803853614$  (4).

The models with many more interacting neighbors are less easy to investigate by transfer-matrix methods, and Monte Carlo methods were used instead. There exists an efficient cluster algorithm [15] for such models: critical slowing down is strongly reduced, and

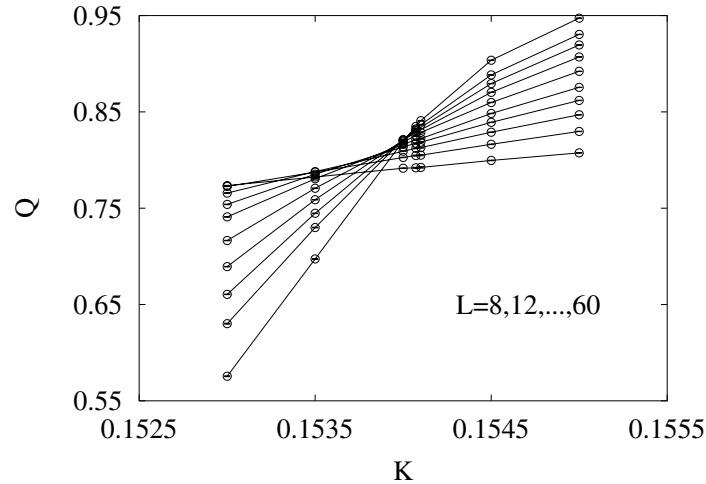


Figure 5.2: Dimensionless ratio  $Q$  of the 20-neighbor 3-state Potts model versus coupling  $K$ , for several system sizes. Data points (circles) for the same system size are connected by lines. Larger system sizes correspond to larger slopes.

the time per spin flip is almost independent of the number of interacting neighbors. The determination of the critical point is based on the Monte Carlo sampling of the moments of the magnetization  $m$  and the determination of their dimensionless ratio  $Q \equiv \langle m^2 \rangle^2 / \langle m^4 \rangle$ , which is related to the Binder cumulant [16] and converges to a universal constant at the critical point in the limit of large system size  $L$ . Multivariate least-squares analysis of Monte Carlo results for  $Q$ , obtained in a narrow interval around the critical point for a sequence of different sizes  $L$ , then yields the critical point. This procedure was described in Ref. [17] and applied there to several equivalent-neighbor Ising models on the square lattice. We quote its result for the 20-neighbor Ising model, in terms of the Potts coupling, as  $K_c = 0.1263852$  (8).

For the three-state Potts model on the square lattice with 20 equivalent neighbors we performed new simulations to determine the critical point. The density  $n_\sigma$  of Potts variables in state  $\sigma$  ( $= 1, 2$ , or  $3$ ) was sampled for 20 system sizes in the range  $8 \leq L \leq 200$ . The quantity  $Q$  is now defined as above but with  $m^2$  replaced by  $[(n_1 - n_2)^2 + (n_2 - n_3)^2 + (n_3 - n_1)^2]/2$ . The data for system sizes  $L \leq 60$  are shown in Fig. 5.2. The apparent convergence of the intersections hints at a phase transition near  $K = 0.154$ . Multivariate least-squares analysis of  $Q$ , along the lines of Ref. [17], but with the Ising correction-to-scaling exponents replaced by the three-state Potts ones, yielded the critical point as  $K_c = 0.154078$  (1). The fit was able to resolve the temperature exponent  $y_t$  which was found to agree well with the three-state Potts universality class. This result confirms that the transition is continuous. In contrast, a first-order transition is predicted by mean-field theory. The predictions of mean-field theory might be considered relevant because they tend to become more accurate when the range of interactions increases.

### 5.2.2 Percolation algorithms

The percolation problem defined in Sec. 5.1 was studied by means of a transfer-matrix technique whose principle was outlined in Ref. [18], and by means of cluster Monte Carlo algorithms for the Potts model [19, 20] and for the non-integer- $q$  random-cluster model [21, 22]. The transfer-matrix method uses in fact the random-cluster representation of the  $q = 1$  Potts model as outlined in Ref. [23]. In particular the ‘magnetic’ connectivities defined there serve to construct a transfer matrix that enables the calculation of ‘magnetic correlations’, i.e., the probability that two sites belong to the same percolation cluster. The fact that we now construct percolation clusters only between variables in the same state makes it necessary to construct a more complicated algorithm than that used in Ref. [23]. These complications were solved in a rather straightforward but tedious way; we do not go into details here.

In contrast, the Monte Carlo construction of percolation clusters between variables in the same state is rather simple; the algorithm is essentially the same as the Wolff algorithm [20] used to generate the Potts configurations for integer  $q$ , but with a different bond probability.

## 5.3 The Ising case $q = 2$

First we search for the stable fixed point of the Ising model ( $q = 2$ ) at  $K = K_c$ ,  $p > 0$ . Ref. [18] suggests that the fixed point lies near  $p = 1.1$  for the square lattice, but a sketch in Ref. [3] shows it at  $p < 1$ . We used the transfer matrix of Ref. [18] to compute the correlation length  $\xi(p, K, L)$  of the probability that two sites at a distance  $r$  along a cylinder of circumference  $L$  belong to the same cluster. From it we define

$$X_h(p, K, L) \equiv \frac{L}{2\pi\xi(p, K, L)}, \quad (5.4)$$

where  $X_h(p, K, L) \simeq X_h$  in the limit of large  $L$ , with  $X_h$  the magnetic scaling dimension at the fixed point attracting the point  $(p, K)$ . We fix  $K = K_c$  and apply finite-size scaling near a stable fixed point at  $p = p_s$ :

$$X_h(p, K_c, L) = X_h(p_s + (p - p_s)L^{y_r}, K_c, 1) + \dots \quad (5.5)$$

with a red-bond exponent  $y_r = -5/8$  [18]. In first order, corrections to scaling  $X_h(p, K_c, L) - X_h$  are proportional to the irrelevant field  $p - p_s$  and can thus be used to determine  $p_s$ . Using numerical data for  $X_h(p, K_c, L)$  for sizes up to  $L = 11$  at several values of  $p$ , and the exact result  $X_h = 5/96$ , and a least-squares fit of an expansion of Eq. (5.5) in  $p - p_s$ , we obtain  $p_s = 1.08$  (3). This bond probability exceeds 1 and is thus unphysical, but there is no sign of a change of universality.

The same algorithm was used to locate percolation transitions for  $K < K_c$ . Near the  $K = 0$  percolation fixed point the data for  $X_h$  were fitted by

$$X_h(p, K, L) = X_h + \sum_k a_k (p - p_c)^k L^{ky_p} + \sum_j b_j L^{jy_i} + \dots, \quad (5.6)$$

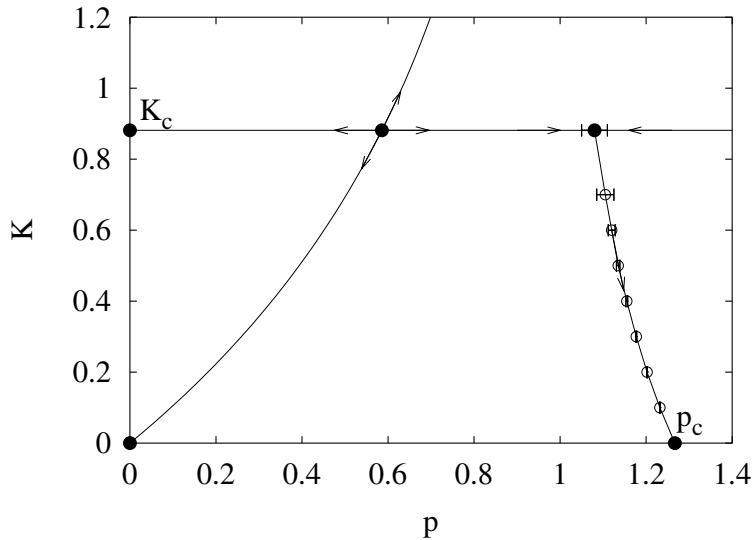


Figure 5.3: Percolation diagram of the square-lattice, nearest-neighbor Ising model. The percolation line lies in the unphysical region  $p > 1$ . It runs from  $p_c = 1.2668$  (2),  $K = 0$  to the stable fixed point on the critical line  $K = K_c$ .

where  $X_h = 5/48$  is the magnetic dimension and  $y_p = 3/4$  the thermal exponent of the percolation model; the irrelevant Potts exponent is  $y_i = -1$  near  $K=0$ . The resulting percolation line is shown in Fig. 5.3. It lies wholly in the unphysical region. Reasonably accurate data could be obtained for  $K \leq 0.7$ ; for larger  $K$ , the available range of finite sizes is insufficient because of crossover phenomena due to the proximity of the Ising critical point. The percolation line seems to connect to the *irrelevant* fixed point. This is remarkable, because then the percolation line is, among infinitely many flow lines in the  $(p, K)$  diagram for  $K < K_c$ , the only one extending down from the stable fixed point  $(p_s, K_c)$  and the only flow line coming in to the percolation fixed point  $(p_c, 0)$ . Coincidence of both flow lines (see Fig. 5.1) hints at a deeper connection involving these two seemingly independent fixed points.

In view of the unexpectedness of this result, we have performed similar analyses of different Ising models. First we studied the  $q = 2$  model with eight equivalent neighbors on the square lattice. Its critical point is known as  $K = 0.3803853614$  (4) [14]. Because of the increased number of neighbors, the percolation line for  $K < K_c$  shifts into the physical range  $p \leq 1$  where Monte Carlo methods can be applied. For several periodic lattices up to size  $L = 360$ , up to  $10^7$  spin configurations were generated by Metropolis or Wolff [20] methods, and percolation clusters were formed. For a range of values of  $p$  and  $K$ , we then sampled the dimensionless ratio

$$Q = \frac{\langle \sum_i c_i^2 \rangle^2}{\langle 3(\sum_i c_i^2)^2 - 2 \sum_i c_i^4 \rangle}, \quad (5.7)$$

where  $c_i$  is the size of the  $i$ -th cluster. In the Ising case  $q = 2$ , the sum over *all* random

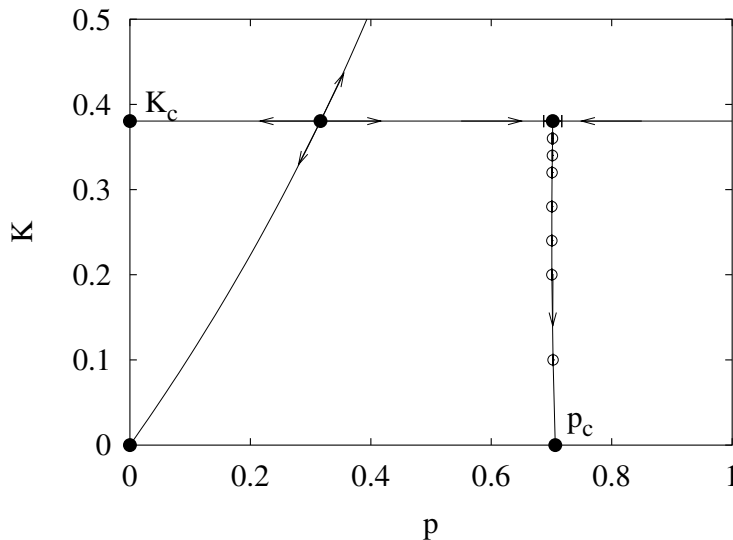


Figure 5.4: Percolation diagram of the Ising model on the square lattice with nearest- and next-nearest-neighbor interactions. The percolation line lies in the physical region  $p < 1$ . It runs from  $p_c = 0.70622(6)$  at  $K = 0$  to the stable fixed point at  $p_s = 0.702(15)$  on the critical line  $K = K_c$ .

clusters (i.e.,  $p = 1 - e^{-K}$ ) yields a result that is equal to the above-mentioned ratio of magnetization moments  $Q = \langle m^2 \rangle^2 / \langle m^4 \rangle$ . However, here the sum includes clusters of *only one* Potts color, to ensure that  $Q$  satisfies universality independent of  $q$ . Near the percolation threshold it scales as

$$Q = Q_0 + \sum_k a_k (p - p_c)^k L^{ky_p} + \sum_{j=1,2,\dots} b_j L^{jy_i} + c(p - p_c) L^{y_p + y_i} + d(p - p_c)^2 L^{y_p} + e L^{y_p - 2y_h} + f L^{d - 2y_h} + \dots \quad (5.8)$$

with  $y_p = 3/4$ ,  $y_h = 91/48$ ,  $y_i = -1$ , and  $Q_0 = 0.87048(5)$ . We determined this value of  $Q_0$  numerically for the square-lattice bond-percolation model, prior to the present analysis. Meanwhile an independent determination of  $Q_0$  has appeared in Ref. [24]. Corrections to the leading scaling behavior are due to the analytic background, nonlinearity of the relevant scaling field in  $p$ , and mixed contributions of other scaling fields to the temperature-like variable. For  $K \neq 0$ , new corrections may appear due to the correlation between the spin variables. These are governed by the irrelevant exponent  $y_i = -1$  governing the flow to the infinite-temperature fixed point ( $p = p_c, K = 0$ ).

In order to locate the percolation line, we have fitted the free parameters in formula (5.8) to our simulation data for  $Q$  at couplings  $K < K_c$ . This procedure was also applied to locate the stable fixed point at  $K = K_c$ , with a different universal value of  $Q_0$ , and with  $y_p$  replaced by the irrelevant exponent  $y_r = -5/8$ . We used the geometric cluster algorithm [25] at zero magnetization, to suppress corrections that obstruct the determination of the fixed point and the error estimation. We verified our results with consistency checks using other

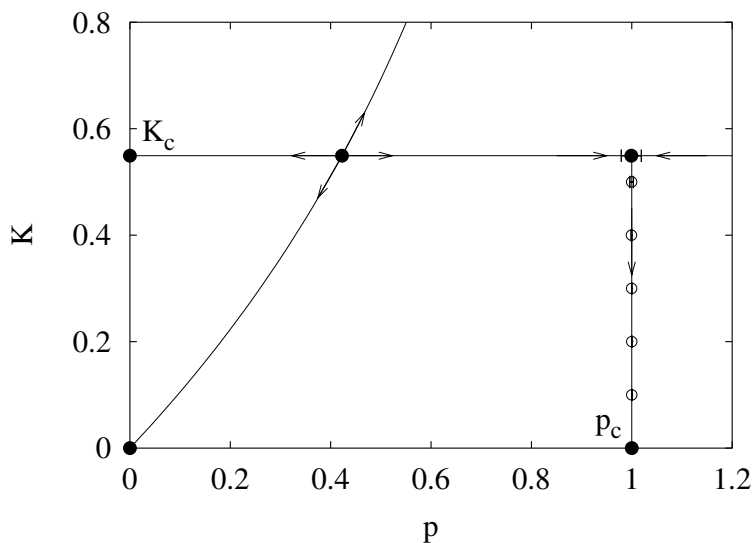


Figure 5.5: Percolation diagram of the triangular Ising model with nearest-neighbor interactions. The percolation line lies exactly at  $p = 1$ .

definitions of  $Q$ , excluding the largest or second largest cluster, using only the largest cluster, or using two colors instead of one. As shown in Fig. 5.4, again the percolation line approaches the stable fixed point.

We have similarly analyzed the triangular Ising model. As shown in Fig. 5.5, we find a percolation line at  $p = 1$ . This is explained by an exact argument. The site percolation threshold is  $p_s = 1/2$  [26] for the triangular lattice. Thus the present bond percolation model is critical at  $K = 0, p = 1$ . However, the ‘matching lattice’ argument [26] behind this result requires only that the site probability distribution is symmetric under the interchange of occupied and empty sites. Thus, the present triangular percolation model is still critical at  $p = 1$  for  $0 < K \leq K_c$ . For  $K > K_c$  the symmetry is broken and the model is no longer critical.

## 5.4 Potts models with $q \neq 2$

This section addresses the question how the phase diagram depends on  $q$ . For  $q = 1$ ,  $K$  is redundant, and the percolation line lies at constant  $p$  and connects to the random-cluster point, i.e., the *unstable* fixed point at  $K = K_c$ . We also studied the square-lattice model at an intermediate value  $q = 2 - 2 \cos(7\pi/18) = 1.31596 \dots$  with a cluster Monte Carlo algorithm [21, 22] for the random-cluster model. The cluster decomposition and the analysis are the same as above. The results in Fig. 5.6 show that, just as for  $q = 1$ , the percolation line connects to the random-cluster point.

Next, we focus on the three-state Potts model. Because of the lower density of sites of one color in the disordered Potts phase, the percolation line of the nearest-neighbor

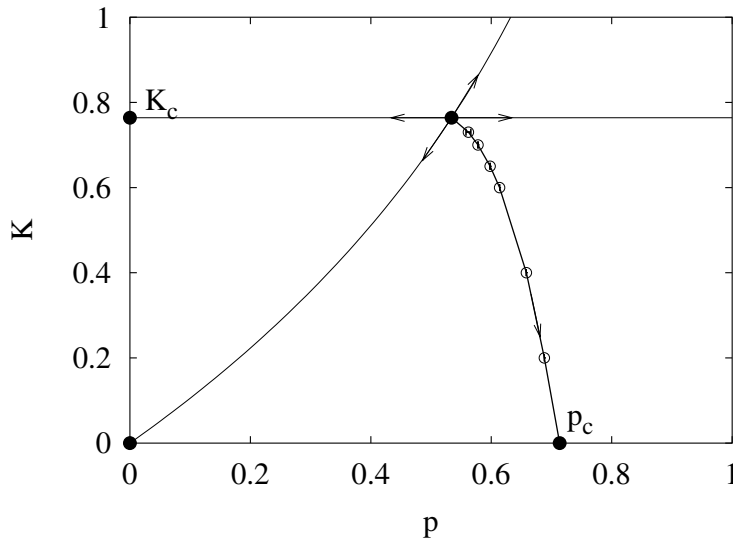


Figure 5.6: Percolation diagram of the  $q = 2 - 2 \cos(7\pi/18)$  Potts model on the square lattice with nearest-neighbor interaction. The percolation line runs from  $p_c = 0.71362(2)$ ,  $K = 0$  to the random-cluster fixed point. We did not locate the stable fixed point  $p_s$  on the critical line; interpolation between  $q = 1$  ( $p_s = 1$ ) and  $q = 2$  (see Fig. 5.3) suggests that it lies in the unphysical range  $p > 1$ .

model moves even farther into the unphysical region than in the case of the Ising model. However, the stable fixed point on the critical line  $K = K_c = \ln(1 + \sqrt{3})$  still lies in the physical range at  $p_s = 0.83(2)$ , as determined by the transfer-matrix technique. In order to bring the percolation line into the physical range, we included couplings with a substantial number of neighbors; we adopted the square lattice model with 20 equivalent neighbors, which has its critical point at  $K_c = 0.154078(1)$  as mentioned in Sec. 5.2. We determined the location of the percolation transition line for  $K < K_c$ , and the location of the stable fixed point by an analysis as described above. The results, shown in Fig. 5.7, indicate that the percolation line does not connect to the stable fixed point located at  $p_s = 0.25(2)$ , but moves to larger  $p$  when  $K \uparrow K_c$ . It seems plausible that the percolation line connects to an unstable fixed point at larger  $p$ , but analysis of our numerical results for the ratio  $Q$  in the physical range  $p \leq 1$  did not reveal clear evidence for such a fixed point.

## 5.5 Discussion and miscellaneous results

The behavior of the percolation line for  $q = 3$  in the preceding section suggests that the percolation line connects to another unstable fixed point at larger  $p$ . Our data indicate that there is no such fixed point in the physical range  $p \leq 1$ .

In view of the possible existence of such a fixed point for  $q = 2$ , we have simulated square-lattice systems with 20 equivalent neighbors up to size  $L = 600$  at the critical point

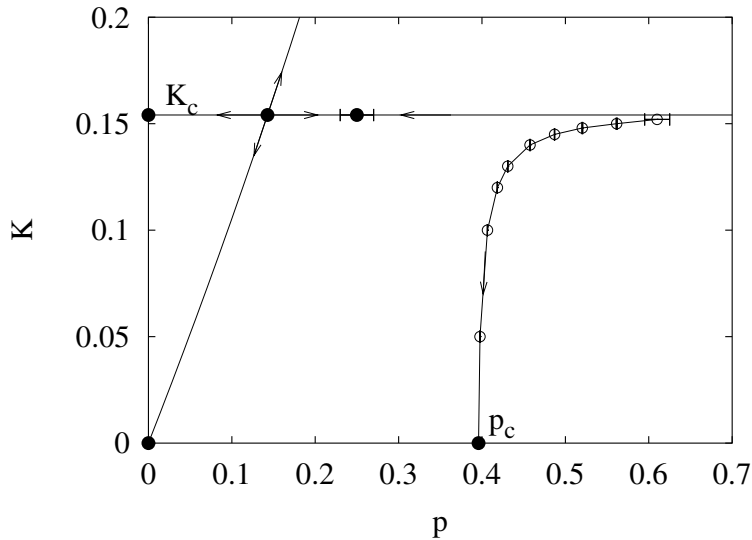


Figure 5.7: Percolation diagram of the three-state Potts model on the square lattice with 20 equivalent-neighbors. The percolation threshold lies at  $p_c = 0.39591(4)$  for  $K = 0$ .

(see Sec. 5.2)  $K_c = 0.1263852(8)$ . Again the percolation line runs toward the  $K = K_c$  stable fixed point, located at  $p_s \simeq 0.210(15)$ . Indeed, from an analysis of the ratio  $Q$  in the interval  $0.8 < p \leq 1$ , using Wolff-type simulations, we found a large- $p$ , unstable fixed point, included in Fig. 5.8. Quantitative analysis is difficult because of large corrections that suggest the presence of an irrelevant exponent  $y_1 \approx -0.4$ . Thus, our results for this new fixed point have a provisional character. Assuming corrections with exponents that are multiples of  $-0.4$ , we locate the fixed point at  $p_u \simeq 0.94(2)$ , and the red-bond exponent as  $y_r = 0.54(3)$ , close to the exact value  $13/24$  at the random-cluster point. The fractal dimension  $X_h$  of the clusters was estimated from a finite-size analysis of the largest cluster near  $p = 0.94$  as  $X_h = 0.035(1)$ .

Our results in the preceding sections indicate that the percolation line connects to the stable fixed point at  $K = K_c$  in the whole two-dimensional Ising universality class. This special topology presumably applies only to  $q = 2$ . It does not apply to the cases  $q \neq 2$  that we have investigated. The special situation at  $q = 2$  is exposed by defining a second bond percolation problem between all sites of the  $q - 1$  remaining colors. Only for  $q = 2$  both problems are equivalent: i.e., there is a symmetry in the model that may force the percolation transitions into a plane parametrized by a zero irrelevant field.

This argument based on symmetry thus predicts that the bond percolation problem involving bonds between sites with *two* out of  $q = 3$  colors would lead to a percolation line connecting to the point acting as the percolation threshold on the line  $K = K_c$  (i.e., an unstable fixed point), but which is no longer the random-cluster point. Indeed, our numerical results, for the nearest-neighbor three-state Potts model on the square-lattice, shown in Fig. 5.9, agree with this prediction. The results yield the percolation threshold at  $K = 0$  as  $p_c = 0.8509(4)$ : the bond percolation threshold on the square lattice with

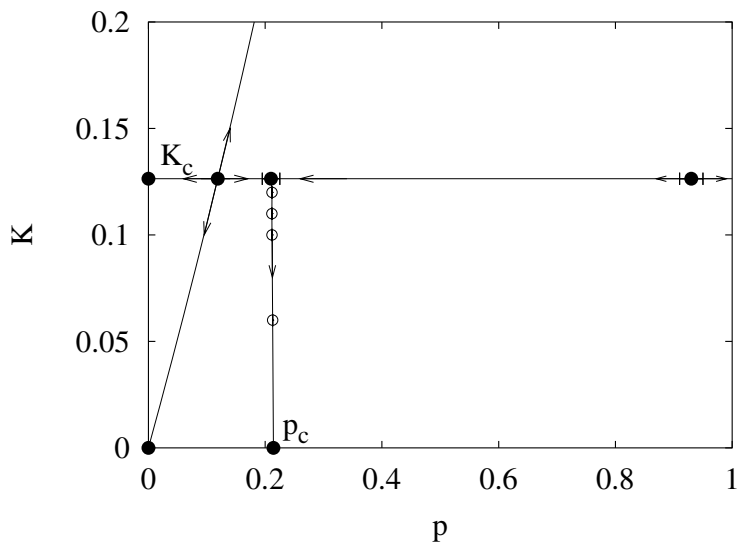


Figure 5.8: Percolation diagram of the Ising model on the square lattice with 20 equivalent neighbors. The percolation threshold lies at  $p_c = 0.21416(2)$  for infinite temperature  $K = 0$ .

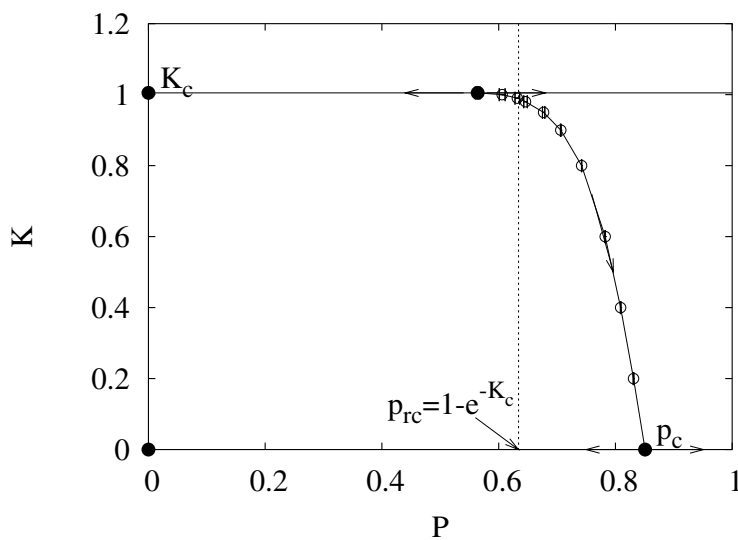


Figure 5.9: Percolation diagram of the three-state Potts model on the square lattice, with percolation clusters including variables of two colors. The percolation threshold on the critical line acts as the end point of the percolation line in the disordered phase. It does not coincide with the random-cluster point.

site probability  $2/3$ . The percolation threshold on the critical line  $K = K_c$  lies at  $p_t = 0.5622(2)$ , which is clearly smaller than the random-cluster probability  $p = 0.63397\dots$ .

We conclude this chapter by mentioning that the above symmetry argument holds generally for planar lattices only. In three dimensional systems, percolation between sites with one of  $q$  colors may thus be expected to display different behavior. For instance, for the dilute Ising model at tricriticality, the bond probability  $p$  at the random-cluster fixed point is irrelevant in two dimensions [5] and relevant in three dimensions [27]. Our preliminary simulation results suggest that, in contrast to the two-dimensional case, the one-color-percolation line in the disordered phase of the simple-cubic Ising model connects to the random-cluster fixed point.

# Bibliography

- [1] M. F. Sykes and D. S. Gaunt, *J. Phys. A* **9**, 2131 (1976).
- [2] A. Coniglio, *Phys. Rev. Lett.* **62**, 3054 (1989).
- [3] C. Vanderzande, *J. Phys. A* **25**, L75 (1992).
- [4] P. J. M. Bastiaansen and H. J. F. Knops, *J. Phys. A* **30**, 1791 (1997).
- [5] Y. Deng, H. W. J. Blöte and B. Nienhuis, *Phys. Rev. E* **69**, 026114 (2004).
- [6] H. -O. Georgii, O. Häggström and C. Maes, in *Phase Transitions and Critical Phenomena*, edited by C. Domb and J. L. Lebowitz (Academic Press, San Diego, 2001), Vol. **18**, p. 1.
- [7] P. J. M. Bastiaansen and H. J. F. Knops, *J. Phys. Chem. Solids* **59**, 297 (1998).
- [8] R. A. Römer, "Percolation, Renormalization and the Quantum-Hall Transition", cond-mat/0106004; and in *Computational Statistical Physics From Billiards to Monte-Carlo*, edited by K. -H. Hoffmann and M. Schreiber, (Springer, Berlin, 2002).
- [9] J. T. Chalker and P. D. Coddington, *J. Phys. C* **21**, 2665 (1988).
- [10] P. W. Kasteleyn and C. M. Fortuin, *J. Phys. Soc. Jpn. Suppl.* **26**, 11 (1969); C. M. Fortuin and P. W. Kasteleyn, *Physica* **57**, 536 (1972).
- [11] R. B. Potts, *Proc. Cambridge Philos. Soc.* **48**, 106 (1952).
- [12] H. Whitney, *Ann. Math. N. Y.* **33**, 688 (1932).
- [13] R. M. F. Houtappel, *Physica* **16**, 425 (1950).
- [14] M. P. Nightingale and H. W. J. Blöte, *Physica A* **251**, 211 (1998).
- [15] E. Luijten and H. W. J. Blöte, *Int. J. Mod. Phys. C* **6**, 359 (1995).
- [16] K. Binder, *Z. Phys. B* **43**, 119 (1981).
- [17] E. Luijten, H. W. J. Blöte and K. Binder, *Phys. Rev. E* **54**, 4626 (1996).

- [18] H. W. J. Blöte, Y. M. M. Knops and B. Nienhuis, Phys. Rev. Lett. **68**, 3440 (1992).
- [19] R. H. Swendsen and J. S. Wang, Phys. Rev. Lett. **58**, 86 (1987).
- [20] U. Wolff, Phys. Rev. Lett. **60**, 1461 (1988).
- [21] L. Chayes and J. Machta, Physica A **254**, 477 (1998).
- [22] Chapter 3 of this thesis; X. Qian, Y. Deng and H. W. J. Blöte, Phys. Rev. E **71**, 016709 (2005).
- [23] H. W. J. Blöte and M. P. Nightingale, Physica A **112**, 405 (1982).
- [24] Y. Deng and H. W. J. Blöte, Phys. Rev. E **71**, 016117 (2005).
- [25] J. R. Heringa and H. W. J. Blöte, Phys. Rev. E **57**, 4976 (1998).
- [26] J. W. Essam, in *Phase Transitions and Critical Phenomena*, edited by C. Domb and M. S. Green (Academic Press, London, 1987), Vol. **2**, p. 197.
- [27] Y. Deng and H. W. J. Blöte, Phys. Rev. E **70**, 056132, (2004).

# Chapter 6

## Dilute Potts model in two dimensions

We study the two-dimensional dilute  $q$ -state Potts model by means of transfer-matrix and Monte Carlo methods. Using the random-cluster representation, we include noninteger values of  $q$ . We locate phase transitions in the three-dimensional parameter space of  $q$ , the Potts coupling  $K \geq 0$  and the chemical potential of the vacancies. The critical plane is found to contain a line of fixed points that divides into a critical branch and a tricritical one, just as predicted by the renormalization scenario formulated by Nienhuis et al. for the dilute Potts model. The universal properties along the line of fixed points agree with the theoretical predictions. We also determine the density of the vacancies along these branches. For  $q = 2 - \sqrt{2}$  we obtain the phase diagram in a three-dimensional parameter space that also includes a coupling  $V \geq 0$  between the vacancies. For  $q = 2$ , the latter space contains the Blume-Capel model as a special case. We include a determination of the tricritical point of this model, as well as an analysis of percolation clusters constructed on tricritical Potts configurations for noninteger  $q$ . This percolation study is based on Monte Carlo algorithms that include local updates flipping between Potts sites and vacancies. The bond updates are performed locally for  $q < 1$  and by means of a cluster algorithm for  $q > 1$ . The updates for  $q > 1$  use a number of operations per site independent of the system size.

### 6.1 Introduction

The renormalization scenario for the dilute  $q$ -state Potts model, as formulated by Nienhuis et al. [1] has been remarkably successful in reproducing known properties of the two-dimensional Potts model such as the qualitative  $q$ -dependence of the temperature exponent, the first-order character of the phase transition [2] when  $q$  exceeds a certain threshold, and the existence of a branch of tricritical points that merges with the critical manifold at this threshold. The renormalization equations as e.g. analyzed by Nauenberg and Scalapino [3] and others [4,5] even allow the accurate reproduction of subtle details in the mathematical form of the free-energy singularity, including the energy discontinuity as a function of  $q$  for  $q > 4$ , which was exactly calculated by Baxter [2]. While this strongly suggests that the

renormalization description of Ref. [1] is true in a fundamental sense, this approach is not very suitable to obtain quantitative information on the phase diagram. For instance, the renormalization equations of [1] locate the threshold value of  $q$  near  $q = 4.73$  instead of at the exact value [2]  $q = 4$ .

The present work aims to obtain some quantitative information about the model described by the three temperature-like parameters of Ref. [1]. In addition to the Potts coupling  $K$  and the chemical potential  $D$  of the vacancies, the model also includes a vacancy-vacancy coupling  $V$ . It is thus described by the Hamiltonian

$$\mathcal{H}/k_B T = -K \sum_{\langle ij \rangle} \delta_{\sigma_i \sigma_j} (1 - \delta_{\sigma_i 0}) - V \sum_{\langle ij \rangle} \delta_{\sigma_i 0} \delta_{\sigma_j 0} - D \sum_k \delta_{\sigma_k 0}, \quad (6.1)$$

where the variables  $\sigma_i$  carry indices that refer to the sites of a square lattice. They can assume values  $\sigma_i = 0, 1, \dots, q$ , where  $\sigma_i = 0$  stands for a vacancy and  $\sigma_i \neq 0$  for one of the Potts states. The sums on  $\langle ij \rangle$  run over all pairs of nearest neighbors. While Nienhuis et al. defined their model on the triangular lattice, we do not expect qualitative differences with respect to the model on the square lattice.

The partition sum of the model described by Eq. (6.1) is

$$Z_\sigma = \left[ \prod_{i=1}^N \sum_{\sigma_i=0}^q \right] \left[ \prod_{\langle ij \rangle} \exp(K \delta_{\sigma_i \sigma_j} \{1 - \delta_{\sigma_i 0}\}) \exp(V \delta_{\sigma_i 0} \delta_{\sigma_j 0}) \right] \left[ \prod_k \exp(D \delta_{\sigma_k 0}) \right]. \quad (6.2)$$

It is convenient to specify the vacancies by a separate variable  $\tau_i$  that assumes the values 0 (for vacancies) or 1. This leads to

$$Z_\sigma = \left[ \prod_{i=1}^N \sum_{\tau_i=0}^1 \sum_{\sigma_i=\tau_i}^{q\tau_i} \right] \left[ \prod_{\langle ij \rangle} \exp(K \delta_{\sigma_i \sigma_j} \tau_i) \exp(V \delta_{\tau_i 0} \delta_{\tau_j 0}) \right] \left[ \prod_k \exp(D \delta_{\tau_k 0}) \right]. \quad (6.3)$$

For the purpose of the mapping on the random-cluster model, we rewrite  $\exp(K \delta_{\sigma_i \sigma_j} \tau_i) = \sum_{b_{ij}=0}^{\tau_i \tau_j} (u \delta_{\sigma_i \sigma_j})^{b_{ij}}$  where  $u \equiv e^K - 1$  is the temperature-like parameter, and with the convention  $0^0 = 1$ . Substitution in Eq. (6.3) yields

$$Z_\sigma = \left[ \prod_{i=1}^N \sum_{\tau_i=0}^1 \right] \left[ \prod_{i=1}^N \sum_{\sigma_i=\tau_i}^{q\tau_i} \right] \left[ \prod_{\langle ij \rangle} \sum_{b_{ij}=0}^{\tau_i \tau_j} (u \delta_{\sigma_i \sigma_j})^{b_{ij}} \exp(V \delta_{\tau_i 0} \delta_{\tau_j 0}) \right] \left[ \prod_k \exp(D \delta_{\tau_k 0}) \right]. \quad (6.4)$$

Nonzero bond variables  $b_{ij} = 1$  may occur only on lattice edges connecting equal, nonzero Potts variables. Also in the presence of vacancies we can execute the summation on the Potts variables  $\sigma_i = 1, \dots, q$ , i.e., perform the Kasteleyn-Fortuin mapping [6]. While Kasteleyn and Fortuin did not include vacancies, they formulated this mapping for a general lattice, so that it can be applied directly to each term in the sum on the vacancy configurations as expressed by the  $\tau_i$ . The sum on the Potts variables yields a factor  $q$  for each cluster of sites connected by nonzero bonds. This yields the random-cluster

representation of the Potts model with vacancies:

$$Z_\sigma = Z_b \equiv \left[ \prod_{i=1}^N \sum_{\tau_i=0}^1 \right] \left[ \prod_{\langle ij \rangle} \sum_{b_{ij}=0}^{\tau_i \tau_j} \right] u^{N_b} q^{N_c} \exp(V N_{vv}) \exp(D N_v), \quad (6.5)$$

where  $N_b \equiv \sum b_{ij}$  denotes the number of nonzero bonds. These bonds divide the lattice in  $N_c$  clusters or components,  $N_v$  denotes the number of vacancies, and  $N_{vv}$  the number of nearest-neighbor vacancy pairs as specified by the site variables  $\tau_i$ .

Although Eqs. (6.1) and (6.2) are meaningful only when the number of states is an integer  $q \geq 1$ , Eq. (6.5) is well defined also for noninteger  $q$ . It has played a useful role (together with its simplified version that excludes vacancies) in mappings on the 8-vertex model and on the Coulomb gas, so that exact critical exponents could be obtained [7]. They can be expressed in the Coulomb gas coupling constant  $g$  which depends on  $q$  by

$$q = 2 + 2 \cos \frac{g\pi}{2} \quad (6.6)$$

with  $2 \leq g \leq 4$  for the critical, and  $4 < g \leq 6$  for the tricritical Potts model. The temperature dimension followed as

$$X_t = \frac{6}{g} - 1 \quad (6.7)$$

and the magnetic dimension as

$$X_h = 1 - \frac{g}{8} - \frac{3}{2g}. \quad (6.8)$$

These dimensions were also exactly derived in the theory of conformal invariance [8]. In this context one characterizes universality classes by a number  $m$  related to the Coulomb gas coupling  $g$  by  $m = g/(4 - g)$  for the critical branch ( $g \leq 4$ ) and by  $m = 4/(g - 4)$  for the tricritical branch ( $g > 4$ ). The theory predicts that there exists a set of scaling dimensions, associated with scalar observables. Some of these dimensions can be labeled by two integers  $p$  and  $q$ , and are determined by the Kac formula as

$$X_{p,q} = \frac{[p(m+1) - qm]^2 - 1}{2m(m+1)}. \quad (6.9)$$

For the critical branch we may identify the  $i$ th temperature dimension with  $X_{i+1,1}$ , and for the tricritical branch with  $X_{1,i+1}$ . The most relevant magnetic dimension is  $X_{(m+1)/2,(m+1)/2}$  for the critical Potts model and  $X_{m/2,m/2}$  for the tricritical Potts model.

While considerable exact information is thus available, there remain some problems that have thus far escaped exact analysis. We mention the backbone exponents [9–11], surface critical phenomena [12–14], and percolation properties of random clusters [15]. These problems can in principle be solved by numerical work. For the critical Potts model, one can simply Monte Carlo simulate the model without vacancies. But for  $q \approx 4$ , strong corrections

to scaling occur due to the subleading temperature field, that becomes marginal at  $q = 4$  and thus generates logarithmic corrections. It is therefore desirable to determine the locus of fixed points, naturally in a truncated parameter space. In a two-dimensional space, the two leading temperature fields thus vanish at this locus. For the critical branch, this would mean that the leading corrections to scaling are suppressed, so that accurate numerical investigations become feasible. For  $q < 4$  one expects to find, in addition to the critical fixed point, a second fixed point corresponding with the Potts tricritical point, which may also be of some use for numerical work. Here we remark that, for some purposes, an exact result of Nienhuis [16] may offer a good alternative for numerical work on tricritical Potts models. Another research subject that may benefit from accurate knowledge of critical points of models with vacancies concerns the finite-size scaling behavior of models with a constraint. The scaling theory of such models in the thermodynamic limit is described by the Fisher renormalization [17] theory. These phenomena can be investigated numerically in systems whose number of vacancies is conserved by the constraint. The geometric cluster algorithm [18] provides a very suitable tool for such investigations, because it does not only conserve the number of vacancies, but also reduces critical slowing down. However, its useful applications are restricted to integer values of  $q$ .

The present work aims to provide accurate information on the location of the fixed points and the phase diagram. Most of this program is realized by means of transfer-matrix calculations which are explained in Sec. II, which also contains a short description of the Monte Carlo algorithms employed in this work. In Sec. III we present results for the phase diagram in the  $(q, K, D)$  parameter space, in particular the line of fixed points consisting of a critical branch and a tricritical one. This part is restricted to the case  $V = 0$ . For one special value  $q = 2 - \sqrt{2}$  we determine the phase diagram in the three-dimensional space  $(K, V, D)$ . The results, which are probably generically true [1] for  $q < 3$  Potts models, are reported in Sec. IV. Section V presents various results including a critical and a tricritical point of the Blume-Capel model, and the location and exponents of the percolation threshold of tricritical Potts clusters for several values of  $q$ . Finally, our conclusions are listed in Sec. VI.

## 6.2 Algorithms

### 6.2.1 Transfer matrix technique

We summarize the calculations performed for the continuous- $q$  model defined by Eq. (6.5). Additional analyses were performed using integer spin representations which are already adequately described in the literature [19] and do not need further explanation. We define the random-cluster model on a lattice on the surface of a cylinder, with one set of nearest-neighbor edges parallel to the transfer direction, i.e., the axis of the cylinder. The cylinder has a length of  $n$  lattice units, and has an open end at the  $n$ th layer of  $L$  sites. The construction of a transfer matrix requires a ‘coding’ of the relevant degrees of freedom at the free end of the cylinder. These degrees of freedom include the positions of the vacancies,

and how the remaining sites are connected by the random-cluster bonds. This information is called ‘connectivity’. The somewhat elaborate task of coding these connectivities is described in Appendix A, and the actual definition of the transfer matrix in Appendix B, which is used to build an algorithm that can multiply a vector  $\vec{v}$  by the transfer matrix  $\mathbf{T}$ :

$$\vec{v}' = \mathbf{T} \cdot \vec{v}. \quad (6.10)$$

It is not necessary to store the full matrix  $\mathbf{T}$ . The availability of a numerical procedure that executes this multiplication is sufficient for the calculation of a few of the largest eigenvalues. The power method, or direct iteration, would lead to the desired result but the projection of the transfer matrix on a relatively low-dimensional Hessenberg matrix, which was explained in detail in Ref. [20], leads to much faster convergence. As explained in Appendix B, the transfer matrix can be viewed as consisting of two independent sectors, a ‘nonmagnetic’ and a ‘magnetic sector. Three different eigenvalues were calculated, namely the largest eigenvalues in both sectors, and a second eigenvalue in the nonmagnetic sector.

Calculations with finite sizes up to  $L = 12$  (for the determination of the critical and tricritical points) or  $L = 13$  (for the determination of the vacancy densities) were performed. The size of the matrix  $\mathbf{T}$  is  $19\,181\,100 \times 19\,181\,100$  for the latter system size.

### Calculation of the scaling dimensions

The Potts magnetic correlation function along the coordinate  $r$  in the length direction of the cylinder is defined as

$$g_h(r) = \frac{\langle q \delta_{\sigma_0 \sigma_r} - 1 \rangle}{q - 1}. \quad (6.11)$$

In the random-cluster representation, this correlation function is equal to the probability that sites 0 and  $r$  belong to the same random cluster. At large  $r$ ,  $g_h(r)$  decays exponentially with a characteristic length scale  $\xi_h$  that depends on  $K$ ,  $D$ ,  $V$ , and  $L$ :

$$g_h(r) \propto e^{-r/\xi_h(K,V,D,L)} \quad (6.12)$$

and can be calculated from the largest two eigenvalues  $\lambda_0$  and  $\lambda_1$  of the transfer matrix:

$$\xi_h^{-1}(K, V, D, L) = \ln(\lambda_0/\lambda_1). \quad (6.13)$$

For the calculation of the eigenvalues, as needed to find  $\xi_h$ , we may employ the following properties of the corresponding eigenvectors. Since the partition sum of the random-cluster model can be expressed using only the ‘nonmagnetic’ connectivities (see Appendix B), it follows that the largest eigenvalue, which determines the free energy, resides in the nonmagnetic sector. Furthermore, the transfer matrix contains a nondiagonal block of zeroes that reflects the fact that the multiplication of a vector with only zeroes on the ‘magnetic’ positions again leads to such a vector. Thus, there exist left-hand eigenvectors with nonzero elements only for ‘magnetic’ connectivities. The one among these with the largest eigenvalue is associated with the magnetic correlation function. The calculation of this eigenvector, and its eigenvalue  $\lambda_1$ , can thus be restricted to the ‘magnetic’ sector.

Application of a conformal mapping [21] relates  $\xi_h$  on the cylinder with the magnetic scaling dimension  $X_h$  (equal to one half of the magnetic correlation function exponent  $\eta$ ). At a critical point (e.g.,  $K$  adjusted to its critical value  $K = K_c$  for given  $D$  and  $V$ ) this exponent obeys

$$X_h \simeq X_h(K, V, D, L) \equiv \frac{L}{2\pi\xi_h(K, V, D, L)}. \quad (6.14)$$

This is asymptotically true for a critical model in the limit of large  $L$ . We may thus use it to estimate  $X_h$  numerically, and thereby obtain evidence about the universality class of the model. Or, if the universality class, and thus  $X_h$ , are considered known, we may solve for  $K$ ,  $V$  or  $D$  in

$$X_h(K, V, D, L) \simeq X_h \quad (6.15)$$

to determine the critical subspace.

In addition to  $\xi_h$ , it is possible to determine a second correlation length  $\xi_t$  describing the exponential decay of the energy-energy correlation function. It is associated with a third eigenvalue  $\lambda_2$  of the transfer matrix with an eigenvector in the ‘nonmagnetic’ subspace, just as the one with eigenvalue  $\lambda_0$ . The pertinent eigenvalue can be obtained by means of the projection technique described in Ref. [20]. In analogy with the case of the magnetic correlation length we can use the third eigenvalue  $\lambda_2$  to estimate the temperature scaling dimension  $X_t$  as

$$X_t(K, V, D, L) \equiv \frac{L}{2\pi\xi_t(K, V, D, L)}, \quad (6.16)$$

where  $\xi_t^{-1} = \ln(\lambda_0/\lambda_2)$ .

### Calculation of the vacancy density

In the calculation of the vacancy density we have to take into account that the transfer matrix for general  $q$  is essentially nonsymmetric. We define a matrix representation of the density with elements  $V_{\alpha\beta} \equiv \delta_{\alpha,\beta}n_v(\alpha)/L$  where  $n_v(\alpha)$  is the number of vacancies as implicit in the ‘connectivity’  $\alpha$ . The expectation value of the vacancy density  $\rho$  is, in vector notation,

$$\langle \rho \rangle = \frac{\sum_{\alpha} [\mathbf{T}^{n-k} \cdot \mathbf{V} \cdot \mathbf{T}^k \cdot \vec{v}_0]_{\alpha}}{\sum_{\alpha} [\mathbf{T}^n \cdot \vec{v}_0]_{\alpha}}, \quad (6.17)$$

where  $\vec{v}_0$  is the Boltzmann weight of the first row of the system. For an infinitely long system we may take both  $k$  and  $n - k$  to infinity. The right-hand eigenvalue problem of the transfer matrix is

$$\mathbf{T} \cdot \mathbf{R} = \mathbf{R} \cdot \mathbf{\Lambda}, \quad (6.18)$$

where  $\mathbf{R}$  is the matrix of right-hand eigenvectors, arranged as columns of  $\mathbf{R}$ , and  $\mathbf{\Lambda}$  is the diagonal matrix containing the eigenvalues of  $\mathbf{T}$ . In general we can similarly formulate the left-hand eigenvalue problem as

$$\mathbf{L} \cdot \mathbf{T} = \mathbf{\Lambda} \cdot \mathbf{L}, \quad (6.19)$$

such that the matrix of left-hand eigenvectors  $\mathbf{L}$  is the inverse of  $\mathbf{R}$ . Next we insert the unit matrix  $\mathbf{R} \cdot \mathbf{L}$  between all inproducts in Eq. (6.17):

$$\langle \rho \rangle = \frac{\sum_{\alpha} [\mathbf{R} \cdot \Lambda^{n-k} \cdot \mathbf{L} \cdot \mathbf{V} \cdot \mathbf{R} \cdot \Lambda^k \cdot \mathbf{L} \cdot \vec{v}_0]_{\alpha}}{\sum_{\alpha} [\mathbf{R} \cdot \Lambda^n \cdot \mathbf{L} \cdot \vec{v}_0]_{\alpha}}. \quad (6.20)$$

Let  $\Lambda_{11}$  be the largest eigenvalue, which is the only one that survives when the powers  $k$  and  $n - k$  become large. After dividing out  $\Lambda_{11}^n$ ,  $\sum_{\alpha} R_{\alpha 1}$  and  $\sum_{\alpha} L_{1\alpha}(v_0)_{\alpha}$ , Eq. (6.20) reduces to

$$\langle \rho \rangle = \sum_{\alpha} L_{1\alpha} V_{\alpha\alpha} R_{\alpha 1}. \quad (6.21)$$

Thus the determination of  $\rho$  requires the determination of both the right- and left-hand leading eigenvectors. This was realized by means of two independent calculations along the lines described in Ref. [20], one employing the sparse-matrix decomposition of  $\mathbf{T}$ , and the other that of the transpose of  $\mathbf{T}$ .

## 6.2.2 Monte Carlo technique

### Local bond update for dilute Potts models with $0 < q < 1$

For non-integer  $q < 1$ , no cluster algorithm is available and we developed an algorithm employing local updates, with bond updates as well as site updates. The latter may flip Potts sites  $\sigma_i > 0$  into vacancies  $\sigma_i = 0$  and vice versa, thus generalizing the algorithms of Sweeney [22] and Gliozzi [23]. A complication in this type of algorithms is that the number of components  $N_c$  in Eq. (6.5) can be changed by a local update, which influences the transition probabilities. Since the determination of the change in  $N_c$  caused by a local update is an essentially nonlocal task, the Monte Carlo algorithms are quite slow in comparison with the cluster methods available for  $q > 1$ . Moreover, now also the four surrounding bond variables enter into the probabilities of flips between vacancies and Potts sites which leads to many possibilities and leads to a rather time-consuming programming task when a relatively optimal algorithm is desired.

The transition probabilities are defined such as to satisfy detailed balance on the basis of the weights defined by the random-cluster partition sum Eq. (6.5). Simulations under the constraint that the density of the vacancies is conserved are realized by excluding updates leading to states with less than  $N_v$  or more than  $N_v + 1$  vacancies.

### Cluster algorithm for dilute Potts models with $q > 1$

A cluster Monte Carlo algorithm for the noninteger  $q > 1$  random-cluster model without vacancies [24] is already available. It appears to be an efficient tool for the study of non-integer  $q$ -state Potts model [25] (see also Chap. 4) and was also applied in Ref. [26] (see also Chap. 5). To include vacancies it is convenient to use a formulation of this algorithm based on a cluster decomposition as given in Ref. [25] (see also Chap. 4) (but here we use a slightly different notation, with number 0 referring to vacancies and 1 to one of the Potts states).

Colors are randomly assigned, such that color 1 is singled out with a probability  $1/q$ . This procedure remains essentially the same in the presence of vacancies. After defining the subset of the lattice in state 1, we can thus include local Metropolis-like updates that may flip state-1 site variables into vacancies and vice versa. The advantage is that the bond variables disappear from the transition probabilities which thus become simple, and a site update requires only a number of operations independent of the system size. The summary of the Monte Carlo procedure, starting from a configuration specified by the subset in state 0 (the vacancies) and the random-cluster decomposition of the remaining sites, is as follows.

1. Assign color 1 to each cluster with probability  $1/q$ ;
2. Apply local updates flipping between color-1 sites and vacancies;
3. Form clusters on the type-1 sites, using a bond probability  $u/(u+1)$ ;
4. Erase the color variables.

The use of a probability  $1/q$  restricts the useful range of the algorithm to  $q > 1$ .

The method enables the study the critical and tricritical properties of dilute Potts models. For instance, it can be used to determine fractal properties of non-integer  $q$  Potts clusters at tricriticality. Simulations conserving the number of vacancies require a modification of step 2: we no longer allow flips between vacancies and color-1 variables. Instead, we propose local configuration changes involving the interchange of two site variables, chosen at two random positions. Only interchanges of vacancies and color-1 sites are accepted, with acceptance probabilities that are subject to the condition of detailed balance.

## 6.3 The line of fixed points for $V = 0$

### 6.3.1 Solving the equations for the fixed points

The transfer-matrix algorithms defined in Sec. 6.2.1 enables the numerical calculation of the functions  $X_h(K, D, L)$  and  $X_t(K, D, L)$  for a range of finite sizes  $L$ . The algorithm numerically calculates these functions for given values of  $K$ ,  $D$ , and  $L$ . The dependence on the parameters  $q$  and  $V$ , which are kept constant for the present, is not explicitly shown. We employ this technique to estimate the critical and tricritical fixed points in the  $V = 0$  subspace, by simultaneously solving for the two unknown  $K$  and  $D$  in the two equations

$$X_h(K, D, L) = X_h, \quad X_t(K, D, L) = X_t, \quad (6.22)$$

in which we substitute the exactly known values of  $X_h$  and  $X_t$  as a function of  $q$  (see Sec. 6.1). However, the results for the fixed points do not critically depend on these exact values, since the numerical procedure includes some redundancy as we shall discuss in Sec. 6.3.3. The solutions are denoted  $K_f(L)$  and  $D_f(L)$ , where the index ‘f’ refers to ‘fixed point’. In order to find their finite-size-scaling properties, we express the functions

$X_h(K, D, L)$  and  $X_t(K, D, L)$  in terms of the two leading temperature fields  $t_1$  and  $t_2$ , and another temperature-like field  $u$  that is taken to be irrelevant. Expansion of the finite-size scaling functions yields the equations

$$\begin{aligned} X_h(t_1, t_2, u, L) &= X_h + a_h t_1 L^{y_{t_1}} + b_h t_2 L^{y_{t_2}} + u L^{y_i} + \dots, \\ X_t(t_1, t_2, u, L) &= X_t + a_t t_1 L^{y_{t_1}} + b_t t_2 L^{y_{t_2}} + u L^{y_i} + \dots, \end{aligned} \quad (6.23)$$

where  $a_h$ ,  $b_h$ ,  $u_h$ ,  $a_t$ ,  $b_t$  and  $u_t$  are unknown constants,  $y_i$  is an irrelevant exponent ( $y_{t_3}$  or the integer  $-2$ ), and  $y_{t_1}$  and  $y_{t_2}$  are the two leading temperature exponents. At the simultaneous solution we thus have

$$\begin{aligned} a_h t_1 L^{y_{t_1}} + b_h t_2 L^{y_{t_2}} + u_h L^{y_i} + \dots &= 0, \\ a_t t_1 L^{y_{t_1}} + b_t t_2 L^{y_{t_2}} + u_t L^{y_i} + \dots &= 0. \end{aligned} \quad (6.24)$$

Elimination of  $t_1$  and solving for  $t_2$  yields

$$t_2 = \frac{(a_t u_h - a_h u_t)}{(a_h b_t - a_t b_h)} L^{y_i - y_{t_2}}. \quad (6.25)$$

Similarly, we find the solution for  $t_1$  as

$$t_1 = \frac{(b_t u_h - b_h u_t)}{(a_h b_t - a_t b_h)} L^{y_i - y_{t_1}}. \quad (6.26)$$

The scaling behavior of the numerical solutions  $K_f(L)$  and  $D_f(L)$  is found by expressing their differences with the asymptotic values  $K_f$  and  $D_f$  as linear combinations of  $t_1$  and  $t_2$ :

$$K_f(L) = K_f + a_0 L^{y_i - y_{t_2}} + a_1 L^{y_i - y_{t_1}} + \dots, \quad (6.27)$$

and

$$D_f(L) = D_f + b_0 L^{y_i - y_{t_2}} + b_1 L^{y_i - y_{t_1}} + \dots, \quad (6.28)$$

where  $a_j$  ( $j = 0, 1, \dots$ ) and  $b_j$  ( $j = 0, 1, \dots$ ) are unknown constants. Since we know, in principle, the exponents  $y_{t_1}$ ,  $y_{t_2}$ , and  $y_i$  (see Sec. 6.1), we can use this knowledge to extrapolate the solutions to obtain  $K_f$  and  $D_f$ . Two subsequent finite-size results  $K_f(L)$  and  $K_f(L+1)$  allow one extrapolation by solving for  $K_f^{(1)}(L)$  and  $a_0$  in

$$K_f(L') = K_f^{(1)}(L) + a_0 L^{y_i - y_{t_2}} \quad (6.29)$$

for  $L' = L$  and  $L+1$ . A second iteration step with a free exponent according to the three-point fits described in Ref. [20] then yielded iterated estimates  $K_f^{(2)}(L)$  from which we obtain final estimates listed in Table 6.1. The numerical uncertainty margin in these numbers was estimated from the differences between the  $K_f^{(2)}(L)$  obtained for the few largest  $L$  available. The data for  $D_f$  were analyzed similarly. The actual numerical accuracies of the fixed points are better in the direction perpendicular to the line of phase transitions than along this line. For this reason we have solved for  $D$  in the equation  $X_h(K, D, L) = X_h$ ,

Table 6.1: Fixed points of tricritical and critical dilute Potts models. These are extrapolations of finite-size data for systems with sizes up to  $L = 12$ , except for the case  $q = 2$  which used sizes up to  $L = 16$ . The vacancy densities  $\rho$  are based on data for system sizes up to  $L = 13$ . The results for  $g < 3$  were rejected (see text). Exact data for the  $q = 1$  tricritical point are included. In order to fit the table in the page, in the table I use the approximate values instead of the exact ones for these cases of  $q$ , namely,  $2 + \sqrt{2 - \sqrt{3}} = 2.517\dots$ ,  $2 + \sqrt{2 + \sqrt{2}} = 3.847\dots$ ,  $2 + \sqrt{2 - \sqrt{2}} = 2.765\dots$ , and  $2 - \sqrt{2 - \sqrt{2}} = 1.234\dots$

$q$	$g$	$K_f$	$D_f$	Refined $D_f$	$\rho$
0.1	2.2021...	0.334 (5)	-1.0 (1)	–	–
0.5	2.4601...	0.596 (4)	-0.46 (3)	–	–
0.8	2.5903...	0.709 (3)	-0.15 (2)	–	–
2.45	3.1444...	1.065 (2)	0.950 (5)	0.94708 (5)	0.0810 (3)
2.517...	19/6	1.0783 (5)	1.004 (3)	1.00460 (5)	0.0838 (2)
2.6	3.1939...	1.0936 (5)	1.068 (2)	1.06687 (5)	0.0871 (1)
2.8	3.2619...	1.1313 (2)	1.2222 (4)	1.22171 (5)	0.09579 (2)
3.0	10/3	1.16941 (2)	1.37655 (5)	1.376483 (5)	0.10528 (1)
3.5	3.5398...	1.27104 (2)	1.77785 (4)	1.777891 (5)	0.13496 (1)
3.8	3.7128...	1.34722 (2)	2.06903 (4)	2.069046 (4)	0.16225 (1)
3.847...	15/4	1.36261 (2)	2.12689 (4)	2.126922 (4)	0.16839 (1)
3.9	3.7978...	1.38194 (2)	2.19915 (4)	2.19917 (1)	0.176431 (10)
4.0	4	1.45791 (2)	2.47845 (4)	2.47847 (1)	0.21207 (1)
3.9	4.2021...	1.525175 (4)	2.719730 (8)	2.719732 (3)	0.250190 (5)
3.8	4.2871...	1.551010 (3)	2.810900 (6)	2.810902 (2)	0.266885 (5)
3.5	4.4601...	1.599352 (3)	2.979260 (6)	2.979263 (2)	0.30202 (2)
$2 + \sqrt{2}$	9/2	1.609715 (5)	3.014962 (10)	3.014971 (3)	0.31031 (2)
3	14/3	1.649903 (5)	3.152149 (10)	3.152152 (2)	0.345766 (10)
2.765...	19/4	1.668155 (5)	3.213760 (10)	3.213758 (3)	0.36396 (4)
2.5	4.8391...	1.686350 (5)	3.274720 (10)	3.274720 (3)	0.3838 (1)
2.0	5	1.715733 (1)	3.372204 (2)	3.372205 (3)	0.42020 (10)
1.5	5.1608...	1.740760 (8)	3.454225 (15)	3.454222 (3)	0.4578 (2)
1.234...	21/4	1.752746 (8)	3.493180 (15)	3.493172 (3)	0.4793 (2)
1	16/3	$2\ln(1 + \sqrt{2})$	$4\ln(1 + \sqrt{2})$	–	1/2
$2 - \sqrt{2}$	11/2	1.77927 (4)	3.57851 (8)	3.578504 (3)	0.5430 (5)
$2 - \sqrt{3}$	17/3	1.79110 (5)	3.61617 (10)	3.616170 (4)	0.5885 (8)
0.1	5.7978...	1.7971 (1)	3.6352 (2)	3.63516 (2)	0.630 (10)

with  $K$  fixed at its estimated fixed-point value  $K_f$ , except for  $g < 3$ , because of reasons given below. The solutions were again fitted using similar methods as above. The fits yield refined estimates of  $D$  that are included in Table 6.1. The latter estimates are likely to lie closer to the line of phase transitions, but not necessarily closer to the fixed point.

The numerical procedure yielded results with a satisfactory finite-size convergence, except for  $q \rightarrow 0$  on the tricritical branch, where the results become less accurate because the scaling exponents become indistinguishable from those at the first-order transition, and for  $q \lesssim 2.5$  on the critical branch, where complications of a different nature arise. First, it has been reported [7, 27] that corrections to scaling due to the second temperature field, i.e., governed by the exponent  $y_{t_2}$ , disappear in most observables for  $q \rightarrow 2$ . This means that, near  $q = 2$ , the numerical solutions (if any) do not suppress the second temperature field, but instead other effects, possibly analytic corrections with exponent  $-2$  as in the Ising model. Second, for  $q < 1$ , we have  $y_{t_2} < -2$  so that the leading corrections to scaling in Eqs. (6.24) are the analytic ones, and the procedure will again try to suppress these, instead of the second temperature field. Although numerical solutions were obtained for  $q < 1$ , they should not be interpreted as fixed points in the truncated space of the two leading temperature fields  $t_1$  and  $t_2$ .

We have also computed the finite-size data for the vacancy density at the estimated fixed points  $(K_f, D_f)$ , using the procedure outlined in Sec. 6.2.1. The scaling behavior of  $\rho$  follows by differentiation of the free energy density to  $D$ . When we substitute the scaling relation of the free energy, and linearize  $D$  in  $t_1$  and  $t_2$ , we obtain

$$\rho(L, u) = \rho_0 + a_1 L^{y_{t_1} - 2} + a_2 L^{y_{t_2} - 2} + \dots + b_1 L^{y_{t_1} + y_i - 2} + \dots \quad (6.30)$$

Fits according to this expression showed no sign of a nonzero amplitude  $a_1$ . Indeed the derivative of the scaling function for the free energy with respect to  $t_1$  must vanish, because the energy of  $L \times \infty$  self-dual Potts strips does not depend on  $L$  [20]. We thus only used exponents  $y_{t_2} - 2$  and  $y_{t_1} + y_i - 2$  in the iterated fitting procedure. The extrapolated values of  $\rho$  are sensitive to small deviations in the estimated location of the fixed point. For comparison, we have also computed the finite-size data for the vacancy density at the corresponding finite-size solutions of Eqs. (6.22). The scaling behavior of these finite-size data for  $\rho$  now also contains contributions due to the deviations expressed by Eqs. (6.26) and (6.25), which may arise from the dependence of  $\rho_0$ ,  $a_1$  etc. on  $t_1$  and  $t_2$ . Which of these contributions dominates depends on the value of  $g$  that parametrizes the fixed line. We have applied many fits, using the predicted correction exponents as well as three-point fits that leave the exponent free. Best estimates were obtained by a comparison between these fits, and with the fit of the data obtained at the extrapolated fixed point. The finite-size dependence of the various fits, and the degree of their mutual consistency allowed us to estimate the numerical accuracy of the extrapolated results for the density as included in Table 6.1.

### 6.3.2 Polynomial approximations at the line of fixed points

The numerical data presented in Table 6.1 appear to behave rather smoothly as a function of the Coulomb gas coupling constant  $g$  defined in Sec. 6.1, especially for  $g > 3$ , as shown in Fig. 6.1. We fitted the quantity  $r \equiv e^D/(e^K - 1)$  by the expression

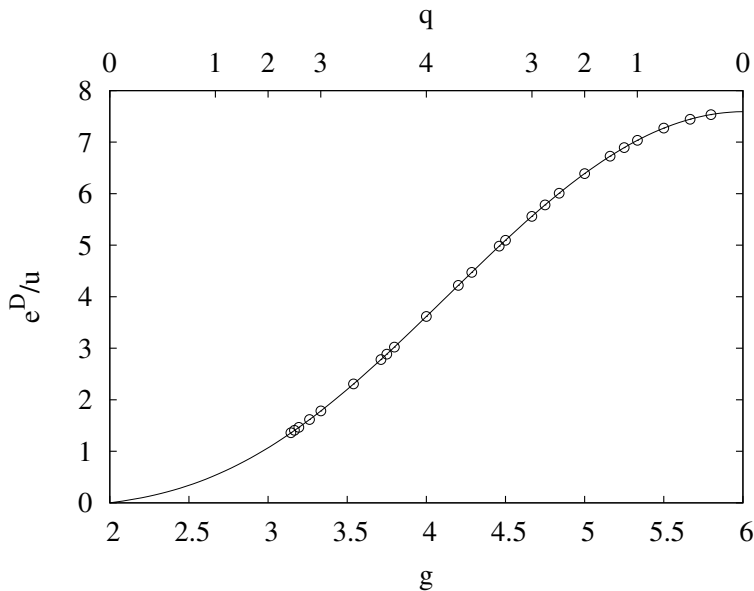


Figure 6.1: The line of critical and tricritical fixed points of the dilute Potts model in terms of the ratio  $e^D/u$  defined in the text versus the Coulomb gas coupling constant  $g$ . These fixed points were obtained in the two-dimensional parameter space  $(K, D)$  while  $V$  was set equal to zero. The error bars are much smaller than the symbol size. The curve shows the polynomial approximation for  $e^D/u$  described in the text. The scale for  $q$  is shown above.

$$r(g) = \sum_{j=0}^5 r_j (g-2)^j, \quad (6.31)$$

where the coefficients  $r_j$  were determined by means of the least-squares criterion. No satisfactory fits, as judged from the residual  $\chi^2$ , were obtained including all data in Table 6.1, because the data for  $g < 3$  did not accurately follow the trend of the remaining data, which is understandable on the basis of the relative magnitudes of  $y_{t_2}$  and  $y_i$  as described in the preceding subsection. A satisfactory fit was however obtained excluding the  $g < 3$  data. The result for the zeroth-order coefficient  $r_0 = -0.027$  was slightly negative but not significantly different from 0. Noting that  $r \geq 0$  for the present model described by Eq. (6.1), we take this small value as an indication that  $r = 0$  in the limit  $q \downarrow 0$  for the critical fixed point, and thus that the vacancies disappear in this limit. We thus fixed  $r_0 = 0$  and recalculated the coefficients. They are listed in Table 6.2. Figure 6.1 shows the fit to the numerical results for  $r$  as a function of the Coulomb gas coupling constant

Table 6.2: Coefficients of the polynomial describing  $r(g)$  along the fixed line as a function of  $g$ .

$k$	$r_k$	error
1	0.39815155	0.00250115
2	0.38326777	0.00431988
3	0.44162858	0.00271091
4	-0.16983072	0.00073526
5	0.01472573	0.00007298

Table 6.3: Coefficients of the polynomial describing  $u(g)$  along the fixed line as a function of  $g$ .

$k$	$u_k$	error
1	1.57118750	0.00122031
2	0.11386463	0.00206715
3	-0.01998229	0.00127897
4	-0.01068977	0.00034315
5	0.00093745	0.00003377

Table 6.4: Coefficients of the polynomial describing  $\rho(g)$  along the fixed line as a function of  $g$ .

$k$	$\rho_k$	error
1	0.01280616	0.00244377
2	0.06353299	0.00594846
3	-0.01922001	0.00564925
4	0.00978198	0.00261807
5	-0.00278903	0.00059244
6	0.00029403	0.00005239

$g$ . The fits made use of the exactly known tricritical point for  $q = 1$ , which is equivalent with the Ising model without vacancies. The exact numbers for this point are included in Table 6.1. The addition of this point does not significantly increase the  $\chi^2$  residual, which indicates that this point joins smoothly with the numerical data for other values of  $g$ .

We have similarly fitted the temperature parameter  $u$  as a function of  $g$  by the expression

$$u(g) = \sum_{j=1}^5 u_j (g-2)^j \quad (6.32)$$

and the density  $\rho$  of the vacancies by

$$\rho(g) = \sum_{j=1}^6 \rho_j (g-2)^j. \quad (6.33)$$

The number of coefficients was based on the requirement that the residual  $\chi^2$  is acceptable. The results are shown in Tables 6.3 and 6.4 respectively. The fitted expression for the density is shown in Fig. 6.2 as a function of  $g$ , together with the numerical data.

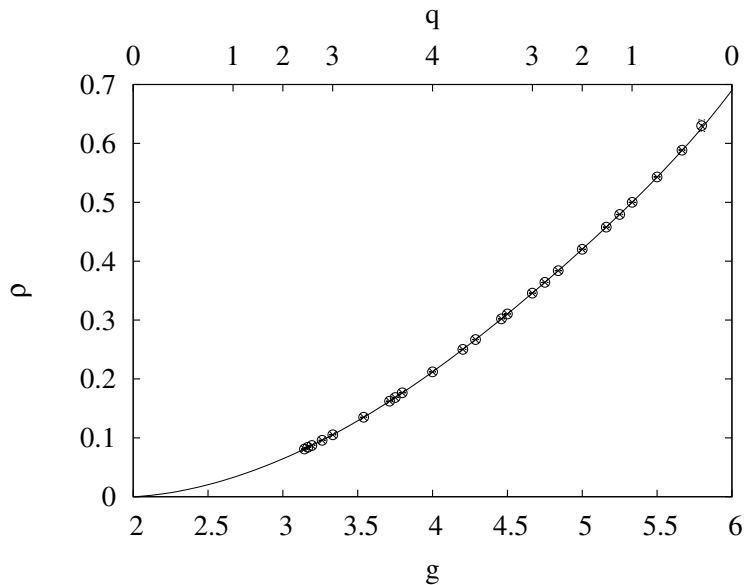


Figure 6.2: The vacancy density  $\rho$  along the line of fixed points of the dilute Potts model as a function of the Coulomb gas coupling constant  $g$ . The error bars are much smaller than the symbol size except for the rightmost data point. The curve shows the polynomial approximation for  $\rho$  described in the text. The scale for  $q$  is shown above.

### 6.3.3 Consistency with theory and universality

Our numerical procedure to determine the fixed points relies heavily on the existing results for the magnetic and temperature scaling dimensions, which are not supported by exact analysis for the general case of the model described by Eq. (6.5). We therefore consider the possibility that the scaling dimensions given by Eqs. (6.7) and (6.8) do not apply to the present model. That would lead to an additional constant in Eqs. (6.23) whose effect is the same as that of a term with an exponent  $y_i = 0$ . Thus, from Eqs. (6.27) and (6.28), we would then expect finite-size corrections proportional to  $L^{-y_{t_2}}$  in the numerical solutions of Eqs. (6.22). For the tricritical branch we have  $y_{t_2} > 0$  so that the solutions for large  $L$  still converge to the tricritical fixed point. For Potts criticality we have  $y_{t_2} < 0$  so that the solutions would fail to converge to the critical fixed point for large  $L$ . However, the analysis of the solutions showed satisfactory convergence.

More specifically, the finite-size dependence of the solutions of Eqs. (6.22) agreed well with the theoretical results for the exponents. This confirms the universality of the Potts model in an extended parameter space.

As another test, we have analyzed the finite-size dependence of the free energies at the extrapolated fixed points given in Table 6.1. Assuming conformal invariance [8], the conformal anomaly  $c$  can be obtained from the reduced free energy  $F(L)$  per unit of length of the cylinder, using the formula [28, 29]

$$F(L) \simeq Lf_\infty - \frac{\pi c}{6L}, \quad (6.34)$$

where  $f_\infty$  is the reduced bulk free energy density. This formula applies to the large- $L$  limit. On the other hand, the reduced free energy  $F(L)$  per unit of length follows from the largest

Table 6.5: Numerical results for the conformal anomaly of the dilute Potts model, for several points on the critical and tricritical branches. Comparison with the exact results (also listed) confirms that the present models fit well within the known Potts universality classes.

$q$	$g$	$m$	$c$ (numerical)	$c$ (exact)
2.45	3.1444...	3.6754...	0.6509 (1)	0.650854...
2.517...	19/6	19/5	0.6711 (1)	51/76
2.8	3.2619...	4.4199...	0.7496 (1)	0.749535...
3	8/3	6	0.8000 (1)	4/5
3.5	3.5398...	7.6936...	0.9103 (1)	0.910294...
3.9	3.7978...	18.7857...	0.9839 (1)	0.983857...
4	14/3	$\infty$	1.0000 (1)	1
3.9	4.2021...	19.7857...	0.9855 (1)	0.985410...
3.5	4.4601...	8.6936...	0.9288 (1)	0.928802...
$2 + \sqrt{2}$	9/2	8	0.9167 (1)	11/12
3	14/3	6	0.8571 (1)	6/7
2.765...	19/4	16/3	0.8224 (1)	0.822368...
2.5	4.8391...	4.7667...	0.7817 (1)	0.781731...
2	5	4	0.7000 (1)	7/10
1.5	5.1608...	3.4457...	0.6083 (1)	0.608321...
1.234...	21/4	16/5	0.5537 (2)	0.553571...
1	16/3	3	0.5000 (1)	1/2
$2 - \sqrt{2}$	11/2	8/3	0.3858 (5)	17/44
$2 - \sqrt{3}$	17/3	12/5	0.262 (4)	9/34
0.1	5.7978...	2.2248...	0.160 (5)	0.163771...

eigenvalue  $\lambda_0$  of the transfer matrix as

$$F(L) = -\ln \lambda_0 \quad (6.35)$$

and can thus be calculated with the procedures outlined in Sec. 6.2.1. Since there are two unknowns,  $f_\infty$  and  $c$ , in Eq. (6.34), the substitution of finite-size data for two subsequent system sizes in Eqs. (6.34) and (6.35) yields one estimate of the conformal anomaly  $c$ . These estimates display a rapid apparent convergence with increasing system sizes, with a finite-size dependence approximately as  $L^{-2}$  for most values of  $q$ , as deduced from three-point fits (see Ref. [20]). The final estimates of  $c$  are shown in Table 6.5, together with its theoretical value [28, 30]

$$c = 1 - \frac{6}{m(m+1)} \quad (6.36)$$

in terms of the parameter  $m$  defined in Sec. 6.1.

## 6.4 Phase diagram for $q = 2 - \sqrt{2}$

We determine the phase diagram in the three-dimensional parameter space  $(K, D, V)$  for  $K \geq 0$  and  $V \geq 0$ , using numerical analysis and some exact arguments. The choice  $q = 2 - \sqrt{2}$ , while somewhat arbitrary, was based on the fact that much is already known for the integer values of  $q$ , and that the exact results for the critical exponents assume simple fractional values.

### 6.4.1 Equivalences and exact limits

Before presenting the numerical results, we list a few exact results and limiting cases that are helpful to construct the phase diagram. The bond weights offer a handle to identify various phase boundaries and critical points. We consider the following cases:

1. If both  $D + 2V \ll 0$  and  $D \ll 0$ , the vacancies disappear and the Potts critical surface then lies at  $K = \ln(1 + \sqrt{q})$  [31].
2. When the Potts coupling vanishes, the dilute Potts model can be mapped on to the Ising model in a field, by interpreting the vacancies as Ising spins of one sign and the remaining site variables as Ising spins of the other sign. The field vanishes for special choices of  $D$  and  $V$ . For  $K = 0$  the partition sum Eq. (6.4) becomes

$$Z_\sigma = \left[ \prod_{i=1}^N \sum_{\tau_i=0}^1 \sum_{\sigma_i=\tau_i}^{q\tau_i} \right] \left[ \prod_{\langle ij \rangle} \exp(V\delta_{\tau_i 0}\delta_{\tau_j 0}) \right] \left[ \prod_k \exp(D\delta_{\tau_k 0}) \right]. \quad (6.37)$$

The summand does not explicitly depend on the  $\sigma_i$ , and the sums on the  $\sigma_i$  can thus be executed trivially:

$$Z_\sigma = \left[ \prod_{i=1}^N \sum_{\tau_i=0}^1 \right] \left[ \prod_{\langle ij \rangle} \exp(V\delta_{\tau_i 0}\delta_{\tau_j 0}) \right] \left[ \prod_k \exp(D\delta_{\tau_k 0}) q^{\tau_k} \right]. \quad (6.38)$$

After dividing each site weight over the four surrounding bonds, this becomes

$$Z_\sigma = \left[ \prod_{i=1}^N \sum_{\tau_i=0}^1 \right] \left[ \prod_{\langle ij \rangle} \exp(V\delta_{\tau_i 0}\delta_{\tau_j 0} + D(\delta_{\tau_i 0} + \delta_{\tau_j 0})/4) q^{(\tau_i + \tau_j)/4} \right]. \quad (6.39)$$

We compare the bond weights specified by this expression to the zero-field Ising weights  $e^{\pm K_I}$  where the sign depends on whether the site variables  $\tau_i$  and  $\tau_j$  are equal or not. The black circles represent Potts variables in one of the  $q$  states, the black square a Potts different state, and the open circles vacancies:

$\sigma_i$	$\sigma_j$	dilute Potts	Ising	
●	●	$q^{1/2}$	$e^{K_I}$	
●	■	$q^{1/2}$	$e^{K_I}$	(6.40)
●	○	$q^{1/4}e^{D/4}$	$e^{-K_I}$	
○	○	$e^{V+D/2}$	$e^{K_I}$	

The dilute Potts model becomes equivalent with the zero-field Ising model when the two types of bond weights are proportional, which holds if

$$K = 0; \quad D + 2V = \ln q. \quad (6.41)$$

The Ising-like critical point occurs at  $K_I = \ln(1 + \sqrt{2})/2$  or

$$K = 0; \quad V = 2 \ln(1 + \sqrt{2}); \quad D = -4 \ln(1 + \sqrt{2}) + \ln q. \quad (6.42)$$

The Ising transition is one between a disordered Potts phase and a phase dominated by vacancies. The Ising locus Eqs. (6.41) contains a first-order line ending in the Ising critical point. It is natural that this coexistence line and critical point extend to nonzero values of  $K$ , so that there exists a coexistence plane in the the  $(K, V, D)$  space, bounded on one side by an Ising critical line.

3. For  $D = 0$  and  $V = K$ , the vacancies become equivalent with the  $q$  Potts states, and the model becomes a  $(q + 1)$ -state Potts model. We illustrate this equivalence by listing the bond weights of the dilute  $q$ -state Potts model according to Eq. (6.2) and the bond weights of the  $(q + 1)$ -state Potts model without vacancies. The meaning of the symbols describing the site variables is the same as above:

$\sigma_i$	$\sigma_j$	dilute Potts	$(q + 1)$ -state Potts	
•	•	$e^K$	$e^K$	
•	■	1	1	(6.43)
•	○	$e^{D/4}$	1	
○	○	$e^{V+D/2}$	$e^K$	

The phase diagram of the  $q$ -state Potts model with vacancies therefore contains a  $(q + 1)$ -state Potts critical point at  $D = 0, V = K = \ln(1 + \sqrt{q + 1})$ .

4. For  $2K = 2V + D$  while  $D \ll 4K$ , the Potts ordered phase and the vacancy-dominated phase balance one another while their interfaces cost much energy. Therefore this condition describes a surface where these two phases coexist.

## 6.4.2 Numerical results

We include the vacancy-vacancy coupling in the transfer-matrix calculation defined in Sec. 6.2.1, and locate the Potts critical surface by solving for  $K$  at selected values of  $D, V$  and  $L$  in

$$X_h(K, V, D, L) = X_h, \quad (6.44)$$

where we make use of the exact result for  $X_h$  quoted in Sec. 6.1. In the vicinity of a critical point, there is only one relevant temperature field, but corrections to scaling may still be generated by irrelevant fields. As a consequence of these corrections, the solution for  $K$  will not precisely coincide with a critical point. The effects of an irrelevant scaling field

$u$  and a small temperature field  $t$ , due to a deviation  $K$  from its critical value  $K_c$ , are expressed by

$$X_h(K, V, D, L) = X_h + auL^{y_i} + btL^{y_{t1}} + \dots, \quad (6.45)$$

where  $a$  and  $b$  are unknown constants, and  $y_{t1}$  is the leading temperature exponent. For the present value  $q = 2 - \sqrt{2}$ , the corrections are dominated by the exponent  $y_i = -2$  which exceeds the second temperature exponent  $y_{t2}$ . The scaling behavior of the numerical solutions  $K_c(L)$  is found by expansion of the appropriate scaling function in the leading temperature field, which is in first order proportional to  $K - K_c$ :

$$K_c(L) = K_c + a_0L^{y_i - y_{t1}} + \dots. \quad (6.46)$$

The numerical results were found to be consistent with this formula, quite clearly so in parts of the critical surface that are not close to its boundary. Near the boundary, crossover effects become important. We determined critical points  $K_c$  for several values of  $V$  along six lines of constant  $D$  in the interval  $-6 \leq D \leq 4$  as shown in Fig. 6.3. For most of the critical surface, it proved to be easy to obtain critical points with an accuracy better than  $10^{-3}$  which is sufficient for the graphical presentation of the phase diagram provided in this subsection. Much better accuracies may be obtained if desired; for  $D \rightarrow -\infty$ , where the model reduced to the Potts model without vacancies, we found, using system sizes up to  $L = 11$ ,  $K_c = 0.568358$ , with an apparent accuracy of less than  $10^{-6}$ . This is consistent with the exact value  $K = \ln(1 + \sqrt{2 - \sqrt{2}})$ .

The plane of these  $q$ -state Potts transitions is bounded by a tricritical line for  $D > 0$ . Several points on the tricritical line were solved by means of the numerical technique described in Sec. 6.3.1 but including  $V$  as a parameter. These results indicate that, as expected, the tricritical line does connect to the  $(q + 1)$ -state critical point, as shown in Fig. 6.3.

We have also used the transfer-matrix technique to numerically investigate the Ising critical point at  $K = 0$ , described in the preceding subsection. Since Potts magnetic correlations are zero, the calculation of  $X_h$  yields only divergent results. The calculation of  $X_t$  yields results approaching the Ising magnetic dimension  $1/8$ . Indeed, the Ising magnetic correlations, corresponding e.g. with vacancy-vacancy correlations, are contained in the Potts nonmagnetic sector. We were thus able, by following the behavior of function  $X_t$ , to follow the Ising line emerging from the  $K = 0$  point. We observed that the discontinuous transition between the disordered Potts phase and the vacancy-dominated phase is accompanied by a minimum in the function  $X_t$ , with values  $< 1/8$  and decreasing with  $L$ . The Ising critical points can be approximated by requiring that the minimum in the function  $X_t$  tends to  $1/8$ . This yields results of a sufficient accuracy for the purpose of constructing Fig. 6.3.

For  $D < 0$ , the Potts critical surface is not bounded by a tricritical line, but by a critical end line located in the plane of first-order transitions.

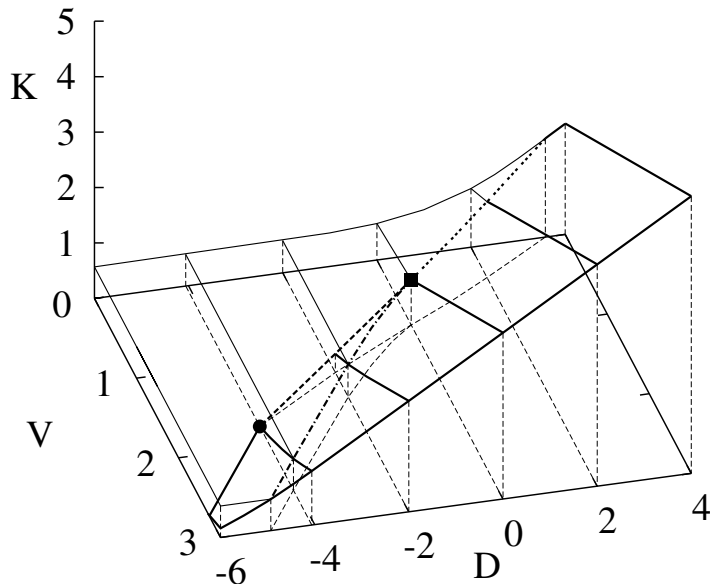


Figure 6.3: Phase diagram of the  $(2 - \sqrt{2})$ -state Potts model in the three-dimensional parameter space  $(V, D, K)$ . The plane of  $q$ -state Potts transitions (left hand side) is outlined by thin solid lines, and that of first-order transitions (right-hand side) by thick solid lines. These lines are shown at constant values  $D = -6, \ln(58 - 41\sqrt{2}) \approx -4.06, -2, 0, 2,$  and  $4$ . The planes of Potts and first-order transitions merge at a tricritical line (dotted, upper right) and at a critical end line (dash-dotted, lower left). At negative  $D$ , the first-order sheet is bounded by an Ising-like critical line on its low- $V$  side (thick dashed, lower left). The intersection of this line with the ground plane  $K = 0$  is indicated by  $\bullet$ . The critical end line, the Ising line and the tricritical Potts line meet at the  $(q + 1)$ -state critical point ( $\blacksquare$ ). This diagram is constructed on the basis of the arguments presented in Sec. 6.4.1 and the numerical results of Sec. 6.4.2.

## 6.5 Miscellaneous results

### 6.5.1 The Blume-Capel model and the dilute $q = 2$ Potts model

We first describe the relation between the Blume-Capel (BC) model [32], which is the spin-1 Ising model with variable fugacity of the zero spins, and the dilute  $q = 2$  Potts model. The reduced Hamiltonian of the BC model with nearest-neighbor interactions is

$$\mathcal{H}/k_{\text{B}}T = -K_{\text{BC}} \sum_{\langle ij \rangle} s_i s_j + D_{\text{BC}} \sum_k s_k^2, \quad (6.47)$$

where  $s_i = 0, \pm 1$ ,  $K_{\text{BC}}$  is the nearest-neighbor coupling, and  $D_{\text{BC}}$  acts as the chemical potential of the vacancies (the sites with  $s_i = 0$ ). This Hamiltonian assumes the form of Eq. (6.1) after the substitution  $\sigma_i \equiv (s_i + 3s_i^2)/2$ . This is most easily shown by comparing the weights per bond for the various values of the site variables. Out of the 9 possibilities, only 4 are independent. Only one quarter of the site energies  $-D_{\text{BC}}s_k^2$  and  $D\delta_{\sigma_k,0}$  belongs to a bond connecting to site  $k$ , because these energies are shared among 4 nearest-neighbor bonds. The comparison

$\sigma_i$	$\sigma_j$	dilute $q = 2$ Potts	BC	
●	●	$e^K$	$e^{K_{\text{BC}} - D_{\text{BC}}/2}$	
●	■	1	$e^{-K_{\text{BC}} - D_{\text{BC}}/2}$	(6.48)
●	○	$e^{D/4}$	$e^{-D_{\text{BC}}/4}$	
○	○	$e^{V+D/2}$	1	

shows that the bond weights differ only by a constant factor when

$$K = 2K_{\text{BC}}; \quad V = -K_{\text{BC}}; \quad D = 4K_{\text{BC}} + D_{\text{BC}}. \quad (6.49)$$

for which both models thus become equivalent. We note that, although the Blume-Capel model Eq. (6.47) does not contain explicit vacancy-vacancy couplings, the resulting value of  $V$  is nonzero in general. Furthermore, the mapping of the  $q = 2$  dilute Potts model in the full three-dimensional parameter space  $(K, D, V)$  on a spin-1 Ising model requires the introduction of an additional parameter in the Blume-Capel model, such as in the Blume-Emery-Griffiths model [33] which contains, in addition to Eq. (6.47), also a biquadratic coupling term proportional to  $\sum s_i^2 s_j^2$ . The Blume-Capel tricritical point is thus not the  $q=2$  tricritical point as determined in Sec. 6.3.1, but arguments of universality predict it to have the same critical exponents. Exact critical exponents in this universality class are known from the mapping of the dilute Potts models with plaquette interactions on a Gaussian model [34] and, in an independent way, from the exact solution of the hard-square model [35, 36].

We used the spin-1 representation to locate the tricritical point, because it enables us to perform transfer-matrix calculations up to finite size  $L = 16$ , while these calculations based on Eq. (6.5) are restricted to  $L \leq 12$ . The solutions of Eqs. (6.22) (with  $K$  and  $D$  replaced by  $K_{\text{BC}}$  and  $D_{\text{BC}}$ ) should, according to Eqs. (6.27) and (6.28), display finite-size dependences proportional to  $L^{y_i - y_{t_1}}$  and  $L^{y_i - y_{t_2}}$ , i.e.,  $L^{-14/5}$  and  $L^{-9/5}$  if we take  $y_i = y_{t_3} = 2 - X_{1,4} = -1$ . However, corrections proportional to  $L^{-9/5}$  were not observed. Three-point fits (see Ref. [20]) to the solutions of Eqs. (6.22) yielded a correction exponent close to  $-2.81$  with an uncertainty of about  $10^{-2}$ . An explanation may be that the amplitudes  $a_t$  and  $u_t$  in Eq. (6.25) vanish, which is the case if the derivatives of the scaling function  $X_t$  to the temperature-like fields  $t$  and  $u$  are zero.

We thus fixed the leading correction exponent as  $-14/5$  in order to extrapolate the solutions of Eqs. (6.22). This leads to a sequence of iterated estimates that can again be subjected to iterated fits. These suggest that the leading finite-size dependence of the iterated fits is as  $L^{-19/5}$  (where the exponent is equal to  $2y_i - y_{t_1}$ ) or  $L^{-4}$ . The final

estimates of  $K_f$  and  $D_f$  are based in iterated fits using the latter exponents, and on fits in which the finite-size exponents is left free. The numerical errors are estimated from the differences between these three types of fits, and on the differences between the results for subsequent finite sizes. We thus obtain the final estimates for the Blume-Capel tricritical point at  $K_{\text{BC}} = 1.6431759(1)$ ,  $D_{\text{BC}} = 3.2301797(2)$ . These numbers are consistent with the literature values [37]  $K_{\text{BC}} = 1.64(1)$ ,  $D_{\text{BC}} = 3.22(2)$ , and are sufficiently accurate for the Monte Carlo analyses mentioned in Sec. 6.1. The finite-size results for the tricritical vacancy density were extrapolated by similar means as used in Sec. 6.3.1. This yielded  $\rho = 0.4549506(2)$ .

We did not try to locate the critical fixed point of the Blume-Capel model because of the vanishing amplitude [7,27] of the irrelevant field. In view of the research of constrained systems, it is still desirable to obtain accurate numbers for the location of a critical point of a system subject to such a constraint. For this purpose we have located the Blume-Capel critical point at Ising coupling  $K_{\text{BC}} = 1$  by solving for  $D_{\text{BC}}$  in the equation for the scaled magnetic correlation length as indicated in Eq. (6.15), using the Ising magnetic dimension  $X_h = 1/8$ . The expected finite-size corrections have exponents equal to  $y_i - y_{t_1} = -3$  and next negative integers  $-4$ ,  $-5$ , and so on. We applied iterated fits as defined in Ref. [20], using a few of these exponents. To test the consistency of this procedure, we varied the procedure by varying the number of iteration steps and by leaving the exponent free in the last step. Our final estimate for the critical point at  $K_{\text{BC}} = 1$  is  $D_{\text{BC}} = 1.70271780(3)$ .

### 6.5.2 Geometric tricritical fixed points for noninteger $q$

We study the fractal properties of percolation clusters constructed at the percolation threshold of tricritical Potts clusters. For integer  $q$ , this problem was already addressed in Ref. [15]. It was found that, when bonds are added with probability  $p$  between neighboring site variables in the same Potts state, the percolation threshold occurs at a value *smaller* than the random-cluster probability  $p_{rc} = 1 - e^{-K}$ . In contrast, the percolation threshold at Potts criticality lies precisely at  $p_{rc}$  [38]. This is natural because the so-called red-bond exponent [38], which governs the renormalization flow in the  $p$ -direction, is relevant on the Potts critical branch, but becomes irrelevant on the tricritical branch. On the tricritical branch, the random-cluster point thus no longer qualifies as a fixed point of this percolation problem. The renormalization flow at the random-cluster point is attracted by a stable fixed point at  $p > p_{rc}$ . A new unstable fixed point, called the geometric fixed point, appears at  $p < p_{rc}$ , with critical exponents that are conjectured in Ref. [15], mainly on the basis of empirical evidence that the universality class of the geometric fixed point on the tricritical line corresponds with that of the random-cluster fixed point on the critical line with the same conformal anomaly, i.e., with the same value of the number  $m$  defined in Sec. 6.1. These two fixed points therefore share the same exponents; the conjecture specifies the correspondence between the two sets, which we shall outline here for the magnetic dimensions  $X_h$  and the red-bond dimension  $X_p$ . To distinguish between the geometric and the random-cluster fixed points, we add superscripts ( $g$ ) and ( $r$ ) respectively. For the

random-cluster fixed point these dimensions are, as a function of  $g$

$$X_h^{(r)} = \frac{(g-2)(6-g)}{8g}, \quad X_p^{(r)} = \frac{(3g-4)(g+4)}{8g}, \quad (6.50)$$

where the expression for  $X_h$  is taken from Sec. 6.1, and that for  $X_p$  was obtained [38] by means of Coulomb gas methods. Consider a Potts model on the critical branch with a coupling constant  $g$  and one on the tricritical branch with a coupling constant  $g'$ . From the relations between  $g$  and  $m$  listed in Sec. 6.1, it follows that the two models are parametrized by the same number  $m$  when  $gg' = 16$ . Therefore, the substitution of  $g$  by  $16/g'$  in Eqs. (6.50) leads to some scaling dimensions on the other branch. The conjecture in Ref. [15] is that these are just the corresponding dimensions at the geometric fixed point. This conjecture supplements a second conjecture [15, 39], in which the superscripts  $g$  and  $r$  are interchanged. Note that the partition sum does not depend on the percolation probability  $p$ , so that  $m$  must be independent of  $p$ . The substitution leads to

$$X_h^{(g)} = \frac{(8-g')(3g'-8)}{32g'}, \quad X_p^{(g)} = \frac{(12-g')(g'+4)}{8g'}. \quad (6.51)$$

Since Eq. (6.51) has only been tested for tricritical Potts models with an integer number of states, we investigate whether it also applies to Potts models with non-integer  $q$ .

In the absence of discrete Potts variables, we choose the random-cluster decomposition as a starting point, while preserving its bond variables. These have a probability  $p_{rc}$  between two Potts variables in the same state; one can thus form percolation clusters with a bond probability  $p < p_{rc}$  by inserting a percolation bond with probability  $p/p_{rc}$  for each random-cluster bond that is present, and no percolation bond otherwise. These percolation bonds define a percolation problem that is, for  $p < p_{rc}$ , different from the random-cluster model. Naturally the investigation of this percolation problem still relies on the Monte Carlo simulation of the random-cluster model.

We performed such simulations, while constructing percolation clusters for a range of values of  $p \leq p_{rc}$ . We sampled the distribution of the cluster sizes and thus obtained the average squared cluster size

$$S^{(2)} = \left\langle \sum_{i=1}^{n_c} c_i^2 \right\rangle \quad (6.52)$$

and the dimensionless ratio

$$Q = \frac{\langle \sum_{i=1}^{n_c} c_i^2 \rangle^2}{\langle 3(\sum_{i=1}^{n_c} c_i^2)^2 - 2 \sum_{i=1}^{n_c} c_i^4 \rangle}, \quad (6.53)$$

where  $c_i$  is the size of the  $i$ th cluster,  $n_c$  the number of clusters. Near the percolation threshold at  $p = p_c$ , the quantity  $Q$  scales as

$$Q = Q_0 + \sum_{k=1,2,\dots} a_k (p - p_c)^k L^{ky_p^{(g)}} + \sum_{j=1,2,\dots} b_j L^{y_j} + c(p - p_c) L^{y_p^{(g)} + y_1} + d(p - p_c)^2 L^{y_p^{(g)}} + \dots, \quad (6.54)$$

and  $S^{(2)}$  scales as

$$S^{(2)} = L^{-2X_h^{(g)}} \{a_0 + a_1(p-p_c)L^{y_p^{(g)}} + a_2(p-p_c)^2 L^{2y_p^{(g)}} + \dots + L^{y_1} [b_0 + b_1(p-p_c)L^{y_p^{(g)}} + \dots]\}, \quad (6.55)$$

where the  $y_j$  ( $j = 1, 2, \dots$ ) are negative exponents describing corrections that will be discussed later, and the  $a_i$ , the  $b_i$ ,  $c$ , and  $d$  are unknown amplitudes.

The ratio  $Q$  is a useful quantity to locate phase transitions and to determine the associated temperature-like exponent. From Eq. (6.54) one finds that the  $Q$  versus  $p$  curves for different values of  $L$  tend to intersect at values approaching  $p = p_c$  for large  $L$ . Moreover, the slopes of these curves behave as  $L^{y_p^{(g)}}$  which allows the estimation of  $y_p^{(g)}$ .

The simulations took place for four values of  $q$ , *viz.*  $q = 2 \pm \sqrt{2}$  and  $q = 2 \pm \sqrt{2 - \sqrt{2}}$ . The number of vacancies was conserved as described in Sec. 6.2.2. Since the number of vacancies in a simulation is restricted to an integer, the result for a given density was obtained by a weighted averaging over two simulations with a different number of vacancies. The simulations for  $q = 2 - \sqrt{2}$  used local updates and were more time consuming than those for the other values of  $q$ , and thus restricted to relatively small system sizes. The data for the system sizes, simulation lengths and intervals of  $p$  are summarized in Table 6.6.

Table 6.6: Parameters describing the simulations of the tricritical Potts models. For each value of  $q$  we list the smallest and largest system sizes that were simulated, and the number  $n_L$  of system sizes in these ranges. We also show the range of  $p$  and the number  $n_p$  of points in this interval used for the simulations, and the number of samples  $n_s$  taken for the smallest and largest system sizes. The number of samples for all system sizes up to  $L = 84$  was equal to that for  $L_{\min}$  in lines 2 and 3, and similar for those up to  $L = 96$  in line 4. For larger system sizes, the number of samples decreases gradually to that for  $L_{\max}$ , except for the system of the first line. The last column specifies the numbers of the Monte Carlo moves taken between subsequent samples. S stands for a site update, B for a bond update, FC for a full cluster decomposition, and M for a Metropolis sweep through the whole lattice.

$q$	$L_{\max}$	$n_L$	range of $p$	$n_p$	$n_s(L_{\min})$	$n_s(L_{\max})$	update inter.
$2 - \sqrt{2}$	36	11	0.56–0.61	6	$1 \times 10^8$	$1 \times 10^8$	$\frac{L^2}{5}S + \frac{L^2}{3}B$
1.234...	160	17	0.58–0.60	5	$6 \times 10^7$	$4 \times 10^6$	$\frac{L}{5}$ (FC + M)
2.765...	200	20	0.61–0.645	8	$12 \times 10^7$	$7 \times 10^6$	$\frac{L}{5}$ (FC + M)
$2 + \sqrt{2}$	160	17	0.63–0.68	6	$1 \times 10^8$	$8 \times 10^6$	$\frac{L}{5}$ (FC + M)

The results for the dimensionless ratio  $Q$  are shown in Fig. 6.4 for the case  $q = 2 - \sqrt{2 - \sqrt{2}}$ . The intersections reveal the location of the geometric fixed point. A more accurate location was determined by a least-squares analysis according to Eq. (6.54). Similar analyses were performed for the other three values of  $q$ . These fits included up to three coefficients  $a_k$ , and three or four coefficients  $b_j$ , depending on the  $\chi^2$  criterion. The corresponding correction exponents  $y_j$  were fixed equal to the third temperature exponent, twice this number, and/or equal to the negative integers  $-1, -2, -3$ , etc., such that largest (closest to 0) exponents appear first.

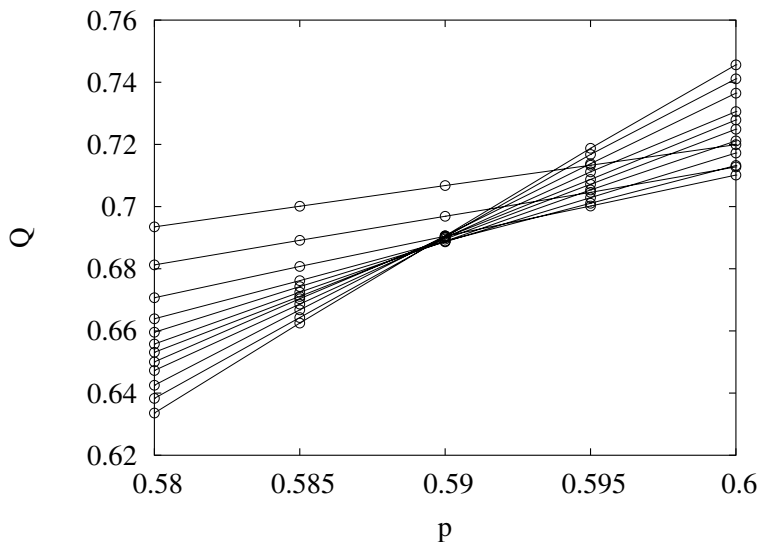


Figure 6.4: Determination of the geometric fixed point of the tricritical ( $2 - \sqrt{2 - \sqrt{2}} = 1.234\dots$ )-state dilute Potts model. The data shown apply to 12 system sizes in the range  $6 \leq L \leq 84$ . The lines connect data points with the same  $L$ . Their slopes increase with  $L$ , and their intersections reveal the location of the unstable fixed point, i.e., the percolation threshold. The error bars of the data points do not exceed the line thickness.

Table 6.7: Geometric fixed points of several tricritical Potts models with a noninteger number of states  $q$ . The numerical values of the percolation threshold  $p_c$ , the red-bond exponent  $y_p^{(g)}$  and the magnetic dimension  $X_h^{(g)}$  at the geometric fixed point are obtained by fitting formulas given in the text to the simulation data. The table also lists the conjectured exact values of  $y_p^{(g)}$  and  $X_h^{(g)}$  (see text). The results for  $p_c$  are listed as  $p_{c_i}$  where  $i = 1, 2$  refer to different fits:  $p_{c_1}$  and  $y_p^{(g)}$  are obtained from fits to the ratio  $Q$  in which  $y_p^{(g)}$  appears as a free parameter, and  $p_{c_2}$  is obtained with  $y_p^{(g)}$  fixed at its conjectured value. The magnetic exponent  $X_h^{(g)}$  is obtained by a fit to the average squared cluster size with  $y_p^{(g)}$  fixed at the conjectured value, and  $p_c$  fixed at  $p_{c_2}$ . Fits that leave  $p_c$  as a free parameter lead to consistent results but with slightly larger error bars.

$q$	$y_p^{(g)}$	$y_p^{(g)}(e)$	$X_h^{(g)}$	$X_h^{(g)}(e)$	$p_{c_1}$	$p_{c_2}$
$2 - \sqrt{2}$	0.59 (4)	$\frac{105}{176}$	0.12 (1)	$\frac{85}{704}$	0.581 (5)	0.581 (4)
1.234...	0.511 (8)	$\frac{115}{224}$	0.125 (2)	$\frac{341}{2688}$	0.5906 (5)	0.5906 (4)
2.765...	0.334 (10)	$\frac{201}{608}$	0.135 (3)	$\frac{325}{2432}$	0.6300 (5)	0.6300 (4)
$2 + \sqrt{2}$	0.225 (8)	$\frac{11}{48}$	0.136 (5)	$\frac{77}{576}$	0.6604 (6)	0.6601 (4)

In order to reduce the residual  $\chi^2$  to acceptable values, the smallest system sizes  $L < 6$  had to be discarded for all four values of  $q$ . Furthermore, we have fitted an expression of the form Eq. (6.55) to the simulation data for  $S^{(2)}$  which is, except for a factor  $L^2$ , a susceptibility-like quantity, using a similar set of finite-size corrections as for  $Q$ . These fits allow the determination of  $X_h^{(g)}$ . The numerical results for the exponents, which are included in Table 6.7, are in a good agreement with the exact values predicted by Eqs. (6.51).

## 6.6 Conclusion

In line with previous work [40] we observe that finite-size scaling analysis based on transfer-matrix calculations provides an efficient tool for the analysis of critical phenomena and the determination of phase diagrams of two dimensional models, even though the accessible range of finite sizes is quite limited. This limitation is compensated by the high numerical accuracy of the transfer-matrix results for the eigenvalues, which allow the application of iterated fitting procedures, especially when the scaling dimensions are known from other sources. The latter point is relevant for an evaluation of the present transfer-matrix analysis of the dilute Potts model. Two points of view are possible. First, one may focus on the question whether the renormalization description of Nienhuis et al. [1], and the exact results for the exponents based on arguments of universality, are applicable to the present model described by Eq. (6.1). While this seems plausible, rigorous evidence is not available so that numerical tests are justified. Our analysis does indeed provide ample numerical evidence. We note that, if the expressions for the scaling dimensions  $X_h$  and  $X_t$  listed in Sec. 6.1 were incorrect, that this would be revealed in the fitting procedures for the fixed points by corrections decaying slower than expected, as mentioned in Sec. 6.3.1, unless the differences with the true exponents would accidentally be very small. Furthermore, also the consistency of the results for the conformal anomaly, listed in Table 6.5, with the existing theory supports the assumptions made. Our results for  $c$  supplement those already given in Ref. [28], in particular most results for the tricritical branch are new. Here we add the comment that the format of Ref. [28] precluded a discussion of the numerical errors. In one case, this led to a somewhat misleading result, namely the entry for the  $q = 4$  Potts model without vacancies in Table II of Ref. [28]. The finite-size data for the conformal anomaly are poorly convergent because of logarithmic corrections induced by the second temperature field which is marginal at  $q = 4$ . However, the fit applied to those finite-size data produced an erratic numerical result that was much closer to the theoretical value of  $c$  than what one could have expected in view of the actual numerical accuracy. Therefore the agreement for  $q = 4$  looked better than it actually was. The present analysis of  $c$  at the estimated fixed point does not noticeably suffer from such numerical problems, and does indeed produce a result (see Table 6.5) very close to the expected value  $c = 1$ . As another confirmation, the results for the fixed line and for the phase diagram of the  $q = 2 - \sqrt{2}$  model, are in a complete qualitative agreement with the results presented in Ref. [1]. We also note that this applies as well to the renormalization analysis of the Blume-Emery-Griffiths model [33], which was worked out in considerable detail by Berker

and Wortis [41].

As a second point of view, one may accept the Potts renormalization scenario and the literature values of the scaling dimensions as true for the present model, and thus interpret our results in terms of relatively accurate information on the phase diagram and the location of what serves effectively as a line of fixed points in the phase diagram in the  $(q, K, D)$  parameter space, including a line of tricritical transitions. These results are well applicable in Monte Carlo investigations of tricritical Potts models and  $q \approx 4$  Potts models, including numerical analysis of the Fisher renormalization phenomenon. Preliminary results have already been used [11, 14, 15]. Minor differences with respect to the values quoted in the present work appear because data for larger system sizes are included here.

# Bibliography

- [1] B. Nienhuis, A. N. Berker, E. K. Riedel and M. Schick, Phys. Rev. Lett. **43**, 737 (1979).
- [2] R. J. Baxter, J. Phys. C **6**, L445 (1973).
- [3] M. Nauenberg and D. J. Scalapino, Phys. Rev. Lett. **44**, 837 (1980).
- [4] J. L. Cardy, M. Nauenberg and D. J. Scalapino, Phys. Rev. B. **22**, 2560 (1980).
- [5] J. Salas and A. D. Sokal, J. Stat. Phys. **88**, 567 (1997).
- [6] P. W. Kasteleyn and C. M. Fortuin, J. Phys. Soc. Jpn. Suppl. **26**, 11 (1969); C. M. Fortuin and P. W. Kasteleyn, Physica **57**, 536 (1972).
- [7] B. Nienhuis, in *Phase Transitions and Critical Phenomena*, edited by C. Domb and J. L. Lebowitz (Academic, New York, 1987), Vol. **11**.
- [8] J. L. Cardy, in *Phase Transitions and Critical Phenomena*, edited by C. Domb and J. L. Lebowitz (Academic, New York, 1987), Vol. **11**.
- [9] P. Grassberger, J. Phys. A **25**, 5475 (1992).
- [10] P. Grassberger, Physica A **262**, 251 (1999).
- [11] Y. Deng, H. W. J. Blöte and B. Nienhuis, Phys. Rev. E **69**, 026114 (2004).
- [12] L. Chim, Int. J. Mod. Phys. A **11**, 4491 (1996).
- [13] I. Affleck, J. Phys. A **33**, 6473 (2000).
- [14] Y. Deng and H. W. J. Blöte, Phys. Rev. E **70**, 035107 (2004).
- [15] Y. Deng, H.W.J. Blöte and B. Nienhuis, Phys. Rev. E **69**, 026123 (2004).
- [16] B. Nienhuis, Physica A **177**, 109 (1991).
- [17] M. E. Fisher, Phys. Rev. **176**, 257 (1968).

- [18] J. R. Heringa and H. W. J. Blöte, *Physica A* **232**, 369 (1996); *Phys. Rev. E* **57**, 4976 (1998).
- [19] M. P. Nightingale, *Phys. Lett. A* **59**, 486 (1977); *Proc. K. Ned. Akad. Wet., Ser. B: Phys. Sci.* **82**, 235 (1979).
- [20] H. W. J. Blöte and M. P. Nightingale, *Physica A* **112**, 405 (1982); and in *Finite-Size Scaling*, edited by J. L. Cardy, (North Holland, Amsterdam, 1988).
- [21] J. L. Cardy, *J. Phys. A* **17**, L358 (1984).
- [22] M. Sweeny, *Phys. Rev. B* **27**, 4445 (1983).
- [23] F. Gliozzi, *Phys. Rev. E* **66**, 016115 (2002).
- [24] L. Chayes and J. Machta, *Physica A* **254**, 477 (1998).
- [25] X. Qian, Y. Deng and H. W. J. Blöte, *Phys. Rev. E* **71**, 016709 (2005).
- [26] X. Qian, Y. Deng and H. W. J. Blöte, *Phys. Rev. B* **71**, 144303 (2005).
- [27] H. W. J. Blöte and M. P. M. den Nijs, *Phys. Rev. B* **37**, 1766 (1988).
- [28] H. W. J. Blöte, J. L. Cardy and M. P. Nightingale, *Phys. Rev. Lett.* **56**, 742 (1986).
- [29] I. Affleck, *Phys. Rev. Lett.* **56**, 746 (1986).
- [30] D. Friedan, Z. Qiu, and S. Shenker, *Phys. Rev. Lett.* **52**, 1575 (1984).
- [31] R. B. Potts, *Proc. Cambridge. Philos. Soc.* **48**, 106 (1952).
- [32] M. Blume, *Phys. Rev.* **141**, 517 (1966); H. W. Capel, *Physica A* **32**, 966 (1966).
- [33] M. Blume, V. J. Emery and R. B. Griffiths. *Phys. Rev. A* **4**, 1071 (1971).
- [34] B. Nienhuis, *J. Phys. A* **15**, 199 (1982).
- [35] R. J. Baxter, *J. Stat. Phys.* **26**, 427 (1981).
- [36] D. A. Huse, *Phys. Rev. Lett.* **49**, 1121 (1982).
- [37] P. D. Beale, *Phys. Rev. B* **33**, 1717 (1986).
- [38] A. Coniglio and W. Klein, *J. Phys. A* **13**, 2775 (1980); A. Coniglio, *Phys. Rev. Lett.* **62**, 3054 (1989).
- [39] W. Janke and A. M. J. Schakel, *Nucl. Phys. B* **700**, 385 (2004);

- [40] For reviews, see e.g. M. P. Nightingale, in *Finite-Size Scaling and Numerical Simulation of Statistical Systems*, edited by V. Privman (World Scientific, Singapore, 1990); and M. N. Barber, in *Phase Transitions and Critical Phenomena*, edited by C. Domb and J. L. Lebowitz (Academic, New York, 1983), Vol. **8**.
- [41] A. N. Berker and M. Wortis, Phys. Rev. B **14**, 4946 (1976) and references therein.

## Appendix A: Coding the connectivities

The construction of the transfer matrix requires a ‘coding’ of the relevant degrees of freedom at the open end of the cylinder, by means of integers  $1, 2, \dots$  that will serve as a transfer-matrix index. This code specifies which sites of the  $n$ th layer are vacant, and how the remaining sites are mutually connected by some path of bonds in rows 1 to  $n$ . Since we are interested in the magnetic correlation function, which in the language of the random-cluster model is the probability that two sites belong to the same cluster, we use connectivities of the ‘magnetic’ type which, in addition, specifies which sites of row  $n$  are still connected to a site in row 1. These connectivities satisfy a ‘well-nestedness’ property which says that the sites labeled  $1, 2, \dots, L$  on row  $n$  obey the following rule: if site  $i$  is connected to site  $k$ , and site  $j$  is connected to site  $l$  while  $i < j < k < l$ , all four sites must be connected. Since a complete definition of the coding of the general connectivities is somewhat elaborate, we make use of some definitions already given in Ref. [20]. There, an  $L$ -point connectivity is represented by a row of  $L$  integers  $i_1, i_2, \dots, i_L$ , such that sites are represented by equal integers if they are connected, and by different integers if not. A subset of sites connected to a ‘ghost site’ (which are not necessarily well-nested) were represented by the special integer 0. These connectivities were coded by an integer  $\tau(i_1, i_2, \dots, i_L)$  defined in Ref. [20]. Since one can alternatively interpret the zeroes in the row  $i_1, i_2, \dots, i_L$  as vacancies, it follows that the same coding  $\tau(i_1, i_2, \dots, i_L)$  applies to nonmagnetic connectivities with vacancies. The number of such connectivities on  $L$  sites is denoted  $d_L$ , also given in Ref. [20]. Here we consider the more general problem of coding the connectivities with well-nested magnetic sites (labeled by  $-1$ ) as well as vacancies (labeled by 0). First, we code the positions of the magnetic sites by means of a binary number  $m = 0, 1, \dots, 2^L - 1$ , where the binary digit 1 denotes a magnetic site. The magnetic sites divide the remaining sites in  $g(m)$  groups such that two sites in different groups are not connected because of the well-nestedness property. Let there be  $t(m, j)$  sites in the  $j$ th group. There are thus

$$h_m \equiv d_{t(m,1)} d_{t(m,2)} \cdots d_{t(m,g(m))} \quad (6.56)$$

connectivities with magnetic subcode  $m$ , and the total number of general connectivities is

$$G_L = \sum_{m=0}^{2^L-1} h_m. \quad (6.57)$$

To assign a unique integer to each of these connectivities, we need to specify an ‘ordering’ of the connectivities. In addition to the ordering defined in Ref. [20], we order the magnetic subcode according to the value of  $m$ . Thus a general connectivity  $i_1, i_2, \dots, i_L$  with magnetic subcode  $m(i_1, i_2, \dots, i_L)$  is coded by the integer

$$\gamma(i_1, i_2, \dots, i_L) \equiv 1 + \sum_{k=0}^{m-1} h_k + \sum_{l=1}^{g(m)} (\tau_l - 1) \prod_{j=2}^l d_j, \quad (6.58)$$

where  $\tau_l$  is the code (using the definition in Ref. [20]) for the  $l$ th group of nonmagnetic sites. A decoding algorithm was constructed on the basis of essentially the same ideas.

## Appendix B: Construction of the transfer matrix

Consider a system on a cylinder with a length of  $n$  circular rows. We denote the variables in row  $j$ , bond as well as site variables, by  $\vec{s}_j$ . Its partition sum is written in the form

$$Z^{(n)} = \sum_{\vec{s}_1, \dots, \vec{s}_n} W_n(\vec{s}_1, \vec{s}_2, \dots, \vec{s}_n) \quad (6.59)$$

with  $W_n(\vec{s}_1, \vec{s}_2, \dots, \vec{s}_n) \equiv \exp[-\mathcal{H}_n(\vec{s}_1, \vec{s}_2, \dots, \vec{s}_n)/k_B T]$  which denotes the Boltzmann factor of the given configuration of variables, including the weights of all bonds, sites and components. Let  $\kappa_n$  be the connectivity on row  $n$ . It is, in principle, a function of all the variables  $\vec{s}_j$ ,  $j = 1, 2, \dots, n$ . We divide  $Z^{(n)}$  in contributions for different values of  $\kappa_n$ :

$$Z_\alpha^{(n)} = \sum_{\vec{s}_1, \dots, \vec{s}_n} \delta_{\alpha, \kappa_n(\vec{s}_1, \dots, \vec{s}_n)} W_n(\vec{s}_1, \vec{s}_2, \dots, \vec{s}_n) \quad (6.60)$$

with

$$Z^{(n)} = \sum_{\alpha=1}^{G_L} Z_\alpha^{(n)}. \quad (6.61)$$

Similarly we have

$$Z_\alpha^{(n+1)} = \sum_{\vec{s}_1, \dots, \vec{s}_{n+1}} \delta_{\alpha, \kappa_{n+1}(\vec{s}_1, \dots, \vec{s}_{n+1})} W_{n+1}(\vec{s}_1, \vec{s}_2, \dots, \vec{s}_{n+1}). \quad (6.62)$$

Here we may substitute

$$W_{n+1} = W_n w(\kappa_n, \vec{s}_{n+1}), \quad (6.63)$$

where  $w$  denotes the weight of the newly appended row, which accounts for the weights of the site variables and the bond variables, and the change in the number of components. Furthermore we can substitute

$$\kappa_{n+1} = \mu(\kappa_n, \vec{s}_{n+1}) \quad (6.64)$$

which expresses that the connectivity on row  $n+1$  depends only on that on row  $n$  and on the variables in the appended row. Thus

$$Z_\alpha^{(n+1)} = \sum_{\vec{s}_1, \dots, \vec{s}_{n+1}} \delta_{\alpha, \mu(\kappa_n, \vec{s}_{n+1})} W_n(\vec{s}_1, \dots, \vec{s}_n) w(\kappa_n, \vec{s}_{n+1}). \quad (6.65)$$

We may insert a factor  $\sum_{\beta=1}^{G_L} \delta_{\beta, \kappa_n(\vec{s}_1, \dots, \vec{s}_n)} = 1$  which leads to

$$Z_\alpha^{(n+1)} = \sum_{\beta=1}^{G_L} \sum_{\vec{s}_1, \dots, \vec{s}_n} \delta_{\beta, \kappa_n(\vec{s}_1, \dots, \vec{s}_n)} W_n(\vec{s}_1, \vec{s}_2, \dots, \vec{s}_n) \sum_{\vec{s}_{n+1}} \delta_{\alpha, \mu(\beta, \vec{s}_{n+1})} w(\beta, \vec{s}_{n+1}). \quad (6.66)$$

The middle part of this expression is  $Z_\beta^{(n)}$ , and the last part is the transfer matrix:

$$T_{\alpha\beta} \equiv \sum_{\vec{s}} \delta_{\alpha, \mu(\beta, \vec{s})} w(\beta, \vec{s}), \quad (6.67)$$

so that we may write the recursion for the restricted partition sum as

$$Z_\alpha^{(n+1)} = \sum_\beta T_{\alpha\beta} Z_\beta^{(n)}. \quad (6.68)$$

The algorithm that performs a multiplication of a vector by the transfer matrix forms the main ingredient for the calculation of a few of the leading eigenvalues of  $T_{\alpha\beta}$ .

To enable calculations for system as large as possible, the transfer matrix is decomposed into  $2L$  sparse matrices, each of which accounts for one bond variable, while  $L$  of these also account for appending a new site variable. This sparse-matrix decomposition leads to a very significant reduction of the required computer time and memory. The decomposition is the same as for the nearest-neighbor Potts model without vacancies, which was described in Ref. [20]. The weights associated with the vertical bonds (which include those of the new sites appended to the cylinder) and the horizontal bonds (which may close a loop, so that their weights depend on whether or not the sites are already connected) are given in Fig. 6.5. These sparse matrices are defined such that they do not only account for

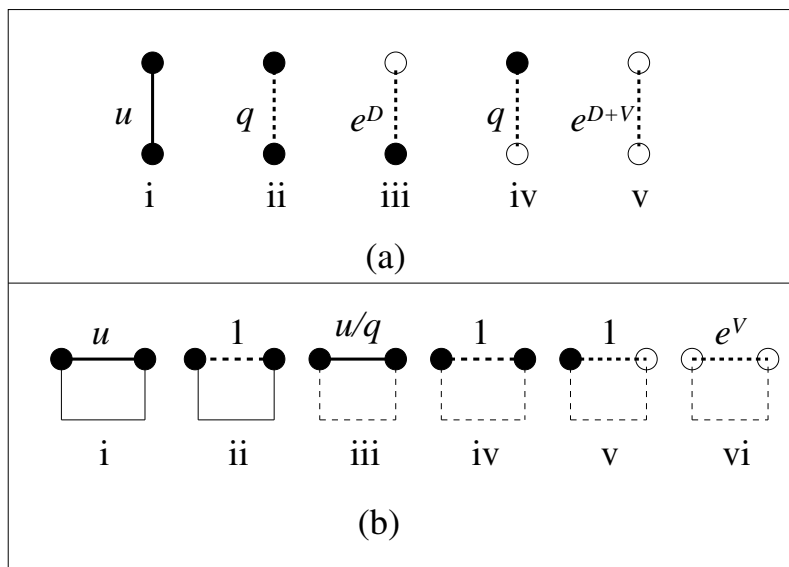


Figure 6.5: Weights of the vertical and horizontal bonds as they appear in the sparse transfer-matrix technique. New sites are appended in the upper row, which thus also accounts for the site weights  $q$  and  $e^D$ .

the weight of a particular bond, they also permute the vertices in such way that only two different sparse matrices remain, one for the vertical bonds and one for the horizontal ones.

# Chapter 7

## Equivalent-neighbor Potts models in two dimensions

We investigate the ordering transitions in the two-dimensional  $q = 3$  and 4 Potts models with medium-range interactions by means of Monte Carlo simulations. We locate the phase transitions for several interaction ranges as expressed by the number  $z$  of equivalent neighbors. For not too large  $z$ , the transitions fit well in the universality classes of the short-range Potts models. However, at longer ranges the transitions become discontinuous. For  $q = 3$  we locate a tricritical point separating the continuous and discontinuous transitions near  $z = 80$ , and a critical fixed point near  $z = 8$ . For  $q = 4$  the transition becomes discontinuous for  $z \gtrsim 16$  and larger.

### 7.1 Introduction

In phase transitions, the range of the interactions plays an important role. Models with interactions decaying as a negative power  $-p$  of the distance appear to display a considerable variety of universality classes as a function of  $p$ , and as a function of the dimensionality [1–3]. For large  $p$  the interactions decay fast and one finds the usual short-range universal behavior. For sufficiently small  $p$  the interactions decay only slowly and one finds mean-field-like critical behavior. For intermediate values of  $p$  the critical exponents may depend continuously on  $p$ .

A different way to modify the range of the interactions is specified in the so-called equivalent-neighbor models, in which the pair interactions are constant up to a range  $R(\propto z^{1/d}$ ,  $d$  is dimensionality) and then abruptly fall to zero. For  $R \rightarrow \infty$ , the equivalent-neighbor model reduces to the mean field model; for sufficiently small  $R$  it will naturally display the usual short-range universal behavior. But it seems that the analogy with the case of power-law decay of interactions ends here. Medium-range Ising models, with interactions of a finite but sufficiently large range display uniform crossover from the vicinity of the mean-field fixed point at  $R = \infty$  to the Ising fixed point at small  $R$  [4]. The model belongs to the Ising universality class for all finite  $R$ . The scaling field parametrizing the

crossover phenomenon is the irrelevant Ising temperature field. The flow diagram for the Ising model is shown in Fig. 7.1.

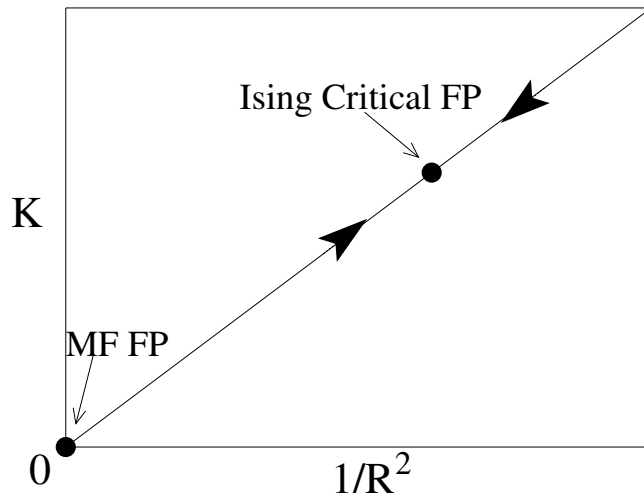


Figure 7.1: Schematic renormalization flow diagram along the line of phase transitions of the Ising model with medium-range interactions. The critical line connecting the mean-field (MF) fixed point and the Ising fixed point is parametrized by the range  $R$  of the interactions. The finiteness of the interaction range is relevant at the MF fixed point and leads to crossover to the Ising fixed point.

The question naturally arises whether such a uniform crossover also occurs in the more general context of the  $q$ -state Potts model, in particular for  $q > 2$ . Another possibility is suggested by the renormalization scenario for the two-dimensional dilute  $q$ -state Potts model [5] with  $0 < q \leq 4$ . In this context the leading irrelevant field, parameterizing the critical surface, is controlled by the activity of the vacancies. When the latter parameter is increased, while adjusting the Potts coupling to maintain criticality, a threshold occurs where the model becomes tricritical. Beyond the threshold the ordering transition becomes discontinuous. If the parameters controlling the irrelevant fields of the dilute and the equivalent-neighbor Potts models are sufficiently analogous for  $q > 2$ , then this scenario, i.e., a tricritical point separating a range of critical and a range of first-order transitions, might also occur for the equivalent-neighbor Potts model.

This possibility is in line with recent work of Biskup et al. [6] which concerns  $q = 3$  models with interactions whose strength decays smoothly to zero at infinite range. For sufficiently slow decay, a first-order transition is found. In order to investigate the similar question for systems with a strictly finite range of interactions, we consider the Potts model with a variable interaction range  $R$ , described by the Hamiltonian

$$\mathcal{H}/k_{\text{B}}T = -K \sum_{i < j} \theta(R - r_{ij}) \delta_{\sigma_i, \sigma_j} \quad (\sigma_i = 1, \dots, q), \quad (7.1)$$

where the Potts variables  $\sigma_i$  carry indices that refer to the sites of a lattice with periodic boundary conditions. Interacting pairs of sites are selected by the step function  $\theta$  (defined by  $\theta(x) = 1$  for  $x \geq 0$  and  $\theta(x) = 0$  for  $x < 0$ ). Thus, interactions of strength  $K$  occur with all neighbors within a distance  $R$ . Equivalently, we may specify the interaction range  $R$  by the number  $z$  of equivalent-neighbors interacting with a spin on a given site.

In particular we investigate the  $q = 3$  and the  $q = 4$  Potts model on the square lattice. This task is performed numerically, by means of a cluster Monte Carlo method [7] that is especially suitable for this problem, because it suppresses critical slowing down, and the required computer time is almost independent of the range  $R$ . During the simulations we sampled the densities  $\rho_i$  of the Potts variables in state  $i$ , from which we obtained the magnetization moments and the Binder ratio [8], as explained in Sec. 7.2. We use finite-size scaling to analyze these data to obtain the location of the phase transitions and their universality classes. In Sec. 7.3 we present results for the  $q = 3$  Potts model for several values of  $z$  with  $4 \leq z \leq 120$ . Results for several  $q = 4$  Potts models with  $4 \leq z \leq 60$  are shown in Sec. 7.4. Finally, discussions and conclusions are listed in Sec. 7.5.

## 7.2 Methods and sampled quantities

We study two-dimensional Potts models with  $z$  equivalent neighbors by means of an efficient cluster Monte Carlo technique [7]. This algorithm requires a computer time that is almost independent of the number  $z$  of interacting neighbors per spin. We used the Wolff-like single-cluster version [9] of the algorithm. Since the location of the phase transition is unknown for general  $z$ , our first task is to determine the critical points. This determination is based on the Monte Carlo sampling of the moments of the magnetization density  $m$ . This quantity depends on the densities  $\rho_i$  of the Potts states  $i = 1, 2, \dots, q$  as

$$m^2 \equiv \frac{1}{q-1} \sum_{i=1}^{q-1} \sum_{j=i+1}^q (\rho_i - \rho_j)^2. \quad (7.2)$$

This definition is in accordance with the interpretation of the Potts spins as vectors with  $q$  equivalent orientations in  $q-1$  dimensional space. For any integer  $q > 1$ , one can derive  $\langle m^2 \rangle$  and  $\langle m^4 \rangle$  in terms of cluster sizes of the random cluster representation as

$$\langle m^2 \rangle = \left\langle \sum_i c_i^2 \right\rangle, \quad (7.3)$$

and

$$\langle m^4 \rangle = \left\langle \frac{q+1}{q-1} \left( \sum_i c_i^2 \right)^2 - \frac{2}{q-1} \sum_i c_i^4 \right\rangle, \quad (7.4)$$

where  $c_i$  is the size of the  $i$ -th cluster. This holds for integer  $q > 1$ , but the formula can also be viewed as a generalization of  $\langle m^2 \rangle$  and  $\langle m^4 \rangle$  for noninteger  $q$ .

The magnetization moments determine a dimensionless ratio  $Q$ , related to the Binder cumulant [8], as defined:

$$Q = \frac{\langle m^2 \rangle^2}{\langle m^4 \rangle}. \quad (7.5)$$

The finite-size scaling behavior of  $Q$  near the transition point is:

$$Q(K, L) = Q_0 + \sum_k a_k (K - K_c) L^{ky_t} + \sum_j b_j L^{y_j} + c(K - K_c) L^{y_t + y_1} + d(K - K_c)^2 L^{y_t} + \dots, \quad (7.6)$$

where the  $y_j$  ( $j = 1, 2, \dots$ ) are negative exponents describing corrections that will be discussed later, and the  $a_k$ , the  $b_j$ ,  $c$ , and  $d$  are unknown amplitudes.

The ratio  $Q$  is a useful quantity to locate phase transitions and to determine the associated temperature-like exponent. From Eq. (7.6) one finds that the  $Q$  versus  $K$  curves for different values of the finite-size parameter  $L$  intersect at values approaching  $K = K_c$  for large  $L$ . Moreover, the slopes of these curves are asymptotically proportional to  $L^{y_t}$ , which thus allows the estimation of  $y_t$ .

For each model, simulations were performed for several system sizes in a suitable range of  $K$  near criticality, and not less than  $6 \times 10^6$  samples were taken for each data point specified by  $q$ ,  $K$  and  $z$ . The intersections of finite-size data for  $Q$  versus  $K$ , taken at different values of  $L$  but for the same  $q$  and  $z$ , reveal the location of the critical point. This is illustrated in Fig. 7.2 for the  $q = 3$  Potts model with  $z = 8$ , i.e., nearest- and next-nearest neighbor interactions.

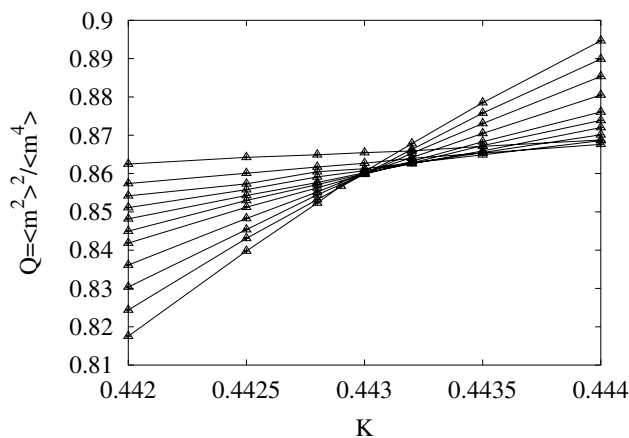


Figure 7.2: The dimensionless ratio  $Q$  of the three-state Potts model with 8 equivalent interacting neighbors vs. coupling  $K$ , for system sizes  $L = 6, 9, 12, 15, 18, 21, 24, 30, 36, 42$ , and  $48$ .

A more accurate location was determined by a least-squares analysis according to Eq. (7.6). Similar analyses were performed for the other choices of  $q$  and  $z$  investigated in the present work.

We have also searched for possible evidence, in the form of hysteresis loops, for first-order transitions at a finite interaction range. We thus determined the behavior of the energy which is defined here as

$$E = \left\langle \sum_j \theta(R - r_{ij}) \delta_{\sigma_i, \sigma_j} \right\rangle, \quad (7.7)$$

and the magnetization as defined in Eq. (7.2), while the coupling  $K$  was changed in small steps separated by long intervals. Furthermore we investigated the autocorrelation time  $\tau$ , and the distributions  $p(E)$  of the energy and  $p(m)$  of the magnetization.

## 7.3 Results for three-state Potts models

### 7.3.1 Location and nature of the phase transitions

The Binder ratio  $Q$  is assumed to be universal for critical Potts models with the same  $q$ , but this universal number still depends on the symmetry of the finite system. The relevant factors are the ratio of the microscopic couplings in different directions, the boundary conditions and the shape of the system, for instance the aspect ratio of a rectangular periodic box. In this work we restrict ourselves to systems with square symmetry, which pertains to the lattice, the couplings and to the boundary conditions. The universal value of  $Q$  can therefore conveniently be determined from the nearest-neighbor Potts model with this symmetry. For this model we know the exact critical point as  $K_c = \ln(1 + \sqrt{3})$ . We therefore simulated the nearest-neighbor three-state Potts model at the critical point for system sizes  $L = 6, 7, 8, \dots, 280, 320$ . We fitted the finite-size data by Eq. (7.6), using the known values of the critical point and the critical exponents [10], of which the temperature exponent is  $y_t = 6/5$  and the leading irrelevant exponent  $y_1 = -4/5$ . We obtain  $Q = 0.85410(10)$  which value will be useful for the analysis of models with more neighbors. As a consistency check, we also simulated the dilute Potts model to determine the dimensionless ratio  $Q$  for the three-state Potts model at the critical fixed point, which is located [11] (see also Chap. 6) at  $K_{crf} = 1.16941$ ,  $D_{crf} = 1.376483$ . At the critical fixed point, the leading correction term with exponent  $y_i = -4/5$  is suppressed. For the model at the critical fixed point, we simulated 21 systems  $L = 6, 8, 10, \dots, 150, 210$ , and obtain  $Q = 0.85408(7)$  and  $y_1 = -1.13(4)$ . This value is close to an expected correction exponent  $X_{h1} - X_{h2} = -6/5$ . The values of the magnetic exponents  $X_{h1}$  and  $X_{h2}$  are given in Ref. [12]. When we fix the correction exponent at the value  $y_1 = -6/5$ , we obtain  $Q = 0.85412(5)$ .

We also simulated the dilute Potts model to determine the dimensionless ratio  $Q$  at the tricritical point of the three-state Potts model, which is located [11] (see also Chap. 6)

at  $K_{trf} = 1.649903$ ,  $D_{trf} = 3.152152$ . For the tricritical Potts model we used system sizes  $L = 6, 8, 10, \dots, 84, 108$ . Fits with  $y_1$  left as a free parameter show that there exists a correction to scaling with an exponent near  $y_1 = -1$ , with an uncertainty margin of a few tenths. This exponent is consistent with  $y_1 = X_{h1} - X_{h2} = -6/7$ . The  $\chi^2$  criterion provides strong indications that another correction to scaling is present, but the data are not accurate enough to allow a reliable determination of its exponent. Further corrections may be expected with exponent  $y_2 = -10/7$  (irrelevant exponent  $X_{14}$  in the Kac table) and with  $d - 2y_h = -38/21$ . The resulting values for the  $Q$  are still somewhat dependent on which correction exponent is included. Taking into account the uncertainty due to this dependence, as well as the statistical error margin, the estimated result is  $Q = 0.743$  (2).

For several values of  $z$ , we determine the critical points, and also estimate the temperature exponent by least square fits. The results are included in Table 7.1. The tendency of

Table 7.1: Results for the dimensionless ratio  $Q$  and thermal exponent  $y_t$  for  $q = 3$  models with varying range  $z$ . These results were obtained by fits to the Monte Carlo data described in the text. The tricritical point lies in the neighborhood of  $z = 80$ , because the result for  $y_t$  is closest to the tricritical value  $y_t = 12/7$  for  $q = 3$ . For smaller  $z$  the results tend to the critical value  $y_t = 6/5$ , and for larger  $z$  to the discontinuity fixed point value  $y_t = 2$  which applies to first-order transitions. The third column lists the number of samples per data point, divided by  $10^6$ . The error margins are quoted as 2 times the standard deviation of the statistical analysis.

$z$	$L$	#S	$K_c$	$Q$	$y_t$	$y_1$	$y_2$
4	6 -320	25	$\ln(1 + \sqrt{3})$ (exact)	0.8542 (1)	1.20 (3)	-0.8	-1.2
8	6 -240	8	0.442907 (3)	0.8536 (8)	1.18 (2)	-0.8	-1.2
12	6 -240	6	0.272027 (1)	0.8537 (4)	1.197 (6)	-0.8	-1.2
20	6 -240	8	0.154075 (1)	0.852 (3)	1.19 (1)	-0.8	-1.2
28	9 -240	8	0.106430 (1)	0.848 (2)	1.15 (2)	-0.8	-1.2
36	9 -270	8	0.081432 (1)	0.853 (6)	1.18 (2)	-0.8	-1.2
48	9 -270	8	0.060112 (1)	0.838 (16)	1.24 (2)	-0.8	-1.2
56	9 -360	10	0.051188 (1)	0.802 (6)	1.36 (2)	-0.8	-1.2
68	12 -600	11	0.0418853 (1)	0.773 (4)	1.45 (2)	-0.8	-1.2
80	12 -600	8	0.03543148 (4)	0.753 (1)	1.64 (2)	-0.8	-2.0
100	18 -160	6	0.0282084 (4)	0.744 (8)	1.98 (6)	-1.0	-2.0
120	18 -120	6	0.0234324 (4)	0.754 (8)	2.01 (5)	-1.0	-2.0

the value of  $y_t$  and of the corresponding  $Q$  provides some information on the nature of the phase transition. For  $z \leq 48$ , the results are consistent with the universality class of the  $q = 3$  short-range model. It is however clear that crossover phenomena occur near  $z = 80$ . For  $z > 80$  the results are consistent with first-order behavior:  $y_t = 2$  is the so-called discontinuity fixed point exponent [10] and the universal ratio is expected to satisfy  $Q = 3/4$  at the coexistence of three ordered phases and one disordered phase [13]. More accurate

estimation of critical points were obtained when the Binder ratio and the temperature exponents were fixed at their expected values. The results are listed in Table 7.2.

Table 7.2: Transition point  $K_c^1$  for three-state Potts model as determined with  $y_t$  fixed at  $6/5$  for  $z < 80$ , at  $y_t = 2$  for  $z > 80$ . For  $z = 80$ ,  $y_t$  was fixed at  $12/7$  although the result for  $y_t$  suggests that the tricritical value of  $z$  is slightly larger than 80. We fixed  $Q = 0.85412$  for  $z \leq 68$ ,  $Q = 0.743$  for  $z = 80$ , and  $Q = 0.75$  for  $z \geq 100$ . For  $z = 4$ , we used the exact critical value. The error margins are quoted as 2 times the standard deviation of the statistical analysis.

$z$	$L_{min}$	$K_c^1$	$Q$	$y_t$	$y_1$	$y_2$	$b_1$
4	6	$\ln(1 + \sqrt{3})$ (exact)	0.85412	1.2	-0.8	-1.2	0.148 (2)
8	6	0.4429080 (10)	0.85412	1.2	-0.8	-1.2	0.085 (5)
12	6	0.2720275 (6)	0.85412	1.2	-0.8	-1.2	-0.155 (2)
20	9	0.1540760 (4)	0.85412	1.2	-0.8	-1.2	-0.68 (2)
28	9	0.1064309 (4)	0.85412	1.2	-0.8	-1.2	-1.94 (5)
36	9	0.0814320 (2)	0.85412	1.2	-0.8	-1.2	-3.37 (5)
48	9	0.0601132 (4)	0.85412	1.2	-0.8	-1.2	-7.85 (7)
56	12	0.0511894 (2)	0.85412	1.2	-0.8	-1.2	-14.3 (8)
68	60	0.0418858 (2)	0.85412	1.2	-0.8	-1.2	-40 (6)
80	48	0.03543150(6)	0.743	12/7	-0.8	-2.0	1.5 (4)
100	18	0.0282086 (1)	0.75	2.0	-1.0	-2.0	-2.3 (5)
120	18	0.0234323 (1)	0.75	2.0	-1.0	-2.0	-2.4 (4)

In order to shed more light on the crossover phenomenon near  $z = 80$ , we study the first derivative of  $Q$  with respect to the coupling  $K$  at criticality, which can be derived from Eq. (7.6) as

$$\left. \frac{dQ}{dK} \right|_{K=K_c} = L^{y_t} (a_1 + cL^{y_i} + \dots), \quad (7.8)$$

where  $a_1$  is the leading amplitude. Only terms of first order in  $(K - K_c)$  in Eq. (7.6) survive. From Eq. (7.8) one finds that, at the transition point,

$$\frac{\ln(dQ/dK)}{\ln L} = y_t + \frac{\ln a_1 + (c/a_1)L^{y_i} + \dots}{\ln L} \quad (7.9)$$

so that, since  $y_i < 0$ , one expects that a plot of  $(\ln(dQ/dK))/\ln L$  versus  $1/\ln L$  will yield a straight line for large  $L$  with an intercept  $y_t$  on the vertical axis. The data for  $dQ/dK$ , as obtained from fits to the  $Q$  versus  $K$  simulation results, are shown accordingly in Fig. 7.3.

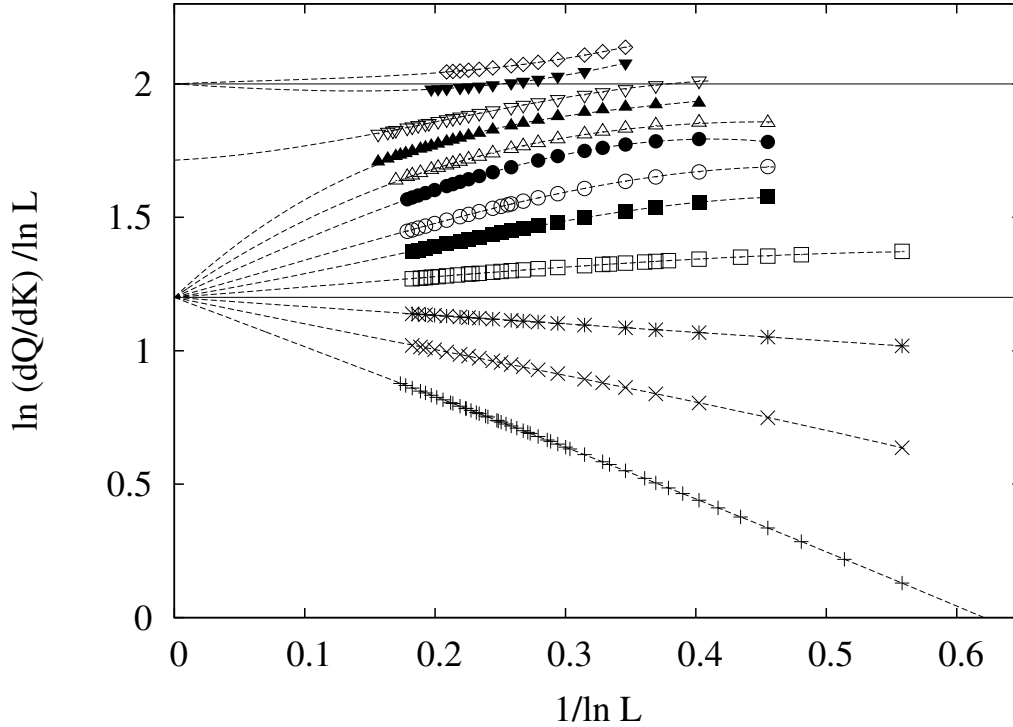


Figure 7.3: Finite-size dependence of the derivative of the dimensionless ratio  $Q$  of the three-state Potts model with respect to  $K$ , taken at  $K_c$ . The quantity plotted along the vertical scale is defined in the text and chosen such that the data should converge, for sufficiently large  $L$ , to the temperature exponent  $y_t$  which is  $6/5$  for the  $q = 3$  critical Potts model,  $12/7$  for the tricritical three-state Potts model, and  $2$  for the first-order range. The data points for each value of  $z$  are connected by a line which is intended for visual aid, and to display the limiting value at  $L = \infty$  on the vertical scale according to our interpretation of the data. The values of  $z$  are, from bottom to top,  $z = 4, 8, 12, 20, 28, 36, 48, 56, 68, 80, 100$ , and  $120$ . For  $z = 80$ , which is close to the tricritical point, the limiting value at  $L = \infty$  on the vertical scale is shown accordingly as  $12/7$ .

### 7.3.2 Hysteresis loop

The data in the preceding subsection indicate that the ordering phase transition for three-state Potts models with  $z \gtrsim 80$  is first-order. To verify the discontinuous character of the transition in the model with  $120$  equivalent neighbors, we have recorded the behavior of the energy and the magnetization of an  $L = 600$  system, while the coupling was stepped up or down in small intervals. While these data display hysteresis loops, the ranges of metastability are small ( $10^{-5}$  in  $K$ ) and tend to shrink when the length of the simulation per data point is increased. To obtain a more clear picture, we have simulated systems with  $z = 120$ . Hysteresis loops of the energy and the magnetization are displayed in Figs. 7.4

and 7.5 respectively.

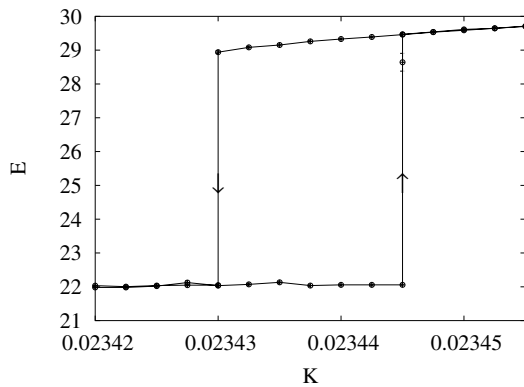


Figure 7.4: Hysteresis loop of the energy  $E$  of the  $q = 3$  Potts model with 120 equivalent neighbors for system size  $L = 600$ . Data points are separated by  $2 \times 10^5$  single-cluster steps.

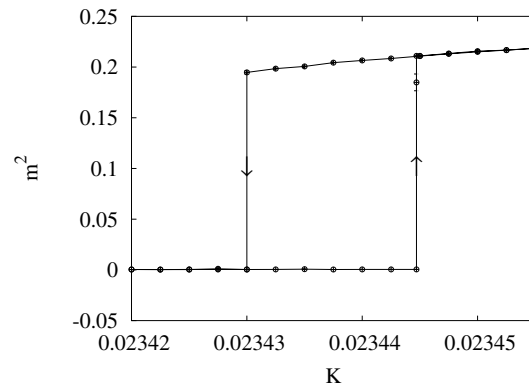


Figure 7.5: Hysteresis loop of the squared magnetization  $m^2$  of the  $q = 3$  Potts model with 120 equivalent neighbors for system size  $L = 600$ . Data points are separated by  $2 \times 10^5$  single-cluster steps.

### 7.3.3 Time evolution, histogram and dynamics

We determined the time evolution of the energy of a system with  $z = 100$  interacting neighbors and of size  $L = 200$  at the transition point  $K = 0.0282085$ . The results which are displayed in Fig. 7.6, show that the system occasionally jumps between a high- and a low-energy state. The difference with the preceding subsection, namely a smaller system and a smaller value of  $z$ , leads to a much faster evolution in time. Histograms of the energy are shown in Fig. 7.7 for several system sizes, taken at couplings chosen such that both maxima have the same height (minor reweighting was applied to this purpose). These results show that the peaks become narrower, and the minima between them deeper. This is in accordance with first-order behavior.

Fig. 7.8 displays the dynamic behavior of the  $q = 3$  model with 100 equivalent neighbors under single-cluster steps. The figure shows the autocorrelation time  $\tau$  versus the system size  $L$ . The autocorrelation time unit is chosen as the number of Wolff-type single-cluster steps equal to the inverse single-cluster size. The use of logarithmic scales leads to a straight line with slope  $z_d$  if  $\tau \propto L^{z_d}$ . The upward curvature of the line is in agreement with a weakly first-order transition.

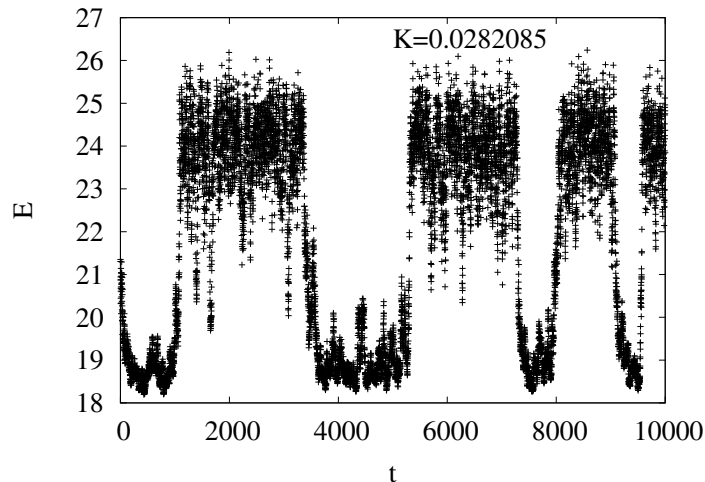


Figure 7.6: Energy versus Monte Carlo time, for a three-state model of size  $L = 200$ , with  $z = 100$  equivalent neighbors, at the estimated transition point. Data points are separated by 25 single-cluster steps, which corresponds with one unit on the horizontal time scale.

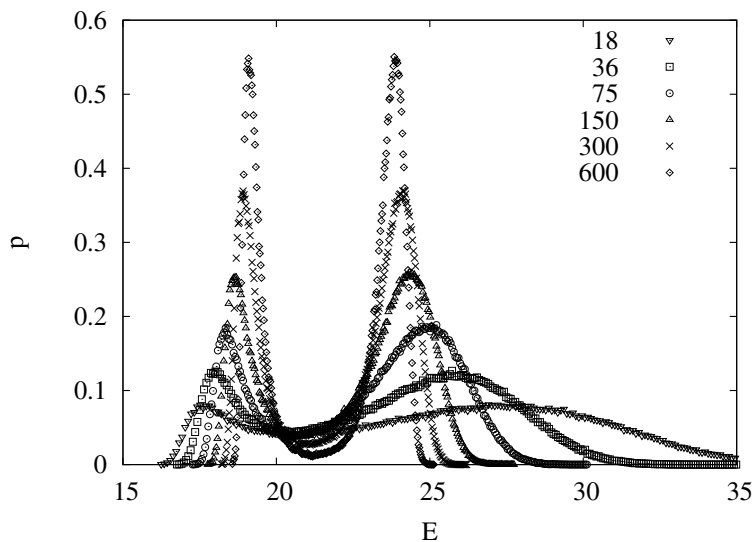


Figure 7.7: Histograms of the energy distributions of finite  $q = 3$  Potts models with  $z = 100$  equivalent neighbors. The values of the finite sizes  $L$  are shown in the figure. The couplings are chosen such that the two peaks are equally high. These data represent  $5 \times 10^5$  samples separated by  $L/4$  single-cluster steps per system size, except for  $L = 600$  where the latter number is  $L/3$ .

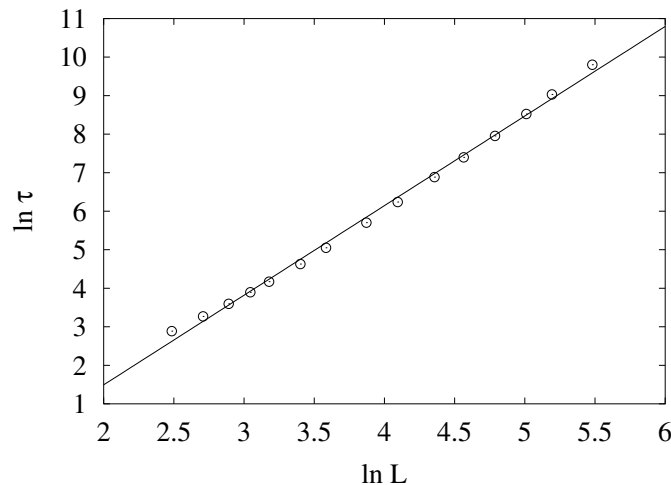


Figure 7.8: Dynamic properties of the cluster simulation of the  $q = 3$  model with  $z = 100$  equivalent neighbors, in terms of the autocorrelation time  $\tau$  versus the system size  $L$ . The use of logarithmic scales leads to a straight line with slope  $z_d$  if  $\tau \propto L^{z_d}$ . The upward curvature of the data is in agreement with a weakly first-order transition. The slope of the straight line corresponds to with a dynamic exponent  $z_d = 2.3258$ . The line is shown for visual aid only.

### 7.3.4 Mean-field analysis for $q = 3$

The mean-field treatment for the three-state Potts model expresses the probability  $\rho_1$  of a spin to be in state 1, as a function of the average magnetization  $m = (3\rho_1 - 1)/2$  and the sum of couplings  $zK$  per spin. The probabilities of the other two spin states are set to  $\rho_2 = \rho_3 = (1 - \rho_1)/2$ . The expectation value  $\langle m \rangle$  of  $m$  can trivially be calculated after replacing the  $z$  neighbor spins by their average. This approach applies to our model Eq. (7.1) in the limit  $z \rightarrow \infty$ . This leads to the equation  $\langle m \rangle = [\exp(zKm) - 1]/[\exp(zKm) + 2]$  which is supplemented by  $\langle m \rangle = m$ . These equations lead to solutions of  $m$  as a function of  $zK$ . This is illustrated in Fig. 7.9 which shows  $\langle m \rangle - m$  versus  $m$ , for three special values of  $zK$ . These are the first-order transition coupling [14]  $zK = 4 \ln 2$ , and the couplings  $(zK)_l = 2.745643 \dots$  and  $(zK)_h = 3$  where the ends of the metastable branches occur. Fig. 7.10 shows the solutions for  $m$  as a function of  $zK$  in the vicinity of the transition point. These results form a clear hysteresis loop. The ends of the metastable branches are indicated by black squares. The transition point is indicated by a dashed line.

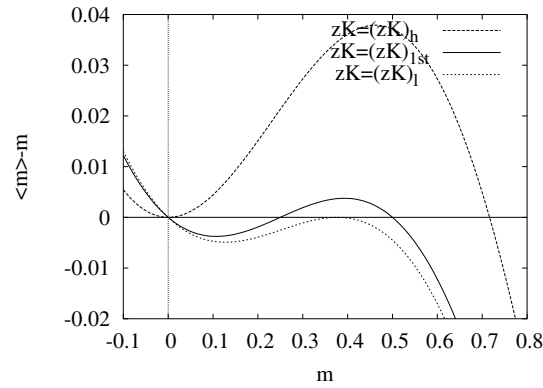


Figure 7.9: Solutions of the self-consistent equations of the  $q = 3$  mean-field model. These equations determine: 1) that the expectation value of the magnetization  $\langle m \rangle$  of a Potts variable as a function of the mean magnetization  $m$  satisfies  $\langle m \rangle = [\exp(zKm) - 1]/[\exp(zKm) + 2]$  (curves) and 2) that  $\langle m \rangle = m$  (horizontal line). The intersections of the curves with the horizontal axis thus represent solutions of the self-consistent equations. Solutions are only stable if the slope of the curve is negative. The three curves represent three values of  $zK$ , namely the transition point  $zK = 4 \ln 2$  and the two values of  $zK$  corresponding with the end of metastability, characterized by an extremum of the curve at the solution.

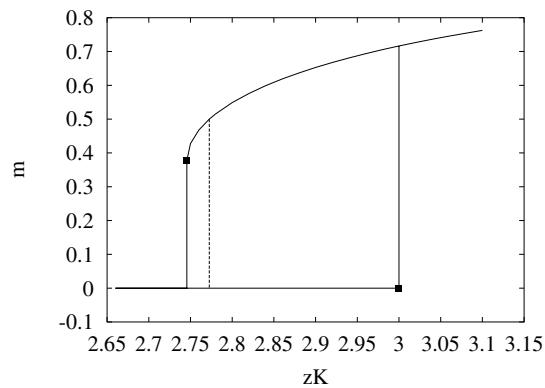


Figure 7.10: Spontaneous magnetization of the mean-field three-state Potts model. The solutions of the self-consistency equation  $m = [\exp(zKm) - 1]/[\exp(zKm) + 2]$  as a function of  $zK$ , which are shown as lines, display the hysteresis loop of the magnetization. The ends of the metastable ranges are shown as black symbols, and the transition point as a dashed line.

## 7.4 Results for four-state Potts models

### 7.4.1 Critical points

As for  $q = 3$ , one may attempt to determine its value from simulations of the nearest-neighbor Potts model at the exactly known critical point. However, logarithmic corrections occur for  $q = 4$  which lead to anomalously slow finite-size convergence and inhibit accurate numerical analysis. Instead, we simulated the dilute  $q = 4$  model at the estimated fixed point  $K_f = 1.45790$ ,  $D_f = 2.478438$ , which is very close to the value reported in [11] (see also Chap. 6). Logarithmic corrections are absent at the fixed point. We simulated this model using finite sizes  $L = 4, 5, \dots, 80$ . We fitted the finite-size data by Eq. (7.6), using the critical exponents  $y_t = 3/2$  and, at first, only one correction term with a free exponent. These fits indicated a strong correction with exponent  $y_{h2} - y_{h1} = -1$ . Next, we included another correction term with a free exponent. These fits were suggestive of a correction term with exponent  $y_{t3} \approx -2$ . Including correction terms with fixed exponents  $y_1 = -1$  and  $y_2 = 2 - 2y_h = -1.75$  (since  $y_h = 15/8$  for the 4-state Potts model), we obtained satisfactory fits including system sizes down to  $L = 7$ . We performed several other fits, including those with exponent  $y_2 = -2.5$  instead of  $-1.75$ , and with various combinations of fixed correction exponents. After discarding the fits with a too large residual  $\chi^2$ , the results are consistent with our final estimate  $Q = 0.81505$  (15) where the error estimate is twice the statistical margin of what appear to be the best fits. This value will be helpful for the interpretation of the results for the models with more neighbors.

For several values of  $z$ , we determined the critical points, and estimated the exponents as free parameters in the fitting procedure. Here our purpose is to determine the qualitative finite-size behavior. The results are included in Table 7.3. The tendency of the estimates of  $y_t$  and  $Q$  provides some information on the nature of the phase transition. For  $z \leq 12$ ,

Table 7.3: Dimensionless ratio  $Q$  and thermal exponent  $y_t$  as estimated from simulations of the medium-range  $q = 4$  Potts model. These results indicate that the ‘tricritical’ point between the critical and first-order range occurs near  $z = 20$ . The error bar margins are quoted as 2 times of the standard deviation of the statistical analysis.

$z$	$L$	$\#S$	$K_c$	$Q$	$y_t$	$y_1$	$y_2$
4	8-108	8	$\ln 3$ (exact)	0.838 (2)	1.41 (2)	-1	-1.75
8	8-108	8	0.49098 (1)	0.841 (4)	1.38 (2)	-1	-1.75
12	8-160	30	0.30625 (1)	0.822 (4)	1.48 (1)	-1	-1.75
20	8-280	10	0.175842 (1)	0.804 (2)	1.56 (4)	-1	-1.75
24	8-120	12	0.144523 (1)	0.795 (1)	1.70 (4)	-2	-3
28	8-96	12	0.122812 (1)	0.788 (1)	1.82 (6)	-2	-3
36	8-84	15	0.094528 (1)	0.780 (1)	1.91 (5)	-2	-3
44	8-48	25	0.076826 (4)	0.781 (6)	2.02 (5)	-2	-3
60	12-44	20	0.055921 (2)	0.804 (8)	2.04 (5)	-2	-3

the results are consistent with the universality class of the nearest-neighbor  $q = 4$  critical model. The deviations with respect to the exact value  $y_t = 3/2$  are just as expected for  $q = 4$  Potts models, because of logarithmic corrections as implied by the renormalization scenario by Nienhuis et al. [5]. The results for  $z > 20$  indicate that the model is in the first-order range. This is probably also the case for  $z = 20$ , since the  $y_t$  result exceeds  $3/2$  which suggests crossover to the discontinuity fixed point value  $y_t = 2$ . More accurate estimation of critical points were obtained when the Binder ratio and the temperature exponents were fixed at their expected values. The results are listed in Table 7.4.

Table 7.4: Critical points  $K_c^1$  for  $q = 4$  as derived from fits with the dimensionless ratio  $Q$  and thermal exponent  $y_t$  fixed as shown in the table. The amplitude  $b_1$  of the leading correction with correction exponent  $y_1$  is also included in this table. The error bar margins are quoted as 2 times of the standard deviation of the statistical analysis.

$z$	$L_{min}$	$K_c^1$	$Q$	$y_t$	$y_1$	$y_2$	$b_1$
4	24	$\ln 3$ (exact)	0.81505	1.5	-1	-1.75	17 (5)
8	12	0.49096 (1)	0.81505	1.5	-1	-1.75	6.4 (8)
12	8	0.306246 (1)	0.81505	1.5	-1	-1.75	1.76 (4)
20	12	0.1758423 (8)	0.81505	1.5	-1	-1.75	-8 (2)
24	8	0.1445234 (8)	0.8	2.0	-0.25(11)	-2	-0.012 (5)
28	8	0.1228137 (8)	0.8	2.0	-0.60 (4)	-2	-0.11 (2)
36	8	0.094531 (1)	0.8	2.0	-0.58 (3)	-2	-0.16 (2)
44	8	0.076829 (2)	0.8	2.0	-0.78 (5)	-2	-0.36 (6)
60	12	0.055920 (1)	0.8	2.0	-2	-3	-30.8 (9)

We have also determined the first derivative of  $Q$  with respect to the coupling  $K$  at criticality, similarly as for  $q = 3$ . In the critical range one thus expects, in principle, convergence of  $(\ln(dQ/dK))/\ln L$  to  $y_t = 3/2$ , but a logarithmic factor in  $dQ/dK$  yields a term proportional to  $(\ln(\ln L))/\ln L$  in  $(\ln(dQ/dK))/\ln L$ , so that the convergence with increasing  $L$  is extremely slow. Thus one would require finite-size data for very large  $L$  to verify this convergence. Investigation of such large systems is not well feasible. Nevertheless, the data for  $(\ln(dQ/dK))/\ln L$  versus  $1/\ln L$ , shown in Fig. 7.11 are sufficiently clear to provide qualitative information on the crossover between the short-range behavior for  $z \lesssim 16$  and first-order behavior for  $z \gtrsim 16$ .

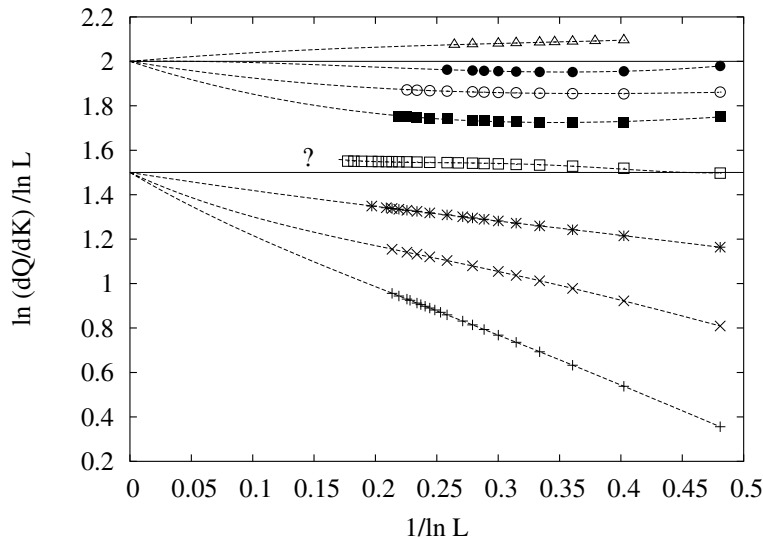


Figure 7.11: Finite-size dependence of the derivative at  $K_c$  of the dimensionless ratio  $Q$  of the four-state Potts model with respect to  $K$ . The quantity plotted along the vertical scale is defined in the text and chosen such that the data should converge, for sufficiently large  $L$ , to the temperature exponent  $y_t$  which is  $3/2$  for the  $q = 4$  critical Potts model and  $2$  for the first-order range. However, due to the presence of logarithmic corrections near the critical fixed point, such convergence is only clearly observable where the marginal field vanishes. The values of  $z$  are, from bottom to top,  $z = 4, 8, 12, 20, 28, 36, 44, 60$ . The data points for each value of  $z$  are connected by a line which is intended for visual aid, and to display the limiting value at  $L = \infty$  on the vertical scale according to our interpretation of the data. The question mark applies to the data for  $z = 20$ . While we suspect that this is already in the first-order range and thus eventually extrapolates to the value  $2$  on the vertical scale, the results are not sufficiently convincing to make a firm statement. The data in this figure suggest that this is the case somewhere between  $z = 12$  and  $z = 20$ .

### 7.4.2 Hysteresis loop

For  $q = 4$  we have determined the behavior of the energy and the magnetization of an  $L = 120$  system with 60 equivalent neighbors, while the coupling was stepped up or down in small intervals. We find very clear hysteresis loops, which are displayed in Figs. 7.12 and 7.13 for the magnetization and the energy respectively.

## 7.5 Discussion and conclusion

The results in Sec. 7.3 indicate that, for the  $q = 3$  Potts model, the renormalization flow is as shown in Fig. 7.14, i.e., the role of the interaction range is similar to that of the fugacity of the vacancies in the dilute Potts model [5]. Similarly, the results for the  $q = 4$  model in

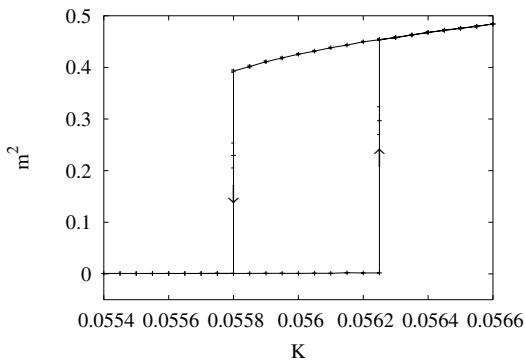


Figure 7.12: Hysteresis loop of the squared magnetization  $m^2$  of the  $q = 4$  model with 60 equivalent neighbors and finite size  $L = 120$ . Data points are separated by  $2 \times 10^5$  single-cluster steps.

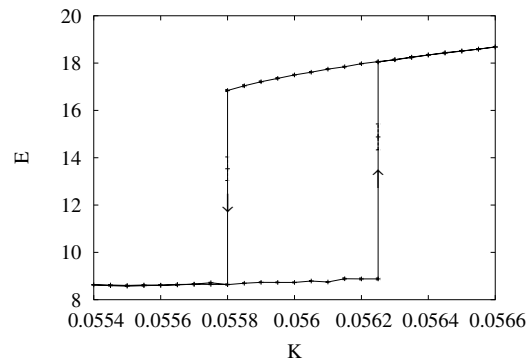


Figure 7.13: Hysteresis loop of the energy  $E$  of the  $q = 4$  model with 60 equivalent neighbors and finite size  $L = 120$ . Data points are separated by  $2 \times 10^5$  single-cluster steps.

Sec. 7.4 display the same type of behavior as the dilute  $q = 4$  Potts model. These results are consistent with the renormalization flow diagram that follows when the critical and tricritical fixed points in Fig. 7.14 merge into a fixed point that is marginally irrelevant on the short-range side and marginally relevant on the long-range side [5] as shown in Fig. 7.15.

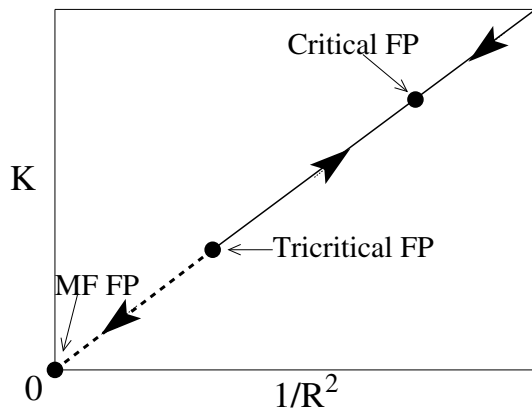


Figure 7.14: The renormalization flow along the line of phase transitions of the three-state Potts model with range  $R$  of interaction.

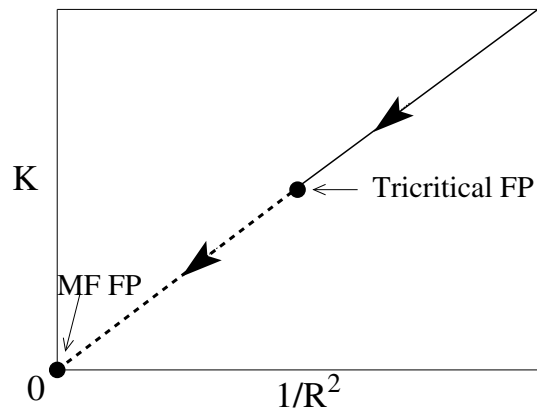


Figure 7.15: The renormalization flow along the line of phase transitions of the four-state Potts model with range  $R$  of interaction.

# Bibliography

- [1] M. E. Fisher, S. K. Ma and B. G. Nickel, Phys. Rev. Lett. **29**, 917 (1972).
- [2] J. Sak, Phys. Rev. B **8**, 281 (1973).
- [3] E. Luijten and H. W. J. Blöte, Phys. Rev. B **56**, 8945 (1997); Phys. Rev. Lett. **89**, 025703 (2002).
- [4] E. Luijten, H. W. J. Blöte and K. Binder, Phys. Rev. E **54**, 4626 (1996).
- [5] B. Nienhuis, A. N. Berker, E. K. Riedel and M. Schick, Phys. Rev. Lett. **43**, 737 (1979).
- [6] M. Biskup, L. Chayes and N. Crawford, J. Stat. Phys. **122**, 1139 (2006).
- [7] E. Luijten and H. W. J. Blöte, Int. J. Mod. Phys. C **6**, 359 (1995).
- [8] K. Binder, Z. Phys. B **43**, 119 (1981).
- [9] U. Wolff, Phys. Rev. Lett. **60**, 1461 (1988).
- [10] B. Nienhuis and M. Nauenberg, Phys. Rev. Lett. **35**, 477 (1975).
- [11] X. Qian, Y. Deng and H. W. J. Blöte, Phys. Rev. E. **72**, 056132 (2005).
- [12] B. Nienhuis, in *Phase Transitions and Critical Phenomena*, edited by C. Domb and J. L. Lebowitz (Academic Press, London, 1987), Vol. **11**. There is a typo in Eq. (4.26) for the second-leading magnetic exponent. In this formula +1 should be replaced by +2.
- [13] The value  $Q = q/(q+1)$  follows from the assumption that, at the discontinuous phase transition, the  $q$  magnetized phases are equally probable as the disordered phase.
- [14] F. Y. Wu, Rev. Mod. Phys. **54**, 235 (1982).
- [15] T. Gobron and I. Merola, "Phase transition induced by increasing the range of interaction in Potts Model", mp arc 05-272, 2005.



# Chapter 8

## Critical line of an $n$ -component cubic model

We consider a special case of the  $n$ -component cubic model on the square lattice, for which an expansion exists in Ising-like graphs. We construct a transfer matrix and perform a finite-size-scaling analysis to determine the critical points for several values of  $n$  in the range  $-2 < n < 2$ . Furthermore we determine several universal quantities, including three critical exponents. For  $n < 2$ , these results agree well with the theoretical predictions for the critical  $O(n)$  branch. This model is also a special case of the  $(N_\alpha, N_\beta)$  model of Domany and Riedel. It appears that the self-dual plane of the latter model contains the exactly known critical points of the  $n = 1$  and 2 cubic models. For this reason we have checked whether this is also the case for other values of  $n$ . However, this possibility is excluded by our numerical results.

### 8.1 Introduction

The  $n$ -component cubic model can be defined in terms of vector spins that are restricted to lie along one of  $n$  Cartesian axes, but are free to assume the positive or negative direction. Only one vector component is nonzero; it is normalized to be  $\pm 1$ . The model can be described by the reduced Hamiltonian

$$\mathcal{H}/k_B T = - \sum_{\langle ij \rangle} [K \vec{s}_i \cdot \vec{s}_j + M (\vec{s}_i \cdot \vec{s}_j)^2], \quad (8.1)$$

where the index  $i$  of the cubic spin  $\vec{s}_i$  refers to the sites of the square lattice. The sum on  $\langle ij \rangle$  stands for all nearest-neighbor pairs. This model obviously combines Potts degrees of freedom (the choice of the Cartesian axis, which is subject to permutation symmetry) with Ising degrees of freedom which specify the sign of the nonzero component. This is more explicit in the following form of the Hamiltonian

$$\mathcal{H}/k_B T = - \sum_{\langle ij \rangle} (K s_i s_j + M) \delta_{\tau_i \tau_j}, \quad (8.2)$$

where we represent the sign of the nonzero component of  $\vec{s}_i$  by  $s_i = \pm 1$  and its Cartesian axis number by  $\tau_i = 1, 2, \dots, n$ . The corresponding bond weight  $w_{ij}$  can be rewritten as

$$\begin{aligned} w_{ij} &= \exp[(Ks_i s_j + M)\delta_{\tau_i \tau_j}] \\ &= 1 + \delta_{\tau_i \tau_j} \{\exp(Ks_i s_j + M) - 1\} \\ &= 1 + \delta_{\tau_i \tau_j} n \{v + xs_i s_j\} \\ &= \sum_{b_{ij}=0}^1 [\delta_{\tau_i \tau_j} n \{v + xs_i s_j\}]^{b_{ij}}. \end{aligned} \quad (8.3)$$

In the third line we have used the definitions

$$v \equiv \frac{e^M \cosh K - 1}{n} \quad \text{and} \quad x \equiv \frac{e^M \sinh K}{n}, \quad (8.4)$$

and in the fourth line we have introduced bond variables  $b_{ij} = 0$  or  $1$ , and the summand is subject to the rule  $0^0 = 1$ . Thus the partition sum assumes the form

$$Z_{\text{cub}} = \sum_{\{s\}, \{\tau\}} \prod_{\langle ij \rangle} \sum_{b_{ij}=0}^1 [\delta_{\tau_i \tau_j} n \{v + xs_i s_j\}]^{b_{ij}}. \quad (8.5)$$

Application of the Kasteleyn-Fortuin mapping [1] involves execution of the sum on the Potts-like variables  $\{\tau\}$ . This leads to

$$Z_{\text{cub}} = n^N \sum_{\{s\}} \left[ \prod_{\langle ij \rangle} \sum_{b_{ij}=0}^1 \{v + xs_i s_j\}^{b_{ij}} \right] n^{n_l}, \quad (8.6)$$

where  $N$  is the number of sites of the lattice. Note that each bond (by which we mean a bond variable  $b_{ij} = 1$ ) contributes, through the Kronecker  $\delta$ , also a factor  $1/n$ , unless it closes a loop. The latter condition is accounted for by the factor  $n^{n_l}$ , where  $n_l$  is the number of loops formed by the bond variables. Each configuration of bond variables  $b_{ij}$  defines a graph on the square lattice covering those and only those edges for which  $b_{ij} = 1$ . For the special case

$$\cosh K = e^{-M} \quad \text{or} \quad v = 0, \quad (8.7)$$

the partition sum reduces, after execution of the sum on  $\{s\}$ , to

$$Z_{\text{cub}} = (2n)^N \sum_{\{b\}} x^{n_b} n^{n_l}, \quad (8.8)$$

where the sum on  $\{b\}$  contains only ‘even’ graphs in which every site is connected to an even number of bonds  $b_{ij} = 1$ . The odd graphs, while included in the sums on the  $b_{ij}$  in Eq. (8.6), do not survive the sum on  $\{s\}$ . The number of bonds in the graph  $\{b\}$  is denoted  $n_b \equiv \sum_{\langle ij \rangle} b_{ij}$ .

The cubic loop model described by Eq. (8.8), is subject to the restriction  $|xn| \leq 1$  because of Eq. (8.7). This model, and the model defined by Eq. (8.1) with  $M = 0$ , (both on the square lattice) have already been investigated by a transfer-matrix method [2]. That work included a determination of the temperature exponent. The results for  $n < 2$  were in agreement with a conjecture of Cardy and Hamber [3] and the analysis of Nienhuis [4]. However, the latter work applies to the  $n$ -component cubic model on the honeycomb lattice, of which the graph expansion reduces to that of the  $O(n)$  model. For other lattices, no such direct correspondence exists, and the relevance of the results of Ref. [4] for the cubic model on the square lattice thus needs further justification. This is provided by renormalization arguments that predict that cubic anisotropy is irrelevant [5] for  $n < 2$ . However, for  $n = 2$  it is marginal and indeed the temperature exponent does not agree with the  $O(2)$  model [2].

The work of Ref. [2] did not include results for  $n < -1$  and  $1 < n < 2$ . Furthermore, the present analysis will purportedly yield more information about universal quantities.

The outline of this chapter is as follows. Section 8.2 discusses a duality transformation in a three-dimensional parameter space containing the cubic model Eq. (8.8). This transformation suggests a possible form of the critical line of the cubic model. However, transfer-matrix calculations, defined in Sec. 8.3, yield numerical results listed in Sec. 8.4, which show that this form is not applicable. The universal properties of the cubic model are investigated in Sec. 8.5. The chapter concludes with a short discussion in Sec. 8.6.

## 8.2 Self-dual plane of the $(N_\alpha, N_\beta)$ model

The partition function of the  $(N_\alpha, N_\beta)$  model [6] is defined as

$$Z_{(m,n)}(e^{K_0}, e^{K_1}, e^{K_2}, e^{K_3}) \equiv \sum_{\sigma=1}^m \sum_{\tau=1}^n \prod_{\text{edges}} B(\sigma, \tau | \sigma', \tau'), \quad (8.9)$$

where  $m = N_\alpha$ ,  $n = N_\beta$ , and

$$B(\sigma, \tau | \sigma', \tau') \equiv \exp[K_0 \delta_{\sigma\sigma'} \delta_{\tau\tau'} + K_1 (1 - \delta_{\sigma\sigma'}) \delta_{\tau\tau'} + K_2 \delta_{\sigma\sigma'} (1 - \delta_{\tau\tau'}) + K_3 (1 - \delta_{\sigma\sigma'}) (1 - \delta_{\tau\tau'})]. \quad (8.10)$$

Just as the cubic model, the model can be viewed as having two Potts spins  $\sigma$  and  $\tau$  on each lattice site, with allowed values  $\sigma = 1, 2, \dots, m$  and  $\tau = 1, 2, \dots, n$ . These spins interact with nearest-neighbor couplings according to the Boltzmann weights (8.10). The  $(N_\alpha, N_\beta)$  model is known to have a self-dual plane [6, 7]. With the notation

$$x_i \equiv e^{K_i - K_0} \quad (i = 1, 2, 3), \quad (8.11)$$

the location of the self-dual plane is

$$1 + (m - 1)x_1 + (n - 1)x_2 + (m - 1)(n - 1)x_3 = \sqrt{mn}. \quad (8.12)$$

A point in this plane does, however, not in general map on itself under the duality transformation. Thus, the duality does not provide a solid basis to find the location of the critical surface of the  $(N_\alpha, N_\beta)$  model. As discussed in [8] the cubic model of Eq. (8.8) forms a subspace of the  $(N_\alpha, N_\beta)$  model with

$$m = 2, \quad x_1 = \frac{1 - nx}{1 + nx}, \quad x_2 = \frac{1}{1 + nx}, \quad x_3 = \frac{1}{1 + nx}. \quad (8.13)$$

For this subspace, the critical points are exactly known for  $n = 1$  and 2. For  $n = 1$  the Ising critical point has  $x_c = \sqrt{2} - 1$ , and the case  $n = 2$ , it corresponds with the Ashkin-Teller model [9] critical point  $x_c = 1/2$ . Remarkably, these points do lie in the self-dual plane of Eq. (8.12) [10]. If this is true in a continuous range of  $n$ , we have

$$x_c(n) = (\sqrt{2n} - 1)/n. \quad (8.14)$$

This possibility will be investigated numerically in Sec. 8.4.

### 8.3 The transfer matrix

The transfer-matrix method used here is related to that used in Ref. [2], and it uses in addition some of the techniques described in Refs. [11] and [12] for the random-cluster and the  $O(n)$  model respectively. The full description of the transfer matrix is somewhat elaborate, and here we only provide a general outline, supplemented with more detailed information where the procedure is different from those in the references given.

As in Ref. [2], the transfer matrix is constructed on the basis of a graph representation of the cubic model that allows  $n$  to be non-integer. However, the present work is restricted to the case  $v = 0$ , so that the graphs are restricted to be even. This allows the use, given a system size, of a smaller transfer matrix than that used in Ref. [2]. We define the model on an  $L \times m$  lattice  $\mathcal{L}_m$  wrapped on a cylinder, such that the finite-size parameter  $L$  is the circumference of the cylinder. The definition of the transfer matrix can be illustrated by appending row  $m + 1$  and determining how this affects the partition sum of the model. The lattice  $\mathcal{L}_m$  has an open end at row  $m$ ; there are  $L$  ‘dangling’ edges that will serve to connect to row  $m + 1$  later. Whereas the partition sum Eq. (8.6) allows only for closed loops, the bond configuration on  $\mathcal{L}_m$  may be considered a part of a larger graph so that we allow the dangling edges to be occupied by loop segments. But all sites are still restricted to connect to an even number of bonds. For the construction of the transfer matrix, we need a coding of all possible ways (called connectivities) that the dangling bonds can be connected by the graph  $\{b\}$  on  $\mathcal{L}_m$ . This coding assigns a unique integer  $1, 2, \dots$ , which will serve as the transfer-matrix index, to each connectivity. Some of the dangling edges may be empty, i.e.,  $b_{ij} = 0$ . The remaining dangling edges, i.e., the dangling bonds, form a ‘dense connectivity’ without vacant positions. Note that these dense connectivities satisfy a ‘well-nestedness’ principle which asserts that, if positions  $i$  and  $k$  are connected, and  $j$  and  $l$  are connected, with  $i < j < k < l$ , then all  $i, j, k, l$  must be connected. Thus, these dense connectivities form a subset of the ‘random cluster’ or ‘Whitney’ connectivities defined

in Ref. [11]. The number of dangling bonds that are connected by a path of bonds must always be even for the cubic model; this restriction does not apply to those of Ref. [11]. By simply excluding groups containing an odd number of connected bonds, we thus find coding and decoding algorithms for the dense cubic connectivities. The coding of the general cubic connectivities including vacant positions then follows analogous to the case of the ‘magnetic’ connectivities in Ref. [11].

This coding allows one to divide the partition sum  $Z^{(m)}$  of the  $m$ -row system in contributions corresponding with different connectivities:

$$Z^{(m)} = \sum_{\alpha} Z_{\alpha}^{(m)}. \quad (8.15)$$

Next, we append a new row  $l_{m+1}$  to the lattice:  $\mathcal{L}_{m+1} \equiv \mathcal{L}_m \cup l_{m+1}$ , and express the restricted partition sums  $Z_{\alpha}^{(m+1)}$  as a linear combination of the  $Z_{\beta}^{(m)}$ . This is possible because the weight due to the newly appended row is completely determined by the bond variables connecting to the appended vertices and the ‘old’ connectivity  $\beta$ , and this information also determines the ‘new’ connectivity  $\alpha$ . We use  $b_{m+1}$  to denote the  $2L$  appended bond variables, and  $\mu(\beta, b_{m+1})$  to denote the function that determines  $\alpha$ . The weight factor associated with the new row satisfies

$$w(\beta, b_{m+1}) = (2n)^L x^{\Delta n_b} n^{\Delta n_l}, \quad (8.16)$$

where  $\Delta n_b$  is the number of appended bonds and  $\Delta n_l$  is the number of loops closed by these bonds. The recursion connecting the restricted sums is

$$Z_{\alpha}^{(n+1)} = \sum_{\beta} T_{\alpha\beta} Z_{\beta}^{(n)}, \quad (8.17)$$

in which the transfer matrix  $T_{\alpha\beta}$  is defined by

$$T_{\alpha\beta} = (2n)^L \sum_{b_{m+1}} \delta_{\alpha, \mu(\beta, b_{m+1})} x^{\Delta n_b} n^{\Delta n_l}. \quad (8.18)$$

In actual calculations, the transfer matrix is represented as the product of  $L$  sparse matrices, each of which appends one new vertex of the  $(m+1)$ -th row. The first vertex of a new row increases the number of dangling edges to  $L+2$ , so that the sparse matrices assume a larger size than  $T_{\alpha\beta}$ . After appending the last vertex of that row, the number of dangling edges decreases to  $L$ . This technical point was described in some detail for the related case of the  $O(n)$  model on the square lattice [12].

The sparse-matrix technique makes it unnecessary to store the full transfer matrix  $\mathbf{T}$ . Some of its eigenvalues can be obtained by repeated multiplication of a vector by  $\mathbf{T}$ , and analysis of the resulting vector sequence. Since  $T_{\alpha\beta}$  is not symmetric in general, we used the method of projection to a Hessenberg matrix as described in Ref. [11]. We restricted the calculations to vectors with ‘translation symmetry’, i.e., vectors that are invariant under a permutation of connectivities corresponding with a cyclic permutation of the dangling

edges. In general, the largest eigenvalue  $\lambda_L^{(0)}$  determines the free energy  $f(L)$  per site in the limit of an infinitely long cylinder ( $m \rightarrow \infty$ ):

$$f(L) = -L^{-1} \ln \lambda_L^{(0)}. \quad (8.19)$$

Furthermore, the next largest eigenvalues  $\lambda_L^{(i)}$  ( $i = 1, 2, \dots$ ) determine the correlation lengths  $\xi_i(L)$  of various types of correlation functions. The latter types depend on the symmetry of the corresponding eigenvector and on possible modifications of  $\mathbf{T}$ . In particular, the correlation length  $\xi_t(L)$  of the energy-energy correlation function is determined by the gap between the two largest eigenvalues:

$$\xi_t^{-1}(L) = \ln(\lambda_L^{(0)}/\lambda_L^{(1)}). \quad (8.20)$$

For the cubic model, magnetic correlations can be represented, in analogy with the  $O(n)$  model, by graphs with odd vertices on the correlated sites. For the present model that means sites connected to one or three bonds. The two correlated sites, which are placed far apart in the length direction of the cylinder, must be connected by the graph, i.e., belong to the same component of the graph. This additional component does not follow the rules of ‘evenness’ listed earlier. The number of dangling bonds at the open end of the cylinder (between the correlated sites) connecting to the additional odd vertex must be odd. To describe such ‘magnetic’ graphs we define a new set of connectivities in which one group of connected dangling bonds is odd. This leads to a modified transfer matrix, which may alternatively be interpreted as the magnetic sector of a larger transfer matrix whose vector space includes both even and odd connectivities. The gap between  $\lambda_L^{(0)}$  and the largest eigenvalue  $\lambda_L^{(2)}$  in the magnetic sector determines the magnetic correlation length  $\xi_h(L)$  as

$$\xi_h^{-1}(L) = \ln(\lambda_L^{(0)}/\lambda_L^{(2)}). \quad (8.21)$$

A different type of magnetic gap is associated with the density of the loops spanning the circumference of the cylinder. The weight of these loops is modified by assigning a bond weight  $-x$  to one bond in each row. A loop spanning the circumference contains an odd number of these modified bonds, and its weight thus changes sign. All other loops contain an even number of modified bonds and their weights are thus unchanged. We denote the largest eigenvalue of the modified transfer matrix by  $\lambda_L^{(3)}$ . It determines the length scale  $\xi_m(L)$  that may be associated with the effect of an ‘antiferromagnetic seam’ running along the cylinder. For the critical Ising case  $n = 1$ , both magnetic length scales are related by duality, but this is not so for general  $n$ . The corresponding length scale is given by

$$\xi_m^{-1}(L) = \ln(\lambda_L^{(0)}/\lambda_L^{(3)}). \quad (8.22)$$

In the actual transfer-matrix calculations, we have used finite sizes up to  $L = 15$  in the nonmagnetic sector, which then has dimensionality 2 004 032, and up to  $L = 14$  in the magnetic sector, which then has dimensionality 3 856 582.

## 8.4 Determination of the critical line of the cubic model

The asymptotic behavior of the magnetic correlation length  $\xi_h(L)$  near a critical point can be expressed in terms of the scaled gap

$$X_h(t, u, L) \equiv \frac{L}{2\pi\xi_h(t, u, L)}, \quad (8.23)$$

where  $t$  parametrizes the distance to the critical point, and  $u$  represents an irrelevant field. Renormalization arguments [13], scaling [14], and conformal invariance [15] predict that for large  $L$

$$X_h(t, u, L) \simeq X_h + a_1 L^{y_t} t + b_1 L^{y_u} u + \dots, \quad (8.24)$$

where  $X_h$  is the magnetic scaling dimension,  $y_t$  the temperature exponent, and  $y_u$  the exponent of the field  $u$ , and  $a_1$  and  $b_1$  are unknown amplitudes. Further corrections may also be present. Since we have an algorithm available that calculates  $X_h(t, u, L)$  (with  $t$  and  $u$  expressed as a function of  $x$ ), we can estimate the critical point by numerically solving  $x$  in the equation

$$X_h(x, L) = X_h(x, L + 1), \quad (8.25)$$

which is a form of ‘phenomenological renormalization’ [16]. After substitution of Eq. (8.24) one finds that, at the solution,  $t$  and  $u$  satisfy

$$t \propto u L^{y_u - y_t}. \quad (8.26)$$

Since  $y_t > 0$  and  $y_u < 0$ , we expect that  $t \rightarrow 0$  for  $L \rightarrow \infty$ , i.e., the solutions of Eq. (8.25), which we denote  $x^{(0)}(L)$ , converge to the critical point. These solutions were fitted by solving for  $x^{(1)}(L)$ ,  $c^{(1)}(L)$  and  $y_u - y_t$  in the three following equations with  $L' = L, L - 1$ , and  $L - 2$ :

$$x^{(0)}(L') = x^{(1)}(L) + c^{(1)}(L) L'^{y_u - y_t}, \quad (8.27)$$

which leads to a sequence  $x^{(1)}(L)$  that is shorter than the original sequence  $x^{(0)}(L)$  but usually shows faster apparent convergence. Another iteration step can be attempted on the basis of

$$x^{(1)}(L') = x^{(2)}(L) + c^{(2)}(L) L'^{y_u - y_t}, \quad (8.28)$$

which may lead to even better estimates of the critical point.

A similar analysis of the critical point can be performed on the basis of the scaled interface gap

$$X_m(t, u, L) \equiv \frac{L}{2\pi\xi_m(t, u, L)}, \quad (8.29)$$

using the same type of fits as for the scaled magnetic gap.

We have also attempted to find solutions of Eq. (8.25) with  $\xi_h$  replaced by the energy-energy correlation length, but here complications arise. The functions  $X_t(x, L)$  typically display an extremum near the critical point, and solutions of the scaling equation Eq. (8.25), with  $X_t$  instead of  $X_h$ , do not always exist. In particular for  $n > 1$  we did not obtain a

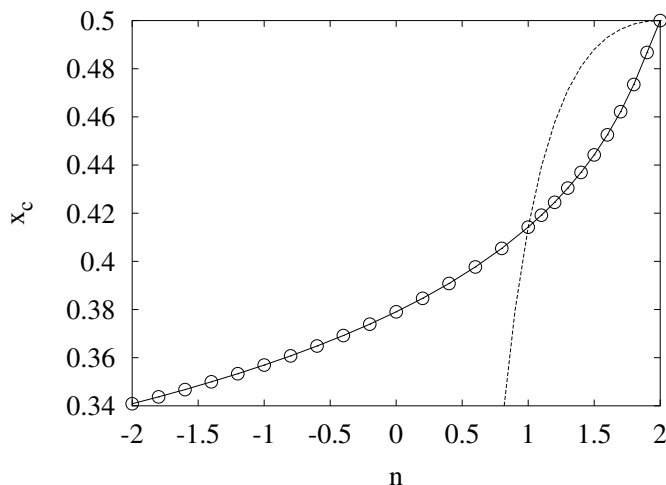


Figure 8.1: Critical points of the  $v = 0$  cubic model. The data points show the numerical results of the transfer-matrix analysis, and the curve is added as a guide to the eye. The estimated error bars are smaller than the size of the symbols. The dashed line shows the critical value of  $x_c$  as function of  $n$  given by Eq. (8.14), which, except for  $n = 1$  and  $2$ , is not consistent with our numerical data.

satisfactory set of solutions, and we have not pursued this way to obtain further data for the critical point. Instead, we located the extremum of  $X_t(x, L)$  as a function of  $x$ . The finite-size-scaling equation for the correlation length indicates that this extremum will converge to the critical point.

The estimated critical points are shown in Fig. 8.1. For  $n \neq 1, 2$  they do not agree with Eq. (8.14). For instance, that equation would predict  $x_c = 0.48803 \dots$  for  $n = 1.5$ , which is incompatible with the numerical result (see also Table 8.1). Thus we have to conclude that Eq. (8.14), which does indeed lack a solid basis, is not valid for all values of  $n$ .

Several modified fitting procedures were applied. Assuming that the cubic model reduces to the  $O(n)$  universality class, we have analytic evidence for the values of  $y_u$  and  $y'_u$  as a function of  $n$ . First, according to the renormalization scenario, the cubic perturbation of the  $O(n)$  symmetry corresponds with an irrelevant field with an exponent [5]

$$y_c = \frac{(1-g)(1+3g)}{2g}, \quad (8.30)$$

where

$$\cos(\pi g) = -n/2, \quad 1 \leq g \leq 2. \quad (8.31)$$

Corrections due to this field are expected to be serious for  $n \rightarrow 2$ , since  $y_c \rightarrow 0$ . Second, irrelevant temperature-like fields may correspond with some scalar operators whose dimensions are entries  $X_{1,q}$  with  $q > 3$  in the Kac table [17, 18]

$$X_{p,q} = \frac{[p(m+1) - qm]^2 - 1}{2m(m+1)} \quad (8.32)$$

with  $m = 1/(g - 1)$  for the cubic model [19]. For  $g = 5$  we find an irrelevant exponent

$$y_i = \frac{6g - 12}{g}, \quad (8.33)$$

which has small values for  $n > 0$  but becomes marginal when  $n \rightarrow -2$ . The final results, and their estimated errors, were obtained from the analyses of the three types of scaled gap, and the degree of consistency between different types of fits mentioned above. The best estimates obtained from  $X_h(t, u, L)$  and  $X_m(t, u, L)$ , and the overall best estimates which also include data from  $X_t(t, u, L)$ , are shown in Table 8.1.

## 8.5 Universal properties of the cubic model

The asymptotic finite-size dependence of the reduced free energy per site at the critical point is [19, 20]

$$f(L) \simeq f(\infty) - \frac{\pi c}{6L^2}, \quad (8.34)$$

where  $c$  is the conformal anomaly of the model, which characterizes universality classes and determines sets of critical exponents [21, 22]. We have calculated the finite size data for the free energy at the extrapolated critical points, and estimated  $c$  as  $c^{(1)}(L)$  from the free energy density for two consecutive system sizes by solving

$$c^{(1)}(L) = 6[f(L) - f(L + 1)] / [\pi\{1/L^2 - 1/(L + 1)^2\}]. \quad (8.35)$$

This leads to a sequence of estimates of  $c$  that can be extrapolated by means of power-law fits, analogous to the procedure used to determine the critical points. After a second iteration step, the estimates of  $c$  seem almost converged, in the sense that the results for the largest few values of  $L$  display differences of only a few times  $10^{-5}$ . But at the same time these data display a shallow extremum (except for  $n = 1$  and  $2$ , where the apparent convergence is much better), so that it is difficult to estimate the uncertainty in the extrapolated results. Because the first iteration step shows that the finite-size dependence of the estimates of  $c$  is close to  $-2$ , we have also applied iteration steps with the exponent fixed at this value. The results were similar to those obtained with free exponents, and again displayed a shallow extremum. Under these circumstances we made a crude error estimate of ten times the difference between the two estimates for the largest available  $L$  values, after two iteration steps. The best estimate was taken by extrapolating the last two estimates, using again ten times the aforementioned difference. A better apparent convergence was found when a fixed exponent  $y_c - 2$  was used in the second iteration step. The results are shown in Table 8.2. The numerical errors were estimated from the finite-size dependence of the results of the last fit procedure, except for  $n = 1.9$ , where the error bars of both fit procedures did not overlap and we used the difference between both types of fit instead. Most of our results are in good agreement with the theoretical values:

$$c = 1 - \frac{6(g - 1)^2}{g}, \quad (8.36)$$

Table 8.1: Critical points  $x_c$  as determined from the scaling formulas for the magnetic and interface correlation length for system sizes  $L$  and  $L + 1$ , and from the extrema of the energy-like correlation length as  $x$  is varied. The estimated numerical uncertainty in the last decimal place is shown in parentheses. The ‘best estimates’ are based on the results in the two preceding columns and on an analysis of the minima in the functions  $X_t(x, L)$  as described in the text. For  $n = 1$  we find accurate agreement with the exact result  $x_c = \sqrt{2} - 1$ , and for  $n = 2$  with  $x_c = 1/2$ . For  $n = 0$ , the absence of loops prevents the determination of  $x_c$  using  $X_m$ .

$g$	$n$	$x_c$ (from $X_h$ )	$x_c$ (from $X_m$ )	$x_c$ (best estimate)
1.0	2.0	0.5000000 (1)	0.4999999 (1)	0.5000000 (1)
1.10108	1.9	0.4869 (2)	0.48673 (5)	0.48675 (5)
1.14357	1.8	0.4736 (1)	0.47345 (2)	0.47346 (2)
1.17660	1.7	0.46212 (5)	0.46214 (1)	0.46214 (1)
1.20483	1.6	0.45257 (5)	0.45254 (1)	0.45254 (1)
1.23005	1.5	0.44423 (5)	0.44424 (1)	0.44424 (1)
1.25318	1.4	0.43695 (2)	0.436935 (5)	0.43694 (1)
1.27477	1.3	0.43042 (1)	0.430415 (5)	0.430416 (5)
1.29517	1.2	0.424530 (5)	0.424527 (2)	0.424528 (2)
1.31463	1.1	0.419155 (5)	0.419154 (2)	0.419154 (2)
1.33333	1.0	0.4142134 (2)	0.4142135 (1)	0.4142135 (1)
1.36901	0.8	0.405384 (1)	0.405384 (1)	0.405384 (1)
1.40301	0.6	0.3976654 (5)	0.397666 (1)	0.397666 (1)
1.43591	0.4	0.3908110 (5)	0.3908115(5)	0.390813 (1)
1.46812	0.2	0.3846495 (5)	0.3846488(5)	0.384649 (1)
1.5	0.0	0.3790528 (3)	—	0.379053 (1)
1.53188	-0.2	0.3739287 (5)	0.3739282(4)	0.373929 (1)
1.56409	-0.4	0.3692057 (5)	0.3692062(4)	0.369206 (1)
1.59699	-0.6	0.3648275 (5)	0.3648278(4)	0.364828 (1)
1.63099	-0.8	0.360748 (1)	0.3607480(5)	0.360748 (1)
1.66667	-1.0	0.373930 (1)	0.3569302(4)	0.356930 (1)
1.70483	-1.2	0.353344 (1)	0.3533436(5)	0.353344 (1)
1.74682	-1.4	0.349962 (2)	0.3499630(5)	0.349963 (2)
1.79517	-1.6	0.346766 (2)	0.3467667(5)	0.346767 (2)
1.85643	-1.8	—	0.343736 (2)	0.343737 (2)
2.0	-2.0	—	0.340856 (3)	0.340856 (3)

Table 8.2: Conformal anomaly and temperature scaling dimension  $X_t$  as determined by transfer-matrix calculations described in the text. Estimated error margins in the last decimal place are given in parentheses. For comparison, we include the theoretical values of the  $O(n)$  model for  $n < 2$ , and of the corresponding Ashkin-Teller model for  $n = 2$ . The numerical results are indicated by ‘num’, theoretical values by ‘theory’.

$n$	$c(\text{num})$	$c(\text{theory})$	$X_t(\text{num})$	$X_t(\text{theory})$
2.0	1.00000 (1)	1.00000	1.500000 (1)	3/2
1.9	0.9464 (9)	0.94432	1.60 (5)	1.63279
1.8	0.8920 (2)	0.89186	1.49 (2)	1.49783
1.7	0.8410 (1)	0.84096	1.405 (5)	1.39962
1.6	0.7912 (1)	0.79106	1.319 (2)	1.31996
1.5	0.7418 (1)	0.74184	1.251 (2)	1.25189
1.4	0.6931 (1)	0.69309	1.192 (1)	1.19187
1.3	0.64465 (5)	0.64465	1.1385 (5)	1.13782
1.2	0.59640 (2)	0.59639	1.0890 (5)	1.08840
1.1	0.54820 (2)	0.54820	1.0428 (5)	1.04269
1.0	0.50000 (1)	1/2	1.000000 (1)	1
0.8	0.40321 (1)	0.40321	0.92182 (1)	0.92182
0.6	0.30541 (1)	0.30541	0.85102 (1)	0.85101
0.4	0.20602 (1)	0.20602	0.78570 (1)	0.78570
0.2	0.10444 (1)	0.10443	0.72456 (3)	0.72458
0.0	0.00000 (1)	0	0.66665 (2)	0.66667
-0.2	-0.10805 (1)	-0.10805	0.6110 (2)	0.61116
-0.4	-0.22065 (1)	-0.22065	0.55735 (6)	0.55739
-0.6	-0.33897 (5)	-0.33900	0.5044 (4)	0.50472
-0.8	-0.4646 (1)	-0.46469	0.4520 (5)	0.45250
-1.0	-0.5997 (3)	-3/5	0.3996 (5)	2/5
-1.2	-0.7479 (5)	-0.74840	0.3463 (4)	0.34627
-1.4	-0.914 (2)	-0.91572	0.288 (2)	0.28988
-1.6	-1.110 (4)	-1.11331	0.2276 (10)	0.22820
-1.8	-1.36 (1)	-1.37060	0.143 (5)	0.15467
-2.0	-1.85 (5)	-2	—	0

which follow after the substitution of the formula [19]  $m = 1/(g - 1)$  in the relation [21] between  $m$  and  $c$ , i.e.,  $c = 1 - 6/[m(m + 1)]$ . But the result for  $n = 1.9$  does not agree well with the theoretical value; we note that the small value of the cubic crossover exponent, which becomes marginal at  $n = 2$ , may well lead to imprecise results and error estimates. Also at and near  $n = -2$  the results do not agree well with the theory. This may be attributed to slowly convergent logarithmic corrections due to the marginal exponent  $y_i$  given by Eq. (8.33).

Next, we analyze the results for the magnetic gaps. After substitution of the solutions of Eq. (8.25), which behave as Eq. (8.26), in Eq. (8.24), one finds that the magnetic scaled gaps at the solutions converge to  $X_h$  as:

$$X_h(L) = \bar{X}_h + ruL^{y_u} + \dots, \quad (8.37)$$

where  $r$  is an unknown constant. The magnetic scaled gaps at the solutions of the scaling equation in the previous section were already available. They were fitted using a similar procedure as used for the determination of the critical points. We found that the leading irrelevant exponent was consistent with the predicted cubic perturbation exponent given in Eq. (8.30), and we accordingly treated  $y_u$  as a known parameter in the fits. The extrapolated magnetic scaling dimensions are shown in Table 8.3. Again, different fit procedures, with the finite-size exponent left free, and more iteration steps, were applied. The error estimates are based on the apparent convergence and on the differences between the various types of fit. The final results appear to agree with the theoretical values for the  $O(n)$  universality class [4]:

$$X_h = \frac{g}{8} - \frac{(1-g)^2}{2g}, \quad (8.38)$$

where we note that the Ashkin-Teller model (or  $(2, 2)$  model) has the same magnetic scaling dimension [23, 24]  $X_h = 1/8$  as the  $O(2)$  model.

A similar analysis was performed on the scaled interface gaps at the solutions of the scaling equation for the interface scaled gap. These scaled gaps converge to the interface scaling dimension. The results for the interface scaling dimension are shown in Table 8.3. They are to be compared with the known interface exponent in the  $O(n)$  universality class [12], which are given by the entry  $p = 1, q = 2$  in the Kac table:

$$X_m = \frac{3}{2g} - 1, \quad (8.39)$$

which is obtained by the substitution of  $m = 1/(g - 1)$  in the more common form  $X_{1,2} = [(m - 1)^2 - 1]/2m(m + 1)$  of the Kac formula.

Our result for  $X_m$  at  $n = 2$  is different from  $X_{1,2} = 1/2$  and thus illustrates that the  $n = 2$  cubic loop model falls outside the  $O(2)$  universality class. It is to be compared with results for the Ashkin-Teller model [24, 25] which are also summarized by Baxter [26]. In the notation used there, we have the exact result  $\beta_e^{8V} = 3/4$  for the end point of the Ashkin-Teller line at  $K \rightarrow \infty$ . This exponent may, in our notation, be put equal to  $X_m/(2 - X_t)$  where  $X_t = 3/2$ . This does indeed lead to  $X_m = 3/8$ .

Table 8.3: The magnetic dimension  $X_h$  and the interface dimension  $X_m$  as extrapolated from their values at the solutions of the scaling equation of the correlation length. Estimated numerical uncertainties in the last decimal place are given in parentheses. For comparison, we include the theoretical values of the  $O(n)$  model for  $n < 2$ , and of the Ashkin-Teller model for  $n = 2$ . The numerical results are indicated by '(num)', the theoretical values by '(theory)'. The absence of loops annihilates the interface gap for all  $L$ , which leads to the exact numerical result  $X_m = 0$ .

$n$	$X_h(\text{num})$	$X_h(\text{theory})$	$X_m(\text{num})$	$X_m(\text{theory})$
2.0	0.12498 (1)	1/8	0.37500 (1)	3/8
1.9	0.128 (1)	0.13300	0.350 (5)	0.36230
1.8	0.1308 (2)	0.13393	0.313 (2)	0.31169
1.7	0.1335 (3)	0.13382	0.274 (2)	0.27486
1.6	0.1320 (1)	0.13319	0.244 (1)	0.24499
1.5	0.1316 (1)	0.13224	0.2195 (5)	0.21946
1.4	0.1307 (1)	0.13107	0.1969 (2)	0.19695
1.3	0.1296 (1)	0.12973	0.1767 (1)	0.17668
1.2	0.1280 (1)	0.12826	0.15814 (5)	0.15815
1.1	0.12647 (1)	0.12668	0.14105 (5)	0.14101
1.0	0.12499 (1)	0.12500	0.12499 (1)	1/8
0.8	0.12138 (3)	0.12139	0.095681 (2)	0.09568
0.6	0.11750 (2)	0.11749	0.069127 (3)	0.06913
0.4	0.11333 (2)	0.11332	0.044636 (3)	0.04464
0.2	0.10889 (2)	0.10888	0.021718 (4)	0.02172
0.0	0.10418 (2)	0.10417	0	0
-0.2	0.09914 (3)	0.09915	-0.020812 (3)	-0.02081
-0.4	0.09378 (3)	0.09379	-0.04097 (1)	-0.04098
-0.6	0.08801 (3)	0.08804	-0.06072 (1)	-0.06073
-0.8	0.08175 (5)	0.08182	-0.08030 (1)	-0.08031
-1.0	0.0748 (3)	0.07500	-0.09999 (1)	-1/10
-1.2	0.0674 (1)	0.06740	-0.12012 (2)	-0.12015
-1.4	0.0585 (3)	0.05871	-0.1412 (1)	-0.14130
-1.6	0.0483 (4)	0.04829	-0.1640 (1)	-0.16442
-1.8	0.031 (5)	0.03450	-0.1901 (2)	-0.19200
-2.0	—	0	-0.227 (3)	-1/4

We also calculated the temperature scaled gaps  $X_t(x, L)$  at the extrapolated critical points. We expect the following behavior of these gaps:

$$X_t(L) = X_t + puL^{y_u} + \dots, \quad (8.40)$$

where  $p$  is another unknown constant. Similar fits as before lead to results for the temperature scaling dimension that are included in Table 8.2. The results agree with the theoretical prediction [4] for the  $O(n)$  model

$$X_t = \frac{4}{g} - 2 \quad (8.41)$$

except for the case  $n = 2$ , where our numerical result goes to  $3/2$  in accordance with the exact result [24, 25] for the temperature scaling dimension of the Ashkin-Teller model for  $K \rightarrow \infty$ .

## 8.6 Discussion

In general, the discreteness of the  $n$ -component cubic model defined by Eq. (8.1) will enforce the existence of a long-range ordered phase at sufficiently low temperatures, also for  $n > 2$ . However, the parameters  $K$  and  $M$  in Eq. (8.1) become infinite at the  $n = 2$  critical point, and Eq. (8.7) indeed restricts these parameters to  $K + M \leq \ln 2$ . This quantity, which specifies the energy difference between parallel ( $\vec{s}_i \cdot \vec{s}_j = 1$ ) spins and perpendicular ( $\vec{s}_i \cdot \vec{s}_j = 0$ ) spins, is not sufficient to reach a long-range-ordered phase in a range  $n > 2$ . We did not search for phase transitions that may occur for  $n > 2$  in the unphysical range of  $K$  and  $M$ , but still corresponding to real values of the bond weight  $x$ .

For  $n \leq 2$  we find clear evidence for a phase transition to the ordered phase. In the interval  $-2 \leq n \leq 2$  we have determined the critical points of the  $n$ -component cubic model as given by Eqs. (8.1) and (8.7), or by Eq. (8.8). For the exactly solved cases  $n = 1$  and  $n = 2$  we find good agreement with the exact values as given in Table 8.1. Our results for the scaling dimensions, i.e.,  $X_t$  associated with the temperature,  $X_h$  associated with the magnetic field, and  $X_m$  associated with the introduction of an antiferromagnetic ‘seam’ in the model, agree accurately with the  $O(n)$  universality classes, with the exception of the case  $n = 2$  where the model reduces to a special case of the Ashkin-Teller model. For the latter case  $n = 2$ , our results for the scaling dimensions agree with the exact results for the Ashkin-Teller model. The fact that these scaling dimensions are different from those for the  $O(2)$  universality class is related with the cubic anisotropy which may be seen as a perturbation of the  $O(n)$  symmetry. This perturbation is irrelevant for  $n < 2$  but marginal [5] for  $n = 2$ . This proof of irrelevance for  $n < 2$  applies to small cubic perturbations of the isotropy. Our numerical results show that the cubic perturbation remains irrelevant even in the extreme anisotropic case described by Eqs. (8.1) and (8.7). However, when  $n$  approaches 2, the exponent  $y_c$  associated with the cubic anisotropy field approaches marginality and our numerical results thus become less accurate. The cubic

anisotropy is truly marginal at  $n = 2$  and parametrizes the Ashkin-Teller model. For this reason, the cubic crossover phenomena are absent for  $n = 2$  and the numerical results are again relatively accurate. The temperature scaling dimension of the cubic model and its consistency with  $O(n)$  universality were already determined [2] for a range  $-1 \leq n \leq 1$ . The present results extend the range of  $n$  and provide more precise numbers, as well as independent evidence involving the dimensions  $X_h$  and  $X_m$ . The numerical accuracy of our analysis is such that the  $O(n)$  universality of the  $n < 2$  cubic model seems reasonably convincing. We note that numerical results for the  $O(n)$  model on the square lattice [12] are even more accurate; however, for that case the exact critical point is known, and the cubic anisotropy field, and thereby the corresponding corrections to scaling, vanish.



# Bibliography

- [1] P. W. Kasteleyn and C. M. Fortuin, J. Phys. Soc. Jpn. suppl. **26**, 11 (1969).
- [2] H. W. J. Blöte and M. P. Nightingale, Physica A **129**, 1 (1984).
- [3] J. L. Cardy and H. W. Hamber, Phys. Rev. Lett. **45**, 499 (1980).
- [4] B. Nienhuis, Phys. Rev. Lett. **49**, 1062 (1982); J. Stat. Phys. **34**, 731 (1984).
- [5] B. Nienhuis, in *Phase Transitions and Critical Phenomena*, edited by C. Domb and J. L. Lebowitz (Academic Press, London 1987), Vol. **11**.
- [6] E. Domany and E. K. Riedel, Phys. Rev. B **19**, 5817 (1979); Phys. Rev. Lett. **40**, 561 (1978).
- [7] F. Y. Wu and Y. K. Wang, J. Math. Phys **17**, 439 (1976).
- [8] W. Guo, X. Qian, H. W. J. Blöte, F. Y. Wu, Phys. Rev. E **73**, 026104 (2006).
- [9] J. Ashkin and E. Teller, Phys. Rev. **64**, 178 (1943).
- [10] This observation is due to F. Y. Wu (see also Ref. [8]).
- [11] H. W. J. Blöte and M. P. Nightingale, Physica A **112**, 405 (1982).
- [12] H. W. J. Blöte and B. Nienhuis, J. Phys. A **22**, 1415 (1989).
- [13] M. Suzuki, Progr. Theor. Phys. **58**, 1142 (1977).
- [14] For reviews, see e.g. M. P. Nightingale, in *Finite-Size Scaling and Numerical Simulation of Statistical Systems*, edited by V. Privman (World Scientific, Singapore, 1990); and M. N. Barber, in *Phase Transitions and Critical Phenomena*, Vol. **8**, edited by C. Domb and J. L. Lebowitz (Academic, New York, 1983).
- [15] J. L. Cardy, J. Phys. A **17**, L385 (1984).
- [16] M. P. Nightingale, Phys. Lett. A **59**, 486 (1977); Proc. K. Ned. Akad. Wet., Ser. B: Phys. Sci. **82**, 235 (1979).
- [17] D. Friedan Z. Qiu and S. Shenker, Phys. Rev. Lett. **52**, 1575 (1984).

- [18] V. G. Kac, in "Group Theoretical Methods in Physics", edited by W. Beiglbock en A. Bohm, Lecture Notes in Physics, Vol. **94**, 441 (Springer, New York, 1979).
- [19] H. W. J. Blöte, J. L. Cardy and M. P. Nightingale, Phys. Rev. Lett. **56**, 742 (1986).
- [20] I. Affleck, Phys. Rev. Lett. **56**, 746 (1986).
- [21] J. L. Cardy, in *Phase Transitions and Critical Phenomena*, edited by C. Domb and J. L. Lebowitz (Academic Press, London, 1987), Vol. **11**.
- [22] A.A. Belavin, A.M. Polyakov and A.B. Zamolodchikov, J. Stat. Phys. **34**, 763 (1984).
- [23] I. G. Enting, J. Phys. A **8**, L35 (1975).
- [24] M. P. M. den Nijs, Phys.Rev. B **23**, 6111 (1981).
- [25] H. J. F. Knops, Ann. Phys. (N. Y.) **128**, 448 (1980).
- [26] R. J. Baxter, *Exactly Solved Models in Statistical Mechanics* (Academic Press, New York, 1982).

# Chapter 9

## Universal parameters of three-dimensional Ising systems

We perform a Monte Carlo analysis of four three-dimensional lattice models that are supposed, on the basis of their symmetry, to belong to the Ising universality class. The models are chosen such that their irrelevant temperature fields cover a relatively wide range, which is helpful in the determination of the parameters describing the corrections to scaling. As a consequence, the error margins of the universal parameters describing Ising criticality in three dimensions can be reduced. The critical exponents describing the thermodynamic singularities are determined by the temperature renormalization exponent  $y_t = 1.58718(8)$  and the magnetic renormalization exponent  $y_h = 2.48160(6)$ . The corrections to scaling are governed by the irrelevant exponent  $y_i = -0.818(3)$ . Furthermore, nonuniversal data including the critical points are obtained for the four Ising-like models, which are the spin- $\frac{1}{2}$  model and a spin-1 model on the simple-cubic lattice, the spin- $\frac{1}{2}$  model on the diamond lattice, and the spin- $\frac{1}{2}$  model on the simple-cubic lattice with 32 equivalent neighbors.

### 9.1 Introduction

The universality class of the three-dimensional Ising model covers a wide range of models and systems with short-range interactions and a scalar order parameter. Among these, the critical points of simple gas-liquid systems may be considered the most common ones. It is thus appropriate to formulate theoretical approaches to describe the phase transitions of this type. In the absence of exact solutions, many efforts have been made to obtain the universal constants of this class as accurately as possible. The development of the renormalization theory [1] yielded not only more and new insight in phase transitions, but also accurate results for the universal exponents; see Refs. [2,3] and references therein. Furthermore, the increasing number of terms in series expansions of the Ising model enables increasingly accurate estimates of these exponents, see e.g., Ref. [4] and references therein. In a different type of approach, the recent availability of fast and relatively cheap computers has opened the possibility to obtain similarly accurate estimates by means of Monte Carlo

simulations and finite-size scaling, see e.g. Ref. [5] and references therein.

Since the latter approach will also be the subject of the present work, we outline the ideas behind it. The finite-size scaling behavior of observables such as the specific heat, susceptibility etc. at criticality is typically described by divergences according to power laws modified by corrections to scaling. In first order, these corrections are proportional to the irrelevant renormalization fields that parametrize the critical subspace of the Ising model.

The presence of such corrections naturally leads to a reduction of the accuracy of the determination of the universal parameters. The numerical analysis of such a correction requires the determination of its amplitude as well as of the associated irrelevant exponent. These corrections are usually important, and neglecting them has yielded incorrect results [6–8].

While an accurate determination of the irrelevant exponent would favor the use of an Ising model with a relatively large correction amplitude, i.e., a large irrelevant field, a problem may arise in the accuracy of the numerical analysis because the quadratic term in the irrelevant scaling field may become important, thus affecting the accuracy of the determination of the irrelevant exponent and other universal parameters. A model with a small irrelevant field can well be used to determine the other universal parameters, at least if the irrelevant exponent is known. However, such a model is obviously not suitable to determine the irrelevant exponent.

The strategy followed in Ref. [5, 9] therefore relied on the simultaneous analysis of several models, with considerably different irrelevant fields. The availability of such Monte Carlo-generated finite-size data enables an analysis that can be done in two stages, the first of which is to check whether the data for the different models are consistent with universality. Then, the second stage, which is based on the assumption that universality is exactly satisfied, combines the relevant Monte Carlo data for all models and applies a fitting procedure in which the universal parameters occur only once.

The choice of the models is based on the observed dependence of the correction-to-scaling amplitudes on further-neighbor interactions [10] and on the introduction of a vacant spin state as specified by the Blume-Capel model [11, 12]. The effects of interactions with further neighbors on the irrelevant field can be understood in terms of the crossover between the long-range mean-field fixed point and the short-range Ising fixed point [13]. This explains why the variation of the number of interacting neighbors has a strong effect on the correction-to-scaling amplitudes. Furthermore the relation between the activity of the vacancies (spin-zero states) and the irrelevant field, which was described in the renormalization analysis of the Potts model by Nienhuis et al. [14], explains the behavior of the correction amplitudes in the Blume-Capel model.

The present chapter selects four of the models of Ref. [5] and adds new simulation results for system size  $L = 256$ , and results for smaller systems with improved statistics, with the intention to narrow down the statistical error margins and thus to improve our knowledge of the universal parameters.

The outline of the next sections is as follows. Section 9.2 defines the four models and the simulation methods, and supplies some further details on the simulations and the

computational resources. Most of the simulations took place on personal computers, but part of the data for the nearest-neighbor Ising model were generated by a special-purpose computer (the Cluster Processor) [15]. Section 9.3 provides finite-size scaling analyses for the four models separately, and the results are subjected to a consistency test with universality. An analysis of the Ising universal parameters by means of a simultaneous fitting procedure is performed in Section 9.4. A short discussion in Section 9.5 concludes this chapter.

## 9.2 Models, simulations and random-number generator

The present Monte Carlo analysis includes four Ising-like models. They are defined in terms of the following spin-1 Hamiltonian

$$\mathcal{H}/k_{\text{B}}T = -K \sum_{i<j} \theta(R - r_{ij}) s_i s_j + D \sum_k (s_k^2 - 1), \quad (9.1)$$

where the sums are over the sites of the diamond lattice (model 1) or the simple cubic lattice (models 2-4). The lattice sites are labeled by  $i, j$  and  $k$ . The distance between sites  $i$  and  $j$  is denoted  $r_{ij}$ , and the step function  $\theta(x)$ , which is equal to 0 for  $x < 0$  and equal to 1 for  $x \geq 0$ , defines a cutoff of the interactions of strength  $K$  at range  $R$ . The ranges  $R$  are chosen such that interactions are restricted to the four nearest neighbors (model 1), the six nearest neighbors (models 2 and 4), or the 32 closest neighbors (model 3). The spins can assume the values  $s_i = \pm 1$  or 0. However, for models 1, 2, and 3 the parameter  $D$  is set to the value  $D = -\infty$  so that the  $s_i = 0$  state is excluded, and the model in effect reduces to the spin- $\frac{1}{2}$  model. For model 4, we take  $D = \ln 2$  which leads to a system with strongly reduced corrections to scaling [9]; moreover, the model can be simply mapped on a spin- $\frac{1}{2}$  model which can be simulated by a cluster algorithm [9]. A newer variant of this algorithm does not use the spin- $\frac{1}{2}$  representation, and acts directly on spins 1, and includes flips between spin-1 and 0 states [5] without the need to include local updates by Metropolis steps.

The definitions of the four models are summarized in Tab. 9.1. For the models on the simple cubic lattice, the unit cell contains one site and the finite-size parameter  $L$  is thus equal to the size of the periodic box, expressed in nearest-neighbor distances. The unit cell of the diamond lattice can be represented as a cubic cell containing eight sites. It is thus convenient to assign a size 2 to this unit cell, so that a system of size  $L$  contains  $L^3$  spins, just as the models on the simple cubic lattice. Expressed in this unit, the nearest-neighbor distance is however  $\sqrt{3}/2$ .

The Monte Carlo simulations used single-cluster updates according to the Wolff method [16]. The algorithms for the diamond and simple-cubic models with nearest-neighbor interactions were more or less standard; those for the spin-1 model and for the model with 32 equivalent neighbors were described elsewhere [5, 17]. These algorithms were applied to

Table 9.1: Definition of the four simulated Ising models. The abbreviation “s.c.” stands for “simple cubic”, “n.b.” for the number of interacting neighbors coupled to each spin.

Model	$D$	Lattice	model description
1	$-\infty$	diamond	spin- $\frac{1}{2}$ with 4 n.b.
2	$-\infty$	s. c.	spin- $\frac{1}{2}$ with 6 n.b.
3	$-\infty$	s. c.	spin- $\frac{1}{2}$ with 32 n.b.
4	$\ln 2$	s. c.	spin-1 with 6 n.b.

systems of size  $L \times L \times L$  with periodic boundary conditions. The bulk of the simulations took place very close to the known critical points [5]. A small fraction of the computer time was used to determine the temperature-dependences of the sampled quantities for smaller systems  $L < 20$ . Table 9.2 presents the number of ten millions of samples taken per system size and the number of simulation sweeps before taking each sample. The system sizes were taken in the range  $4 \leq L \leq 256$ . The essential parameters describing the simulations are listed in Tab. 9.2.

Table 9.2: Simulation lengths (in ten million samples) and number of Wolff steps per sample. The notation  $M \times N$  means that  $10^7 M$  samples were taken at intervals consisting of  $N$  single-cluster updates. Smaller system sizes  $L < 20$  are not shown in this table but were also included in the analysis.

Model\ $L$	20	22	24	28	32
1	$205 \times 10$	$205 \times 10$	$202 \times 10$	$202 \times 10$	$282 \times 10$
2	$148 \times 10$	$92 \times 10$	$80 \times 10$	$75 \times 10$	$69 \times 10$
3	$87 \times 20$	$60 \times 22$	$60 \times 24$	$59 \times 28$	$48 \times 32$
4	$175 \times 6$	$160 \times 6$	$167 \times 6$	$160 \times 6$	$125 \times 8$
Model\ $L$	40	48	64	128	256
1	$200 \times 10$	$142 \times 20$	$104 \times 20$	$20 \times 40$	$3.48 \times 64$
2	$108 \times 10$	$60 \times 20$	$56 \times 32$	$19 \times 64$	$3.4 \times 128$
3	$66 \times 40$	$96 \times 48$	$48 \times 64$	$16 \times 128$	$2.7 \times 256$
4	$118 \times 10$	$100 \times 12$	$56 \times 16$	$23 \times 32$	$3 \times 64$

Much attention is needed in order to obtain Monte Carlo results free of biases due to imperfect random number generators. This means actually that such biases must be reduced to a level that is small in comparison with the statistical uncertainties. In this work we employ pseudo-random-number generators based on binary shift registers. It is known that such pseudo-random-numbers are not sufficiently random for some purposes and introduce significant errors (see, e.g., Refs. [18–24]). In many applications, the deviations from randomness are dominated by three-bit correlations which are a direct consequence

of the production rule.

In order to avoid systematic effects we have to deal with the problem that the present simulations are of a considerable length, and we wish to avoid tests that have a similar magnitude. For this reason we make use of the ‘scalability’ of the biases as reported earlier for cluster simulations [25]. On this basis we can extrapolate the biases found for smaller systems and shorter shift registers to estimate the bias effects in our simulations. Additional confidence in the validity of our approach is based on the observation [25] that the magnitude of the observed biases decreases rapidly as a function of the number of correlated bits. By modulo-two addition of two maximum-length shift registers with a three-bit production rule, it is possible to form a new sequence whose dominant correlation is a nine-bit one, which does almost satisfy the maximum-length criterion. This procedure suppresses the biases below the observable threshold according to reasonable extrapolations [25].

## 9.3 Separate finite-size-scaling analyses

### 9.3.1 Dimensionless ratio $Q$

During the simulations, the magnetization density  $m$  was sampled, as well as its second moment  $\langle m^2 \rangle$  and fourth moment  $\langle m^4 \rangle$ . On this basis we derived the ratio  $Q = \langle m^2 \rangle^2 / \langle m^4 \rangle$ , which is related to the Binder cumulant [26], and tends to a universal constant at criticality. The analysis of  $Q$  formulated here is based on renormalization arguments. Since both  $\langle m^2 \rangle$  and  $\langle m^4 \rangle$  can be expressed in terms of derivatives of the free energy to the magnetic field, the scaling of the free energy yields the scaling behavior of  $Q$  near the critical point. Since the geometric factors, which contain the derivative of the magnetic scaling field to the physical magnetic field coupled to  $m$ , cancel between the numerator and denominator of  $Q$ , the zeroth order term in  $Q$  is dimensionless. The finite-size-scaling behavior of  $Q$  follows by including the finite-size parameter  $L$  in the free energy, taking the appropriate derivatives, and renormalization to finite size 1, as

$$Q(t, u, L) = \tilde{Q}(L^{y_t} t, L^{y_1} u) + \sum_k b_k L^{y_k}, \quad (9.2)$$

where  $y_1 \equiv y_i$  is the irrelevant temperature exponent. The temperature field which is denoted  $t$ , and the irrelevant field denoted  $u$ , are nonuniversal parameters, while the function  $\tilde{Q}$  and the exponents  $y_t$  and  $y_1$  are universal. A few correction terms on the right may be included. One is due to the analytic background term in the second derivative of the free energy to the magnetic field, whose leading term is of order  $L^{2y_h - d}$ , where  $d = 3$  is the dimensionality and  $y_h$  is the magnetic renormalization exponent. This effect leads to a correction exponent  $y_2 = d - 2y_h$ . Furthermore the temperature scaling field may depend in second order on the physical magnetic field, so that higher order derivatives of the free energy to the magnetic field will include corrections with finite-size exponent  $y_3 = y_t - 2y_h$ . In order to bring Eq. (9.2) in a suitable form to describe Monte-Carlo generated finite-size

data for  $Q$ , one may expand the parameters  $t$  and  $u$  in the physical field which is the coupling  $K_i$  for model  $i$ . We append the index  $i$  also to other model-dependent nonuniversal parameters:

$$\begin{aligned} t &= a_i(K_i - K_{ci}) + e_i(K_i - K_{ci})^2 + \dots, \\ u &= u_i + v_i(K_i - K_{ci}) + \dots, \end{aligned} \quad (9.3)$$

where  $a_i$  and  $e_i$  describe the first- and second-order dependence of  $t$  on  $K_i$ , and  $u_i$  is the irrelevant field of model  $i$  at its critical point  $K_{ci}$ . The universal function  $\tilde{Q}$  is expanded as

$$\begin{aligned} \tilde{Q}(L^{y_t}t, L^{y_1}u) &= Q^{(0,0)} + L^{y_t}tQ^{(1,0)} + L^{2y_t}t^2Q^{(2,0)} + L^{3y_t}t^3Q^{(3,0)} + \dots \\ &+ L^{y_1}uQ^{(0,1)} + \dots + L^{y_t+y_1}tuQ^{(1,1)} + \dots, \end{aligned} \quad (9.4)$$

where the expansion coefficients  $Q^{(k,l)}$  are universal. Combination of Eq. (9.2) and the two expansions yields a result of which the leading terms are

$$\begin{aligned} Q &= Q^{(0)} + q_{1i}(K_i - K_{ci})L^{y_t} + q_{2i}(K_i - K_{ci})^2L^{2y_t} + q_{3i}(K_i - K_{ci})^3L^{3y_t} + \\ &+ q_{4i}(K_i - K_{ci})^4L^{4y_t} + c_i(K_i - K_{ci})^2L^{y_t} + b_{1i}L^{y_1} + b_{2i}L^{y_2} + b_{3i}L^{y_3} + \\ &+ d_i(K_i - K_{ci})L^{y_t+y_1}, \end{aligned} \quad (9.5)$$

where we abbreviated  $Q^{(0,0)}$  as  $Q^{(0)}$ . The constants  $q_{ji}$  are the product of universal and nonuniversal constants from both expansions. These as well as other free parameters in Eq. (9.5) were estimated by means of least-squares fits to the Monte Carlo data, for each of the four models. Our first aim is now to determine the universal quantity  $Q^{(0)}$ . To this purpose we set  $y_1 = -0.82(3)$ ,  $y_2 = -1.963(3)$ , and  $y_3 = -3.375(3)$  as already specified in earlier analyses of  $Q$  in Refs. [9, 28], and  $y_t$  was taken to be 1.587 [4, 5]. The data for system sizes  $L < 8$  were not fitted because additional corrections become troublesome in such small systems, as becomes apparent from the residual  $\chi^2$ . The results of these fits are summarized in Tab. 9.3. The statistical errors in the fitted results are shown between parentheses as one standard deviation in the last decimal place. The agreement between the results for the universal quantity  $Q^{(0)}$  in the third column confirms that the four systems fit well in one common Ising universality class. The uncertainty margins are reduced in comparison with the results of Ref. [5].

Another test of universality is possible by a comparison of the amplitudes  $q_{1i}$  and  $q_{2i}$  for the four models. From the expansions given in Eqs. (9.4) and (9.5), one finds that the quantity  $q_{2i}/q_{1i}^2 = Q^{(2,0)}/[Q^{(1,0)}]^2$  is a universal quantity. This is confirmed in the fifth column of Tab. 9.3, which shows that the results are mutually consistent within about one standard deviation.

Also included in Tab. 9.3 are the amplitudes of the corrections due to the irrelevant field of these models. Up to a constant factor these results represent the actual values of the irrelevant scaling field. As mentioned in Ref. [5], these values reflect the positions of the critical points of these systems under a renormalization mapping on the Landau-Ginzburg-Wilson Hamiltonian of the  $\phi^4$  model, which is

$$-\mathcal{H}(\phi)/k_B T = \int d\mathbf{r} [r\phi^2(\mathbf{r}) + v\phi^4(\mathbf{r}) + \nabla^2\phi(\mathbf{r})], \quad (9.6)$$

Table 9.3: Results of the separate fits to the dimensionless ratio  $Q$ . The irrelevant exponent was fixed at  $y_1 = -0.82$ .

Model	$K_c$	$Q^{(0)}$	$q_1$	$q_2/(q_1)^2$	$b_1$
1	0.36973982(5)	0.62343(6)	0.5130(12)	0.78(6)	0.1135(12)
2	0.22165461(3)	0.62347(6)	0.848(4)	0.82(5)	0.0935(12)
3	0.034326874(6)	0.62349(20)	4.98(4)	0.87(11)	-0.228(10)
4	0.39342219(4)	0.62350(4)	0.6643(12)	0.84(4)	-0.0034(5)

where the square-gradient term represents the Ising particle-particle interaction, while the parameter  $r$  is temperature-like, and  $v$  is the irrelevant field. Renormalization analysis of such a system in less than four spatial dimensions [1] shows two fixed points, one of which is located at  $(0, 0)$  and represents the mean-field fixed point, while the other sits at nonzero values ( $r^* < 0, v^* > 0$ ) and represents the Ising fixed point. The crossover scaling function for the Binder ratio [27] provides a scale for the interval between both fixed points, as parametrized by the Ising irrelevant field. The determination of the amplitudes of the irrelevant corrections in  $Q$  thus determine the positions of the four models in the ( $r^* < 0, v^* > 0$ ) diagram shown in Fig. 9.1.

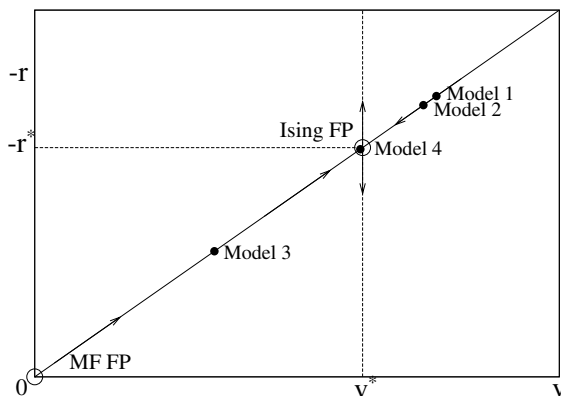


Figure 9.1: Location of the four Ising-like models as projected (as black dots) on the  $(r, v)$  plane of the  $\phi^4$  model, where  $r$  is a temperature-like parameter and  $u = v - v^*$  reflects the amplitude of the irrelevant field. The mean-field and Ising fixed points, denoted as  $\circ$ , lie at  $(0, 0)$  and  $(r^*, v^*)$ , respectively.

The results in Tab. 9.3 were obtained under the assumption that the irrelevant exponent equals  $y_1 = -0.82$ . This value is taken from the literature, e.g., Ref. [5] and references therein.

Next, we proceed without this assumption and treat  $y_1$  as a free parameter in the fit. Understandably, the data for the spin-1 model do not yield meaningful results because

the amplitude of the pertinent correction is too small. But reasonable, although not very accurate, results are obtained for the other three models as summarized in Tab. 9.4.

Table 9.4: Results of separate fits to  $Q$  for models 1 to 3, with  $y_1$  as a free parameter.

Model	$K_c$	$Q^{(0)}$	$y_1$
1	0.36973981(8)	0.6234(4)	-0.81(6)
2	0.22165461(4)	0.6234(4)	-0.81(7)
3	0.034326875(10)	0.6238(4)	-0.77(4)

### 9.3.2 The susceptibility $\chi$

Along similar lines as followed for the dimensionless ratio, one finds that the magnetic susceptibility  $\chi$  behaves as

$$\chi(t, u, L) = x(t) + L^{2y_h - d} \left( \frac{\partial h}{\partial H} \right)^2 \chi(L^{y_t} t, L^{y_1} u, 1), \quad (9.7)$$

where the function  $\chi$  on the right hand side is universal in its two remaining arguments. The contribution  $x(t)$  is determined by the second derivative of the analytical part of the free energy density with respect to the physical magnetic field  $H$ . The dependence of the magnetic scaling field  $h$  on  $H$  is not universal and may, in first order, be denoted as  $h = \sqrt{w_i} H$ . Taylor-expansion of Eq. (9.7) yields

$$\begin{aligned} \chi &= x_i + s_i(K_i - K_{ci}) + L^{2y_h - d} [p_{0i} + p_{1i}(K_i - K_{ci})L^{y_t} + p_{2i}(K_i - K_{ci})^2 L^{2y_t} \\ &+ p_{3i}(K_i - K_{ci})^3 L^{3y_t} + p_{4i}(K_i - K_{ci})^4 L^{4y_t} \\ &+ \sum_k b_{ki} L^{y_k} + d_i(K_i - K_{ci})L^{y_t + y_1}], \end{aligned} \quad (9.8)$$

where we have used the expansion of the temperature field as in Eq. (9.3). The constants  $p_{ji}$  denote the product of universal expansion parameters of the function  $\chi$  and nonuniversal constants including the  $w_i$ . The results of the fits for the four models are given in Tab. 9.5.

### 9.3.3 The derivative $Q_p$

During the Monte Carlo simulations, the nearest-neighbor sum  $e$

$$e = \langle S_{nn} \rangle = \sum_{\langle nn \rangle} \langle s_i s_j \rangle, \quad (9.9)$$

Table 9.5: Separate fits to the susceptibility  $\chi$  with the irrelevant exponent fixed at  $y_1 = -0.82$ . The minimum system sizes used for this fit are  $L = 8$ .

Model	$K_c$	$p_0$	$y_h$	$b_1$
1	0.36973979 (5)	1.758 (3)	2.48147 (14)	-0.47 (1)
2	0.22165462 (3)	1.553 (2)	2.48165 (15)	-0.33 (1)
3	0.034326875 (7)	0.874 (4)	2.4815 (4)	0.44 (2)
4	0.39342227 (8)	0.932 (4)	2.48162 (7)	0.00

was sampled. This quantity represents the interaction energy density for models 1, 2 and 4. For model 3, the nearest-neighbor sum is not the interaction energy but it is still as a quantity that scales as the energy.

Combination with the magnetization data allows the Monte Carlo sampling of the derivative  $Q_p \equiv \partial Q / \partial K_{\text{nn}}$  of the Binder ratio  $Q$  with respect to the nearest-neighbor interaction:

$$Q_p = 2 \frac{\langle m^2 S_{\text{nn}} \rangle}{\langle m^2 \rangle} - \frac{\langle m^4 S_{\text{nn}} \rangle}{\langle m^4 \rangle} - \langle S_{\text{nn}} \rangle = \frac{1}{Q} \frac{\partial Q}{\partial t} \frac{\partial t}{\partial K_{\text{nn}}}. \quad (9.10)$$

The quantity  $Q_p$  is known [5, 9, 28] to yield fairly accurate result for the thermal exponent  $y_t$ . The reason will be discussed later on the basis of its scaling behavior. According to Eq. (9.2), the quantity  $Q_p$  behaves near the critical point as

$$Q_p(t, u, L) = L^{y_t} \frac{\partial t}{\partial K_{\text{nn}}} Q_p(L^{y_t} t, L^{y_1} u, 1). \quad (9.11)$$

Expansion of  $t$  and  $\partial t / \partial K_{\text{nn}}$  in  $K$ , and of the function  $Q_p$  in its two remaining arguments, yields

$$Q_p = L^{y_t} \left[ r_{0i} + r_{1i}(K_i - K_{ci})L^{y_t} + r_{2i}(K_i - K_{ci})^2 L^{2y_t} + r_{3i}(K_i - K_{ci})^3 L^{3y_t} + r_{4i}(K_i - K_{ci})^4 L^{4y_t} + b_{1i}L^{y_1} + d_i L^{y_1 - y_t} + c_i(K_i - K_{ci}) \right]. \quad (9.12)$$

The leading contribution is seen to diverge with  $L$  as  $L^{y_t}$ . This is a much stronger divergence than that of the specific heat which displays only weakly divergent behavior as  $L^{2y_t - 3}$ . Therefore,  $Q_p$  is more suitable than  $C$  to determine the temperature exponent  $y_t$ . The free parameters in Eq. (9.12) were fitted according to the least-squares criterion. The critical points were fixed at their best estimates that will be listed later (see Tab. 9.7). The results are shown in Tab. 9.6.

Table 9.6: Separate fits to the derivative  $Q_p$  of the Binder ratio with the irrelevant exponent fixed at  $y_1 = -0.82$ . The minimum system sizes used for this fit are  $L = 8$ .

Model	$r_0$	$y_t$	$b_1$
1	0.822 (2)	1.5871 (4)	-0.057 (6)
2	1.351 (3)	1.5874 (4)	-0.073 (10)
3	1.439 (4)	1.5866 (4)	0.09 (2)
4	1.062 (2)	1.5872 (1)	0.00

## 9.4 Simultaneous finite-size-scaling analyses

### 9.4.1 Simultaneous analysis of $Q$

The results of Sec. 9.3 indicate that the four models under investigation belong to the same universality class. We thus assume that the universal parameters of these four models are exactly equal and we analyze the combined numerical data for  $Q$  of these systems simultaneously. Separation of the universal and nonuniversal constants in Eqs. (9.3) and (9.4) yields

$$\begin{aligned}
 Q = & Q^{(0)} + Q^{(1)} a_i (K_i - K_{ci}) L^{y_t} + Q^{(2)} a_i^2 (K_i - K_{ci})^2 L^{2y_t} + Q^{(3)} a_i^3 (K_i - K_{ci})^3 L^{3y_t} + \\
 & Q^{(4)} a_i^4 (K_i - K_{ci})^4 L^{4y_t} + c_i (K_i - K_{ci})^2 L^{y_t} + b_{1i} L^{y_1} + b_{2i} L^{y_2} + b_{3i} L^{y_3} + \dots + \\
 & d_i (K_i - K_{ci}) L^{y_t + y_1} + \dots, \tag{9.13}
 \end{aligned}$$

where we abbreviated  $Q^{(j,0)}$  as  $Q^{(j)}$  and combined the other  $Q^{(k,l)}$  with their nonuniversal prefactors into constants denoted  $c_i$  and  $b_{li}$ . The term with amplitude  $c_i$  is due to the nonlinear dependence of the temperature field  $t$  as a function of  $K_i$ . The exponent of the leading correction term  $y_1$  was left free to be fitted, while the other two exponents  $y_2$  and  $y_3$  were set at the literature values as given above.

In this type of simultaneous fit, the universal constants  $Q^{(j)}$  and the exponents appear only once, so that the total number of free parameters is reduced appreciably. Also the effect mentioned in Sec. 9.1 contributes to the accuracy of the fit, in particular to that of the irrelevant exponent  $y_1$ . The results, which are summarized in Tab. 9.7, do indeed display a substantially improved accuracy in comparison with those of the separate fits.

### 9.4.2 Simultaneous analysis of $\chi$

We rewrite the parameters  $p_{ji}$  as the product of universal expansion parameters  $\chi^{(j)}$  of the function  $\chi$  in the right-hand side of Eq. (9.8) in its first argument, and nonuniversal

Table 9.7: Results of simultaneous fits to the ratio  $Q$ .

$Q^{(0)}$ 0.62350(3)	$y_1$ -0.818(3)		
$Q^{(1)}$ 1 (fixed)	$Q^{(2)}$ 0.85(2)	$Q^{(3)}$ -3.21(9)	$Q^{(4)}$ -6.0(14)
$K_{c1}$ 0.36973985(4)	$K_{c2}$ 0.22165462(2)	$K_{c3}$ 0.034326874(4)	$K_{c4}$ 0.39342219(4)
$a_1$ 0.5118(8)	$a_2$ 0.846(3)	$a_3$ 4.98(3)	$a_4$ 0.6637(10)
$b_{11}$ 0.1092(12)	$b_{12}$ 0.0908(11)	$b_{13}$ -0.226(5)	$b_{14}$ -0.0034(5)

expansion parameters  $a_i$  and  $w_i$ . Then Eq. (9.8) changes into

$$\begin{aligned}
\chi = & x_i + s_i(K_i - K_{ci}) + L^{2y_h-d} w_i [\chi^{(0)} + \chi^{(1)} a_i (K_i - K_{ci}) L^{y_t} + \chi^{(2)} a_i^2 (K_i - K_{ci})^2 L^{2y_t} \\
& + \chi^{(3)} a_i^3 (K_i - K_{ci})^3 L^{3y_t} + \chi^{(4)} a_i^4 (K_i - K_{ci})^4 L^{4y_t} + \sum_k b_{ki} L^{y_k} \\
& + c_i (K_i - K_{ci}) L^{y_t+y_1} + \dots], \tag{9.14}
\end{aligned}$$

where we have expanded the temperature field as in Eq. (9.3).

Fits were made to the Monte Carlo data for  $\chi$  on the basis of Eq. (9.14). The results are presented in Tab. 9.8. Just as for  $Q$ , the scale of the temperature and magnetic scaling fields may be chosen freely so that we may fix two parameters, namely  $\chi^{(0)} = \chi^{(1)} = 1$  in Eq. (9.14) during the fit. Again the reduction of the number of free parameters is accompanied by an improved accuracy of the results.

Table 9.8: Results of simultaneous fits to the magnetic susceptibility  $\chi$  with  $\chi^{(0)} = 1$  and  $\chi^{(1)} = 1$  fixed .

$y_h$ 2.48160(6)	$\chi^{(2)}$ 0.439(4)	$\chi^{(3)}$ -0.040(5)	$\chi^{(4)}$ -0.12(2)
$K_{c1}$ 0.36973983(4)	$K_{c2}$ 0.22165461(2)	$K_{c3}$ 0.034326877(3)	$K_{c4}$ 0.39342217(4)
$w_1$ 1.7559(9)	$w_2$ 1.5536(8)	$w_3$ 0.8762(5)	$w_4$ 0.9347(4)
$a_1$ 1.990(3)	$a_2$ 3.28(2)	$a_3$ 19.4(10)	$a_4$ 2.608(6)

### 9.4.3 Simultaneous analysis of $Q_p$

Separation of the universal parameters following from the expansion of the universal function  $Q_p$  in Eq. (9.11) and the nonuniversal ones yields

$$Q_p = L^{y_t} z_i [Q_p^{(0)} + Q_p^{(1)} a_i (K_i - K_{ci}) L^{y_t} + Q_p^{(2)} a_i^2 (K_i - K_{ci})^2 L^{2y_t} + Q_p^{(3)} a_i^3 (K_i - K_{ci})^3 L^{3y_t} + Q_p^{(4)} a_i^4 (K_i - K_{ci})^4 L^{4y_t} + b_i L^{y_1} + d_i L^{y_1 - y_t} + c_i (K_i - K_{ci})], \quad (9.15)$$

where the universal parameters  $Q_p^{(j)}$  are determined by the function  $Q_p$ . The nonuniversal parameters  $p_i$  are defined as  $\partial t / \partial K_{nn}$  for the  $i$ th model. As above we took the critical points from Tab. 9.7 as fixed parameters in the fitting procedure. The results of these least-squares fits of Eq. (9.15) to the Monte Carlo results are shown in Tab. 9.9. We performed several variations of this procedure. For instance we included a term proportional to  $L^{y_t + y_1} (K_i - K_{ci})$  in the square brackets of Eq. (9.15). However, this did not lead to a clear reduction of the residual  $\chi^2$  of the fit. The uncertainty margins shown in Tab. 9.9 include the variations due to different procedures, and the dependence on the cutoff at small system sizes.

Table 9.9: Result of simultaneous fits to the numerical data for  $Q_p$ .

$Q_p^{(0)}$ 1 (fixed)	$Q_p^{(1)}$ 0.1 (fixed)	$Q_p^{(2)}$ −9.0(7)	$Q_p^{(3)}$ −7.2(6)	$Q_p^{(4)}$ 50(8)
$y_t$ 1.58718(8)	$z_1$ 0.8215(3)	$z_2$ 1.3526(6)	$z_3$ 1.4372(6)	$z_4$ 1.0606(3)

## 9.5 Discussion

By means of an analysis of extensive Monte Carlo simulations of four three-dimensional Ising-like models, we have succeeded in refining the results for several universal constants of the Ising universality class. Furthermore, the margins for deviations from universality between the four models are reduced, which is significant because a rigorous basis for universality is still lacking. The present confirmation of universality is in line with earlier findings [5, 29]. The results obtained in the simultaneous fit allow an additional confirmation of universality. The derivative  $a_i$  of the temperature field to the coupling of the  $i$ th model occurs in the expansion of  $Q$  as well as in that of  $\chi$ . Table 9.10 accordingly displays the ratio  $a_i^{(Q)} / a_i^{(\chi)}$  for the four models. The results are clearly in agreement with universality.

The improvement of the results in comparison with Ref. [5] is based on better statistical accuracies, and simulation of larger systems of size  $L = 256$ . The four models were selected such that the irrelevant field covers a wide range. On the one side of this range we have the

Table 9.10: Results for the ratio  $a_i^{(Q)}/a_i^{(\chi)}$  where the superscripts refer to the expansion parameters used in the fits for  $Q$  and  $\chi$  respectively.

Model	1	2	3	4
ratio	0.257(1)	0.258(3)	0.257(3)	0.255(2)

model on the diamond lattice with only 4 nearest neighbors, and on the other side we have the equivalent-neighbor model on the simple-cubic lattice with four layers of neighbors, which is, as illustrated in Fig. 9.1, relatively close to the mean-field model in terms of crossover between the mean-field and Ising fixed points.

In agreement with earlier findings, the simultaneous analysis of the Monte Carlo data helps to reduce the uncertainly margins, especially for the errors of the irrelevant exponent  $y_1$  and of quantities, like the Binder ratio  $Q$ , that are sensitive to the value of  $y_1$ .

The reduction of the error margins in our final results is not a simple and direct result of the better statistics of the Monte Carlo data. Reduction of the statistical errors can reveal new corrections to the leading scaling behavior that were below the detection threshold in earlier analyses. For instance, this applies to the correction term with exponent  $y_1 - y_t$  in the analysis of  $Q_p$ . Since the addition of new free parameters in the fit formula typically increases the statistical error margins of the results, the improvement of the results is less than expected on the basis of statistics only. Another problem with a similar effect is that the cutoff at small systems may have to be chosen at a larger value of  $L$ .

Our results are summarized in Tabs. 9.11 and 9.12. These tables also include some existing results for easy comparison.

Table 9.11: Comparison between present results and existing values for the critical points.

Model	$K_c$ (present)	$K_c$ Ref. [5]	$K_c$ (other refs.)	$K_c$ (other refs.)
1	0.36973985(4)	0.36973980(9)	0.36978(4) [30]	0.3697(8) [31]
2	0.22165462(2)	0.22165455(5)	0.2216546(10) [9]	0.221655(2) [37]
3	0.034326874(4)	0.03432687(2)	0.03432685(15) [27]	
4	0.39342219(4)	0.39342225(9)	0.3934220(7) [9]	

Table 9.12: Comparison between the present results for the renormalization exponents and the universal ratio  $Q^{(0)}$  for the three-dimensional Ising universality class and literature values. The methods to obtain these results are abbreviated as follows: RG – renormalization of  $\phi^4$  model; HTE – high-temperature series expansion; MC – Monte Carlo and finite-size scaling; MCRG – Monte Carlo renormalization; CAM – coherent-anomaly method.

Refs.	Year	$y_t$	$y_h$	$y_1$	$Q^{(0)}$	Method
Le Guillou <i>et al</i> [2]	1980	1.587(4)	2.485(2)	-0.79(3)		RG
Nickel and Rehr [32]	1990	1.587(4)	2.4821(4)	-0.83(5)		HTE
Nickel [33]	1991	1.587	2.4823	-0.84		HTE
Baillie <i>et al</i> [34]	1992	1.602(5)	2.4870(15)	-0.825(25)		MCRG
Landau [35]	1994	1.590(2)	2.482(7)			MC
Kolesik <i>et al</i> [36]	1995	1.586(4)	2.482(4)			CAM
Blöte <i>et al</i> [9]	1995	1.587(2)	2.4815(15)	-0.82(6)	0.6233(4)	MC
Blöte <i>et al</i> [10]	1996	1.585(2)	2.4810(10)			MCRG
Guida <i>et al</i> [3]	1998	1.586(3)	2.483(2)	-0.799(11)		RG
Blöte <i>et al</i> [28]	1999	1.5865(14)	2.4814(5)	-0.82(3)	0.62358(15)	MC
Campostrini <i>et al</i> [4]	2002	1.5869(4)	2.48180(15)	-0.82(5)		HTE
Deng and Blöte [5]	2003	1.5868(3)	2.4816(1)	-0.821(5)	0.62341(4)	MC
Butera and Comi [37]	2005	1.5870(5)	2.4818(4)			HTE
Present	2006	1.58718(8)	2.48160(6)	-0.818(3)	0.62350(3)	MC

# Bibliography

- [1] K. G. Wilson and M. E. Fisher, Phys. Rev. Lett. **28**, 240 (1972).
- [2] J. C. Le Guillou and J. Zinn-Justin, J. Physique **48**, 19 (1987).
- [3] R. Guida and J. Zinn-Justin, J. Phys. A **31**, 8103 (1998).
- [4] M. Campostrini, A. Pelissetto, P. Rossi and E. Vicari, Phys. Rev. E **65**, 066127 (2002).
- [5] Y. Deng and H. W. J. Blöte, Phys. Rev. E **68**, 036125 (2003).
- [6] A. Yamagata, Physica A **222**, 119 (1995).
- [7] A. Yamagata, Physica A **231**, 495 (1996).
- [8] J. García, J. A. Gonzalo, and M. I. Marqués, preprint, cond-mat/0211270.
- [9] H. W. J. Blöte, E. Luijten and J. R. Heringa, J. Phys. A **28**, 6289 (1995).
- [10] H. W. J. Blöte, J. R. Heringa, A. Hoogland, E.W. Meyer and T. S. Smit, Phys. Rev. Lett. **76**, 2613 (1996).
- [11] M. Blume, Phys. Rev. **141**, 517 (1966).
- [12] H. W. Capel, Physica A **32**, 966 (1966); Phys. Lett. **23**, 327 (1966).
- [13] E. Luijten, H. W. J. Blöte and K. Binder, Phys. Rev. E **54**, 4626 (1996).
- [14] B. Nienhuis, A. N. Berker, E. K. Riedel and M. Schick, Phys. Rev. Lett. **43**, 737 (1979).
- [15] A. L. Talapov, H. W. J. Blöte and L. N. Shchur, Pis'ma v ZhETF **62**, 157 (1995); JETP Lett. **62**, 174 (1995).
- [16] U. Wolff, Phys. Rev. Lett. **60**, 1461 (1988).
- [17] E. Luijten and H. W. J. Blöte, Int. J. Mod. Phys. C **6**, 359 (1995).
- [18] A. Hoogland, J. Spaa, B. Selman and A. Compagner, J. Comp. Phys. **51**, 250 (1983).

- [19] M. N. Barber, R. B. Pearson, D. Toussaint and J. L. Richardson, *Phys. Rev. B* **32**, 1720 (1985).
- [20] G. Parisi and F. Rapuano, *Phys. Lett. B* **157**, 301 (1985).
- [21] A. Hoogland, A. Compagner and H. W. J. Blöte, *Physica A* **132**, 593 (1985).
- [22] G. Bhanot, D. Duke and R. Salvador, *Phys. Rev. B* **33**, 7841 (1986).
- [23] A. Hoogland, A. Compagner and H. W. J. Blöte, *The Delft Ising System Processor*, Chapter 7 of *Architecture and Performance of Specialized Computers*, edited by B. Alder, in the series *Computational Techniques* (Academic, New York, 1988).
- [24] A. M. Ferrenberg, D. P. Landau and Y.J. Wong, *Phys. Rev. Lett.* **69**, 3382 (1992).
- [25] L. N. Shchur and H. W. J. Blöte, *Phys. Rev. E* **55**, 4905R (1997).
- [26] K. Binder, *Z. Phys. B* **43**, 119 (1981).
- [27] E. Luijten, *Phys. Rev. E* **59**, 4997 (1999).
- [28] H. W. J. Blöte, L. N. Shchur, and A. L. Talapov, *Int. J. Mod. Phys. C* **10**, 1137 (1999).
- [29] P. Butera and M. Comi, *Phys. Rev. B* **69**, 174416 (2004).
- [30] M. F. Sykes and D.S. Gaunt, *J. Phys. A* **6**, 643 (1973).
- [31] O. G. Mouritsen, *J. Phys. C* **13**, 3909 (1980).
- [32] B. G. Nickel and Rehr, *J. Stat. Phys.* **61**, 1 (1990).
- [33] B. G. Nickel, *Physica A* **177**, 189 (1991).
- [34] C. F. Baillie, R. Gupta, K. A. Hawick, and G. S. Pawley, *Phys. Rev. B* **45**, 10 438 (1992).
- [35] L. D. Landau, *Physica A* **205**, 41 (1994).
- [36] M. Kolesik and M. Suzuki, *Physica A* **215**, 138 (1995).
- [37] P. Butera and M. Comi, *Phys. Rev. B* **72**, 14442 (2005).

# Summary

Finally, let me summarize the work presented in this thesis. I gave an account of my PhD work during the last four years, which was done in collaboration with several others. The subjects we investigated mainly focus on critical phenomena and phase transitions of spin models on low dimensional lattices. The techniques used in this thesis are based on combinations of numerical analysis and analytical and mathematical tools, such as renormalization theory, mean-field approach, lattice mappings, and conformal transformations. The numerical results were obtained by existing and newly developed computational tools that include transfer-matrix techniques and Monte Carlo methods. One key aspect of these algorithms is their efficiency. We have attempted to improve this aspect in order to be able to compute numerical data of a good accuracy, and to study systems with sizes that are as large as possible.

For instance, during the work on the triangular antiferromagnetic Ising model in a field in Chaps. 2 and 3, we have been able to apply transfer matrices to relatively large system sizes, and the geometric cluster algorithm was found quite effective. Extensive studies were done for two models, one without next-nearest-neighbor interactions ( $K_{\text{nnn}}$ ), and the other with such interactions. For  $K_{\text{nnn}} = 0$ , we determined a critical line of field-induced three-state Potts-like phase transitions at nonzero temperatures, ending in a KT-like critical point at zero temperature in a finite value of the reduced field. We also analyzed the shape of the critical line in the vicinity of the KT point. The numerical results appear to be inconsistent with a theoretical scenario based on the  $O(2)$  invariance of a related vertex model. The assumptions underlying this scenario thus appear to be wrong.

For the case including ferromagnetic interactions with next-nearest neighbors, we obtained the phase diagram in the three-parameter  $(K_{\text{nn}}, K_{\text{nnn}}, H)$  space. A tricritical line of phase transitions was located which separates the sheet of phase transitions into a part of critical transitions and a part of discontinuous transitions.

In the next chapter (Chap. 4), we perform a comparison of several simulation algorithms for simulating the random cluster model with continuous values of  $q$ . The algorithms include a full cluster decomposition Chayes-Machta algorithm, a version of the local bond-update Sweeny algorithm, an uncorrelated reweighting Hu algorithm, and a newly formulated single cluster algorithm. The comparison indicates that for non-integer  $q$ , the full cluster decomposition algorithm is the most efficient one. Applications of this algorithm and a slightly modified version are given in the next two chapters.

In Chap. 5, we explore percolation phenomena on a substrate formed by one of the

$q$  colors of the Potts model. We include several cases that include  $q < 2$ ,  $q = 2$ , and  $q > 2$ . By using the cluster algorithm for the Potts models with continuous values of  $q$ , we are also able to include a model with noninteger value of  $q$ , for which we choose  $q = 2 - 2 \cos(7\pi/18) (= 1.3159\dots)$ . We determined the phase diagram of this percolation problem for  $T_c \leq T \leq \infty$ . For  $T \downarrow T_c$ , the topology of the phase diagrams appears to depend on the value of the  $q$ . The Ising model ( $q = 2$ ) turns out to be special. We explain this on the basis of the symmetry between the selected Potts state and the remaining states taken together. In this context we also performed a somewhat different analysis of the  $q = 3$  Potts model, different in the sense that we form percolation clusters on the basis of two out of three Potts colors. The resulting behavior then appears to bear some resemblance to the earlier case  $q = 2 - 2 \cos(7\pi/18)$ .

Chap. 6 presents a study of the dilute Potts model. The main purpose is to perform a sensitive test of the renormalization scenario of the Potts model. We include vacancies and determine a line of fixed points for  $0 < q \leq 4$  without vacancy-vacancy coupling. This fixed line appears to contain a critical and a tricritical branch. For a special case of  $q = 2 - \sqrt{2}$ , we introduce nonzero vacancy-vacancy coupling, and determine the phase diagram in the parameter space  $(K, V, D)$ . The diagram contains a special point associated with the critical  $q + 1$ -state Potts model, a line of tricritical transitions, a critical Potts sheet, a first-order sheet, and a line of Ising transitions. Our findings confirm the renormalization scenario perfectly. Furthermore, we study geometric properties of tricritical Potts clusters, using several of the accurately located fixed points for noninteger values of  $q$ . We confirmed a conjectured correspondence between the random cluster fixed point of critical Potts models and the geometric fixed point of tricritical Potts models.

The study of the Ising model by Luijten *et al.*, shows no sign of a first-order transition when the range of the interactions is increased. The question arises whether this holds for other values of  $q$ . For this reason, we investigate two dimensional  $q = 3$  and  $4$  Potts models with a variable interaction range, as reported in Chap. 7. We find that the  $q = 3, 4$  Potts models undergo first-order transitions when the range of interactions is sufficiently large.

In Chap. 8, we study an  $n$ -component cubic model with  $-2 \leq n \leq 2$  on the square lattice using transfer matrix techniques. This model is chosen such that an expansion exists in Ising-like graphs. We located a line of critical points as a function of  $n$ , and also studied their universal quantities, such as temperature, magnetic, and interface exponents.

In the absence of an exact solution of the three-dimensional Ising model, one requires numerical data that are as accurate as possible, in order to determine the universal parameters of the 3D Ising universality class. With the assistance of efficient cluster algorithms and fast personal computers, analysis of large system sizes becomes possible. Here, we have generated numerical data for system sizes up to  $L = 256$ . These are analyzed in Chap. 9. The new simulations enable us to improve the accuracy of several universal quantities.

# Samenvatting

Tenslotte geef ik een samenvatting van dit proefschrift over mijn promotieonderzoek van de afgelopen vier jaar. De onderwerpen liggen op het gebied van de kritieke verschijnselen en faseovergangen van spinmodellen. De in dit proefschrift gebruikte technieken combineren numerieke analyse met analytische en wiskundige hulpmiddelen, zoals renormalisatie en moleculaire-veld theorie, afbeeldingen tussen roostermodellen en conforme transformaties. De numerieke gegevens zijn verkregen met bestaande, maar ook met nieuw ontwikkelde rekenmethoden, met inbegrip van transfermatrixtechnieken en Monte Carlo simulaties. Een hoeksteen van deze algoritmen is hun efficiëntie. We hebben hier veel aandacht aan besteed, om nauwkeurige gegevens voor zo groot mogelijke systemen te kunnen verkrijgen.

Bijvoorbeeld, tijdens het werk aan de triangulaire Ising antiferromagneet in een veld in Chaps. 2 en 3 konden we transfermatrices toepassen op betrekkelijk grote systemen, terwijl ook de ‘geometrische Monte Carlo methode’ erg effectief bleek. Uitgebreid onderzoek vond plaats aan twee modellen, een met wisselwerking tussen naaste burens, en het andere met bovendien wisselwerking  $K_{\text{nnn}}$  met volgende-naaste burens. Voor  $K_{\text{nnn}} = 0$  hebben we de kritieke lijn van veld-geïnduceerde drie-toestanden Potts-achtige overgangen bij eindige temperaturen bepaald. Deze lijn eindigt bij temperatuur nul in een KT-achtig kritiek punt, bij een eindige waarde van het gereduceerde veld. Analyse van de vorm van de lijn nabij dit KT punt heeft aangetoond dat de numerieke resultaten niet kloppen met een theoretisch scenario gepostuleerd op basis van de  $O(2)$  symmetrie van een equivalent vertexmodel. De in dit scenario gebruikte aanname blijkt dus onjuist.

We hebben het fasediagram van het model bepaald als functie van drie parameters  $(K_{\text{nn}}, K_{\text{nnn}}, H)$ , voor  $K_{\text{nnn}} \geq 0$ . Het bevat o.a. een vlak van drie-toestanden Potts kritieke punten, door een trikritieke lijn gescheiden van een vlak van discontinue overgangen.

In het volgende hoofdstuk (Chap. 4) vergelijken we enkele algoritmen voor de simulatie van het random-cluster model met niet-geheeltalig aantal toestanden  $q$ . Deze algoritmen zijn de volledige clusterdecompositie volgens Chayes-Machta, een versie van de bond-update algoritme volgens Sweeny, een ongecorrleerde simulatie met statistische herweging volgens Hu, en een nieuwe algoritme die bestaat uit afzonderlijke clusterstappen. Vergelijking van deze methoden toont aan dat, voor niet-geheeltalige  $q$ , de methode met de volledige clusterdecompositie de meest efficiënte is. Toepassingen van deze algoritmen, en van varianten ervan, worden gegeven in de volgende twee hoofdstukken.

In Chap. 5 onderzoeken we percolatieverschijnselen op een substraat bestaande uit Potts variabelen van een van de  $q$  kleuren, voor de gevallen  $q < 2$ ,  $q = 2$ , and  $q > 2$ . Met de cluster algoritme voor het Potts model met continue waarden van  $q$ , kijken we ook naar een model met een niet-geheeltalige  $q$ , namelijk  $q = 2 - 2 \cos(7\pi/18) (= 1.3159\dots)$ .

We bepalen het fasediagram van dit percolatieprobleem voor  $T_c \leq T \leq \infty$ . Voor  $T \downarrow T_c$  blijkt de topologie van het fasediagram af te hangen van  $q$ . Het blijkt dat het Ising geval  $q = 2$  speciaal is. Dit is begrijpelijk op basis van de symmetrie, voor  $q = 2$ , tussen de geselecteerde Potts kleur en de overige kleuren tesamen. In dit verband hebben we het geval  $q = 3$  nog op een andere manier bekeken, we hebben namelijk percolatieclusters gevormd op een substraat gevormd door twee van de drie kleuren. Het gedrag blijkt nu te lijken op dat van het eerder genoemde geval  $q = 2 - 2 \cos(7\pi/18)$ .

Het volgende hoofdstuk (Chap. 6) gaat over het verdunde Potts model. Het doel is een nauwkeurige test van het renormalizatiescenario voor het Potts model. We introduceren een extra Potts toestand nul, die correspondeert met een vakature. We bepalen een lijn van vaste punten voor  $0 < q \leq 4$  voor het geval dat vakatures niet wisselwerken. De vaste lijn bevat een kritieke en een trikritieke tak. Voor het geval  $q = 2 - \sqrt{2}$  en koppeling  $V$  tussen naburige vakatures bepalen we het fasediagram in een ruimte van drie parameters. Het bevat een  $q+1$ -toestanden Potts kritiek punt, een lijn van Potts trikritieke punten, een vlak van Potts kritieke punten, een vlak van eerste-orde overgangen, en een lijn van Ising overgangen. Onze resultaten stemmen volmaakt overeen met het renormalizatiescenario. Vervolgens hebben we geometrische aspecten van trikritieke Potts clusters bestudeerd, op basis van de genoemde resultaten voor de vaste punten voor niet-geheeltallige  $q$ . We bevestigen een bestaand vermoeden omtrent de equivalentie van random-cluster kritieke punten en geometrische vaste punten van trikritieke Potts modellen.

Een onderzoek van Luijten *et al.* aan het Ising model levert geen evidentie voor eerste-orde overgangen wanneer het aantal wisselwerkende burens toeneemt. We onderzoeken of dit ook het geval is voor Potts modellen met  $q > 2$ . We doen dit voor modellen met  $q = 3$  en  $4$  in twee dimensies met interacties van een variabele dracht, zoals beschreven in Chap. 7. We vinden dat de overgang van Potts modellen met  $q = 3$  en  $4$  discontinu worden boven een bepaalde dracht.

In Chap. 8 onderzoeken we, met gebruik van transfermatrices, een  $n$ -componenten kubisch model met  $-2 \leq n \leq 2$  op het vierkante rooster. Het model is zodanig gekozen dat een expansie bestaat in diagrammen die afbeelden op Isingconfiguraties. We bepalen de kritieke lijn van dit model als functie van  $n$ , alsmede enige universele parameters zoals de magnetische, de thermische, en de interface exponenten.

Het ontbreken van een exacte oplossing van het driedimensionale Ising model maakt een zo nauwkeurig mogelijke numerieke aanpak nodig om de onbekende parameters van de betreffende universaliteitsklasse te bepalen. Met efficiënte clusteralgoritmen en snelle PC's wordt het mogelijk om betrekkelijk grote systemen te analyseren. We hebben hier data gegenereerd tot systeemgrootte  $L = 256$ . De analyse hiervan gebeurt in Chap. 9. Deze nieuwe simulaties maken het mogelijk om de nauwkeurigheid van enkele universele parameters verder te vergroten.

# Acknowledgments

During the four years of my PhD work, I have benefited from the help and support that I received from many people.

First of all, I should mention my supervisor Prof. Henk Blöte, whose continuous guidance and teaching contributed a lot to this thesis. His wife Anke also helped to create an environment, for work as well as for relaxation, that enabled me to perform the tasks required for this thesis.

Secondly, my thanks go to the people of the Lorentz Institute for the friendly atmosphere they provided. In particular I would like to mention Daniel, Chiara, and Maurizio. I also thank the people from LION and P&O for their help with all kinds of documents, most of which were written in Dutch.

I am also grateful to my coworkers for the interesting collaborations and fruitful discussions. Here I would like to mention Dr. Youjin Deng and Prof. Wenan Guo. I wish to express my thanks to all my other friends, Chinese as well as non-Chinese. Their help meant a great support for my life in Leiden.

Finally I consider it essential to express my thanks to my family for their unlimited support and sacrifice that enabled me to study. They provided the basis from which I could come as far as I now am.



# Curriculum Vitae

I was born on the 9th of October 1976 in Yongxin, a small town in the province Jiangxi, which lies in the south-east part of China. From 1989 to 1995, I received my middle school and high school education in my hometown.

I started my four-year bachelor program at the Physics Department of Jiangxi Normal University in 1995, and obtained my Bachelor of Science degree in 1999. In the same year I continued with my three-year master program in theoretical physics under the guidance of Prof. J. Zhu. Part of this program took place in the group of Prof. Z.R. Yang at the Beijing Normal University. I received my Master of Science degree in July 2002.

In the middle of August 2002, I came to the Netherlands and started my PhD study in the Lorentz Institute of the Leiden University under the supervision of Prof. H.W.J. Blöte, whom I met the first time at the Beijing Normal University. My PhD work mainly focuses on the study of phase transitions and critical phenomena of spin models on lattices, as well as on the development of algorithms for this purpose.



# List of Publications

- X. Qian, M. Wegewijs and H. W. J. Blöte, *Critical frontier of the triangular Ising antiferromagnet in a field*, Phys. Rev. E **69**, 036127 (2004).
- X. Qian and H. W. J. Blöte, *The triangular Ising model with nearest- and next-nearest-neighbor couplings in a field*, Phys. Rev. E **70**, 036112 (2004).
- X. Qian, Y. Deng, and H. W. J. Blöte, *Simulation algorithms for the random-cluster model*, Phys. Rev. E **71**, 016709 (2005).
- X. Qian, Y. Deng, and H. W. J. Blöte, *Percolation in one of  $q$  colors near criticality*, Phys. Rev. B **71**, 144303 (2005).
- X. Qian, Y. Deng, and H. W. J. Blöte, *Dilute Potts model in two dimensions*, Phys. Rev. E **72**, 056132 (2005).
- W. Guo, X. Qian, H. W. J. Blöte, F. Y. Wu, *Critical line of an  $n$ -component cubic model*, Phys. Rev. E **73**, 026104 (2006).
- X. Qian, Y. Deng, H. W. J. Blöte, and A. Sokal, *Equivalent-neighbor Potts models in two dimensions*, in preparation (2006).
- Y. Deng, X. Qian and H. W. J. Blöte, *Single-cluster algorithm for the random-cluster model*, in preparation (2006).
- X. Qian, L. N. Shchur, Y. Deng, and H. W. J. Blöte, *Universal parameters of three-dimensional Ising systems* in preparation (2006).

